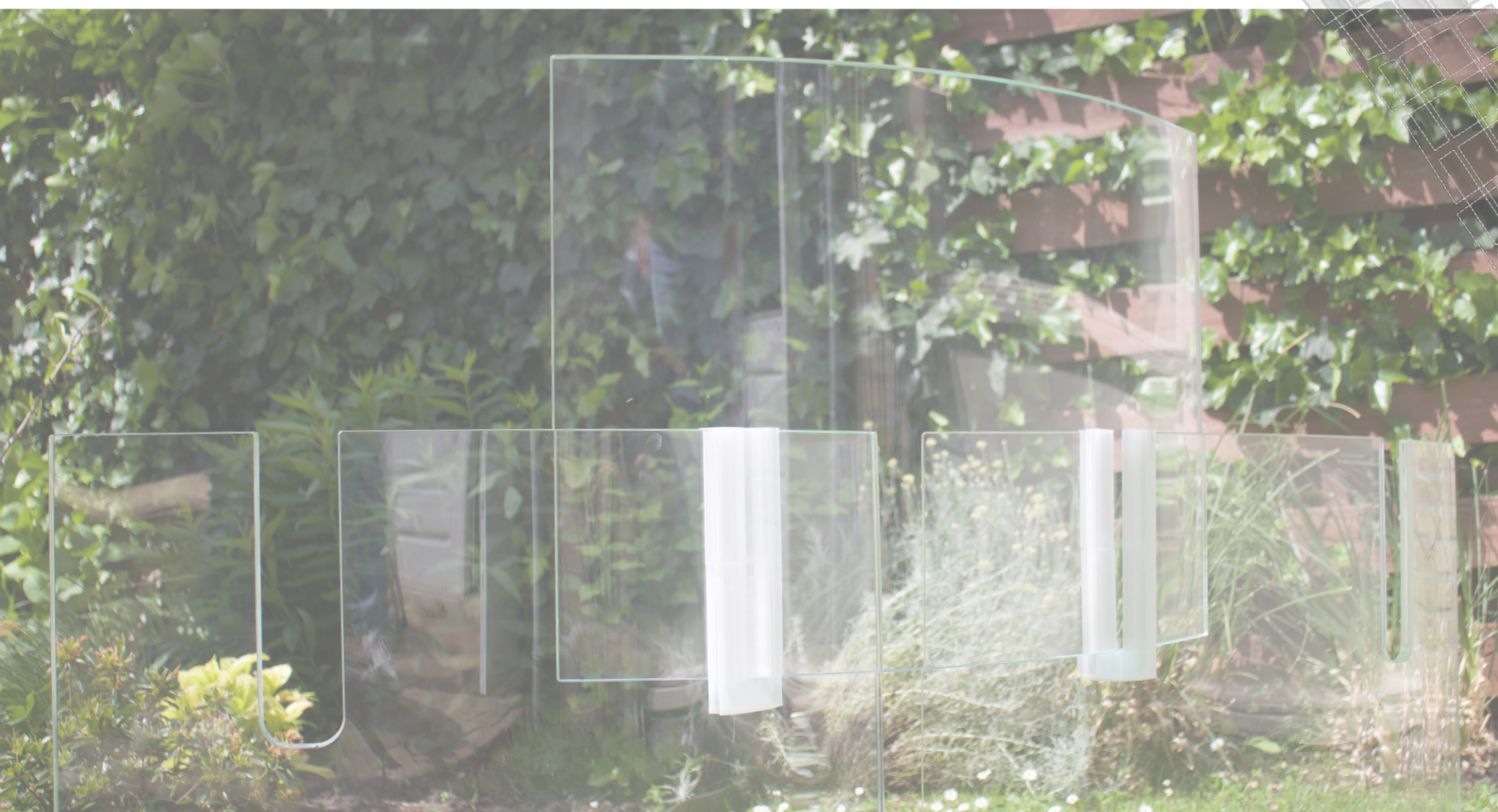
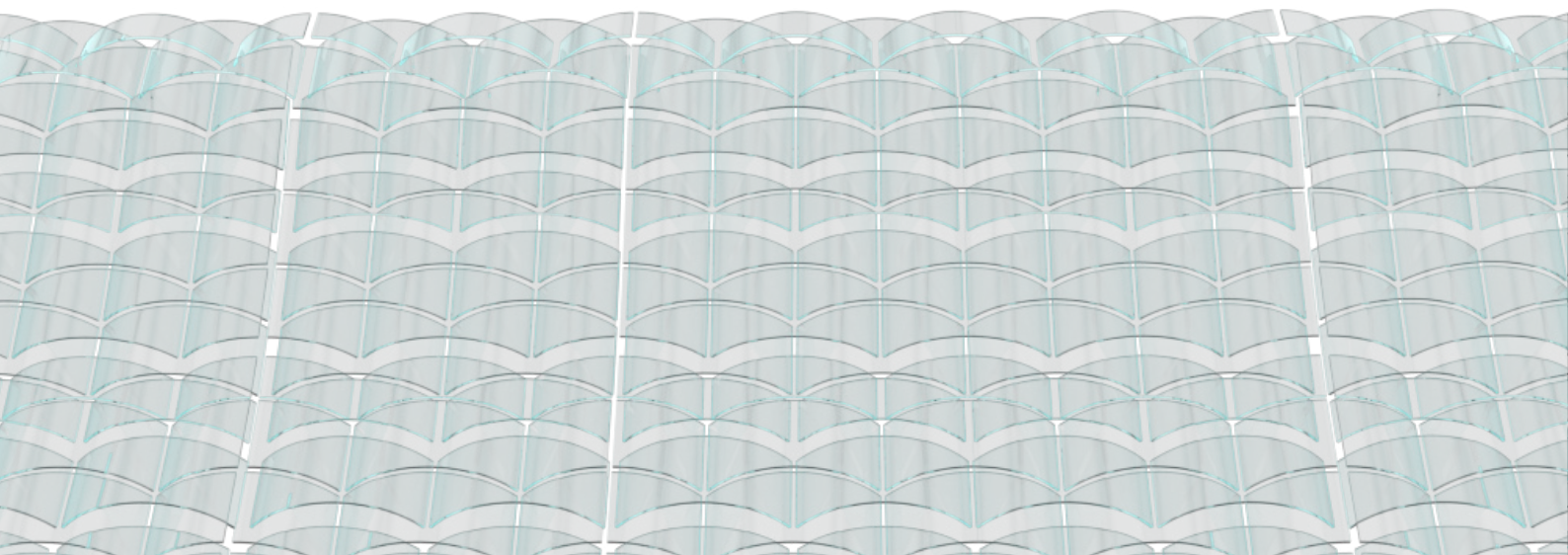




Design of a Reusable Float Glass System

Extending the Life Cycle of Primary Glass Structures





Master Thesis Architecture, Urbanism and Building Sciences
Track: Building Technology

Author

Minke Venus
4998502
May 17th, 2025

1st Mentor

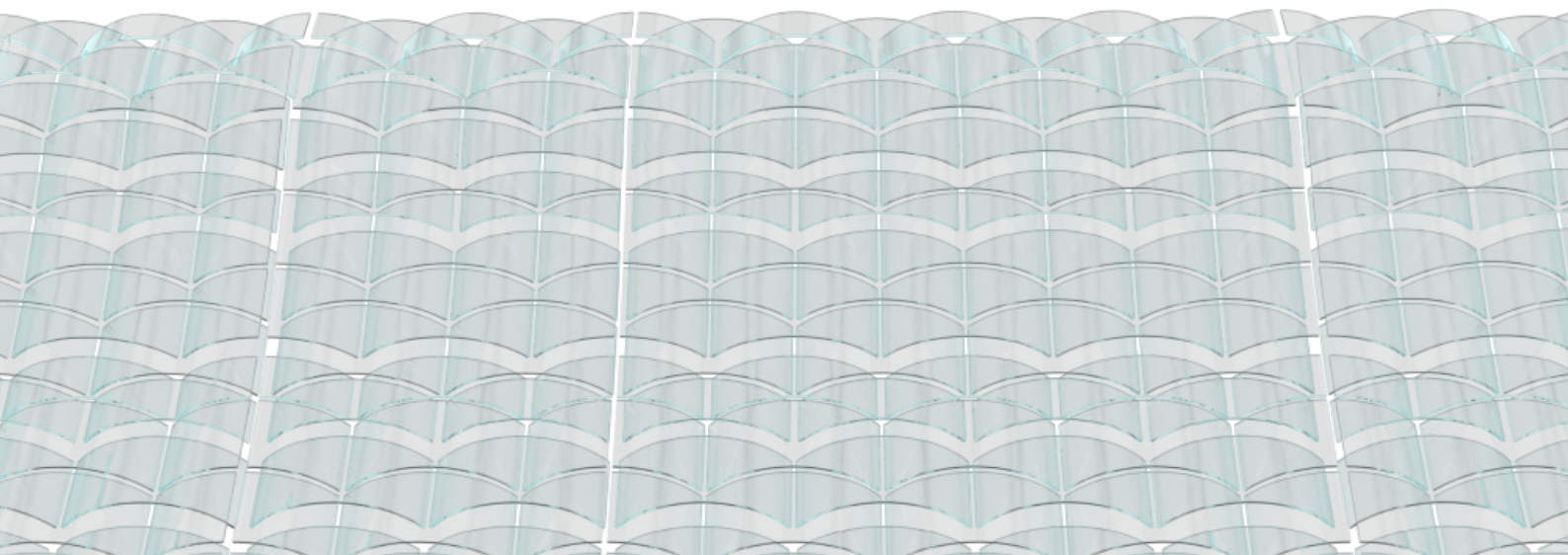
Prof. James O'Callaghan
Architectural Glass TU Delft / EOC Engineers

2nd Mentor

Dr. Gabriele Mirra
Digital Technologies
TU Delft

Delegate of the Board of Examiners

Prof. Dr. Alexandra den Heijer





Acknowledgements

This graduation project gave me the opportunity to combine two fields that I find both fascinating and challenging: structural Design and computational design. What I enjoy most about structural design is when it becomes an integral part of the architectural expression. For that reason, I am especially grateful to have carried out this thesis under the supervision of Prof. James O'Callaghan. His work clearly demonstrates how technology and architecture can seamlessly merge. His insights throughout my design process were invaluable, and I learned a great deal from his way of thinking.

Using computational tools allowed me to explore the spatial possibilities of the system, while simultaneously engaging with the technical aspects through detailed structural analyses and a full-scale laboratory test. I would like to thank my second mentor, Gabriele Mirra, for his support during the computational design process. With his guidance, I was able to deepen my understanding of this field in a relatively short time. I also want to thank Ziead Metwally for his feedback on the structural analysis, and Dr. Fred Veer for his help and advice regarding the laboratory test.

I am also grateful to Tvitec | Cricursa for playing a crucial role in this research by supplying the glass components required for the structural test and final model. This enabled me to evaluate the system in practice, a necessary step toward bringing such a design concept closer to real-world application. Additionally, I would like to thank Van Zijl Constructie B.V. for their quick fabrication of the steel profiles needed for the laboratory test.

Lastly, I want to give special thanks to my study advisor, Sylvia. Throughout my studies, she has always been supportive and approachable.





Abstract

The environmental impact of construction materials, particularly in structural applications, has become a pressing concern in the building industry. A key strategy to reduce this impact is the transition to a circular economy, in which reuse is considered the most effective way to extend the lifespan of a product or component (Platform CB'23, 2019).

Float glass has increasingly been used as a primary load-bearing material in recent decades, driven by the fascination of architects and engineers with its aesthetic and structural qualities (Rammig, 2022). This interest has contributed to significant advancements in its technical development (Giese et al., 2024). Nevertheless, despite the material's inherent durability and its widespread use in both historic and modern contexts, the reuse potential of float glass remains largely underexplored.

This research explores how a reusable float glass system can be designed, enabled by spatial adaptability and modularity. By creating a practical system design, the study encourages designers and researchers to go beyond traditional recycling and consider other circular strategies. In doing so, it explores a potential pathway to extend the functional lifespan of structural glass, reducing waste, conserving resources, and limiting unnecessary energy use.

The study combines theoretical, computational, and experimental research methods. A literature review laid the groundwork for the conceptual design of structural elements and connections and identified key design principles for structural float glass. Using parametric design experimentation, various spatial configurations were explored based on a selected concept: bent laminated glass modules that dry-interlock, allowing for reconfiguration and straightforward assembly. This parametric exploration showed that a system based on two standardized bent float glass modules – each around one meter in length and with two variable heights of up to half a meter to reduce weight and allow manual handling – enables the creation of variable spans of several meters. This is achieved by interlocking the modules at both positive and negative angles and by varying the assembly sequence of the two standardized heights.

Based on these findings, a parametric tool was developed to generate compression-driven forms using the system. These forms are tailored to the span and shape requirements of a specific location, while optimizing both structural weight and ease of assembly.

In the final phase, structural analyses and laboratory testing demonstrated that the adaptable system, made from 2×6 mm fully toughened glass, is structurally feasible when loaded in compression via the slots. A single slot was experimentally shown to withstand at least 2.5 times the design load of 3 kN, accounting for a worst-case configuration of 70 stacked modules – corresponding to a maximum span of approximately 8 meters. If 2×5 mm heat-strengthened glass is to be used, additional testing will be required to verify its structural performance.

Keywords: Float Glass System, Reusable Float Glass, Adaptable System, Modular System

Table of Contents

Acknowledgements

Abstract

1. Introduction
2. Research Framework
 - 2.1 Context
 - 2.2 Problem Statement
 - 2.3 Research Main and Sub-questions
 - 2.4 Boundary Conditions
 - 2.5 Final Products
 - 2.6 Approach and Methodology
 - 2.7 Relevance

PART I : CONCEPT DEVELOPMENT

3. Classification of Adaptable Structural Systems

- 3.1 Modular Structures
- 3.2 Transformable Structures
- 3.3 Case Studies

4. External and Internal Forms for a Lightweight Glass Structure

- 4.1 Mechanical strength of float glass
- 4.2 External and internal geometry

5. Key Design Guidelines

6. Design Concepts for an Adaptable Float Glass Structure

- 6.1 Big scale modularity
- 6.2 Small scale modularity

PART II: DESIGN ELABORATION

7. Design Elaboration

7.1 PART I: Parametric Exploration

- 7.1.1 Research on parameters affecting adaptability
- 7.1.2 Creation of a generative model
- 7.1.3 Case studies
- 7.1.4 Objective functions
- 7.1.5 Multi-objective optimization

7.2 PART II: Preliminary Calculations and Stress Analysis

- 7.2.1 Structural behavior and preliminary hand calculations
- 7.2.2 Parameterization of the slot geometry
- 7.2.3 Ansys structural analysis

7.3 PART III: Structural Verification through Laboratory Testing

- 7.3.1 Laboratory test setup
- 7.3.2 Pre-test calculations for required materials
- 7.3.3 Test preparations
- 7.3.4 Test execution and results

8. Conclusion

9. Discussion and further research

References

Appendix

1. Introduction

The historical development of float glass – from limited transparent cast glass window panes in Roman times (Giese et al., 2024) to the first clear structural glass beams in the 1980s (Jóźwik, 2022) – illustrates how technical innovations have enhanced both the visual quality and structural performance of the material. As a result, glass has evolved into a structural material that is increasingly used not just as cladding, but also as a primary load-bearing element now competing with traditional structural materials (Barou et al., 2018).

While the architectural and technological potential of structural float glass has received attention, concerns about the environmental impact of building materials are growing. The construction sector accounts for approximately 40% of global greenhouse gas emissions (Alexandrou et al., 2022), with structural systems contributing significantly due to high material consumption, energy-intensive production, and waste generation over their lifecycle (Dalalbashi et al., 2024).

A key strategy to mitigate this impact is the transition to a circular economy, which extends the lifespan of materials while minimizing waste, resource depletion, and unnecessary energy consumption. Reuse is one of the most effective approaches (Platform CB'23, 2019). It is assumed that glass is particularly suitable because it is one of the most durable materials in construction (Rammig, 2022). This thesis therefore focuses on designing a float glass system that is reusable by making it spatially adaptable and manageable to build by a small team, leading to the central research question:

“Which structural elements and connections enable the design of a structurally feasible and spatially adaptable float glass system that can be assembled and disassembled by a small team for reconfiguration at different locations, ensuring its reusability?”

The thesis is divided into two main parts. The first part, Concept Development (Chapters 3, 4, and 5), explores adaptable structures through literature research and examines how both external and internal geometries influence the development of lightweight glass structures. Literature research also informs about key design guidelines for structural glass. This research leads to the development of a conceptual design, which is presented in Chapter 6.

The second part focuses on the Elaboration of the Concept Design, presented in Chapters 7 and 8. Chapter 7 investigates the design parameters that influence the system's adaptability. This insight is used to develop a generative model that produces a range of design options based on the concept. A multi-objective optimization is then performed using this model, aiming to identify solutions that balance ease of assembly and module weight, while also meeting specific site span requirements. Chapter 8 examines the structural feasibility of the proposed system through finite element analysis and laboratory testing.

2. Research framework

2.1 Context

The context outlines the development of glass in recent decades and how it has contributed to the contemporary application of structural float glass in construction. At the same time, modern applications of glass as a structural material show a clear gap between the current state of the art and the steps yet to be taken to make such structures fully circular.

The use of glass as a primary structural material in modern architecture is the result of a long developmental process, characterized by continuous advancements in production that have enhanced both its technical performance and transparency. At the same time, these innovations have fueled a growing demand for glass as a building material (Giese et al., 2024).

Over the centuries, glass has always had a special appeal, although the reasons have changed over time. In ancient and medieval times, glass was a luxury product. It was used in tableware and mosaic work. In the Middle Ages, it was mainly used in buildings of status and glass had a religious significance; stained-glass windows in churches brought the 'divine light' into dark spaces (Giese et al., 2024).

In modern times, the material is still very popular for its transparency, but mainly to create open and light buildings for the benefit of health and cleanliness: core values that became important during the modernist era. Today, glass as a building material is still an inseparable part of modern buildings, where letting daylight in combined with protecting it from outside influences is an important function (Wurm, 2007).

The history of glass production dates back to ancient Mesopotamia and Egypt, where glass was mainly used for decorative objects such as jewellery and vessels around 2500 BC. In Roman times, the first window panes of cast glass appeared. Liquid glass was poured onto a flat, heat-resistant surface and rolled out, producing thick, irregular sheets with limited transparency, suitable for filling small openings (Giese et al., 2024).

During the Middle Ages, new production techniques were developed in Europe. The so-called Crown Glass Method involved spinning molten glass at the end of a rod until it expanded into a disc. (Fig. 1). This produced relatively clear glass, but with limited dimensions and a bulge in the middle, the so-called 'bull's eye' (Fig. 2). Plates of up to half a meter were mainly used in windows of churches, cathedrals, and houses of the bourgeoisie and rich citizens (Giese et al., 2024).



Figure 1: Production of float glass (Giese et al., 2024).



Figure 2: Use of the crown glass method resulting in a "Bull's eye window" (Giese et al., 2024).

In the late 17th century, plate glass was developed, where liquid glass was poured onto a metal table, rolled, and polished (Fig. 3). This allowed for the production of larger, smooth sheets of glass compared to earlier techniques. Due to its high cost, cast glass was primarily used in prestigious applications such as palaces and upscale commercial buildings (Giese et al., 2024).



Figure 3: Production of plate glass (Giese et al., 2024).

During the Industrial Revolution in the eighteenth and nineteenth centuries, glass production was scaled up and increasingly standardized. The cylindrical glass was manufactured by blowing molten glass into a long cylinder (Fig. 4), which was then cut open, reheated, and folded flat. This process made it possible to produce larger sheets of glass than with crown glass, although visible ridges and unevenness remained on the surface. However, by grinding and polishing the glass, a smoother result could be obtained (Giese et al., 2024).

A breakthrough followed with the introduction of a mechanical cylinder-blowing method, in which the glass was no longer blown by hand, but by machine. This led to the production of even larger sheets of cylinder glass that could be up to 12 m long and had a diameter of 80 cm (Giese et al., 2024).



Figure 4: Production of hand-blown cylinder glass (Giese et al., 2024).

In the second half of the 19th century, glass increasingly became a standardized mass-produced product as it became cheaper to produce. This was due to some important innovations: soda, a crucial raw material for glass production, could be extracted more efficiently (Solvay process, 1864), transport improved, and Friedrich and Wilhelm Siemens developed a gas-fired tank furnace in 1861 in which waste heat was recovered. These improvements led to lower prices for sheet glass, so the glass was widely used in railway stations, market halls, department stores, and shopping galleries (Giese et al., 2024).

At the beginning of the 20th century, the Fourcault Process was introduced (1904). In this technique, liquid glass was pulled up through a nozzle using rollers and cut to the desired length (Fig. 5). This process eliminated the labor-intensive and time consuming polishing step required with cast and cylinder glass. This allowed larger sheets of glass to be produced more efficiently, significantly reducing production costs and enabling the mass production of flat glass. This formed the basis for the further standardization of window glass (Giese et al., 2024).

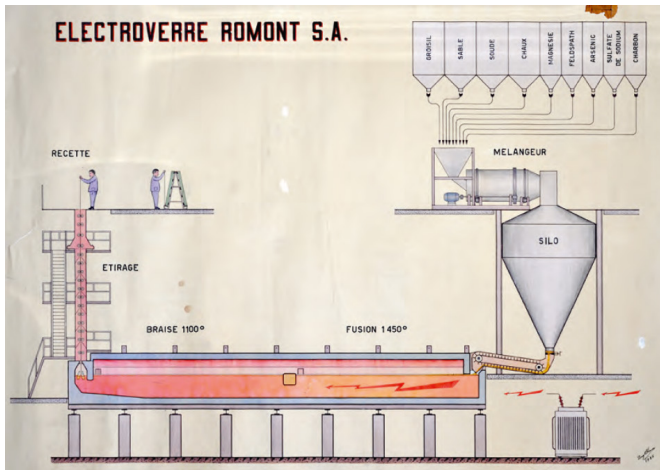


Figure 5: The Fourcault process (Giese et al., 2024).

A real breakthrough came in the 1950s with the introduction of the float glass process, developed by the Pilkington Brothers. In this process, molten glass floats on a bath of liquid tin, allowing completely flat glass of uniform thickness and optical clarity to be produced (Louter, 2011). To this day, it is the most widely used production method for glass for architectural applications. The float glass process enabled the mass production of large, high-quality sheets of glass at a lower cost. Float glass was immediately embraced by modernist architects such as Mies van der Rohe because of the desire for light, transparency, and minimalism. In this period, however, glass was still mainly used as cladding: in windows, curtain walls, and as infill elements, often in combination with steel or concrete (Giese et al., 2024).

In parallel with the development of float glass, new post-treatment techniques emerged during the 20th century to meet stricter safety requirements, thermal insulation needs, and aesthetic preferences. For instance, techniques were introduced to chemically or thermally toughen glass, making it stronger and safer. In addition, glass could now be bent, laminated for extra strength, and tinted or coated for improved functionality and appearance. Furthermore, techniques such as sand-blasting and etching enabled refined surface finishes. These production improvements and the further development of post-treatment techniques allowed increasingly large and more heavily loaded glass elements to be used as a primary load-bearing structural material. Glass was now no longer used exclusively as a cladding material, but also as a structural element (Wurm, 2007).

The use of glass as a primary structural material is mainly aimed at creating transparent architecture (Jóźwik, 2022). Around 1950, the first glass fins were introduced to stabilize storefront windows. From the late 1980s onward, glass beams became increasingly common in roof structures (Wurm, 2007). This development ultimately led to the adoption of various structural systems in all-glass buildings, including frames (a), grills (b), beam-wall systems (c), and plate-wall systems (d) (Fig. 6) (Jóźwik, 2022).

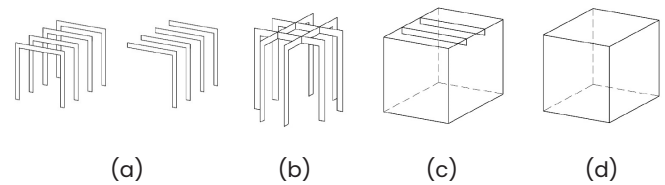


Figure 6: Structural systems used in all-glass buildings (Jóźwik, 2022).

Glass buildings can serve various functions and fit in different architectural contexts, from historical to modern (Barou et al., 2018) & (Jóźwik, 2022). Below are several examples showing this.

Building Entrances

Glass is often used at building entrances to symbolize openness and welcome visitors. A striking example of this is The Apple Cube in New York, built in 2006 (Fig. 7) as an entrance to the underground Apple Store. The original structure consisted of glass panels measuring 3.0 x 6.2 meters, but in 2011, thanks to rapid technological developments, it was replaced by larger glass panels of 10.3 meters high, covering the full height of the building (Fig. 8). By reducing the number of interruptions, transparency was increased (Jóźwik, 2022) & (Rammig, 2022).



Figure 7: Version 1.0 of the Apple Cube in New York (Rammig, 2022).



Figure 8: Version 2.0 of the Apple Cube in New York with improved transparency (Rammig, 2022).

The all-glass entrance to 60 Victoria Embankment in London (Fig. 9) shows how accessibility is emphasized while the design blends with the surrounding historic building. As with the Apple Cube, a grillage system consisting of main beams and cross beams was used here. This system ensures an even distribution of forces across the beams, eliminating the need for columns and maximizing the openness of the entrance (Jóźwik, 2022).



Figure 9: The 60 Victoria Embankment entrance, in London (Jóźwik, 2022).

Exhibition functions

Glass is widely used in pavilions and showcases where optimal transparency is essential to exhibit objects. A good example is the Kubus Export Pavilion in Vienna (Fig. 10), where the glass façade presents the exhibited objects without visual obstructions, thus enhancing the viewing experience.

The glass structure, located under the railway bridge over the Gürtel (Fig. 11), transforms an otherwise unused and enclosed space into an accessible cultural venue. The transparency of the glass breaks the visual barrier of the bridge, emphasizing the connection between the two street sides (Jóźwik, 2022) & (TW-Architects, 2021).



Figure 10: Export Pavilion in Vienna, used as a theater space (TW-Architects, 2001). Photo by Franziska Safrane, Larry Williams, and Bele Marx.

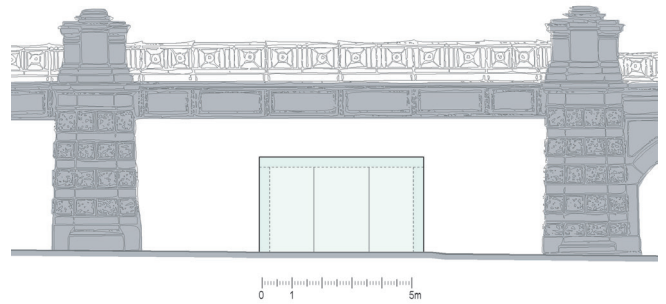


Figure 11: Export Pavilion over the Gürtel in Vienna (TW-Architects, 2001). Photo by Franziska Safrane, Larry Williams, and Bele Marx.

Links and extensions

Links are primarily used to connect different buildings. In Figure 12, a 25-meter-long, 2.5 meter spanning linear structure is positioned at ground level, connecting a 13th-century castle to a foyer. Conversely, Figure 13 depicts an elevated linear walkway in a modern setting, linking a department (Jóźwik, 2022).x

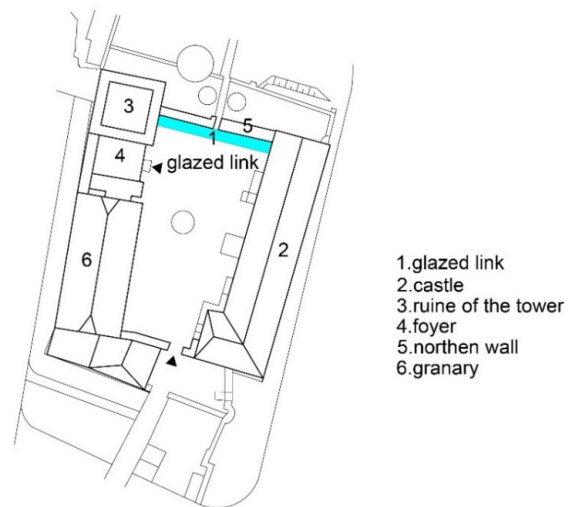


Figure 12: A glazed link connecting two historic buildings (Jóźwik, 2022).



Figure 13: A glazed link connecting modern buildings (Jóźwik, 2022).

Glass as a restoration material

Glass can even be used as a restorative material. It is an appropriate material because of the clear separation the glass creates between the old and the new, while at the same time enhancing the historical experience through its transparency. An example of this is the restoration of the façade of the Augustan Temple in Pozzuoli in Italy (Fig. 14), where glass fins were placed where the original columns once stood (Barou et al., 2018).



Figure 14: Restoration of the façade of the Augustan Temple in Pozzuoli (Barou et al., 2018)

Social gathering places

The Costa Coffee pavilion in London (Fig. 15) is a half glass frame structure built to keep view to the surrounding historic structures and emphasize the relationship between the modern intervention and it's heritage context (Jóźwik, 2022).



Figure 15: Costa Coffee pavilion in London, made of a glass frame system (Jóźwik, 2022).

A similar frame can be seen in the Tea Room Pavilion at the New Visitor Centre in Clevedon (Fig. 16). Here, transparency of the structure had also been employed so as not to restrict the view of the surrounding buildings (Jóźwik, 2022).

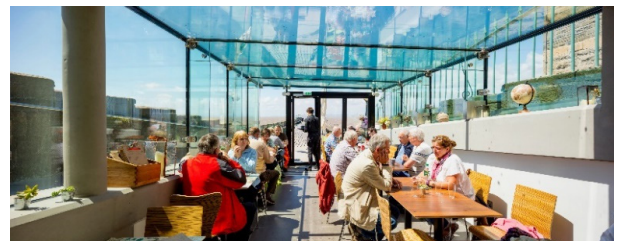


Figure 16: Transparent Tea Room Pavilion (Jóźwik, 2022).

2.2 Problem Statement

The historical evolution of glass technology shows that numerous innovations have enhanced its quality and structural capabilities. As a result, glass has established itself as a competitive structural material alongside traditional alternatives (Barou et al., 2018). To this day, glass continues to fascinate architects and engineers as it challenges them to the limits of their capabilities. This constant pursuit of innovation drives the further development of glass technologies (Rammig, 2022).

While much attention has been given to the architectural and technological potential of float glass, the environmental impact of building materials has become an increasingly critical consideration. The construction sector is responsible for approximately 40% of global greenhouse gas (GHG) emissions (Alexandrou et al., 2022). In particular, load-bearing structures have a substantial environmental footprint due to their high material consumption, energy-intensive production processes, and waste generation throughout their lifecycle (Dalalbashi et al., 2024). Within the EU, construction activities account for an estimated 25% to 30% of total waste production (Bristogianni & Oikonomopoulou, 2023).

The linear life cycle of float glass (Fig. 17) begins with the extraction of raw materials such as silica sand, soda ash, and limestone. These mining activities contribute to the depletion of finite natural resources, cause habitat destruction, and generate CO₂ emissions (Ganapathi & Phukan, 2020).

Following extraction, the production phase involves melting these raw materials at approximately 1600°C. This process is highly energy-intensive, predominantly reliant on fossil fuels, and accounts for a significant share of the glass industry's carbon emissions. Additionally, transportation to manufacturing sites and construction locations further increases fuel consumption and greenhouse gas emissions (Elstner et al., 2024).

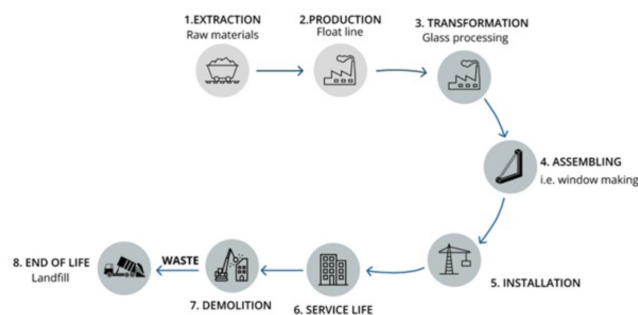


Figure 17: Linear life-cycle of float-glass (Rota et al., 2023)

While glass exhibits high durability during its use phase, its end-of-life processing remains an environmental challenge. Although glass is theoretically infinitely recyclable, the practical reality is more complex, particularly for flat glass in the construction sector. In the Netherlands, for instance, only 7.5% of collected float glass is recycled into new float glass, while 42.8% is downcycled into glass bottles and 41.2% is further downcycled into insulation materials or aggregates. This downcycling leads to a loss of material quality and embedded energy, as the glass is no longer suitable for high-quality architectural applications (Bristogianni & Oikonomopoulou, 2023).

Transitioning towards a circular economy is essential to minimizing the environmental impact of materials. Circular construction seeks to extend the lifespan of materials within the cycle, preserving their value while reducing waste, resource depletion, and unnecessary energy consumption (Elstner et al., 2024).

A practical approach to achieving this is through the 10R Model of Circularity (Fig. 18), developed by Platform CB between 2018 and 2023 to establish national, sector-wide agreements and promote the transition to a circular construction sector. The R-ladder ranks circular strategies based on their effectiveness in resource conservation, with the most preferable strategies – including refuse, reduce, and reuse – at the top, and less preferable options, such as recycling and recovery, positioned lower (Platform CB'23, 2019).

Many studies highlight the recycling of float glass as a key strategy for advancing a circular economy. However, compared to research on float glass recycling, relatively few studies focus on higher-ranking strategies within the R-ladder, such as reuse.

Reuse of existing glass components is generally more desirable than recycling, as it retains the highest amount of embedded energy and material value. Unlike recycling, which involves melting glass for reprocessing, reuse eliminates the need for remelting and the extraction of new raw materials. For instance, repurposing an intact glass panel in a new building avoids the energy consumption and CO₂ emissions associated with melting and re-manufacturing, making it a more sustainable alternative (Reshamvala et al., 2024).

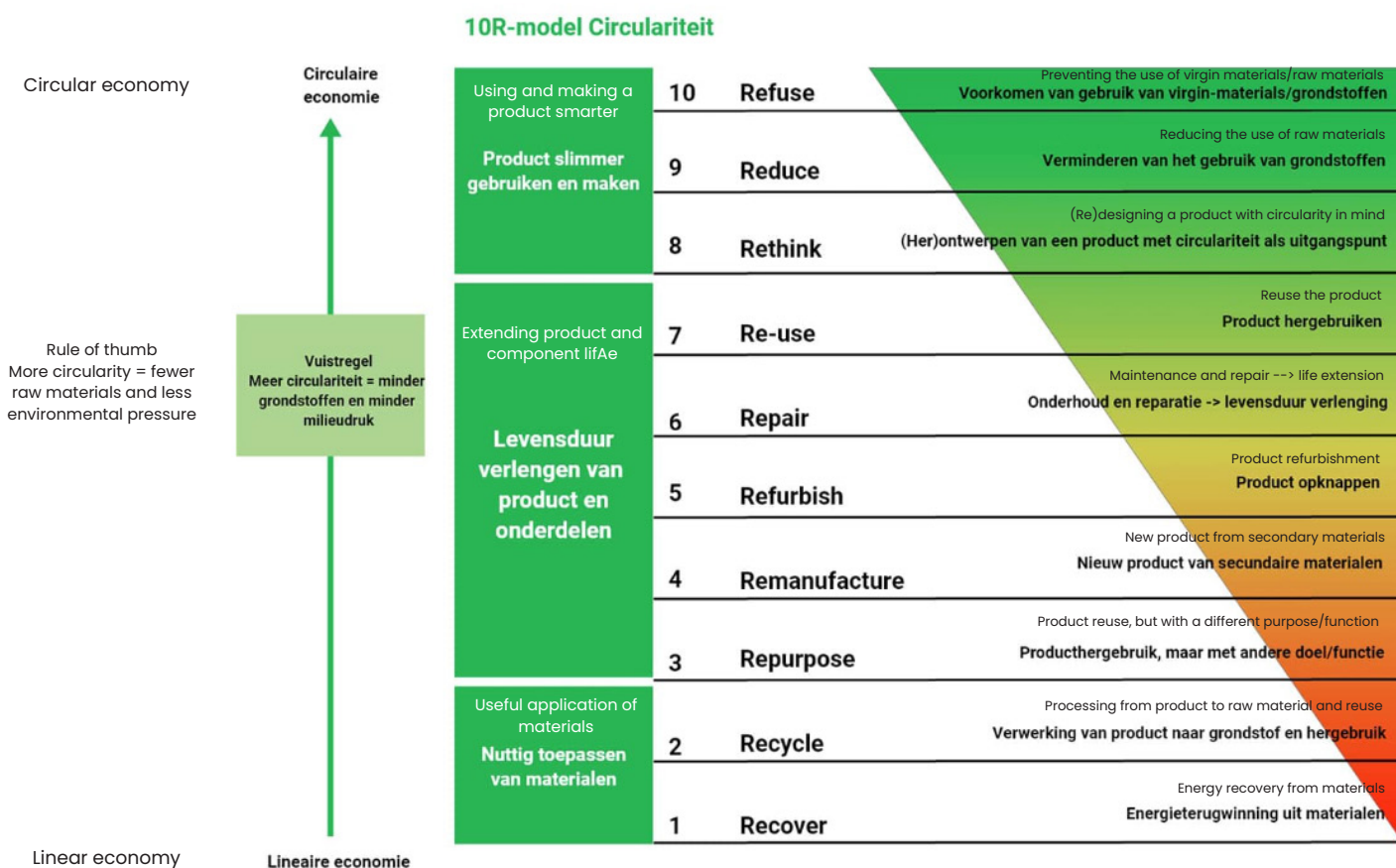


Figure 18: Framework for a circular building practice (translated from Platform CB'23, 2019)

2.3 Research Main and Sub-questions

The problem statement can be compactly summarized as:

The lack of reusable design strategies for float-glass structures leads to premature material disposal, necessitating new production and resulting in higher CO₂ emissions, resource depletion, and increased waste generation.

General Objective

This problem statement leads to the following research objective:

This research aims to design a reusable float glass system that is spatially adaptable and can be manually assembled and disassembled by a small team. By evaluating its structural feasibility, the project takes a first step toward practical application. In doing so, it seeks to encourage designers and researchers to look beyond traditional recycling methods and actively explore new circular strategies

“Which structural elements and connections enable the design of a structurally feasible and spatially adaptable float glass system that can be manually assembled and disassembled by a small team for reconfiguration at different locations, ensuring its reusability?”

This study narrows down the desire for spatial adaptability and manual assembly and disassembly to the following main requirements:

1. The system should be scalable by **expansion in the x-direction**, while **maintaining an open floor plan** (Fig. 19).
2. The system should be **extendable in the y-direction** to accommodate different spans, while **maintaining an open floor plan** (Fig. 19).
3. The system should be designed to be **as lightweight as possible** to support manual assembly and disassembly.
4. The system should be designed to allow **manual assembly and disassembly without** the need for **complex building instructions**.

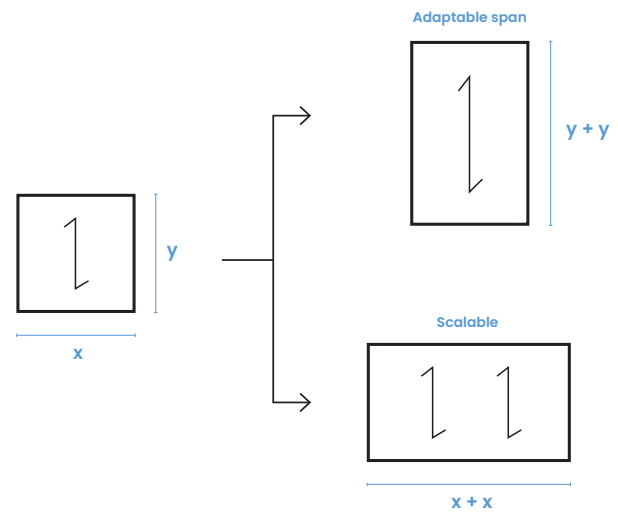


Figure 19: Expansion possibilities of the system (own work, 2025)

Additionally, it should meet the following secondary requirements:

5. The proposed system is a response to existing all-glass structures, in which transparency is a key design principle. The new system will therefore be developed in such a way that it **does not compromise the transparent quality** of all-glass structures.
6. The system must consist of a **minimal number of standardized building components** to simplify the manufacturing and construction process, and to optimize the reuse potential of structural components.
7. It should provide **basic protection against rain and overheating**.

The main research question and its underlying requirements were addressed through a combination of literature review and design-based research. This led to the formulation of the following sub-questions, which together guided the conceptual development of the system:

1. What types of adaptable structural systems exist?
2. Which external and internal geometries are suited for glass as a structural material with the aim of minimizing structural mass?
3. What key design guidelines should be considered when working with structural glass?
4. What potential design concepts can be developed for an adaptable float-glass system?

In Part II, where the concept design is elaborated, the following research questions are answered by means of computational tools and a laboratory test:

5. Which design parameters influence the adaptability of the system?
6. Can the critical location in the structure withstand the expected primary load, as verified by numerical simulation and experimental testing?

2.4 Boundary Conditions

Both the hand calculations and the developed algorithm account for a maximum span of approximately 8 meters. This constraint prevents the generation of an infinite number of span variations and provides a clear framework within which the structural performance can be assessed.

2.5 Final Products

Drawings and renders showing the:

- Final designed structural elements
- Possible design configurations generated using the standardized components

A parametric tool developed in Grasshopper, capable of:

- Generating a range of design variations using the proposed system.
- Generating design solutions with the proposed system that fit the span and shape requirements of a specific location, while optimizing both structural weight and ease of assembly.

Structural Analysis results, obtained through Finite Element Modelling (FEM), offering insight into the structural performance of the designed structural components.

Laboratory test results to compare to the FEM simulations, providing a more realistic understanding of the system's structural performance and draw a final conclusion about the structural feasibility and dimensions of the system.

A physical scale model and a 1:1 model to make the final design tangible and revealing discrepancies between the digital model and reality, providing insights for future research.

2.6 Approach and Methodology

Figure 20 on the next page gives an overview of the research workflow and the relationships between the sections.

The study is structured into two main phases:

I. Concept Development, in which literature research informs the creation of several concept designs, leading to the selection of a final concept based on the programme of requirements.

II. Design Elaboration, which focuses on exploring the system's spatial adaptability, optimization, and verification of its structural performance.

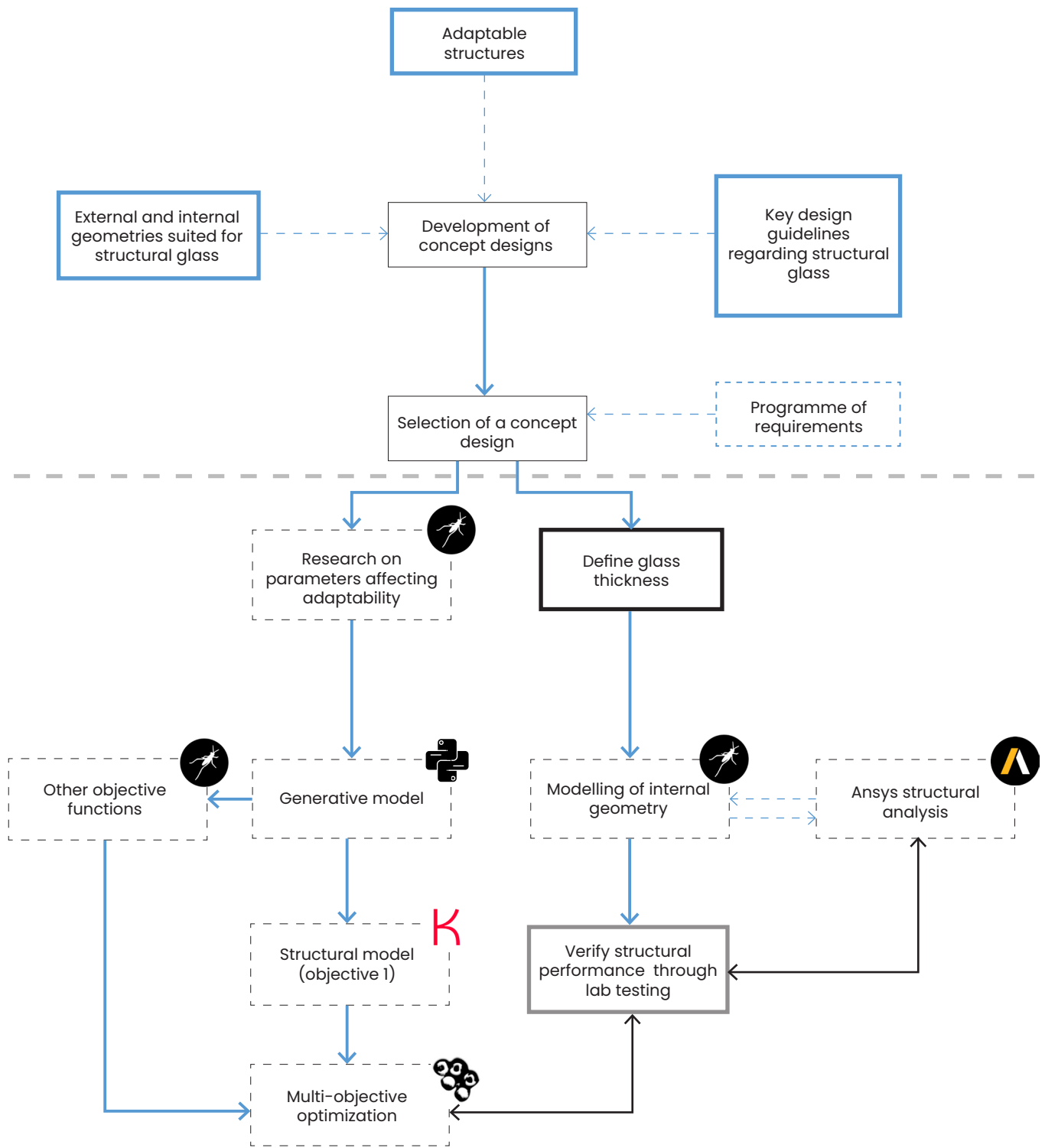


Figure 20: Research methodology (own work, 2025)

2.7 Relevance

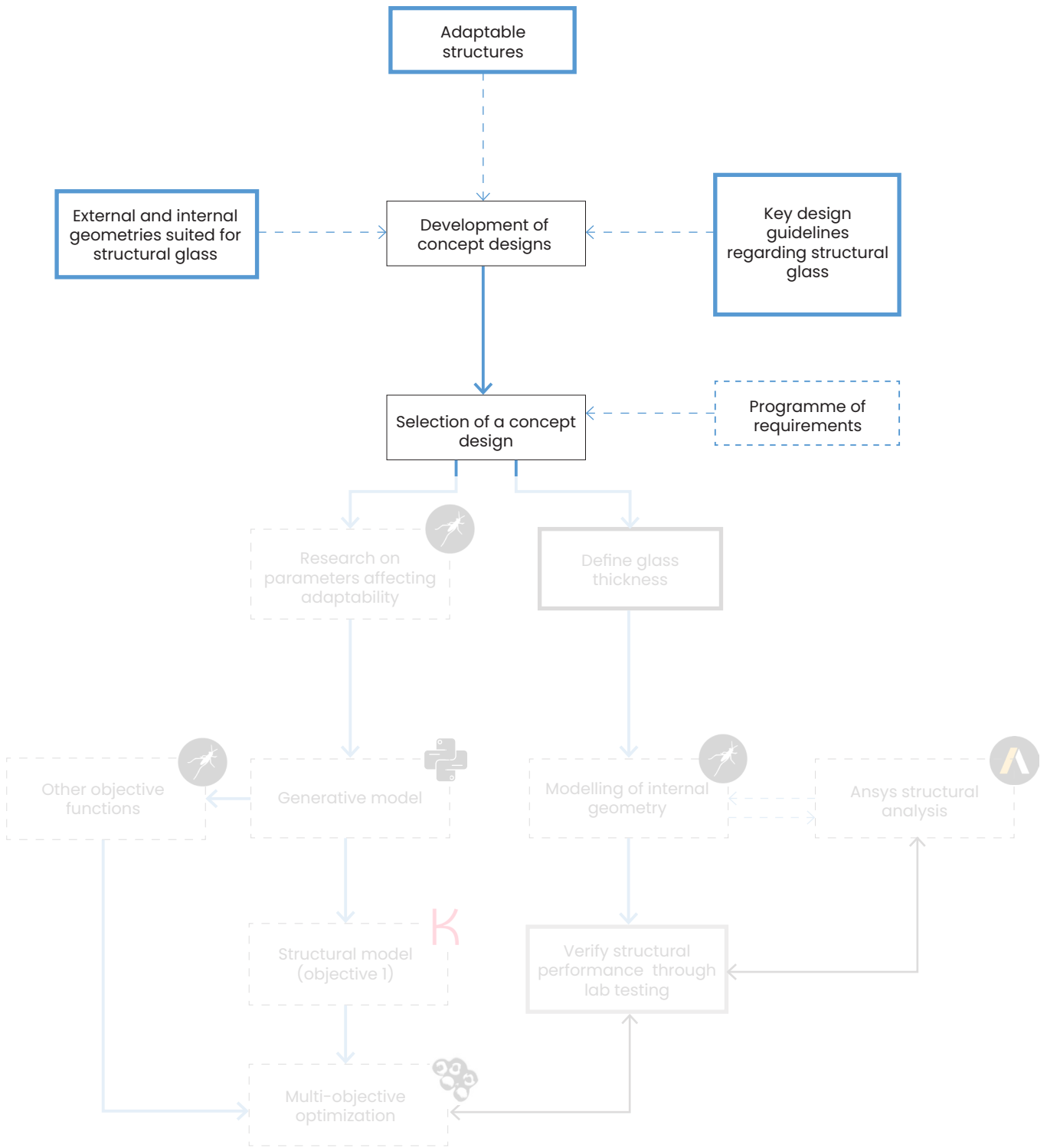
Scientific Relevance

This research, which focuses on developing a reusable float glass system, is a starting point for further studies on circular float glass structures. Given the limited research on circular design strategies for the reuse of float glass structures – an approach that ranks high in the circular economy model – this study provides valuable insights into the structural feasibility and adaptability of such a system, laying the groundwork for future development.

Societal Relevance

This study contributes to sustainable building practices by addressing the lack of reuse strategies in the float glass industry, a key step in reducing CO₂ emissions, resource depletion, and material waste in construction. By enabling structures to be assembled, disassembled, and reconfigured efficiently, it enhances architectural flexibility, allowing buildings to adapt or relocate rather than be demolished. This supports the transition to a circular economy and advances global sustainability goals in the built environment.

PART I: CONCEPT DEVELOPMENT



 Literature

 Design

 Computational design

 Physical test

 Hand calculations

 Comparison

 Next step

 Input

3. Classification of Adaptable Structural Systems

This chapter investigates the concept of adaptable structures, focusing on their definition, the methods by which adaptability can be achieved, and the extent to which it is possible. Subsequently, case studies are studied that provide insights into the potential technical development of adaptable structures. The chapter results in a partial conclusion that gives the first direction of the conceptual design.

Two categories of Adaptable Structures

A structure capable of adapting to varying spatial needs is referred to as reconfigurable (Mesa et al., 2015). The ability to adopt new configurations is essential for structures designed to meet evolving functional and environmental demands (Mitsimponas & Symeonidou, 2024). Research categorizes adaptable structures into two main types: Modular Structures and Transformable Structures (Brancart et al., 2017).

3.1 Modular Structures

Modular Structures are composed of standardized units, referred to as modules. Modules reduce complexity by utilizing similar elements, while variety can be created (Mitsimponas & Symeonidou, 2024). The concept of modularity spans a spectrum (Fig. 21), where the scale of modularity increases with the number of components within a module. Small-scale modularity refers to single structural elements functioning as modules. Big-scale modularity involves assemblies of multiple components forming larger building units.

Reconfigurability in Modular Systems

The adaptability of modular systems is realized by adding, removing, or rearranging modules. This flexibility enables:

1. Expansion or reduction of the structure to accommodate capacity changes.
2. Reconfiguration of modules to modify the shape or floor plan of a building.

The principle of tessellation, commonly known as tiling, offers a framework for exploring reconfiguration possibilities. Tessellation involves subdividing a planar region into smaller, identical, non-overlapping pieces. This approach facilitates the investigation of various geometric shapes and configurations. While typically two-dimensional, tiling patterns can be extended into three-dimensional spaces, enabling the design of modular constructions that are easily adaptable and reconfigurable to accommodate changing needs (Fig. 22)

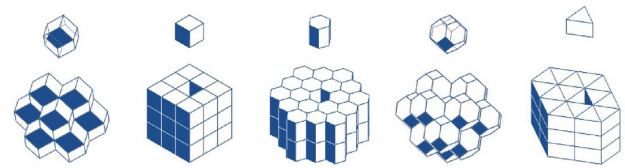


Figure 22: Tessellation on a big modular scale (Mitsimponas & Symeonidou, 2024).

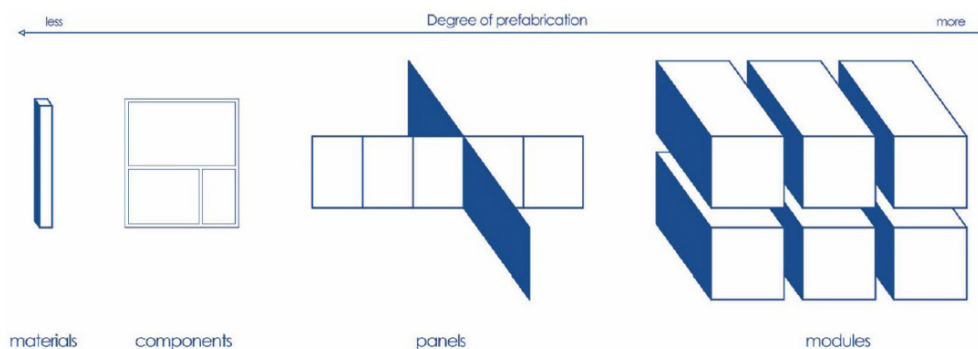


Figure 21: From small to big-scale modularity (Mitsimponas & Symeonidou, 2024)

3.2 Transformable Structures

Transformable structures can be categorized into deployable and free-form structures. Deployable structures are designed to transition between compact and deployed states, primarily for ease of transportation and rapid assembly. However, they typically offer only a limited number of configurations (Brancart et al., 2017). These structures are often made from materials like steel or aluminium. Examples include spatial scissor-pair mechanisms (Fig. 23) that use straight or angled bars and reciprocal structures composed of bars or plates arranged in closed-loop formations (Fig. 24).



Figure 23: Scissor mechanism for a deployable structure (Brancart et al., 2017)

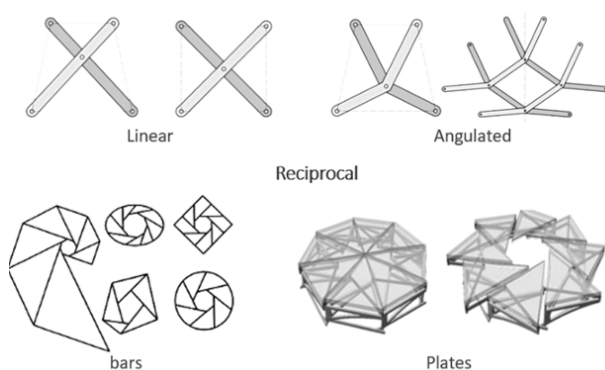


Figure 24: Deployable spatial-bar structures (Hussein et al., 2021)

Free-form structures achieve shape and volume transformation through mechanisms such as folding, sliding, rotating, or extending. For instance, a spatial bar structure can adjust the lengths of its bars to reach a desired configuration (Fig. 25). Similarly, bar linkage systems use hinged connections to modify the angles between bars, enabling changes in volume (Fig. 26) (Phocas & Matheou, 2021).

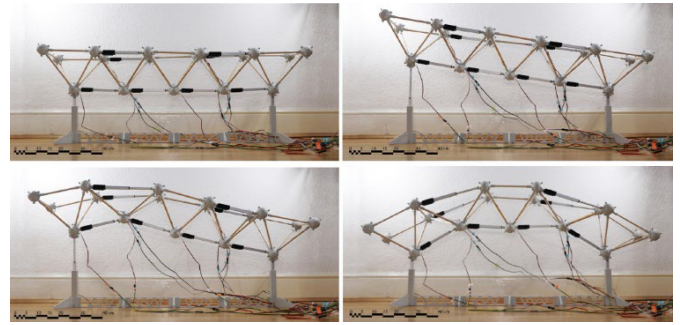


Figure 25: Free-form Transformable Structure (Hussein et al., 2021)

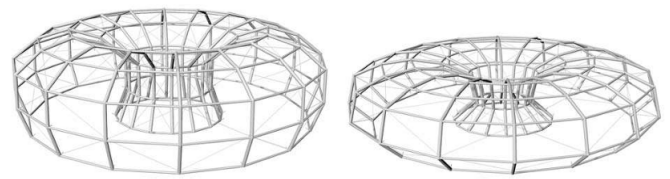


Figure 26: Bar linkage system that changes in volume (Phocas & Matheou, 2021)

3.3 Case Studies

Origami-inspired adaptable structure from MDF plates

The following case-study information is based on a research by Zhu & Filipov (2024).

The Uniformly Thick Origami-Inspired Structure (MUTOIS) is a system made from tessellated triangular panels with 25 cm long sides. The design employs flexible, dry connections between the modules, enabling the structure to transform its shape and function. This modularity also allows for the addition, removal, or reconfiguration of modules, making the system adaptable (Fig. 27). This study was conducted in response to the lack of adaptability and future reuse of current civil structures.

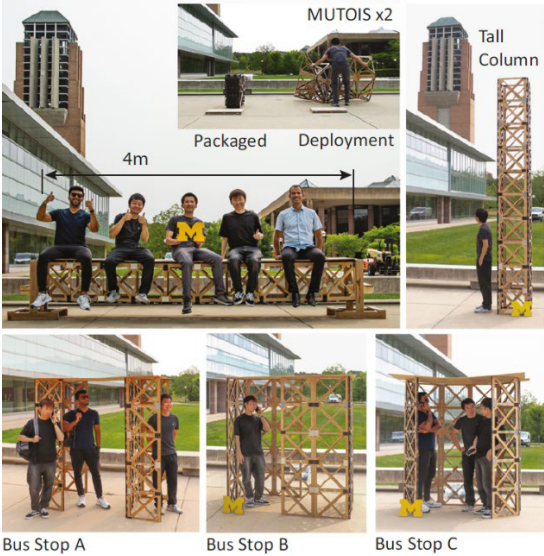


Figure 27: Reconfigurations of the MUTOIS system (Zhu & Filipov, 2024).

The triangular panels are uniformly thick, ensuring efficient force transfer and robust load-bearing capabilities after locking them (Fig. 28).

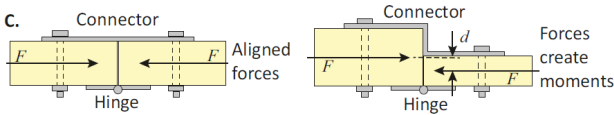


Figure 28: Uniformly thick panels for efficient force transfer

These panels can be fabricated from various materials, in this case a 4-layer mid-density fiberboard (MDF). What sets MUTOIS apart is its ability to reconfigure into multiple shapes and functions through multi-path folding motions (Fig. 29). By strategically locking and unlocking specific fold lines or hinges within the system, the structure can transform between compact storage states and functional configurations. The system's adaptability is further enhanced by locking mechanisms like sliding locks and latch locks, which ensure secure connections while allowing quick and efficient reassembly (Fig. 30).

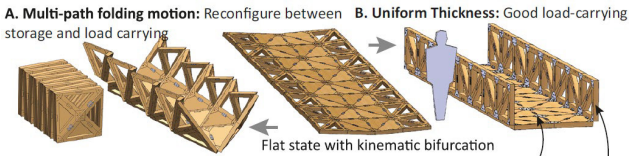


Figure 29: Adaptability between different structural states through multipath folding movements (Zhu & Filipov, 2024).

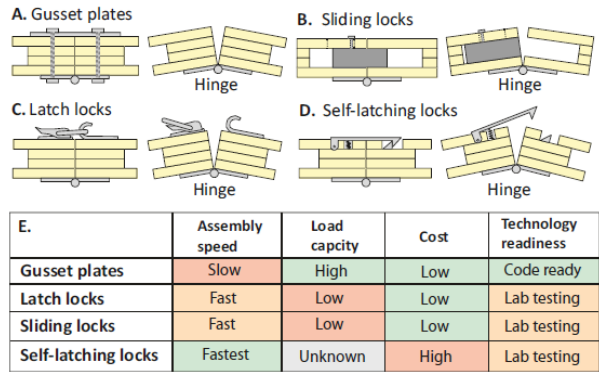


Figure 30: Locking mechanisms allowing for reassembly (Zhu & Filipov, 2024).

Modular Hollow Glass Units (HGU's)

The following case-study information comes from a study by Yost et al, 2022. This research focuses on the design of a modular unit called the Hollow Glass Unit (HGU).

Each Hollow Glass Unit (HGU) is shaped as an elongated hexagonal prism. The modules comprise two deck plates, two long side plates, and four short side plates, all fabricated from 10 mm thick soda-lime annealed glass (Fig. 31). The HGUs are manufactured using regular float glass and acrylic, employing 5-axis water jet cutting and CNC milling for precise fabrication.

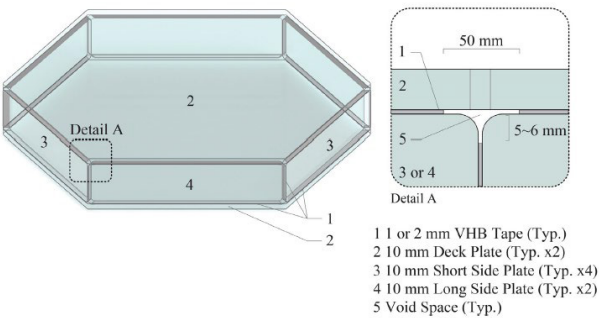


Figure 31: A Hollow Glass Unit (HGU) with deck and side plates (Yost et al., 2022)

Connections and assembly

The connections between the HGU components are achieved using Very High Bond (VHB) Tape, a double-sided foam tape with an acrylic adhesive that ensures a robust and durable bond without requiring wet adhesives or sealants. VHB tape is applied to the edges of the glass panels. The assembly begins with connecting one long side plate to two short side plates, forming a three-sided unit. This process is repeated to create two such units, which are then joined to form the side-wall hexagon. The first deck plate is subsequently attached. 3D-printed clips are temporarily used during assembly to align and hold the glass plates in place. These clips, positioned at the deck plate corners, are removed once the assembly is complete. Figure 32 shows the assembly process.

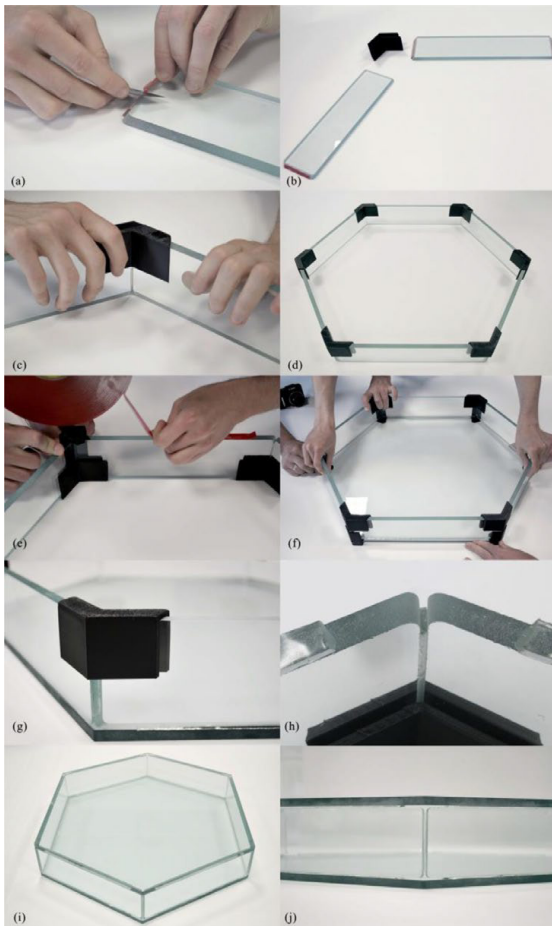


Figure 32: Assembly process of the HGU modules (Yost et al., 2022).

Glass bridge prototype

Later research by Lu et al. (2022) utilized HGUs in constructing a glass bridge prototype with a 3-meter span (Fig. 33). Each HGU was designed to be lightweight and manageable by a single person during construction.



Figure 33: Modular glass bridge prototype (Lu et al., 2022).

Not all side plates were made from glass, as some needed to incorporate intricate connection mechanisms, such as the butterfly locking system. Acrylic side plates were chosen for their precision and ease of fabrication compared to glass (Fig. 34).

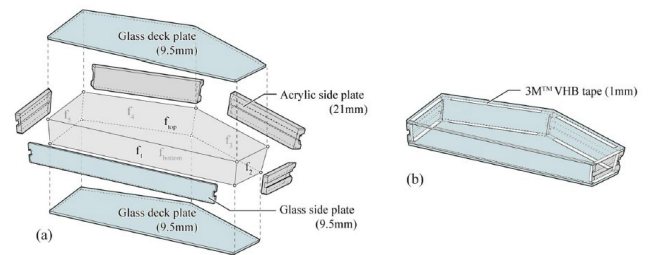


Figure 34: Deck and side plates, with acrylic side plates on the inside (Lu et al., 2022).

The butterfly locking mechanism features grooves carved into the side plates, with a locking strip inserted into the channels to secure neighboring HGUs and enhance structural stability. The locking strip can be removed for disassembly, thanks to a bevel and a hole on one end (Fig. 35). Bevel cuts are included on the short edges of the side plates (and so at each corner of the module) to ensure precise alignment of the HGUs and to evenly distribute compressive loads, reducing stress concentrations on the glass panels.

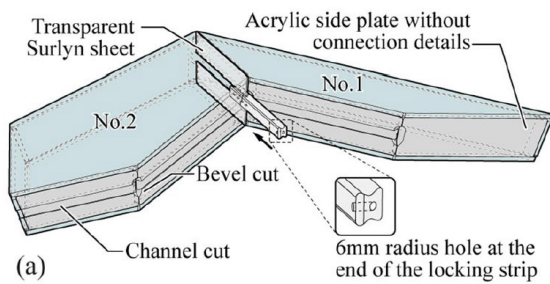


Figure 35: Butterfly locking mechanism and locking strip in the pocket channels (Lu et al., 2022).

Folded Glass Plate Structures

Trometer and Krupna's (2006) research explores innovative connections in glass folded plate structures. Inspired by origami (Fig. 36), the system uses folds as functional connections, eliminating the need for bar structures and maximizing transparency.

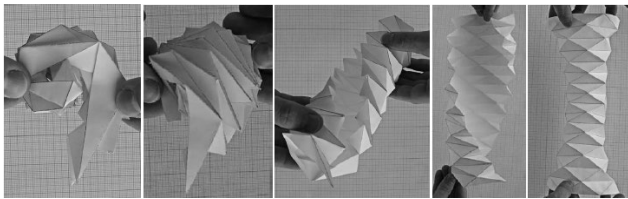


Figure 36: Freeform paper model as a starting point (Trometer & Krupna, 2006)

Folding mechanism and geometry

The folding mechanism incorporates hinged connections, allowing movement between a flat, two-dimensional state and a folded configuration. This design is based on the Rhombus-Wing-Element, a geometric unit that provides flexibility while ensuring structural integrity (fig. 37).

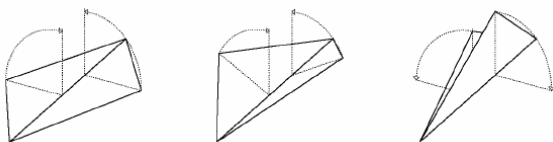


Figure 37: Rhombus-Wing-Element (Trometer & Krupna, 2006)

Connections

The integration of hinges between glass plates enables folding and transformation of these structures. This system employs silicone adhesives as structural sealants to bond glass edges to the T or U-shaped stainless steel hinges (Fig. 38). This connection can distribute three-dimensional loads effectively handling tensile forces, shear stresses, and their combined effects. The adhesive is engineered to resist deformation, ensuring it does not stretch or compress significantly. This resistance to deformation helps maintain the integrity of the connection, preventing lateral strain (sideways movement) and compression (squeezing). The sealant can also handle minor movements of the glass plates. This flexibility mitigates bending stresses and enhances structural stability.

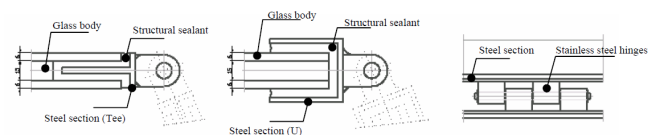


Figure 38: Stainless steel hinges from T and U sections and structural sealant (Trometer & Krupna, 2006)

Kinematics of Folded Glass Plate Structures

The information below is based on Krousti, Snijder, and Turrin's (2018) Study.

This research explores the design and structural performance of a deployable roof system made from folded glass plates. Conducted through experiments, the study focuses on a one-directional deployable roof for an outdoor swimming pool, examining its stability during deployment (Fig. 39) (Krousti et al., 2018).

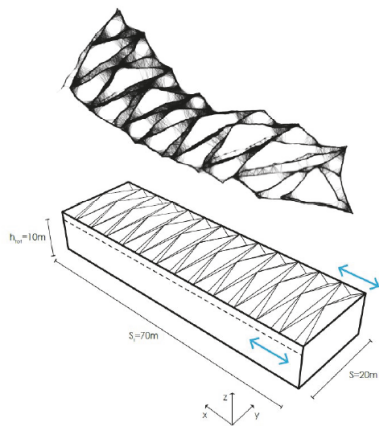


Figure 39: Deployable roof concept for the swimming pool (Krousti et al., 2018).

Connections

The hinged connections between the plates are crucial for providing structural stability. They can handle tensile strengths of up to 200MPa. In this research, achieving optimal transparency of the connections was a priority for high architectural quality. PURE composite sheets, made from a thermoplastic composite, are used as an alternative to traditional hinges. This composite is flexible and very strong, consisting of 70% fiber composition and polypropylene. Other benefits include being lightweight, flexible, high impact-resistance, fatigue-resistant, durable, recyclable, easy to produce, and waterproof compared to normal sealants.

The PURE sheets are kept in place by glass panes. They can not be directly bonded to the glass, so glass or steel disks are glued between the glass panes to keep the sheet in place (Fig. 40). This type of connection can be developed along the length where the plates come together, making the system waterproof. Customized covers can be placed on the meeting points between adjacent sheets.

If a part of the structure gets damaged, only the disks need to be re-adhered to the new external pane during the repair process.

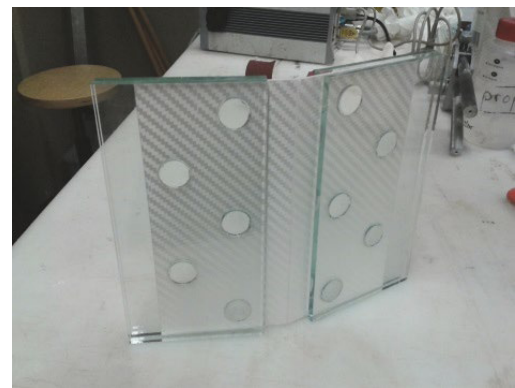


Figure 40: Hinged connection from PURE sheets (Krousti et al., 2018)

Conclusion

Adaptable structures can be categorized into modular structures and transformable structures. Modular structures consist of standardized components (modules) that can be added, removed, or re-arranged to modify the external shape and size of a structure (Fig. 41).

Transformable structures, on the other hand, enable continuous adaptability (Fig. 42) by incorporating mechanisms such as folding, sliding, rotating and subsequently locking the connections.

Although both modular and transformable structures offer potential for expansion along the x and y axes while maintaining an open floor plan, this research opts for a modular approach for several reasons:

Transformable systems typically require connections capable of rotation and locking, which can result in complex and visually prominent joints. This complexity conflicts with the stated design requirements, which emphasize ease of production and assembly, as well as maintaining the visual transparency highly valued in all-glass structures.

Moreover, engineering a deployable glass system introduces additional challenges related to maintaining structural integrity throughout various deployment stages, during expansion and retraction, and during transportation. This complexity does not contribute to the intended simplicity of the design.

A modular approach appears more feasible, aligning better with the project's goal of achieving simplicity in the design.

MODULAR STRUCTURES

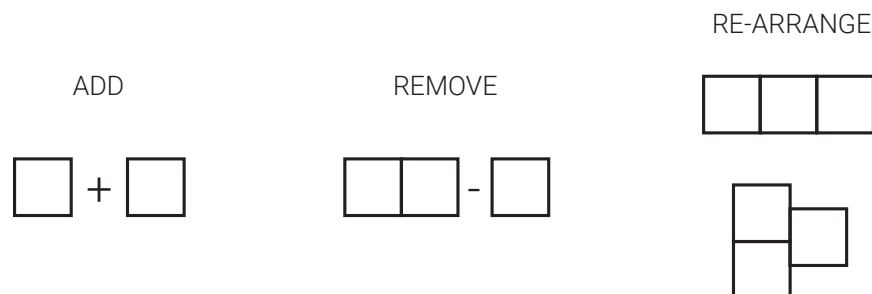


Figure 41: Reconfigurability of a modular structure (own work, 2025)

TRANSFORMABLE STRUCTURES

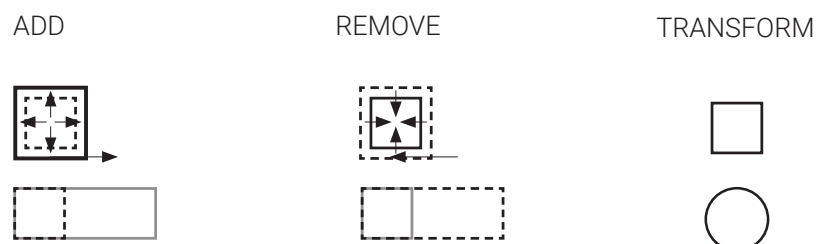


Figure 42: Reconfigurability of an adaptable structure (own work, 2025)

4. External and Internal Forms for a Lightweight Glass Structure

This chapter first examines the mechanical strength of glass and the underlying factors that determine its structural behavior. Understanding these properties explains why glass performs best under compressive loads, a key consideration in designing lightweight structures.

Next, the chapter explores external structural forms that facilitate compressive load transfer, followed by examples of how these forms can be realized through structural elements and connections. The insights gained serve as a foundation for developing material efficient design concepts.

4.1 Mechanical strength of float glass

Float glass production

Soda-lime silica glass is the most commonly used type of glass in the building industry. It is produced by melting silica (silicon dioxide) from sand, soda (sodium carbonate), dolomite (to slow down the crystallization process), and lime (to lower the melting temperature) in an oil-fired furnace. The molten glass is then floated on a bath of liquid tin, where it is rapidly cooled to 600°C, reaching a viscous state (Louter, 2011).

In this state, glass has an amorphous structure, meaning its atoms are arranged randomly, similar to a liquid. This is why glass is often referred to as a ‘supercooled liquid,’ even though it is technically a solid. When a liquid is rapidly cooled, as in float glass production, the molecules do not have enough time to form a crystalline structure, leaving the material in an unstable supercooled state. Essentially, the molecules are “frozen” in their disordered arrangement, forming glass. This unique structure is what gives glass its characteristic transparency, making it a highly valued material (Pour-Moghaddam, 2020).

Afterward, the glass enters the annealing lehr, a specialized oven where it is gradually cooled to relieve internal stresses. At the end of this process, the glass is cut to size, resulting in what is known as annealed float glass (Louter, 2011) (Fig. 43).

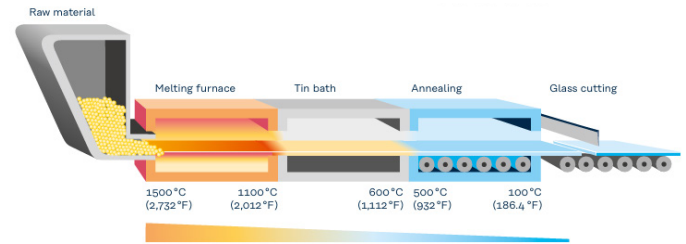


Figure 43: Float glass production process (Louter, 2011)

The amorphous structure of glass atoms is what makes glass a brittle material. Because glass has no fixed atomic lattice, it also lacks sliding planes on which atoms can shift. This means that when force is applied to the glass, the atoms transmit the stress directly through their bonds, without the ability to move or adjust, as in crystalline materials. As a result, glass cannot absorb or distribute stress, and once the force becomes too great, the bonds break all at once, causing the glass to fracture suddenly and without warning (Yuan & Huang, 2014). Figure 44 shows the difference between a crystalline (a) and an amorphous (b) atomic orientation.

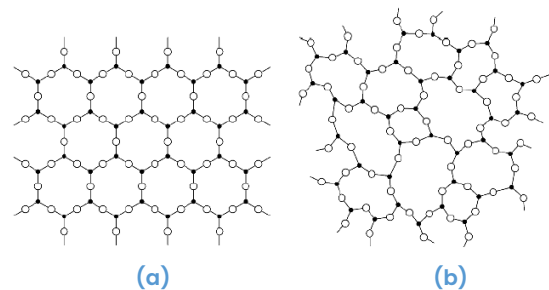


Figure 44: Difference between a crystalline structure (a) and an amorphous structure (b) (Pour-Moghaddam, 2020)

In contrast, materials like steel exhibit localized yielding due to their ductility, which allows them to deform before reaching catastrophic failure. Figure 45 shows the difference in failure behavior between steel and glass. It shows that glass deforms perfectly elastically until the moment the interatomic bonds suddenly break (Pour-Moghaddam, 2020).

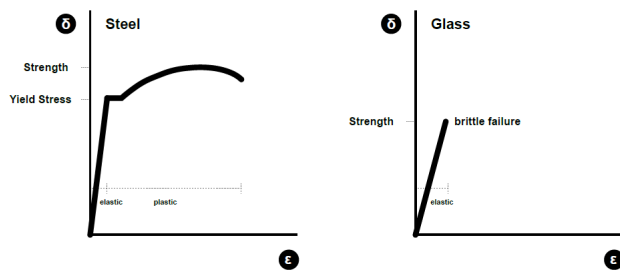


Figure 45: Stress/strain curves for steel and glass (Rammig, 2022)

Glass is fragile under tensile loads, as fractures almost always occur due to tensile stresses activating surface flaws that arise during production, installation, and service life, leading to crack formation. These flaws act as stress concentrators, ultimately causing the material to fail. Over time, the depth of these flaws can increase, reaching a critical length at which the glass breaks. This process depends on factors such as load duration, stress intensity, and the presence of moisture, which reacts with silica bonds, weakening the glass molecules. As a result, the tensile strength of glass decreases over time under sustained loading (Louter, 2011).

The combination of brittle failure and the presence of surface flaws makes the characteristic (tensile) strength of glass highly variable and difficult to determine (Pour-Moghaddam, 2020).

In contrast, glass is significantly stronger under compressive loads, as surface cracks cannot propagate due to the compressive forces that prevent their growth (Louter, 2011).

4.2 External and internal geometry

External geometry

The form of a structure – also referred to as the external geometry (Wurm, 2007) – can be dependent on both the mechanical and the spatial function (Sandaker, 2007). The functional form arises from the building's intended use; in the context of this study, it specifically relates to the potential for expansion in both span and length to accommodate varying spatial requirements. This topic is further developed during the concept design phase, as discussed in Chapter 6.

The mechanical form, on the other hand, is the shape of the external structure, determined by how forces are transferred through the structure (Wurm, 2007) & (Sandaker, 2007) (Fig. 46). Although glass has enabled the replacement of linear structural elements traditionally made from other building materials, certain external geometries better utilize glass's mechanical properties, resulting in more economical designs (Wurm, 2007).

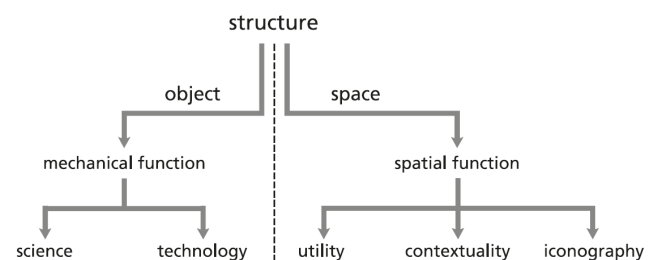


Figure 46: The external form of a structure, defined by the mechanical and spatial function (Sandaker, 2007)

Such economical external geometries for glass as the structural material are forms that transfer loads primarily in compression, such as arches, barrel vaults, and domes (Fig. 47) (Wurm, 2007).

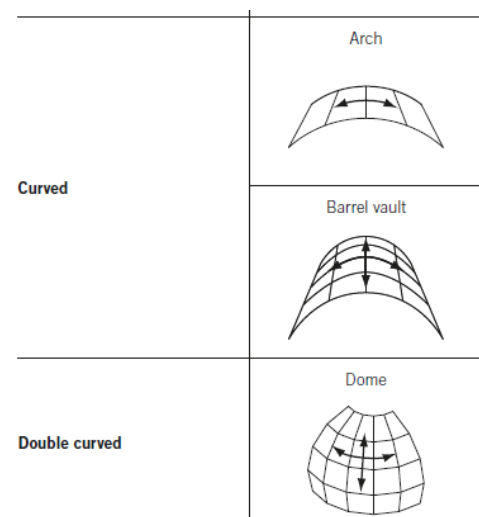


Figure 47: External structural forms designed to resist compressional loads (Wurm, 2007)

Arches

When a load is applied perpendicular to an arch, compressive forces develop within the structure and are transferred along the curve to the foundation.

Figure 48 shows different arch shapes and their influence on force distribution. A parabolic arch optimally matched to the load ensures that the forces flow along an ideal pressure line, preventing internal bending moments. In contrast, the elliptical arc (b) deviates significantly from this line, resulting in significant bending moments. The circular arc (c) lies between these two forms in terms of efficiency, as the pressure line remains closer to the geometry of the arch. When a hinge joint is added at the center of the structure (d), the pressure line can better position itself within the material of the arch. This minimizes bending stresses and keeps the structure working largely in compression (Wurm, 2007).

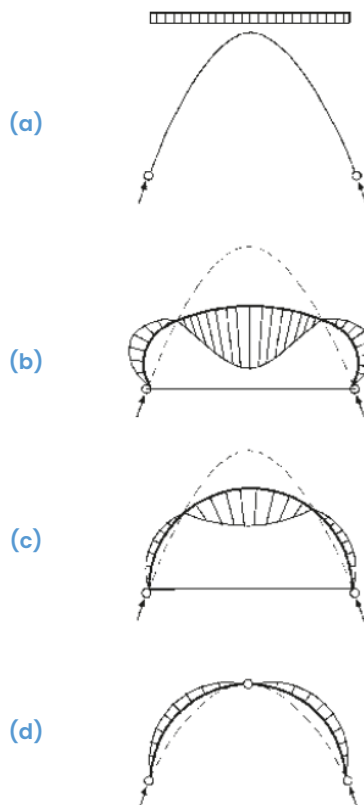


Figure 48: The extent of force transfer through compression, determined by the arch shape and a hinge joint (Wurm, 2007)

Barrel vaults

A barrel vault transfers forces not only in the arching direction but also in the longitudinal direction of the structure.

With a long barrel vault, where the supports are far apart, a bending effect similar to that of a beam occurs. As a result, the structure is mainly loaded in compression, while the bottom experiences tensile stresses (Fig. 49).

In contrast, a shorter barrel vault behaves more like an arch, where forces are dissipated mainly through compression without significant bending (Wurm, 2007).

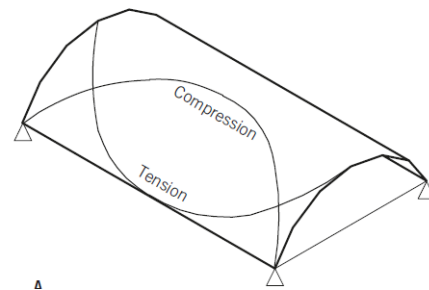


Figure 49: Force distribution in a barrel vault (Wurm, 2007)

Domes

A dome is an arc, extended 360 degrees all around. The rotational symmetry of an arc creates a spherical surface (Wurm, 2007) (Fig. 50).

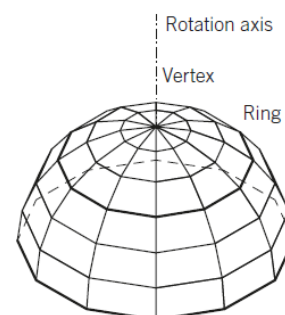


Figure 50: Rotational symmetry of an arch, creating a spherical surface (Wurm, 2007)

Meridional forces are present on this surface, running from the top of the dome to the lower edge and acting in compression. In addition, there are ring forces (circumferential forces) that run horizontally along the dome. In the upper part of the dome, these ring forces act in compression, while in the lower part, they change to tension. This is because the outward splash forces in the lower ring must be counteracted by ring tensile forces (Wurm, 2007) (Fig. 51).

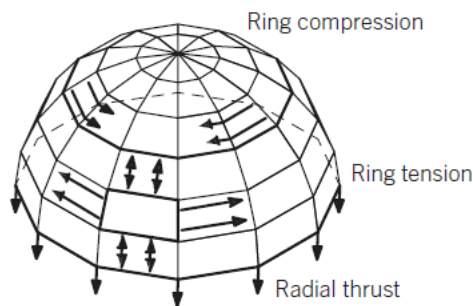


Figure 51: Force distribution in a dome, showing the transition from compressive to tensile ring forces along the structure (Wurm, 2007)

The so-called zero-ring force line marks the interface where compressive ring forces in the upper part of the dome turn into tensile stresses in the lower part (Wurm, 2007) (Fig. 52).

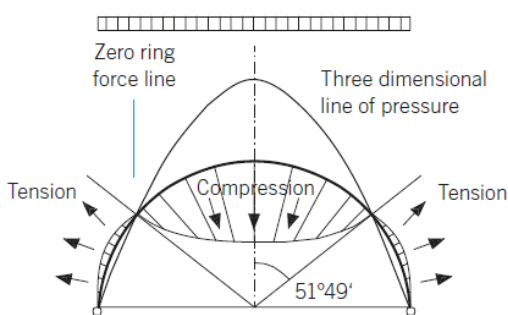


Figure 52: Compression and tension areas in a dome (Wurm, 2007)

Internal geometry

From Wurm, 2007, it can be concluded that the internal geometry describes how the external geometry is 'filled in' with structural elements, connections, and subdivisions. Whereas the external geometry determines the direction in which forces propagate through a structure and whether compression is promoted, the internal geometry determines how these forces are actually absorbed, distributed, and transferred within the structure.

A distinction is made between Skeleton Structures and Skin Structures (Fig. 53). Skeleton Structures consist of fins, beams, or struts as primary load-bearing elements. With Structural Skins, the cladding itself bears the load and acts as the primary load-bearing element. Within the Structural Skins, a distinction can be made between Plates and Prisms. Prisms are three-dimensional modules composed of several flat glass sheets and form an integral structural whole, also called a module. Plates, on the other hand, are flat or curved elements that function as individual structural components.

A distinction can be made between point connections and linear connections. Point connections lead to local stress concentrations, which is challenging due to the brittleness of glass. Linear joints, on the other hand, distribute the forces over a larger surface area, allowing the load to be transferred more gradually between elements. When a series of point connections are closely spaced, the force transfer can be considered linear in some cases. (Wurm, 2007).

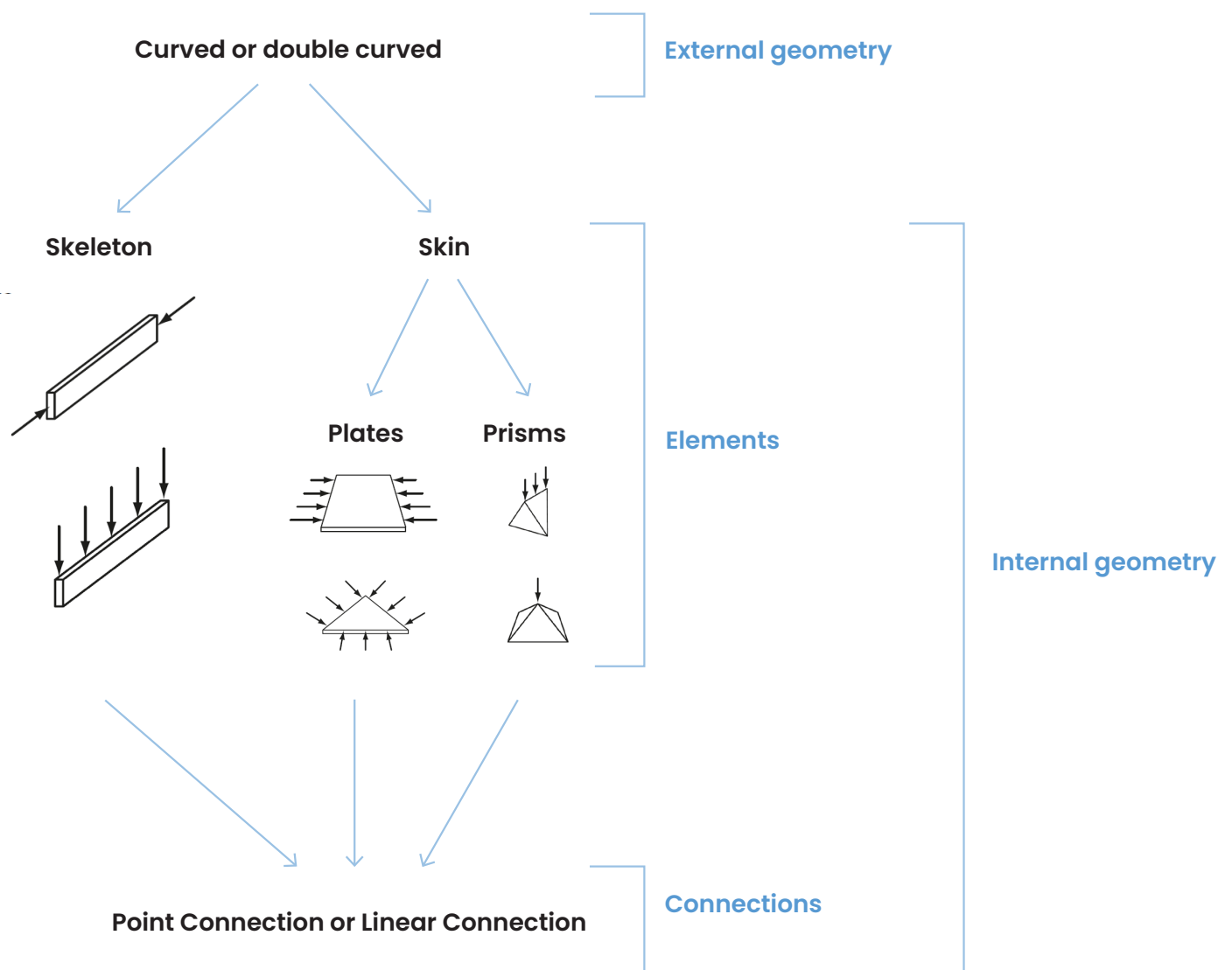


Figure 53: Subdivision of the external structural form into structural elements and connection types (own work, based on Wurm, 2007).

Design examples

The following design examples provide insight into how different external geometries can be composed using structural elements and connections (the internal geometry) and how this composition influences the compressive performance of the external system.

All information presented in this section is based on Wurm (2007).

Skeleton Structures

A skeleton structure is often composed of segmented beams to achieve specific spans, as plate dimensions are restricted by production constraints. Figure 54 shows a segmented skeleton structure designed as a three-pinned arch. The presence of pinned connections eliminates internal moments, allowing the structure to efficiently transfer loads primarily through compression.



Figure 54: Segmented three-pinned arch structure (Wurm, 2007).

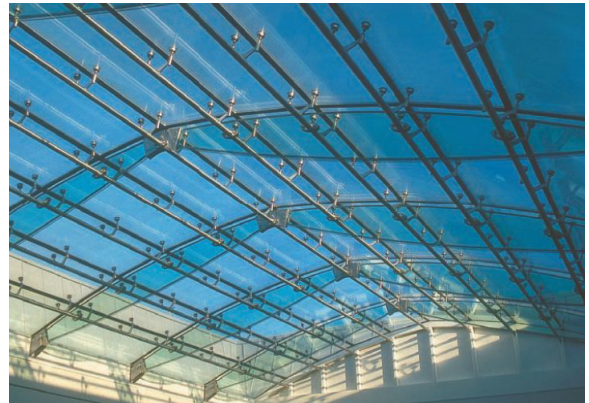


Figure 55: Another example of a three-hinged segmented arch (Wurm, 2007)

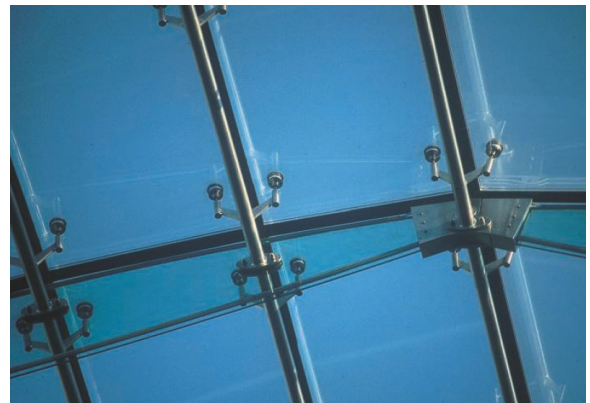


Figure 56: A hybrid structure, showing glass beams with a tension cable at the bottom (Wurm, 2007)

Figure 55 illustrates a Skeleton Structure, also designed as a three-hinged arch. Based on previous theories on arches, it can be concluded that the hinged connections minimize bending stresses, allowing the arch to function more efficiently in compression. It is a hybrid structure, since the remaining tensile forces are counteracted by steel tension cables running along the underside of the beams (Fig. 56).

Perpendicular to the glass beams, steel tubes prevent buckling while also serving as secondary beams that support the glass roof panels.

Structural Skins – Plates

All information presented in this section is based on Wurm (2007).

Delft Glass Dome

The Delft Glass Dome is an example of a dome that consists of self-supporting plates. The structure was built as a prototype for a glass pavilion at the Technical University of Delft between 2002 and 2004 (Fig. 57).



Figure 57: The Delft Glass dome (Wurm, 2007)

It has a diameter of 5 meters and is segmented into flat trapezoidal plates by four rings and 16 meridians. While an ideal shell structure typically requires double-curved panels, this design utilizes flat elements to avoid the high costs associated with thermal bending.

The primary load transfer within the glass panels occurs axially, with the dome predominantly subjected to compressive forces. This is due to the position of the dome's surface, which is approximately 90 cm above the zero ring force line. As a result, under permanent loading, the structure primarily experiences compression forces in both the ring and meridian directions.

Two types of connections are used between the panels: an adhesive-bonded connection and a friction grip connection, both positioned at the corners with a slight offset from the fragile glass edges (Fig. 58).



Figure 58 Linear connections in both the meridian and ring directions, positioned at the panel corners (Wurm, 2007)

The first consists of stainless steel profiles that is adhesively bonded to the glass along the meridian seams. This connection (Fig. 59) serves multiple functions, primarily by absorbing tolerances and evenly distributing loads across the glass panel edges. Unlike point fixings, which can introduce local stress peaks, the continuous adhesive layer ensures a more uniform force distribution, minimizing stress concentrations that could lead to glass failure.

The visco-elastic nature of the adhesive allows for slight deformation under load, helping to mitigate thermal expansion differences between the glass and the steel profiles and prevents excessive internal stresses caused by manufacturing or installation tolerances.

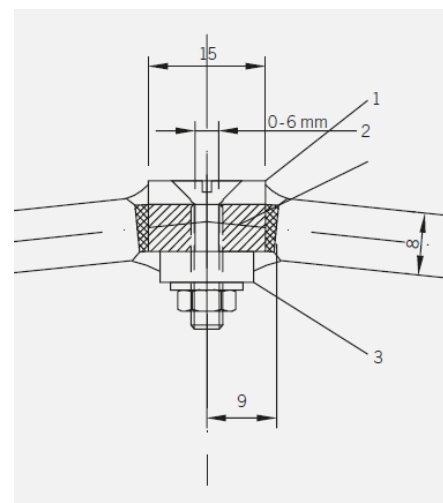


Figure 59: Connection of two glass plates using a visco-elastic glue, also showing the small angle between the glass plates (Wurm, 2007)

The friction grip connection (Fig. 60) is located in the ring direction (horizontal seams) and is responsible for allowing controlled movement between adjacent glass panels while preventing excessive stress buildup. In this system, stainless steel rods embedded in the edges of adjacent glass panels are mechanically clamped together using steel flats and bolts with washers, applied at 100 mm intervals. The generated contact pressure ensures that forces are transferred through friction, allowing the connection to absorb tolerances in the ring direction.

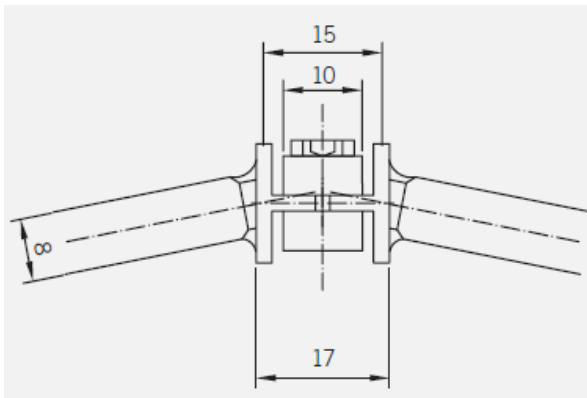


Figure 60: Friction grip connection (Wurm, 2007)

Unlike the visco-elastic adhesive, which primarily absorbs stress and tolerances in the meridian direction, the friction grip connection also facilitates a slight rotational effect between panels. This hinged behavior in the ring direction prevents the development of large bending moments in the glass, ensuring that most forces remain axial. By reducing bending stresses, this connection contributes significantly to the folded plate behavior of the dome, where axial force transfer dominates.

Structural Skins – Prisms

All information presented in this section is based on Wurm (2007).

Tetra Glass Arch

The Tetra Glass Arch is a glass structure presented at the Glasstec trade fair in 2000. Its design is based on a modular system of tetrahedrons (Fig. 61).



Figure 61: Presentation of the Tetra Glass Arch at the Reiff Museum in Aachen (Wurm, 2007)

The external geometry consists of a semicircular arch spanning 8 meters. By linking multiple arches together, the structure can be extended. At the top, point connections are present, which function practically as linear connections along the edges of the tetrahedra, where the forces from the roof plate, also known as the top chord, are transferred to the diagonals (Fig. 62)

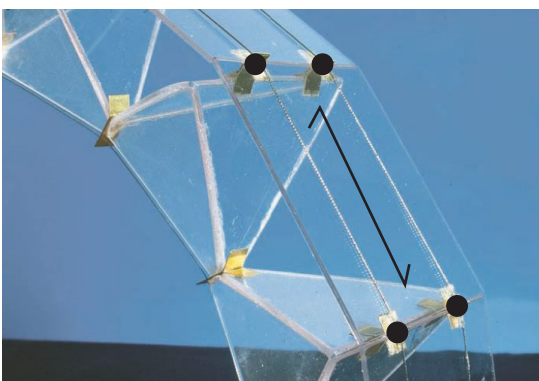


Figure 62: Point connections on the edges of the tetrahedrons, supporting the top chord (roof) (adapted from Wurm, 2007)

Two sides per tetrahedron form the diagonals, distributing the forces three-dimensionally to the bottom chord (Fig. 63).

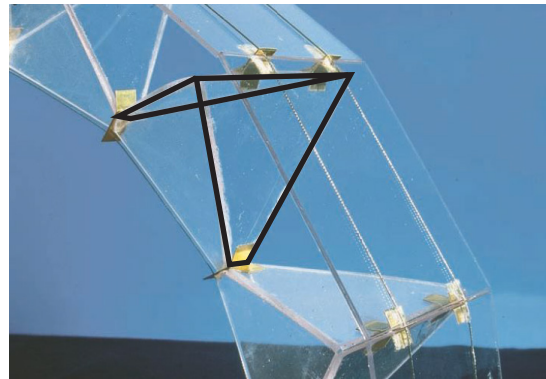


Figure 63: Force transfer from the top chord to the bottom chord through the diagonal panes (adapted from Wurm, 2007)

The tetrahedrons are interconnected at the points, forming a continuous line, called the bottom chord (Fig. 64).

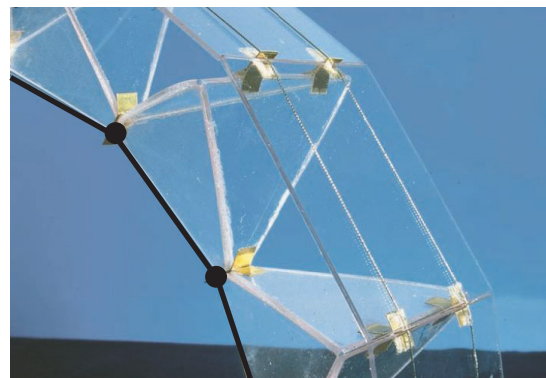


Figure 64: Point connections at the corners of the tetrahedra, forming the bottom chord (adapted from Wurm, 2007)

The bottom chord operates in compression regardless of the load case because pre-stressed cables are installed along the top chord (Fig. 65). These cables exert a constant radial compressive force on the arch, keeping the pressure line within the structural form and allowing the entire structure to continue operating in compression. This allows the arch to adapt to changing load cases without tensile stresses occurring in the glass elements.

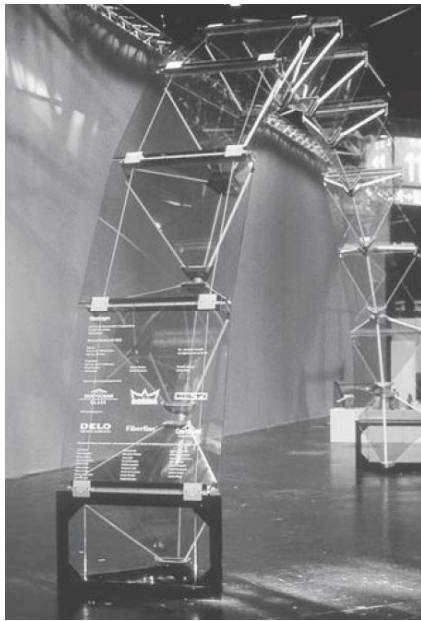


Figure 65: The arch at Glasstec, with visible tension cables at the top chord (Wurm, 2007)

Because permanent compressive forces are running through the arch, the connections could be implemented as dry contact joints. Figure 66 shows the point connection at the location of the bottom chord. The edges of the glass plates are clamped in a U-profile, which is connected to a cap-shaped end plate. These end plates ensure that the forces are evenly distributed across the U-profile. Coupling between these components is done via spherical joints, which helps to accommodate tolerances caused by variations in manufacturing and assembly. These joints allow forces to be transmitted without additional stresses, contributing to efficient load transmission.

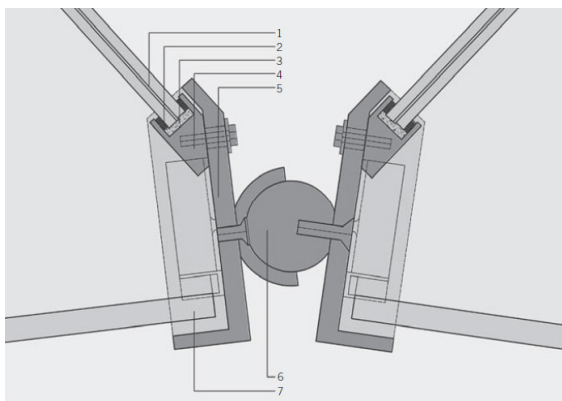


Figure 66: Point connection between the tetrahedrons, illustrating the dry interlocking joint designed to accommodate tolerances (Wurm, 2007)

Conclusion

Due to its amorphous structure, glass is an inherently brittle material. Fracture occurs primarily under tensile stresses, where surface flaws can deepen over time to a critical length, leading to sudden and unexpected failure. This explains why glass has a relatively low characteristic tensile strength compared to its compressive strength. To achieve slender and efficient glass structures, it is essential to incorporate external geometries in the conceptual design that primarily transfer forces through compression, such as arches, barrel vaults, or domes.

The internal geometry - consisting of structural elements and their connections - determines how these compressive forces are absorbed, distributed, and transferred to the supports. To support external force transfer in compression, the internal geometry should avoid moment-resisting connections; using pinned joints, for example, helps ensure that bending moments are minimized and forces are transferred more effectively through axial compression.

Besides, it is important to account for potential stress concentrations caused by production and assembly tolerances. These can be mitigated by incorporating viscoelastic materials in direct contact with the glass.

5. Key Design Guidelines

This chapter outlines essential design guidelines for structural glass that should be considered both during the conceptual design phase and throughout the design elaboration.

Strengthening methods

Through tempering, the inherently low tensile strength of glass can be increased. After the float glass process described in Chapter 4, the glass is reheated to approximately 650°C and then rapidly cooled using jets of cold air. This causes the outer surfaces to cool and solidify faster than the inner core. As the interior gradually cools and contracts, it pulls on the already solidified surface, placing it under compressive stress. This compressive layer effectively closes surface flaws, thereby improving the tensile strength of the glass compared to annealed glass (Louter, 2011).

There are two main heat-based strengthening methods: heat strengthening and fully tempering. Fully tempered glass is stronger because it is cooled more rapidly during the treatment process, creating a larger temperature gradient between the core and the surface. This results in a higher level of surface compression, also known as pre-stress. This pre-stress must first be overcome before surface flaws can propagate, which enhances the glass's ability to resist tensile failure (Louter, 2011).

Glass can also be strengthened chemically, although this method is used less frequently due to higher costs (Haldimann et al., 2008). Chemical strengthening is typically applied when thermal toughening is not feasible, such as in gravity-bent glass (Sedak, n.d.). In this process, the glass is immersed in a bath of electrolytes at around 300°C, where smaller sodium ions in the glass surface are replaced by larger potassium ions. This ion exchange creates compressive stress in the surface layer, improving the strength of the glass. This method is particularly suited for complex geometries where uniform cooling is difficult to achieve – such as in bent glass, where convex or concave sections cool at different rates, potentially leading to uneven internal stresses.

Figure 67 illustrates the characteristic tensile strengths achieved through different post-treatment methods.

Glass type	Characteristic tensile strength
Annealed	45 MPa
Heat Strengthened	40–80 MPa (24–52 acc. to ASTM C 1048-04)
Fully Tempered (toughened)	150 MPa
Chemically tempered	Up to 700 MPa

Figure 67: Characteristic tensile strength for different types of glass (Rammig, 2022)

In addition to enhancing the tensile strength of glass, tempering also influences its breakage behavior, and therefore its structural safety. The level of surface pre-stress directly affects the glass shattering pattern.

Figure 68 shows the pre-stress distribution across the glass cross-section for the three main post-treatment methods (Rammig, 2022).

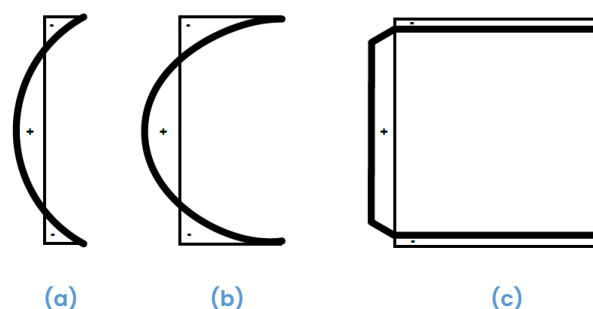


Figure 68: Pre-stress distribution of (a) Heat Strengthened, (b) Fully Tempered, and (c) Chemically Strengthened glass (Rammig, 2022)

An increased pre-stress correlates directly with the amount of energy released upon fracture. This relationship is illustrated by the distinct fracture patterns presented in figure 69, which demonstrates that fully tempered glass fragments fracture into numerous small particles upon breakage. Such fracture behavior is typically regarded as safer compared to that of non-tempered glass, which generally fractures into large, sharp-edged shards. These larger fragments elevate the risk of injury due to their size and sharpness (Rammig, 2022).

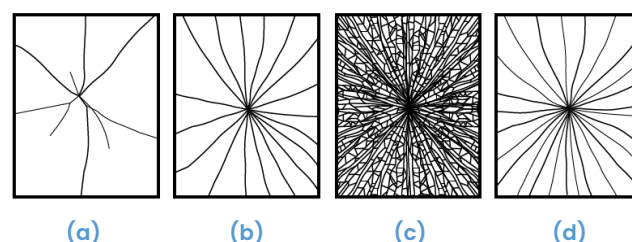


Figure 69: Breakin patterns of (a) Annealed, (b) Heat Strengthened, (c) Fully Tempered, and (d) Chemically Strengthened glass (Rammig, 2022)

Lamination

Fully tempered glass elements shatter into numerous small fragments upon breakage, losing their structural integrity entirely, unlike other glass types. Incorporating lamination into structural glass elements provides redundancy and enhances safety. Laminated glass typically consists of at least two glass panes – either identical or differing in thickness and heat treatment – bonded by an interlayer (Haldimann et al., 2008).

The lamination process begins with thorough cleaning of the glass panes (Fig. 70). Subsequently, interlayers, typically applied in multiples of 0.38 mm thickness, are placed between the panes and subjected to heating. The actual bonding process occurs in an autoclave at approximately 140 °C under high pressure, causing the interlayer to become transparent and achieving a secure bond (Van Dooren, 2014) & (Haldimann et al., 2008).

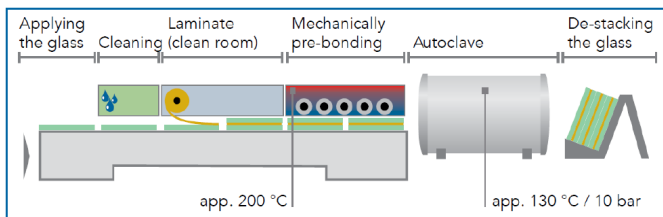


Figure 70: Lamination process (Van Dooren, 2022)

Due to lamination, glass fragments remain adhered together following fracture. Consequently, the laminated glass element retains sufficient structural integrity to prevent collapse (Rammig, 2022; Louter, 2011). This type of glass is referred to as Laminated Safety Glass (LSG). Figure 71 illustrates the load-bearing behavior of laminated glass composed of different heat-treated types – including heat-strengthened and fully tempered glass – after one or two panes have fractured (Van Dooren, 2014).

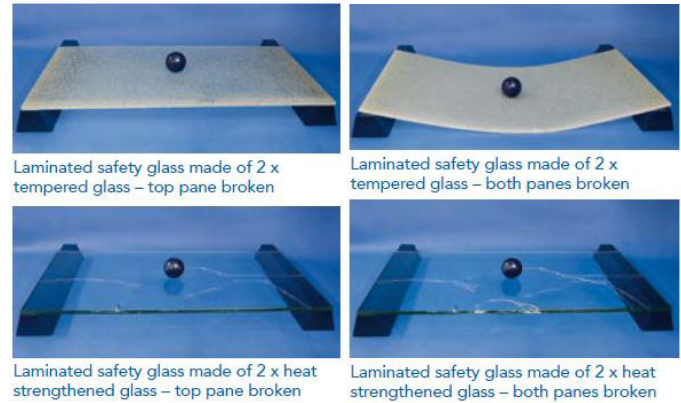


Figure 71: Load bearing behavior of LSG after fracture (Van Dooren, 2014)

Even in the worst-case scenario, where both glass panes fracture into small fragments, the laminated structure remains intact, preventing glass fragments from falling down. However, laminated fully tempered glass loses all residual load-bearing capacity when both panes are broken, unlike laminated heat-strengthened glass, which maintains some residual structural performance (Van Dooren, 2014). Therefore, it is crucial to assess whether glass elements remain safe for passage after fracture.

Interlayers

Interlayers can be categorized into adhesive resins and adhesive films. Adhesive resins are directly poured between the glass panes and subsequently cured using UV radiation. In contrast, adhesive films are positioned between the glass panes, after which the assembly is heated and subjected to pressure in an autoclave, resulting in a durable bond.

Polyvinyl butyral (PVB) is the most commonly used film interlayer in the construction industry. For structural applications, more rigid materials such as stiff PVB or SentryGlas® are increasingly preferred. Specifically, SentryGlas® was developed to enhance resistance against vandalism, hurricanes, and burglaries, offering greater strength and stiffness compared to standard PVB (Louter, 2011).

PVB exhibits viscoelastic behavior, responding elastically under short-term, rapid loading conditions and returning to its original shape once the load is removed. Under prolonged or slow loading conditions, however, PVB demonstrates creep behavior. Additionally, its mechanical properties are temperature-dependent. Shear force transfer between glass panes reaches its maximum efficiency at temperatures below 0°C and under short-duration loading. Figure 72 shows the shear stiffness of standard PVB, stiff PVB, and SentryGlas® interlayers in laminated glass, highlighting their time- and temperature-dependent characteristics (Jóźwik, 2022).

Properties \ Interlayer	PVB	Extra stiff PVB (Trosifol®)	Ionomer (SentryGlas®)
Density [kg/m ³]	1065	1081	950
Coefficient of linear expansion [°C ⁻¹]	$2.2 \cdot 10^{-4}$	$1.6 \cdot 10^{-4}$	$10 \sim 15 \cdot 10^{-5}$ (-20°C ÷ 32°C)
Tensile strength [MPa]	23	32	34.5
Tear strength (tear energy) [MJ/m ³]	10–15	–	50
Tensile elongation [%]	> 280	> 180	400
Poisson's ratio	0.5	0.5	0.5
Young's relaxation modulus $E(t)$ [MPa] 30° for 1 hour	0.97	2.7	178
Young's relaxation modulus $E(t)$ [MPa] 50° for 1 hour	0.20	1.0	12.6
Shear relaxation modulus $G(t)$ [MPa] 30° for 1 hour	0.33	0.92	60.0
Shear relaxation modulus $G(t)$ [MPa] 50° for 1 hour	0.068	0.34	4.2

Figure 72: Table showing a decrease in stiffness for interlayers, based on temperature and load-duration (Jóźwik, 2022)

The table illustrates that the Young's relaxation modulus for all interlayers decreases with rising temperatures, indicating increased flexibility and reduced capacity to maintain stiffness under load. This decline in stiffness simultaneously leads to a decrease in the shear relaxation modulus, weakening the shear coupling between glass layers, thus causing increased deflection and diminished structural performance of the laminated glass. For elements subjected to bending, it is essential during preliminary sizing to accurately calculate the effective glass thickness, considering the interlayer's shear modulus, element geometry, load duration, and temperature. Figure 73 depicts various shear transfer mechanisms between two glass panes (Jóźwik, 2022).

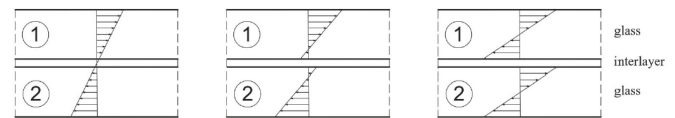


Figure 73: Different levels of shear transfer between the glass panes: (a) full, (b) partial, and (c) no shear transfer (Jóźwik, 2022).

Edge treatment

Glass cutting and processing can introduce surface flaws on the edges of glass elements, directly affecting their fracture strength. Therefore, the edges undergo specific treatment procedures, illustrated in Figure 74, prior to the tempering process (Haldimann et al., 2008). A seamed edge aims to remove sharp corners to minimize the risk of injury. For glass elements intended as primary structural components, edge treatment extends up to step 4 to ensure optimal strength and safety (Rammig, 2022).

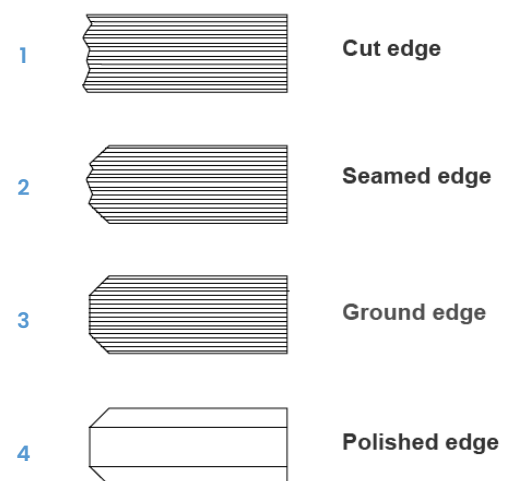


Figure 74: Steps of glass edge treatment after cutting (Rammig, 2022)

Bending

After the glass sheets have undergone surface and edge treatments, they can be bent.

Introducing curvature to glass elements not only serves aesthetic purposes but also significantly enhances structural performance by increasing stiffness. Research indicates that for glass with a bending radius of 5000 mm, the tensile bending stress is reduced by approximately 30% compared to flat glass, while deformation decreases to about 13% of the value observed in flat glass (Fig. 75) (Van Dooren, 2014).

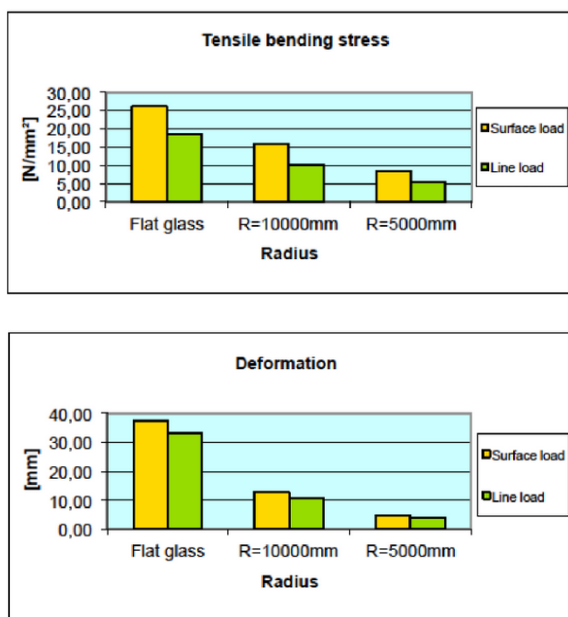


Figure 75: Decrease in bending stress and deformation through curvature (Van Dooren, 2014)

Glass can be bent using either hot or cold bending techniques.

Cold Bending

Due to its linear elastic behavior, glass can undergo elastic deformation (cold bending) after the tempering process. A supporting structure is required to maintain the glass in its intended curved shape (Fig. 76). A limitation of this technique is that only relatively small curvatures are achievable (Van Dooren, 2014). An advantage of this method is that it saves energy, as the glass does not have to be in a viscous state to be bent (Datsiou, 2017).

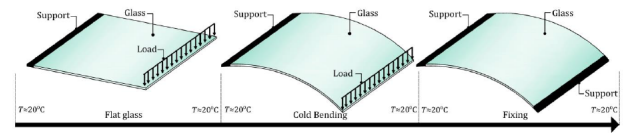


Figure 76: Cold bending process (Datsiou, 2017)

Figure 77 illustrates the tensile stresses transferred within the pane of a cold bent glass plate, which already account for approximately 60% of the maximum allowable total stress. Consequently, cold-bent glass exhibits a lower load-bearing capacity compared to hot-bent glass, directly affecting the achievable minimum bending radius.

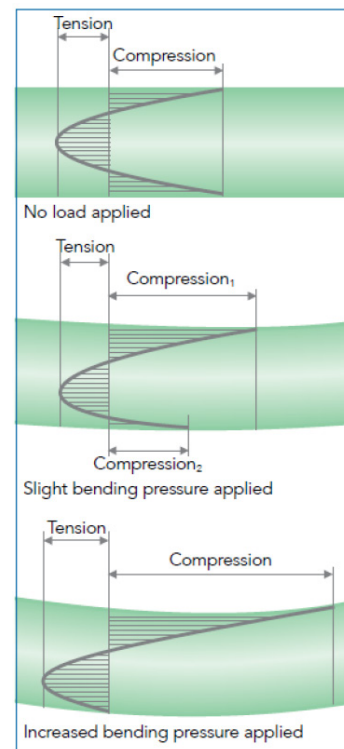


Figure 77: Increase of tensile forces when the glass is cold bent (Van Dooren, 2014)

Cold Bending – Cold Lamination Bending

Cold lamination bending can also be applied to laminated glass. In this process, multiple glass layers are elastically bent simultaneously, with polymer sheets placed between them. Once the desired curvature is achieved, the entire assembly is heated in an autoclave, which bonds the layers together. After cooling, the bending forces are released, but the interlayer retains the curved shape of the glass. The glass may partially spring back towards its original flat form. (Datsiou, 2017) (Fig. 78).

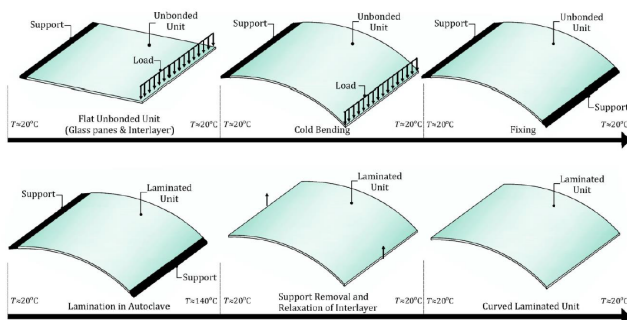


Figure 78: Process of cold lamination bending (Datsiou, 2017)

Hot Bending – Static Mould Bending

Static Mould Bending is suitable for producing multiple panels with identical complex geometries. In this method, a single glass pane is heated above its softening point ($T > 550^{\circ}\text{C}$). The specific temperature depends on the desired curvature. The glass pane conforms to a mold shape under its own weight (Fig. 79). The glass is subsequently slowly cooled and removed from the mold. For double-curved panels, additional pressing into the mold is necessary (Haldimann et al., 2008). Glass panes up to 11.5 meters can be processed using this method (Sedak, n.d.).

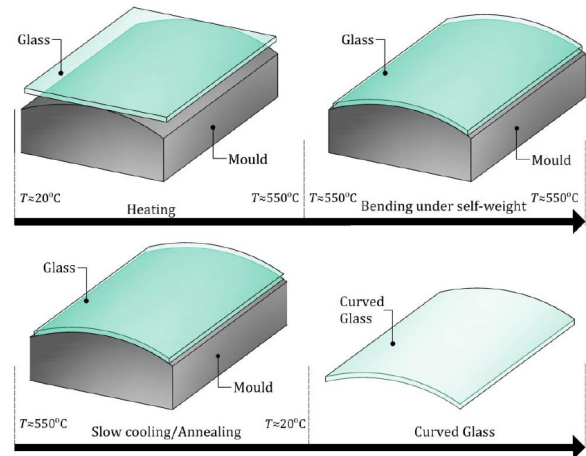


Figure 79: Static Mould Bending process (Datsiou, 2017)

Hot Bending – Thermal Bending

Thermal bending is another method of hot bending in which float glass is heated in an autoclave and shaped by individually adjustable rollers (Haldimann et al., 2008). The final shape is preserved by cooling the glass in its curved form (Fig. 80). After this step, the glass can be laminated. Thermal bending is particularly suitable for producing repetitive cylindrical shapes, double curvatures, convex and concave forms, and wave-like shapes. The size limitations for this bending method are up to 3.6 x 18 meters (Sedak).

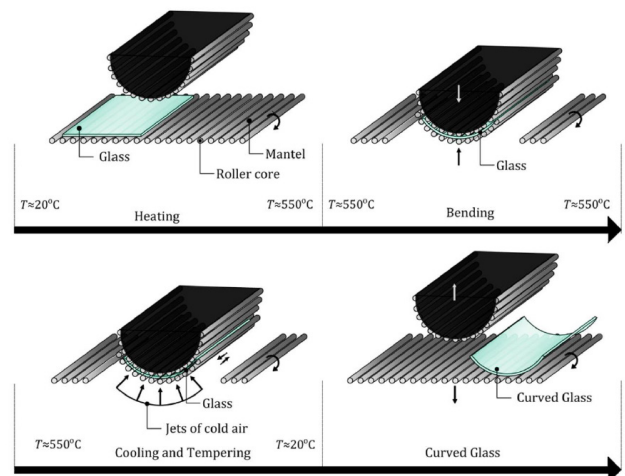


Figure 80: Thermal Bending process (Datsiou, 2017)

Size Limitations

Glass panels are available in various thicknesses. Standard thicknesses produced through the float glass process include 2, 3, 4, 5, 6, 8, 10, 12, 15, 19, and 25 mm, with 8, 10, and 12 mm being most commonly used in practice (Louter, 2011).

The final cross-sectional dimension of a laminated glass element depends on the number and thickness of the interlayers. Typically, laminates exceeding five to six layers or a total thickness of 50–100 mm are uncommon. During lamination, interlayers are heated and compressed between glass panes. If the glass is too thick or comprises numerous layers, uneven heating and compression may occur, leading to air bubbles or local delamination due to uneven pressure distribution (Louter, 2011).

Tempering

Panel dimensions also depend on the size of ovens used for structural tempering, which typically have a maximum width of approximately 2.4 meters. However, lengths up to 24 meters can be produced (Louter, 2011).

Transparent Solar Control

Approximately 3% of the shortwave solar radiation reaching the Earth's surface consists of ultraviolet (UV) light, about 42% consists of visible (VIS) light, and around 55% is near-infrared (NIR) radiation. VIS and NIR radiation account for the largest portion of the energy (Haldimann et al., 2008).

Several solutions block short-wave infrared from the sun to block direct solar heat while maintaining optimal glass transparency:

Low-emissivity coatings were originally designed to reflect longwave infrared radiation from the interior back inside, thus reducing heat loss (Berardi & Khaled, 2024). In situations where the structure itself does not serve an insulating function, this particular application becomes irrelevant.

An alternative is provided by so-called NIR-shielding films, which incorporate nanoparticles that absorb near-infrared radiation and subsequently radiate this heat outward or directly reflect it (Berardi & Khaled, 2024) (Fig. 81). The combination with a low-E coating can also be seen in this figure within an insulated glass façade; however, this combination is inapplicable for the current project.

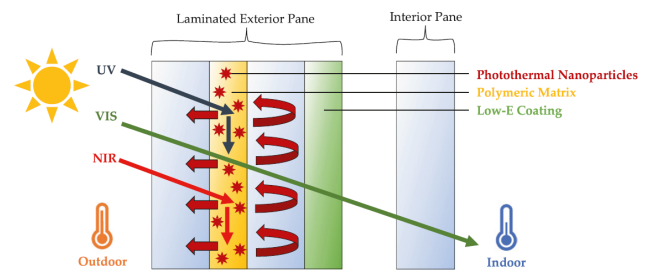


Figure 81: Functioning of NIR shielding through reflection or absorption (Berardi & Khaled, 2024)

However, NIR-blocking components can offer benefits. They are available as films that can be laminated between glass layers. Additionally, these components can be integrated directly into the interlayer of laminated glass. An example of such a technology is Saflex® Solar (Qdel, n.d.).

Finally, it is possible to apply NIR-blocking materials as a soft coating onto the glass surface. However, a disadvantage of this method is the increased susceptibility to damage, often necessitating an additional protective layer (Haldimann et al., 2008).

DESIGN CONCEPTS

6. Design Concepts for an Adaptable Float Glass Structure

Based on the principle of modular design, various concepts have been developed, considering the constraint that the external structure primarily transfers loads through compression. This approach integrates the goal of lightweight construction already early in the design process.

Whereas Chapter 4 emphasized the mechanical form, this chapter focuses on the functional form. Various design concepts have been developed with particular attention to their expandability in both the x and y-direction.

Each design is subsequently evaluated against the program of requirements to arrive at a final design choice. The most critical requirements in this phase are highlighted in blue in the tables. For instance, protection against weather influences is considered a preference rather than a strict requirement, given that the research primarily focuses on expandability, reusability, and ease of assembly.

6.1 Big scale modularity

Concept 1

First, experiments were conducted on a large modular scale, with each module representing an individual building unit. Following this, various internal geometries were explored to determine how they could define the external form (Fig. 80). The goal was to ensure that the panels shaping the modules could also be disassembled, supporting recyclability at the end of the building's lifecycle.

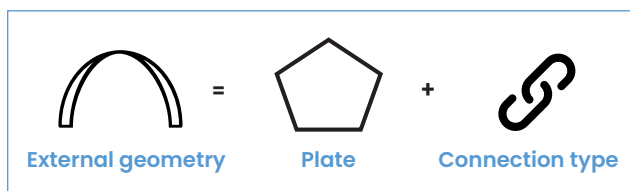
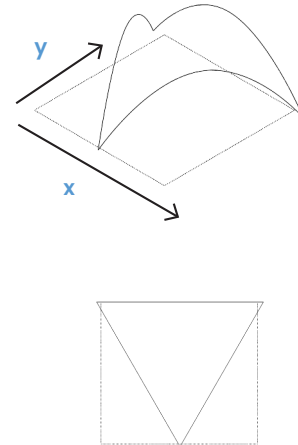


Figure 82: Principle of a big scale modularity concept (own work, 2025)

One of the initial experiments involved individual shell units with a triangular floor plan. By tessellating these shell units, their potential for spatial expansion was explored in both the x and y-direction (Fig. 83 & 84)

1 module



Extension in x-direction

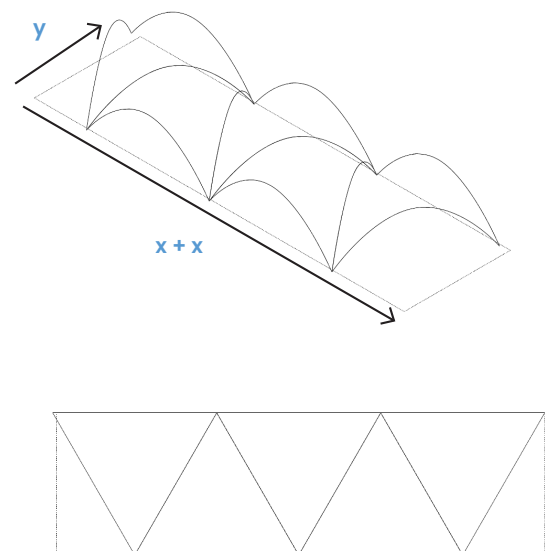


Figure 83: Tessellation of shell units with a triangular floor plan in the x-direction (own work, 2025)

Extension in y-direction

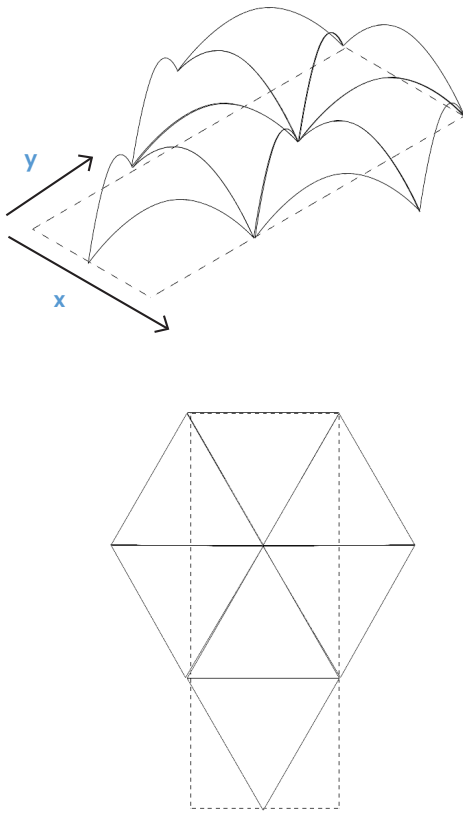


Figure 84: Tessellation of shell units with a triangular floor plan in the y-direction (own work, 2025)

Ways of dividing the shell into different structural elements were then investigated. The shell can possibly be divided into two or more parts of double-curved glass by gravity bending (Fig. 85)

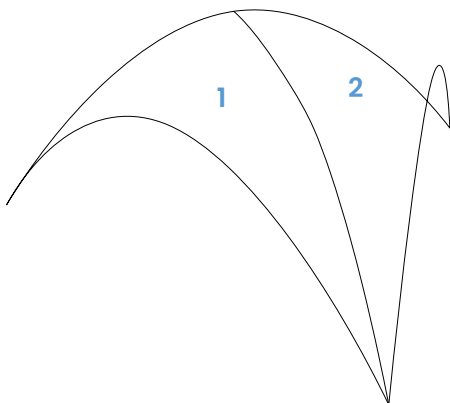


Figure 85: Concept of double curved structural elements to form a shell (Own work, 2025)

For the connections, inspiration can be drawn from traditional woodworking joints. For instance, a dovetail joint could be used to create a geometric interlock between the plates (Fig. 86).



Figure 86: A dovetail joint to geometrically interlock structural wooden components (Robeller & Weinand, 2015)

Another way to subdivide the surface is by using planar quadrilateral facets: flat, four-sided panels such as rectangles. When multiple panels are connected at angles to one another along their edges, they form a folded plate structure, which increases the overall stiffness of the system (Fig. 87) (Mesnil et al., 2017).

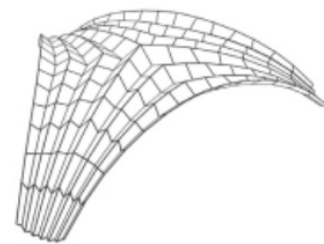







Figure 87: Folded plate structure with planar quadrilateral facets (Mesnil et al., 2017)

Programme of requirements

Evaluation

Extendable in the x-direction, while maintaining an open floor plan	Adding multiple shell modules results in a subdivision of the space due to the placement of the supports 
Extendable in the y-direction, while maintaining an open floor plan	Adding multiple shell modules results in a subdivision of the space due to the placement of the supports 
A lightweight system to support manual assembly and disassembly	The form has potential for a lightweight system due to its external geometry. Selecting the appropriate internal geometry can further contribute to this 
Possibility for manual assembly and disassembly without the need for complex instructions	It depends. Manual assembly and disassembly are not feasible if the shell is divided into panels that are too large and heavy to be carried by hand, although this approach can be more advantageous in terms of transparency
The design should not compromise the transparent quality of all-glass buildings	It depends. Dividing the shell into very small panels means more connections are needed, which can be visually very present
Minimal number of standardized building components to simplify the manufacturing and construction process and to optimize the reuse potential of structural components	A subdivision that is too small – necessary for manual assembly – results in numerous variable panels and likely multiple types of connections. As a result, the system tends to lean more toward a customizable design 
Basic protection against rain and overheating	The system is closed, and transparent solar control can be integrated 

 Important requirements

6.2 Small scale modularity

Concept 2

The next approach is based on small-scale modularity. In this approach, the modules are considered as plates that make up the external geometry instead of the other way around (Fig. 86).

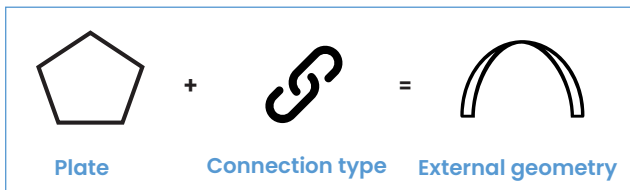


Figure 88: Workflow for small scale modularity concepts (own work, 2025)

An arch can be constructed by joining rectangular, standardized panels at specific angles (Fig. 89).

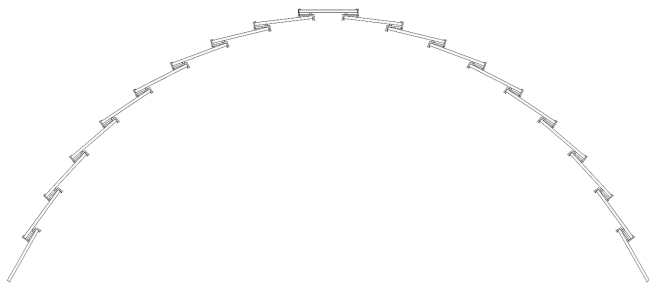


Figure 89: An arch formed by rectangular panels (own work, 2025)

If the connection – whether linear or discrete – can adapt the parameter 'h' (Fig. 90), the structure can adjust its span and thereby extend or contract along the y-direction (Fig. 91).

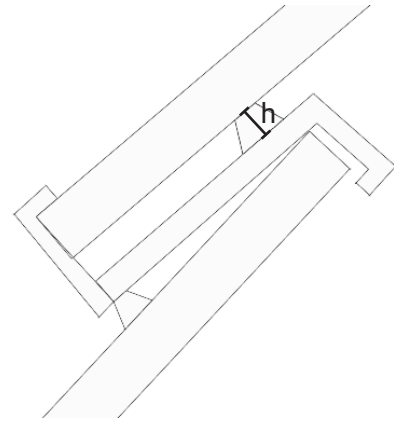


Figure 90: Conceptual connection adjustable through parameter 'h' (own work, 2025)

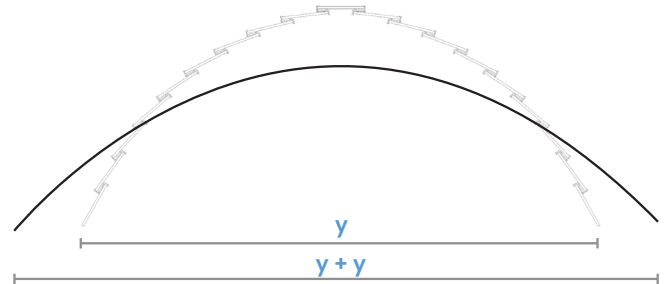


Figure 91: Extension in the span direction (own work, 2025)

A single arch represents one row. By adding additional rows, the structure can theoretically extend infinitely in the x-direction, as shown on the next page (Fig. 92).

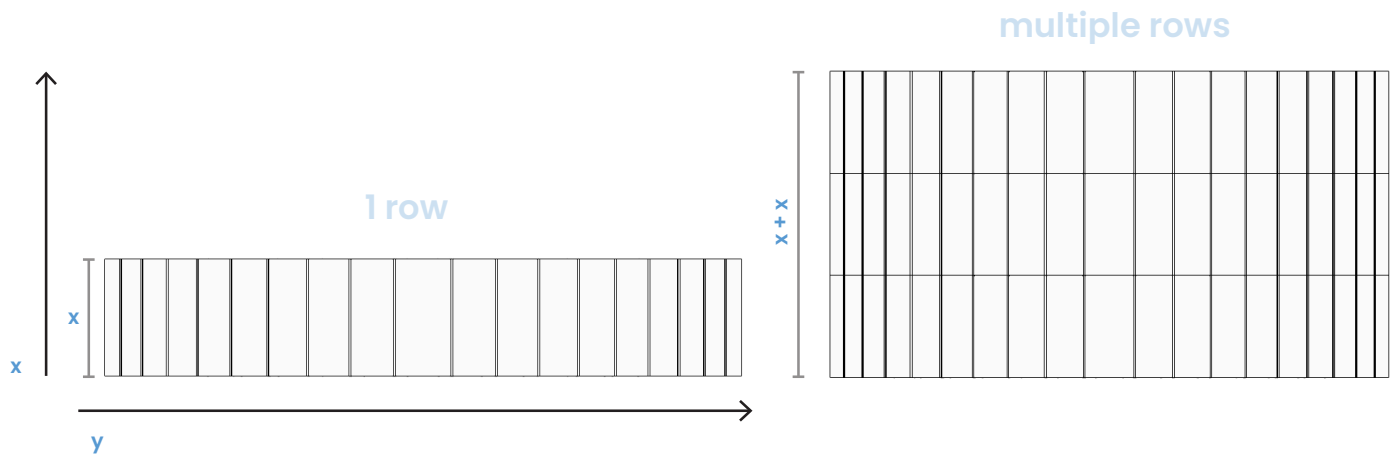


Figure 92: Extension in the x-direction (own work, 2025)

By adjusting the angle of the connection, the span can be altered. Ideally, this change in angle is accommodated within a single connection (Fig. 93).

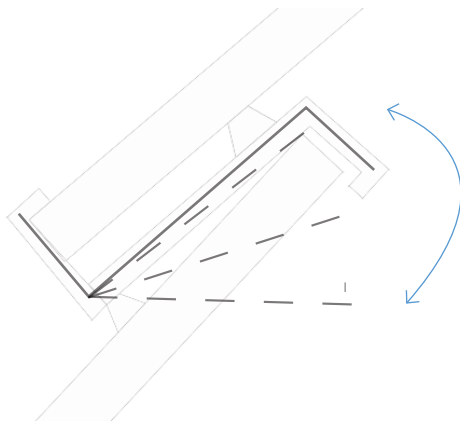


Figure 93: Concept for a connection with Integrated Adjustable Angle (own work, 2025)

One option that was explored is the application of kerfing - a technique in which cuts or notches are made in a material to increase its flexibility (Naboni & Marino, 2021). When wedges are inserted between the kerfs, the material maintains in the curved state (Fig. 94). Besides, another concept was developed involving the integration of tension cables (Fig. 95).

However, applying this method in the context of this project appears overly complex. The need to repeatedly replace tension rods or wedges, combined with the fabrication of a kerfing pattern, does not result in a system that is easy to produce or assemble. Therefore, the connection described on the previous page offers greater potential.

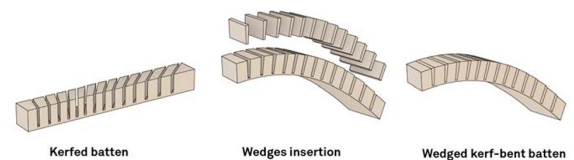


Figure 94: Keeping a kerfed element in place by means of disks in the slots (Naboni & Marino, 2021)

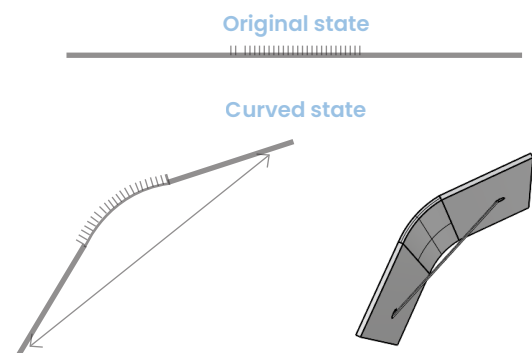


Figure 95: Bended connection, kept in place by a tension cable or by disks in the slots (own work, 2025)

Programme of requirements

Evaluation

Extendable in the x-direction, while maintaining an open floor plan	The structure can be extended without the floor plan being interrupted by supports ✓
Extendable in the y-direction, while maintaining an open floor plan	The structure can be extended without the space being interrupted by supports ✓
A lightweight system to support manual assembly and disassembly	The form has potential for a lightweight system due to its external geometry. Selecting the appropriate internal geometry can further contribute to this ✓
Possibility for manual assembly and disassembly without the need for complex instructions	The panel dimensions can be chosen to ensure they are manageable for a single person to carry. Additionally, each connection within the system is identical, allowing for a repetitive and straightforward assembly process ✓
The design should not compromise the transparent quality of all-glass buildings	The connection concept inspired by a roof batten joint, can be designed in such a way that it does not compromise the transparency of the system ✓
Minimal number of standardized building components to simplify the manufacturing and construction process and to optimize the reuse potential of structural components	All panels are standardized and easy to produce. The connections still have potential to be further simplified in their design ✓
Basic protection against rain and overheating	The system is closed, and transparent solar control can be integrated. Additionally, transparent solar control can be integrated ✓

To minimize the use of visible connections between the rows, inspiration can be taken from wooden joints. Mortise-and-tenon joints offer inspiration for interlocking modular glass plates, where a 'tenon'-like element in one glass panel fits into a corresponding 'mortise' of another panel (Bühlmeier & Hilcken, 2023) (Fig. 96 & 97).

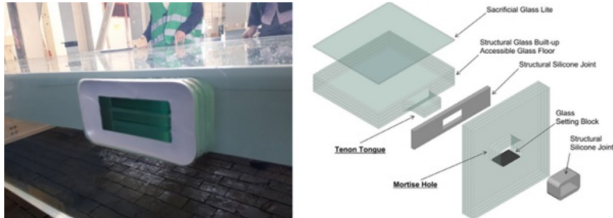


Figure 96: Mortise-and-tenon joint (Bühlmeier & Hilcken, 2023)

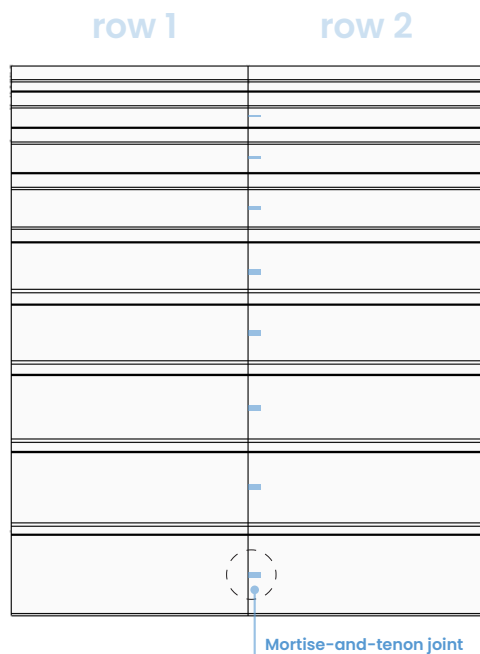


Figure 97: Possible location of the mortise-and-tenon joint in the structure (own work, 2025)

Concept 4

The next concept developed combines a structure that works in tension with modules that operate in compression (Fig. 98). The modules in this system consist of glass panels that interlock with tension cables (Fig. 99). The tension exerted by the cables places the glass panels under in-plane compression (Fig. 100).

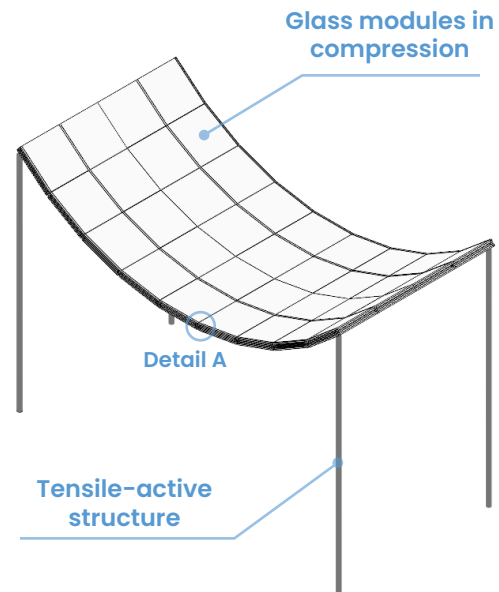


Figure 98: Glass modules in a tensile-active structure (own work, 2025)

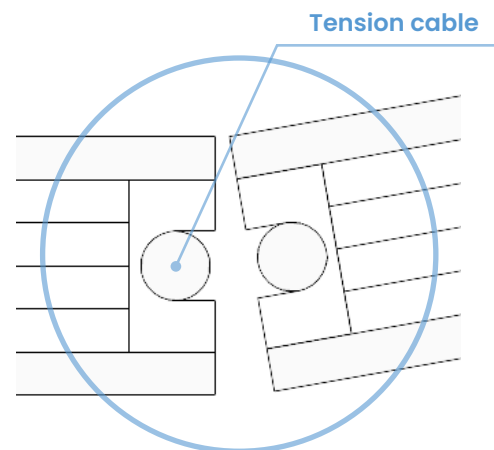


Figure 99: Detail A - glass modules, interlocking with tension cables (own work, 2025)

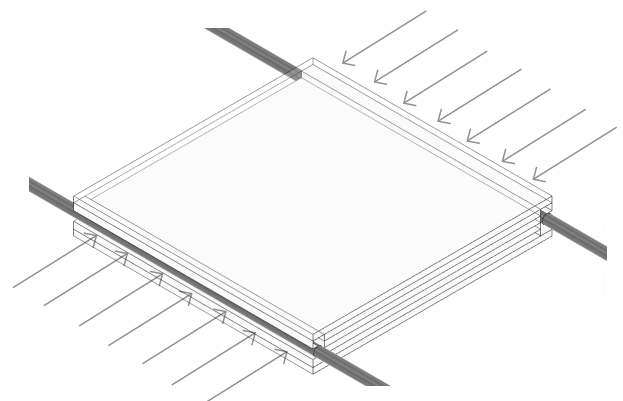


Figure 100: Cables causing the module to be loaded in-plane (own work, 2025)

As in the previous concept, the system is composed of rows. In this case, multiple rows are grouped together to form a base unit. Connecting several of these row clusters allows the structure to be expanded in the x-direction (Fig. 101). By using clusters of rows rather than individual ones, the need for additional columns during expansion is minimized.

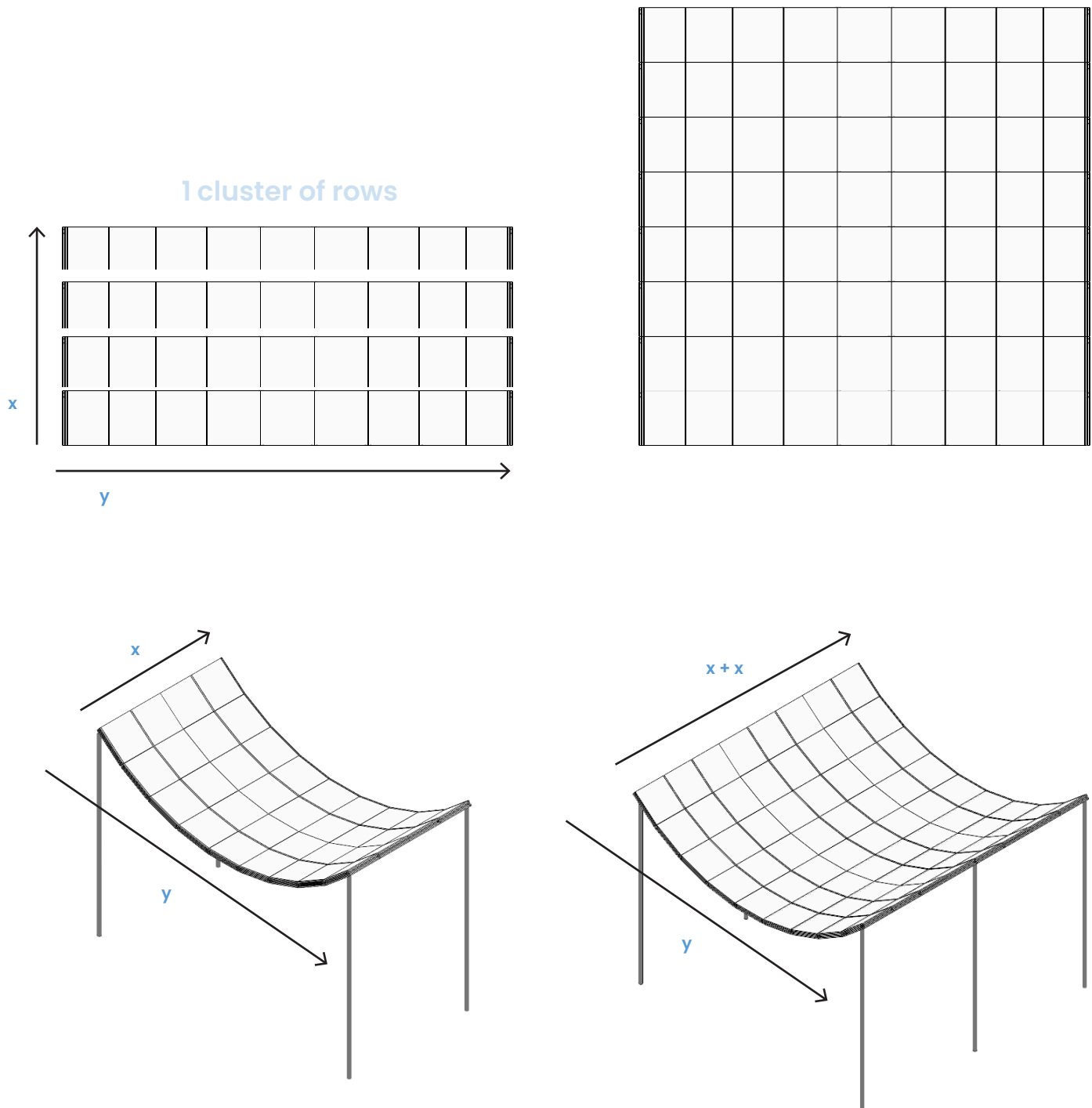


Figure 101: Extension in the x-direction (own work, 2025)

Expansion in the y-direction can be enabled by tightening or loosening the cables running in that direction (Fig. 102).

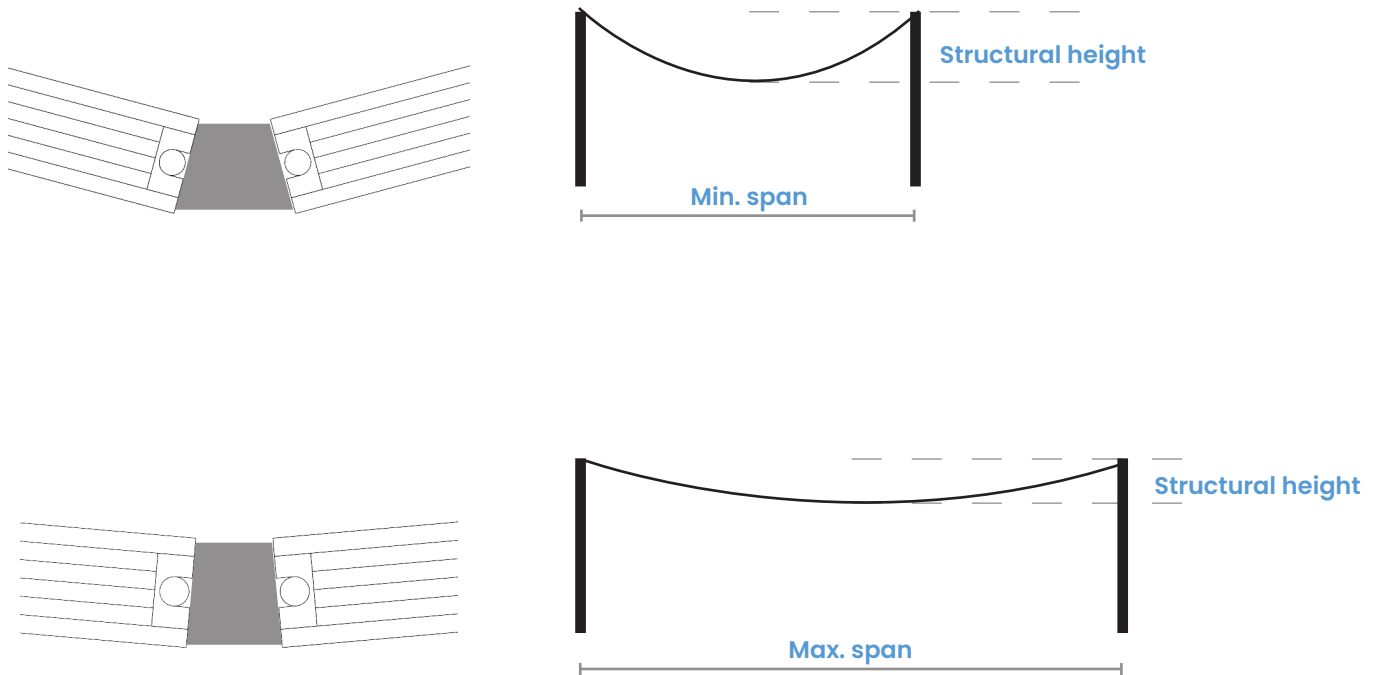


Figure 102: Extension in the y-direction (own work,

Programme of requirements

Evaluation

Extendable in the x-direction, while maintaining an open floor plan	The structure can be extended without the floor plan being interrupted by supports. However, the supports of the tension-active structure are visually quite prominent ✓
Extendable in the y-direction, while maintaining an open floor plan	Tightening or loosening the cables does not require the addition of supports ✓
A lightweight system to support manual assembly and disassembly	The concept has potential for a lightweight structure, as the cables absorb the tensile forces while simultaneously forcing the modules to act in compression ✓
Possibility for manual assembly and disassembly without the need for complex instructions	The cable system possibly large and heavy, making it difficult to install manually. It is also assumed that placing the glass panels within the cable nets demands significant effort ✗
The design should not compromise the transparent quality of all-glass buildings	The use of a tension system undermines the overall aesthetic of an all-glass structure ✗
Minimal number of standardized building components to simplify the manufacturing and construction process and to optimize the reuse potential of structural components	The panels and connections are repetitive, and the cables are concealed within the modules ✓
Basic protection against rain and overheating	The concept is theoretically waterproof, but the connections require careful attention. Additionally, transparent solar control can be integrated ✓

 Important requirements

Concept 5

The fifth concept was developed with the primary goal of creating a simplified system, in which connections and modules are not separate components, but instead integrated into a single unit. This was achieved by geometrically interlocking the modules. The mortise-and-tenon joint was already an example of such an approach. The study explored whether a spanning structure could be created using the simplest panel shapes – rectangles or squares – by interlocking them using slots (Fig. 103).

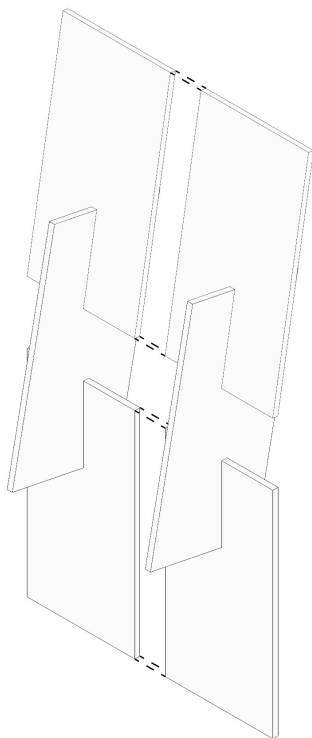


Figure 103: Geometrical interlocking modules (own work, 2025)

The span of the system can be made adaptable by adding several slots along the length of the module that allow interlocking at a different angle. However, the problem here is that the slots are not on the module's centreline, introducing moments and making the system unstable (Fig. 104).

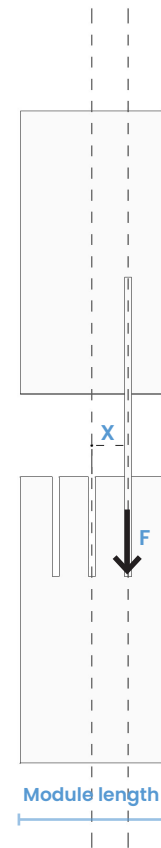


Figure 104: Slots located outside the module's center line introduce bending moments (own work, 2025)

In addition, this interlocking method creates large openings within the structure, allowing rainwater to pass through easily.

The connection between the rows can be achieved using a mortise-and-tenon joint. However, a potential limitation is that the cross-section of the system may need to be oversized to ensure sufficient thickness for this type of connection.

A new design iteration has been developed (Fig. 105) that ensures the following improvements:

1. The module rows can also interlock in the horizontal direction
2. The openings within the system are reduced
3. The structural stability is enhanced
4. The system exhibits increased stiffness

The improved concept consists of V-shaped modules that interlock with one another (Fig. 105). Each module is composed of two rectangular laminated float glass panes, bonded together at an angle.

The V-shape allows for multiple slots to be integrated along the length of the module without generating bending moments, as module 1 is symmetrically supported by modules 2 and 3.

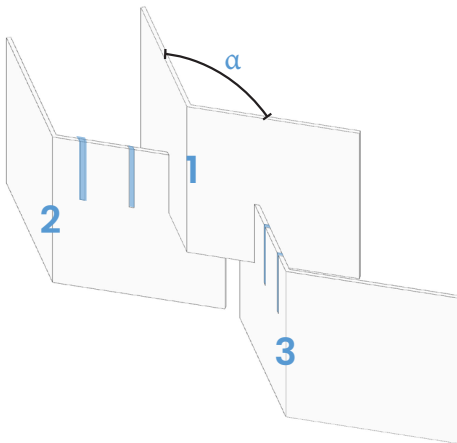


Figure 105: Interlocking V-shaped modules
(own work, 2025)

The structure can be divided into several rows that interlock with one another. The slots are positioned at the top of each module, allowing the bottom of one module to slide into the slots of the module below (Fig. 106).

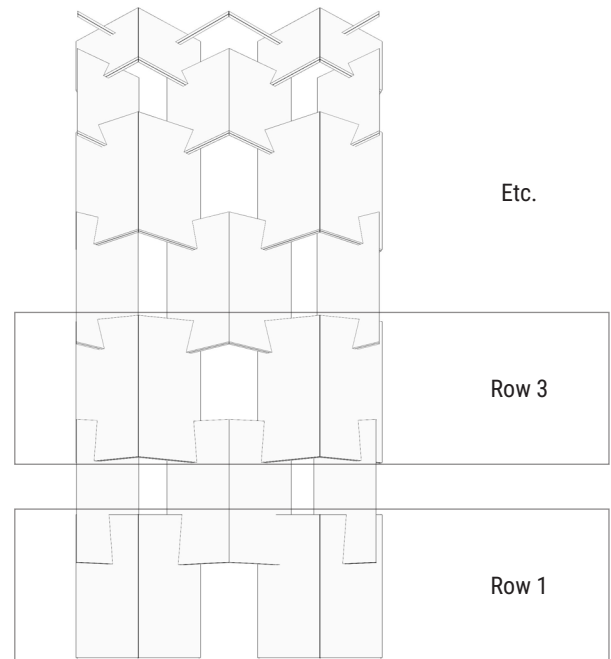


Figure 106: Side view showing the rows of the system
(own work, 2025)

By interlocking the modules at an angle, an arch can be formed (Fig. 107).

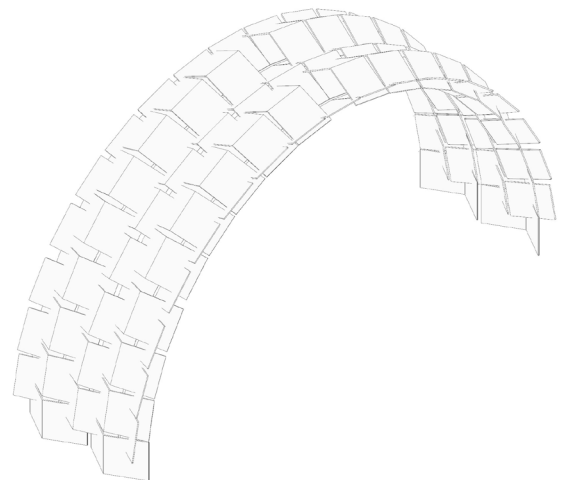


Figure 107: Arch created out of V-shaped modules
(own work, 2025)

If the structure needs to be expanded in the x-direction, either the standard system shown in Figure 107 can be duplicated and interconnected (Fig. 108), or the smaller side modules must be removed, and the entire structure rebuilt with additional rows (Fig. 109).

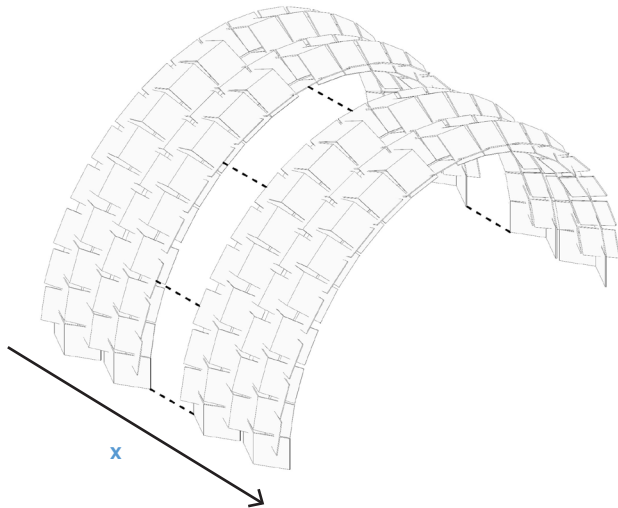


Figure 108: Extension in the x-direction
(own work, 2025)



Figure 109: Side panels that have to be removed
to extend the structure in the x-direction
(own work, 2025)

Programme of requirements

Evaluation

Extendable in the x-direction, while maintaining an open floor plan	✓
Extendable in the y-direction, while maintaining an open floor plan	✓
A lightweight system to support manual assembly and disassembly	The form has potential for a lightweight system. In addition, the folded plate structure provides increased stiffness and stability ✓
Possibility for manual assembly and disassembly without the need for complex instructions	The modules can be manufactured in compact sizes, and the system employs a straightforward assembly method where each module slides seamlessly into the one before it ✓
The design should not compromise the transparent quality of all-glass buildings	The use of geometrical interlocking, combined with the fact that the joint does not run along the edges of the glass, reduces the visual impact of the connections - allowing the transparent modules to remain the primary visual focus ✓
Minimal number of standardized building components to simplify the manufacturing and construction process and to optimize the reuse potential of structural components	All modules have an identical form and can be manufactured and assembled uniformly. Only the slots might require custom fabrication, though this will not be immediately visible ✓
Basic protection against rain and overheating	While the system is not inherently weather-resistant, its performance can be enhanced by reducing the size of the openings in the structure. Furthermore, transparent solar protection can be incorporated into the glass panels ✓

 Important requirements

Chosen design concept

After evaluating all concepts against the program of requirements - with the most critical criteria carrying the most weight - it becomes clear that concept 2 and 5 (Fig. 110) score the highest. Both meet all the specified requirements, although concept 5 scores slightly lower regarding protection against rain. However, concept 5 offers more significant advantages compared to concept 2. For instance, the intended assembly and disassembly process is considerably more straightforward, as the modules only need to be slid together or apart.

Additionally, the connections - which, unlike in concept 2, are not located at the edges of the modules - have much less impact on the transparency of the structure.

The slight disadvantage in rain resistance is therefore outweighed by the greater benefits that concept 5 offers in terms of the more important requirements.

Improvement of the chosen design concept

The lamination layer between the glass plates represents a critical point in the construction. On one hand, small deviations in the angle between the plates that may arise during production can lead to asymmetrical force transfer. On the other hand, the lamination layer itself is a structural weak point. It must be sufficiently stiff in order for the module to function as a unified element (Fig. 111).

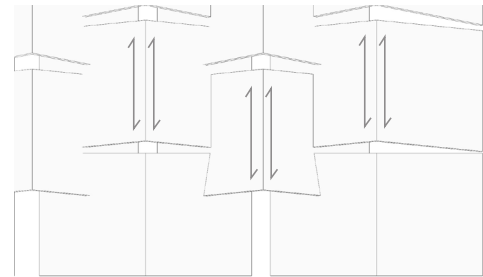
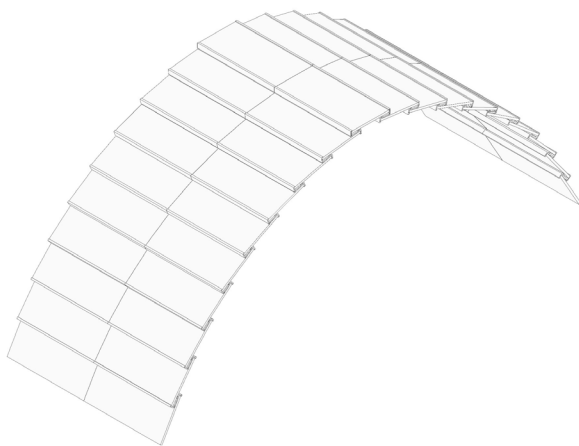


Figure 111: The stiff interlayer, responsible for transferring shear forces between the glass plates (own work, 2025)

Concept 2



V.S.

Concept 5

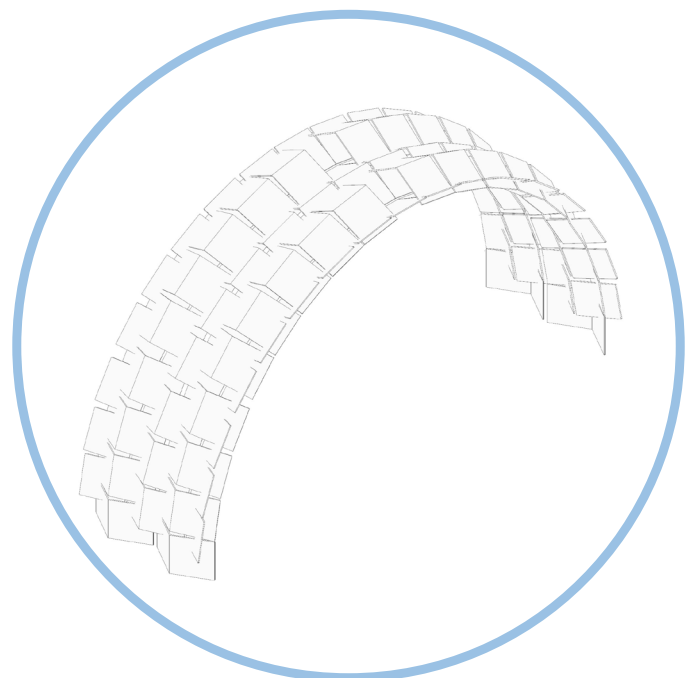


Figure 110: Concept 2 v.s. Concept 5 (own work, 2025)

Several design considerations were made for the point where the modules come together. For instance, aluminum could potentially be used to hold the modules in place (Fig. 112)

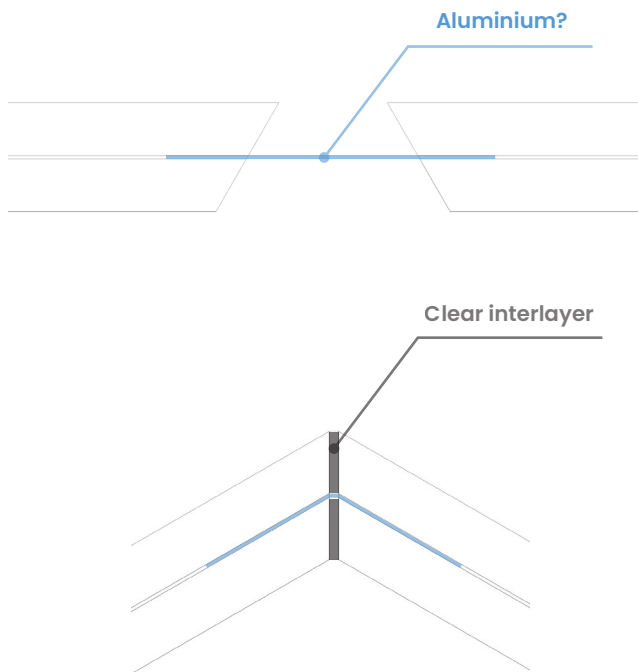


Figure 112: Ontwerpvariant voor de verbinding tussen de gevouwen platen (own work, 2025)

Geometrically interlocking panels were also considered (Fig. 113)

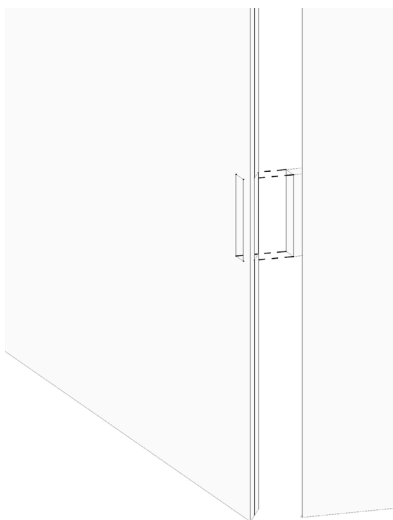


Figure 113: Connecting the two panes by geometrical interlocking (own work, 2025)

To get around the critical point and to minimize the number of connections within the structure, it was ultimately decided to use curved glass for the modules. Thanks to their curvature, these modules still offer high stiffness and contribute to the overall stability of the system, while eliminating the need for shear force transfer within the module itself (Fig. 114)

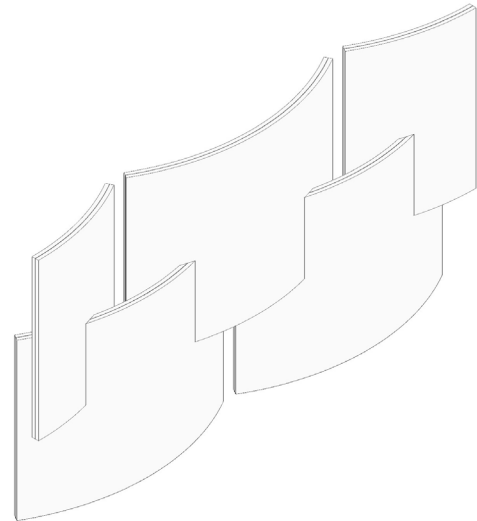
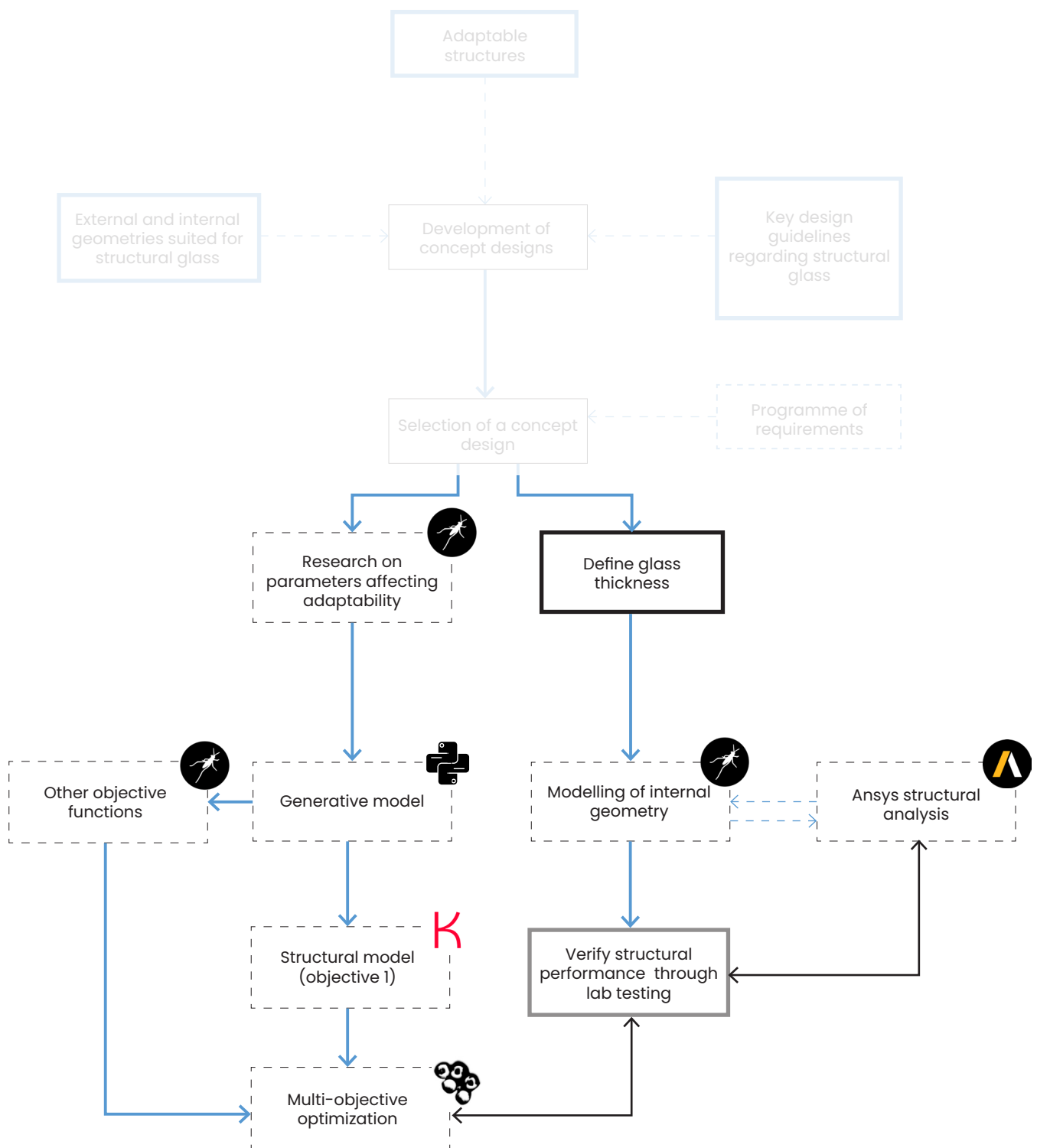


Figure 114: Official concept design, made out of curved modules (own work, 2025)

It is likely that the modules can be produced using the hot bending technique. Each glass pane is bent individually, after which they can be laminated together.

PART II : DESIGN ELABORATION



 Literature

 Design

 Computational design

 Physical test

 Hand calculations

 Comparison

 Next step

 Input

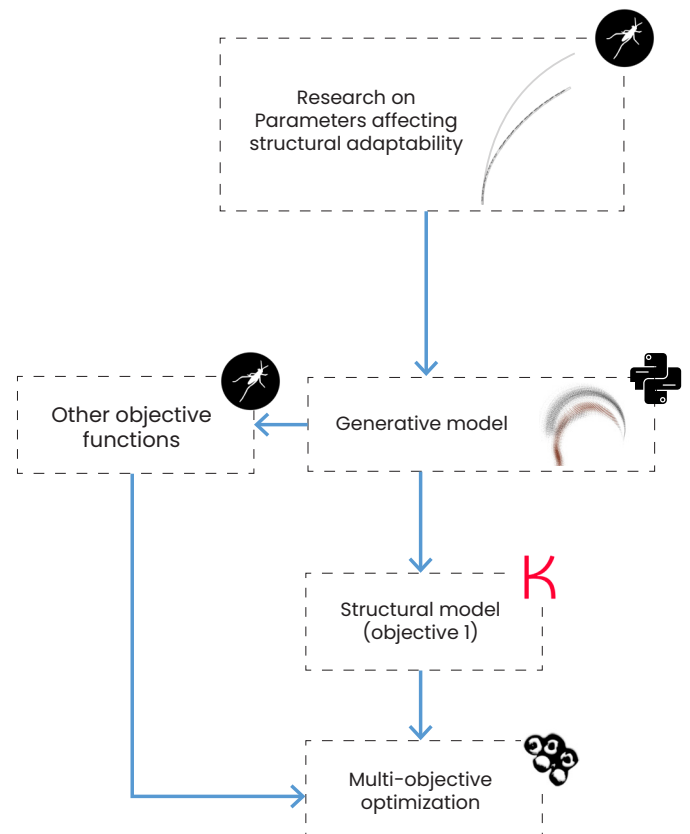
7. Design Elaboration

The design elaboration is structured into three different parts.

Part I: Parametric Exploration

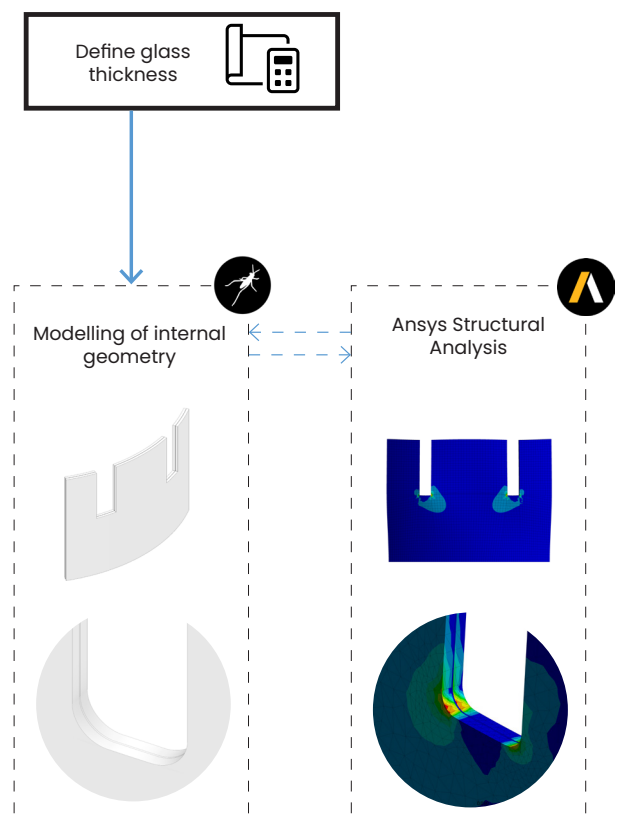
The goal of Part I is to develop an algorithm capable of generating a wide range of design solutions based on variables that influence the structural span. A parametric study was conducted to identify the key parameters affecting adaptability in the y-direction, which informed the development of a generative model.

Combined with defined objective functions – such as global deflection derived from the structural model built in Karamba – a multi-objective optimization was carried out. This resulted in design solutions that not only meet the required span but also perform well in terms of material efficiency and ease of assembly.



Part II: Preliminary Calculations and Stress Analysis

In Part II, preliminary hand calculations establish a starting value for the glass thickness. From that minimum value, a range is defined for a Grasshopper number slider, which parameterizes the internal geometry of the module and its connections. This creates a seamless workflow between Grasshopper and Ansys, enabling stress analysis of the critical connection of the system for different glass thicknesses and connection geometries.

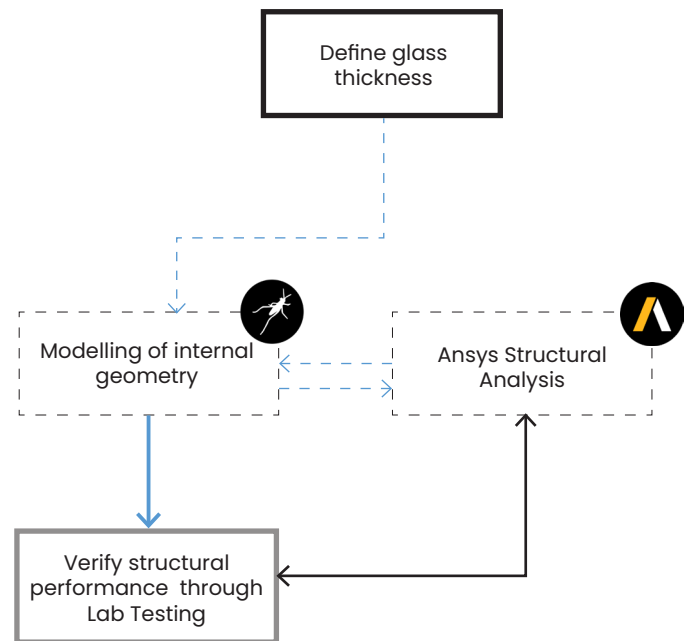


PART III: Structural Verification through Laboratory Testing

Part III tests the most critical location of the module in a laboratory setting. Based on the Ansys simulation, this critical zone is identified and the stress resulting from the hand-calculated compressive design load in the slots is quantified and visualized.

A 1:1 scale test is then conducted on a suitable module thickness to assess its real-world structural performance and verify whether it can withstand the expected load. Finally, the test results are compared with the Ansys simulation results and with the final required module length, which depends on the number of slots needed to achieve adaptability in the y-direction.

From this, a final conclusion can be drawn regarding the structural feasibility within the defined boundary conditions. It also informs the final dimensioning of the modules and provides insight into material efficiency and other design considerations.



7.1 PART I

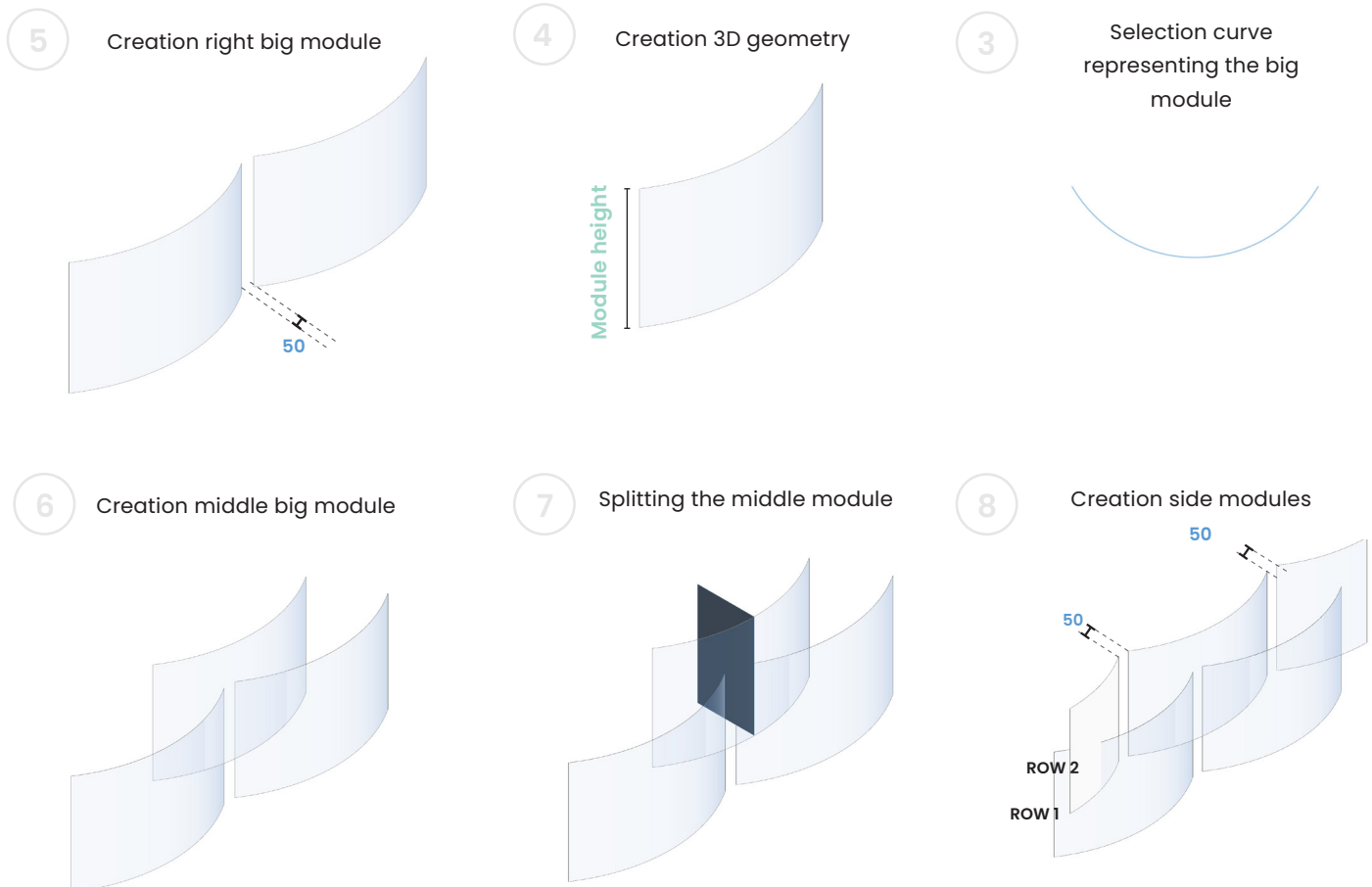
7.1.1 Research on parameters affecting adaptability

In this thesis, the adaptability of the structure is limited to its ability to adjust in span (y-direction) to meet varying spatial requirements, achieved through the use of standardized modular components.

The influence of the interlocking angle and module height on the span has been explored using a parametric model. The model's setup is first explained to provide a clearer understanding of how these parameters affect adaptability. The underlying principle involves the creation of so-called 'target planes,' onto which the module geometry is later projected.



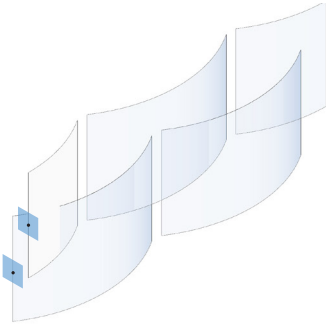
CREATION OF MODULES AND SOURCE PLANES OF ROW 1 AND 2



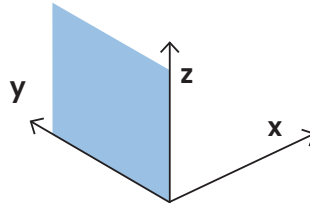
CREATION OF TARGET PLANES FOR ROW 1 AND 2



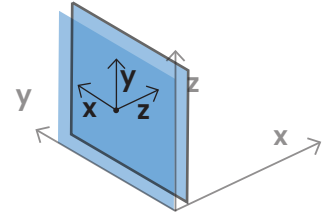
- 9 Creating a 'source' plane on row 1 and 2



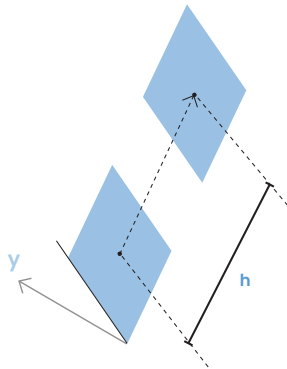
- 10 Creation of yz world plane



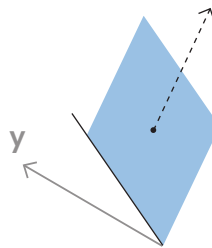
- 11 Plane is copied



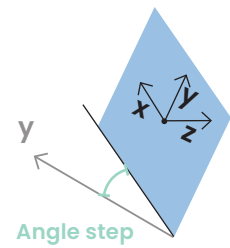
- 14 Plane moves with 'h' in the local y-direction



- 13 Creation y vector of plane



- 12 Copied plane rotates around it's local Z-axis



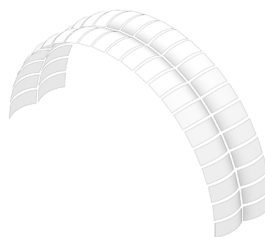
- 15 Separating even and uneven planes

3 ▢
2 ▢
1 ▢
0 ▢

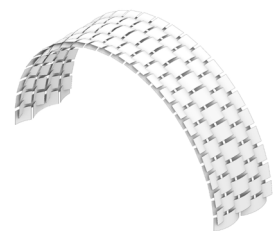
PROJECTION MODULES ON TARGET PLANES



- 16 Projecting row 1 on the even planes



- 17 Projecting row 2 on the uneven planes



Parameter 1: Interlocking angle

Consistent interlocking angle

In the code workflow explained on the previous page (see Appendix code 1), each plane is rotated by a constant interlocking angle, referred to as the 'angle step.' This results in a cumulative rotation, where each subsequent plane is rotated by an additional consistent amount, forming a circular arch shape. For instance, with an angle step of 3°, the planes are rotated successively by 3°, 6°, 9°, and so on relative to the starting point. Even a small change in the angle step – such as from 1° to 3° – can lead to a significant difference in span, amounting to several meters, as illustrated in Figure 116.

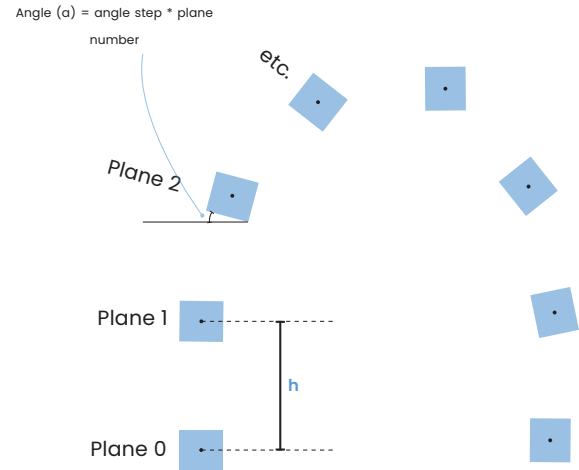


Figure 115: Different interlocking angles (own work, 2025)

Different interlocking angles

The influence of using different interlocking angles was also tested (see Appendix Code 2). In this scenario, the interlocking angle increases incrementally at each step by the 'angle step' value. In the algorithm, the angle step is multiplied by the module number to create a varying interlocking angle (Figure 115).

For example, with an angle step of 0.5 degrees:

Angle (α) of plane 1: $0.5 \times 1 = 0.5^\circ$

Angle (α) of plane 2: $0.5 \times 2 = 1.0^\circ$

Angle (α) of plane 3: $0.5 \times 3 = 1.5^\circ$

As a result, each module is rotated an additional 0.5 degrees compared to the previous module, causing the rotation to accumulate towards the top. This creates a geometry that gradually becomes more pointed at the top and flatter at the sides (Fig. 117). It becomes clear that because of the accumulation, the arch reaches the top sooner compared to a constant angle, causing the arch to reach a shorter span. It can be imagined that when the opposite happens, so when the angle reduces each step, the top becomes wider, resulting in a bigger span. Thus, the span can be controlled by the interlocking angle by increasing or decreasing it. The location at which the angle decreases or increases, defines the shape of the arch.

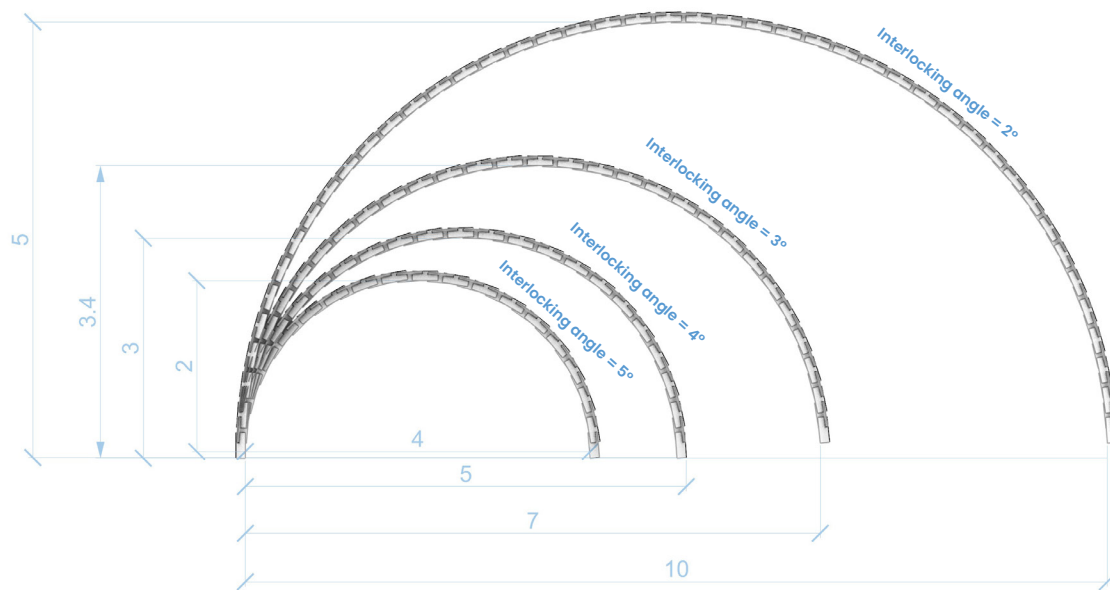


Figure 116: Consistent interlocking angle (own work, 2025)

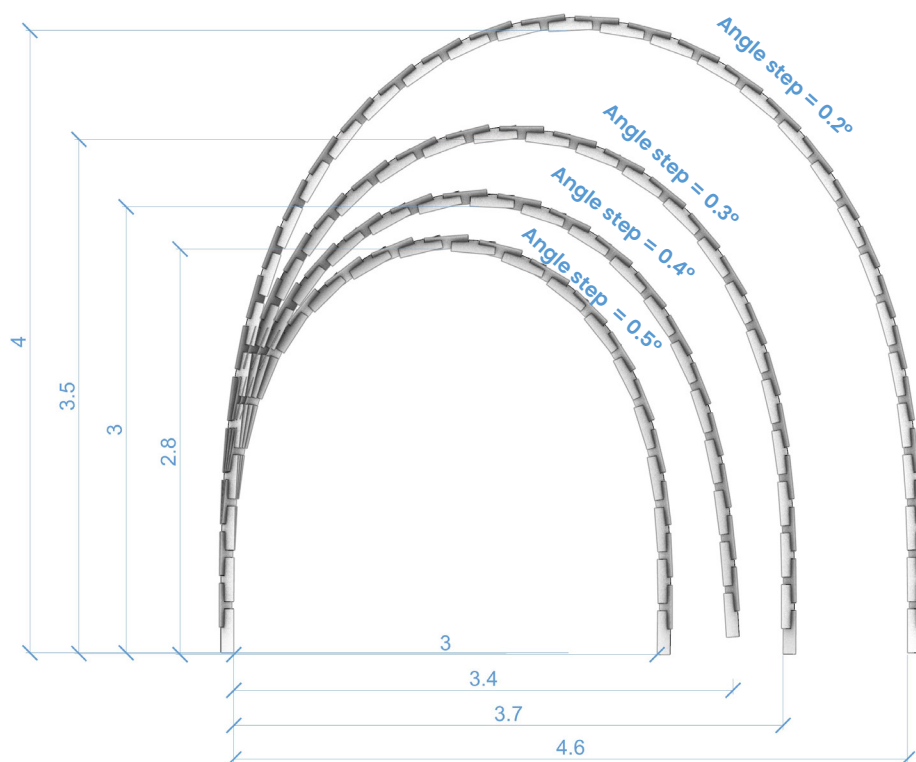


Figure 117: Different interlocking angles, accumulating with each module (own work, 2025)

Consistent amount of modules

To further clarify the influence of the angle on both shape and span, the following example uses a consistent number of modules, equal module heights, and identical angle steps. In Arch **A**, a constant interlocking angle of 2° is applied, while in Arch **B**, the interlocking angle accumulates by 2° with each module.

Figure 118 illustrates this comparison. It is evident that the curvature of Arch A develops gradually, whereas Arch B exhibits a more rapid increase in curvature due to the accumulating angle. As a result, Arch B tends to 'complete' the arch shape earlier than Arch A, which explains the difference in span.

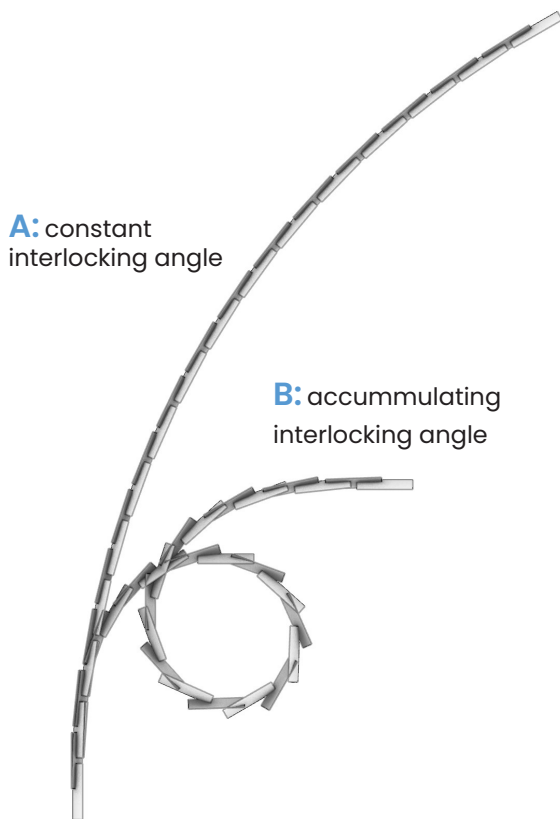


Figure 118: Comparison of shape generation using a constant versus an accumulating interlocking angle (own work, 2025)

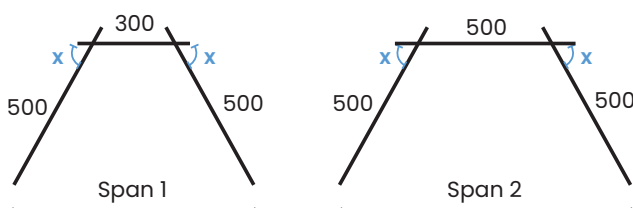


Figure 119: (own work, 2025)

Parameter 2: Module height

Changing the module height all at once

Changing the height of a module by just 5 cm can already result in a span difference of up to one meter in a circular arch, and somewhat less in an arch with an accumulating interlocking angle (Fig. 122 & 123).

Additionally, two standardized module heights – 300 mm and 500 mm – were tested. In this test, the shorter modules were repeated several times at the base of the arch, followed by a sequence of 500 mm modules towards the top (Fig. 120). The workflow of this code is illustrated on the next page, and the script itself is included in Appendix Code 3. The algorithm allows control over the number of clusters and the number of planes within each cluster, making it possible to project a specific module height onto each group. By adjusting both the number of clusters and the number of planes per cluster – alongside the geometry assigned to each – various patterns of module height alternation could be created.

The resulting curve was compared to a version composed entirely of 500 mm modules (Fig. 121). It is immediately noticeable that repeating the shorter module causes the arch to curve more sharply in the beginning. The transition to the longer modules is clearly visible, as the curvature becomes more gradual toward the top.

The figure also shows that a significant number of modules of the same height must be clustered to achieve a noticeable difference in span. This is likely due to the relatively small height difference of only 20 cm between the modules.

This test confirms that the order of module heights has a direct impact on the shape and, consequently, the span of the structure. This effect can also be illustrated in a simplified example.

For instance, if $n = 3$, an initial configuration might be 500–300–500. Replacing the middle 300 mm module with a 500 mm one alters the shape of the structure and results in an increased span (Fig. 119).

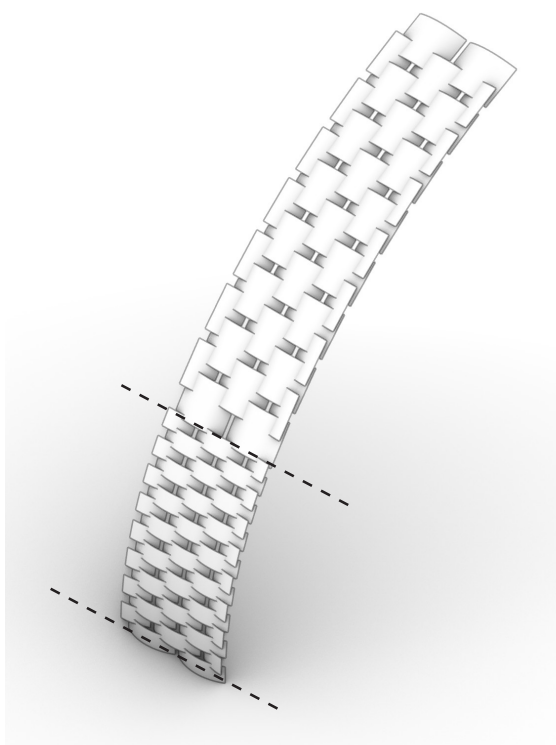
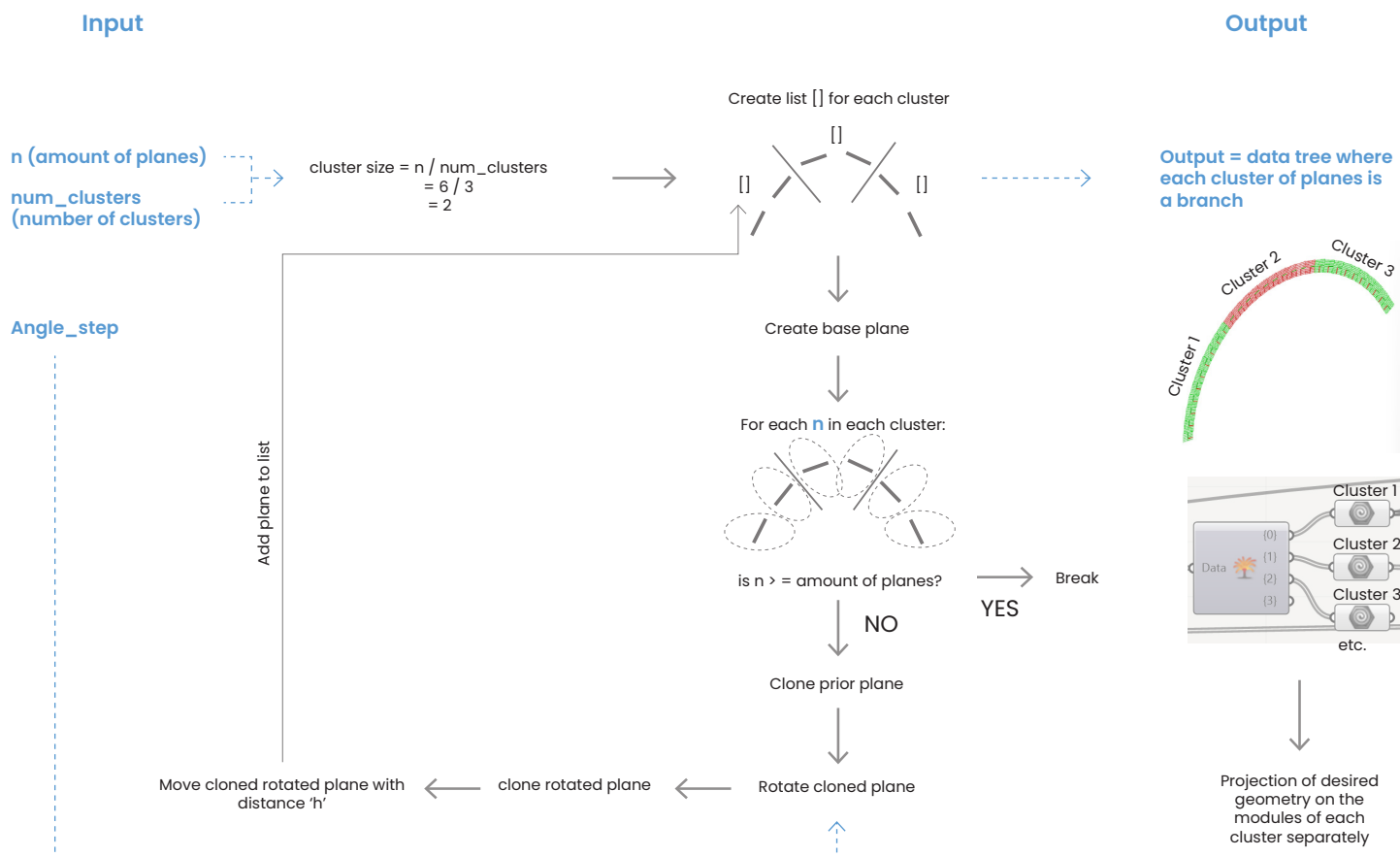


Figure 120: Controlling the sequence of two module heights (own work, 2025)

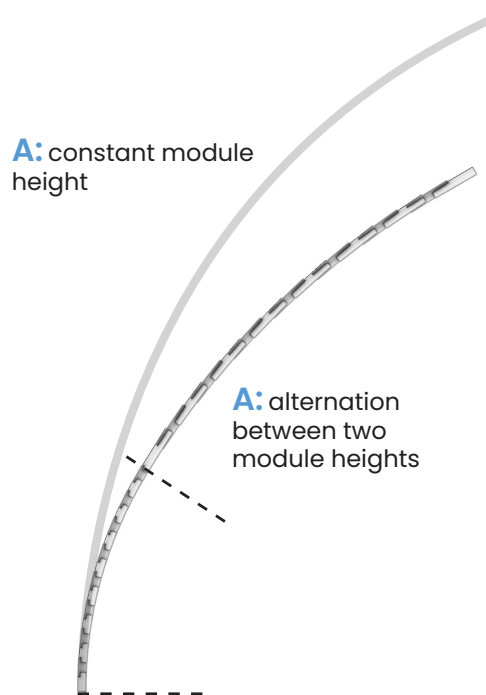


Figure 121: Effect of module sequence on arch shape and span (own work, 2025)

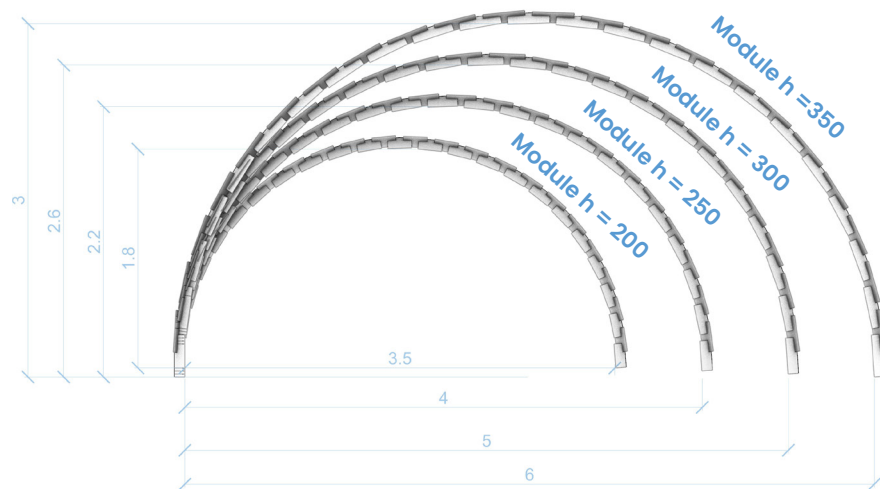


Figure 122: Influence of different module heights on the span for a consistent interlocking angle (own work, 2025)

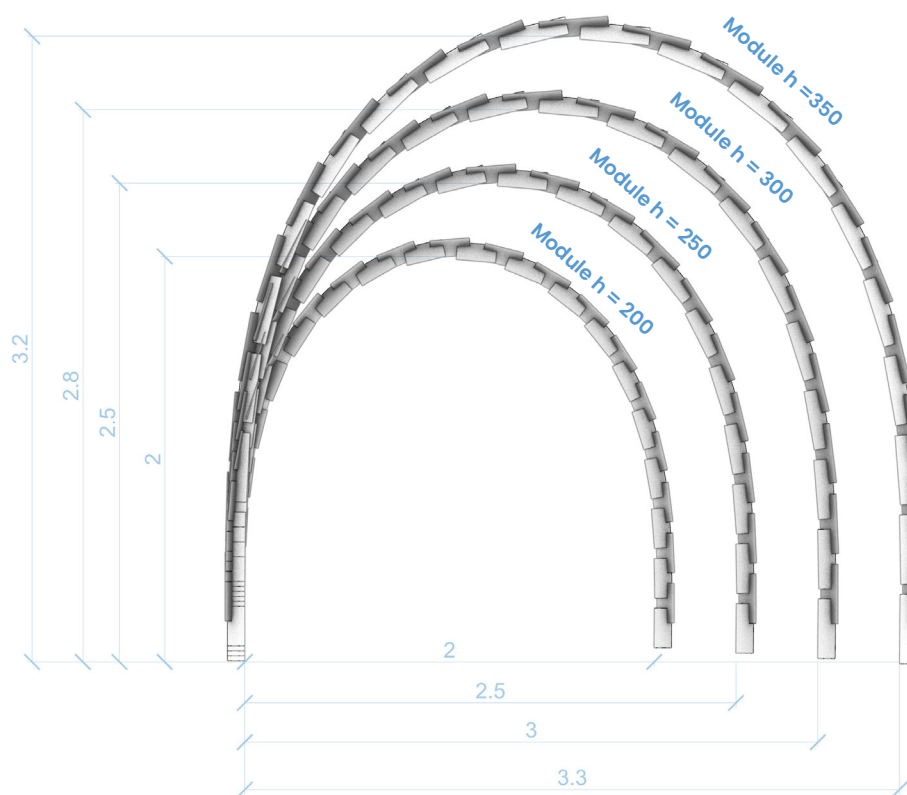


Figure 123: Influence of different module heights on the arch span for different interlocking angles (own work, 2025)

Conclusion

It has become evident that the interlocking angle significantly influences the shape of the structure and, indirectly, its span. A smaller interlocking angle results in a larger span, while a larger angle leads to a reduced span.

Span variation can be achieved by applying either a uniform interlocking angle across the entire arch or by varying the angle between different segments. This variation becomes possible through the integration of at least two slot pairs within a single module.

Additional variability can be introduced by using multiple module heights and arranging them in different sequences.

For even greater shape flexibility, incorporating negative interlocking angles may offer potential. While a constant positive angle will eventually cause the arch to close or terminate, introducing a negative angle allows the curvature to reverse and continue, enabling the formation of a concave (or 'hollow') curve.

7.1.2 Creation of a generative model

Given that the interlocking angle and module height are key in determining the span of the structure, these parameters form the foundation of the generative algorithm developed.

In essence, the algorithm operates as follows (Fig. 124):

The structure is subdivided into clusters - groups of consecutive modules - where the number of clusters is defined as a parameter. The adaptability of the structure is controlled by varying the sequence of module heights and the interlocking angles within each cluster.

Each cluster can be assigned a specific configuration, controlled by a variable called `clusterMode`. This variable determines whether the cluster consists solely of 300 mm modules (`clusterMode = 0`), solely of 500 mm modules (`clusterMode = 1`), or a mixed sequence of both (`clusterMode = 2`).

For instance, if the structure is divided into two clusters, each can independently adopt any of the three cluster modes, allowing for a broad range of design variations.

Another variable allows control over the number of clusters. Increasing the number of clusters results in smaller module groups. For example, clusters of just two modules enables fine-tuned adjustments to module height sequences or interlocking angles. Conversely, larger clusters lead to fewer but more impactful changes.

The following pages outline the fixed parameters and the variable parameters used for the algorithm. The algorithm's operation is then illustrated through a flowchart diagram.

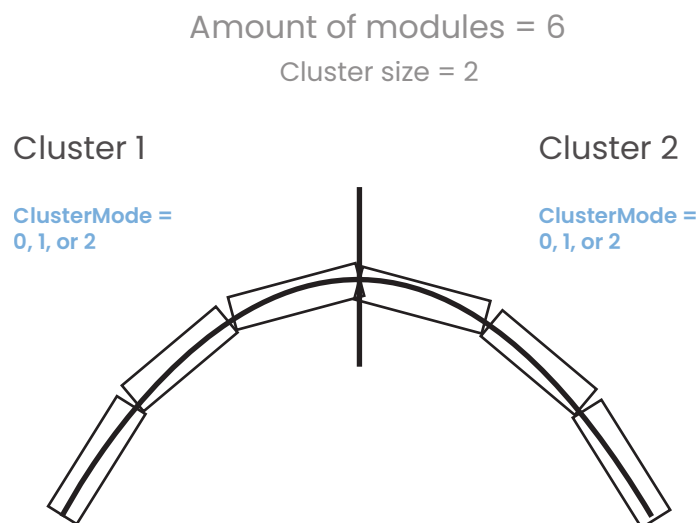


Figure 124: Illustration of the algorithm's operation (own work, 2025)

Fixed parameters: bending radius, module length, and module height

The module length is dependent on the number of slots that will be integrated into a module. However, to ensure that each module remains lightweight to be suitable for manual handling and minimize the compressional force due to self-weight, it is ideal to keep the module as short as possible.

For the modules, the bending radius is a fixed number, chosen at 650 mm because it is the smallest one for cylindrical glass shapes, according to Serdak in Germany (Fig. 125). In the worst-case scenario, the maximum net length of a module corresponds to the diameter of the circle, $2 \times 650 = 1300$ mm. This would still be considered as a manageable size, provided that the height of the module is kept within practical limits.

Figure 126 illustrates various module lengths derived from this 650 mm radius. Additionally, Figure 127 shows how a module can be interlocked at different slot positions, positioned closer to either the interior or exterior of the structure. In the algorithm, this exact interlocking location has not been considered.

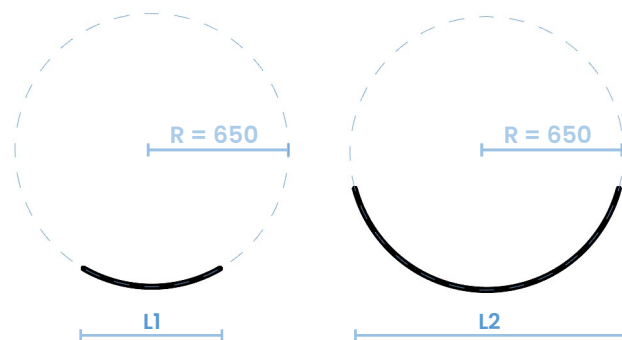


Figure 126: Different possibilities in module length for a bending radius of

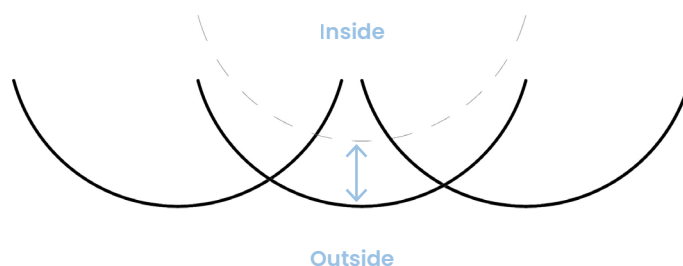


Figure 127: Interlocking position more to the inside or outside of the structure (own work, 2025)

bending	length	width	thickness	bending shape	Rmin.*	max. bending angle
gravity curved glass	11,500 mm / 453 in	3,300 mm / 130 in	2–19 mm / $\frac{3}{16}$ – $\frac{3}{4}$ in	cylindrical, conical, spherical, toroidal, J-shape, double-curvature, free-form		
tempered curved glass	2,440 mm / 96 in	1,570 mm / 62 in	4–8 mm / $\frac{1}{8}$ – $\frac{5}{16}$ in	cylindrical	1,000 mm / 39 in	90°
	4,200 mm / 165 in	2,440 mm / 96 in	6–12 mm / $\frac{1}{4}$ – $\frac{1}{2}$ in	cylindrical	1,500 mm / 59 in	90°
	2,440 mm / 96 in	4,500 mm / 177 in	6–15 mm / $\frac{1}{4}$ – $\frac{1}{2}$ in	cylindrical	2,500 mm / 98 in	90°
	3,000 mm / 118 in	1,500 mm / 59 in	5–10 mm / $\frac{3}{16}$ – $\frac{3}{8}$ in	cylindrical	650 mm / 26 in	105°
	2,500 mm / 98 in	1,500 mm / 59 in	5–8 mm / $\frac{3}{16}$ – $\frac{5}{16}$ in	J-shape	350 mm / 14 in	90°
	5,000 mm / 197 in	3,200 mm / 126 in	6–12 mm / $\frac{1}{4}$ – $\frac{1}{2}$ in	cylindrical, J-shape	1,500 mm / 59 in	90°
	3,300 mm / 130 in	3,600 mm / 142 in	6–15 mm / $\frac{1}{4}$ – $\frac{1}{2}$ in	cylindrical	1,500 mm / 59 in	90°
	3,300 mm / 130 in	2,500 mm / 98 in	6–12 mm / $\frac{1}{4}$ – $\frac{1}{2}$ in	cylindrical	900 mm / 35 in	90°
	6,500 mm / 256 in	3,600 mm / 142 in	6–19 mm / $\frac{1}{4}$ – $\frac{3}{4}$ in	cylindrical	2,000 mm / 78 in	90°
	6,500 mm / 256 in	3,600 mm / 142 in	6–19 mm / $\frac{1}{4}$ – $\frac{3}{4}$ in	double-curvature	y = 4,250 mm / 167 in x = 7,000 mm / 276 in	
cold bending during lamination (min. bending radius 1,500xthickness)	18,000 mm / 709 in	3,600 mm / 142 in	6–15 mm / $\frac{1}{4}$ – $\frac{1}{2}$ in	cylindrical	1,000 mm / 39 in	90°
	20,000 mm / 787 in	3,600 mm / 142 in	6 mm, 8 mm, 10 mm / $\frac{1}{8}$ in, $\frac{5}{16}$ in, $\frac{3}{8}$ in		9,000 mm, 12,000 mm, 15,000 mm / 354 in, 472 in, 591 in	National Technical Approval: Z-70.3-175

Figure 125: Production limits for cylindrical shapes (Sedak, n.d.)

As illustrated in Figure 138, it is possible to carry a panel longer than one's own height. Given that wood is lighter than glass, it can be assumed that carrying a glass panel approximately equal to a person's height is still manageable, possibly with more than one person. Naturally, a shorter length is preferable for manual handling. Therefore, a net module length of 1300 mm appears to be a feasible and practical choice.



Figure 128: A long module with a limited height, to find a compromise between adaptability and manual assembly (own work, 2025)

Variable parameters

1. amount_of_modules

Range from 0 – 70 (max. 70 modules)

The number of modules is defined as a range. The maximum has been set to 70, as this allows for reasonable spans of up to approximately 8 meters. It was necessary to impose this limit, since without it, the generative algorithm could theoretically select an unlimited number of modules, resulting in an infinite design space. Moreover, this span was considered appropriate for testing the structural capacity of the modules.

2. amount_of_clusters

Ranges from 1 (all planes are 1 cluster together) to 30

The number of clusters is defined to range between 1 and 30. A minimum of 1 means the entire arch functions as a single cluster, which can consist of either a single module height or a random alternation of the two. The maximum is set to 30 to ensure that, with a maximum of 60 modules, each cluster contains only a few modules. This enables sufficient variation in module sequences – ranging from clusters with many modules to those with only a few – allowing the algorithm to explore a wide spectrum of design possibilities.

3. ClusterModes

The clustermode can be either 0, 1 or 2

A cluster mode of 0 means the entire cluster is filled with 300 mm modules, while mode 1 uses only 500 mm modules. In mode 2, a random sequence of 300 mm and 500 mm modules is generated within the cluster.

4. AngleChoice

For each module, the angle choice can be 0, 1, 2, or 3

The AngleChoice (0, 1, 2, or 3) determines which interlocking angle is assigned to a module. Two distinct angles were selected: -2° and 10° – as they differ significantly but not excessively, preventing abrupt transitions in curvature. The remaining two AngleChoice values represent the negatives: -2° and -10° . These negative angles introduce additional shape flexibility, enabling more varied span possibilities (Fig. 129). Moreover, selecting a small angle versus a large one allows for either gradual or more dramatic changes in the overall form.

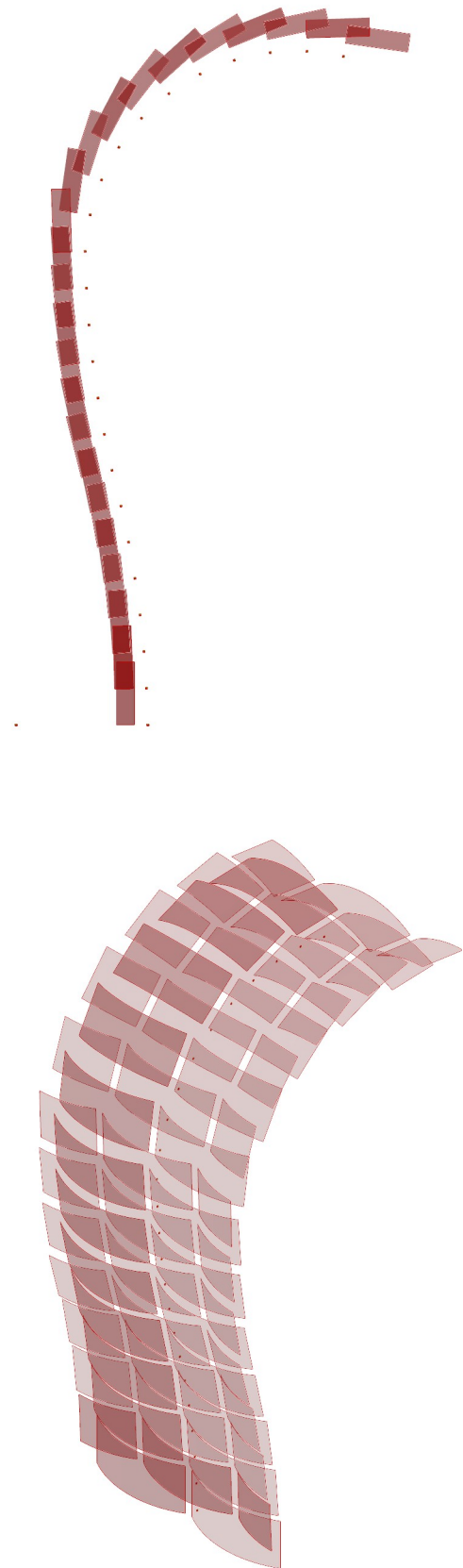


Figure 129: Enabling free form generation through negative interlocking angles (own work, 2025)

5. module_heights

The algorithm works with two standardized module heights

It was found that span differences of several meters could already be achieved using just two standardized module heights: 300 mm and 500 mm. The number of standardized components was intentionally kept to a minimum to maximize reusability across different structures and to simplify assembly instructions.

Additionally, the maximum height was limited to 500 mm to allow the module to be longer, which is necessary for integrating multiple slot angles, as explained earlier.

A minimum module height of 300 mm was also defined to maximize the contrast between the module height of 500 – and thereby encourage greater variation in span outcomes.

Although the two module heights are fixed values, they function as variables in the sense that their order and frequency within the structure can be adjusted.

Workflow of the algorithm

The workflow of the generative algorithm is presented on the following page, and the corresponding Grasshopper Python code can be found in the Appendix (Code 4).

The algorithm begins by checking whether the number of clusters is equal to 1 or greater than 1. If there is only one cluster, all modules in the structure belong to that single cluster, and the cluster size is therefore equal to the total number of modules.

If the number of clusters is greater than one, the number of modules per cluster is calculated by dividing the total number of modules by the number of clusters. Since this division does not always result in a whole number, any remainder modules are distributed evenly among the first few clusters. A list is then generated that includes the number of modules in each cluster.

With the number of modules per cluster now defined, the starting position of each cluster can be calculated.

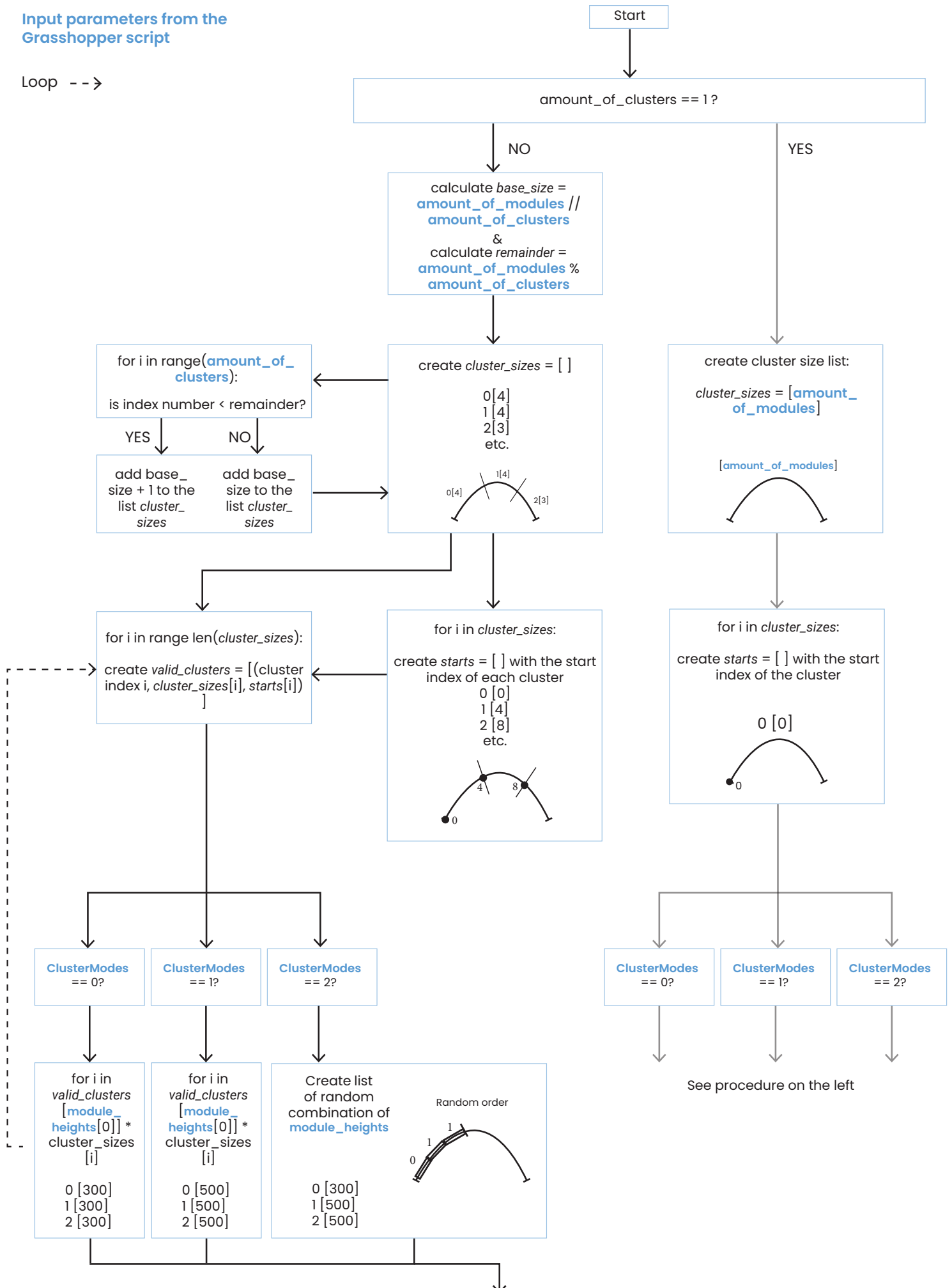
Next, a list is created containing, for each cluster: the index number, the number of modules it contains, and the starting index. For each cluster in this list, a new sublist is generated where the module heights are assigned based on the cluster mode. Once the module height sequence for each cluster is determined, these are combined into a single list, forming the final module height pattern for the entire arch.

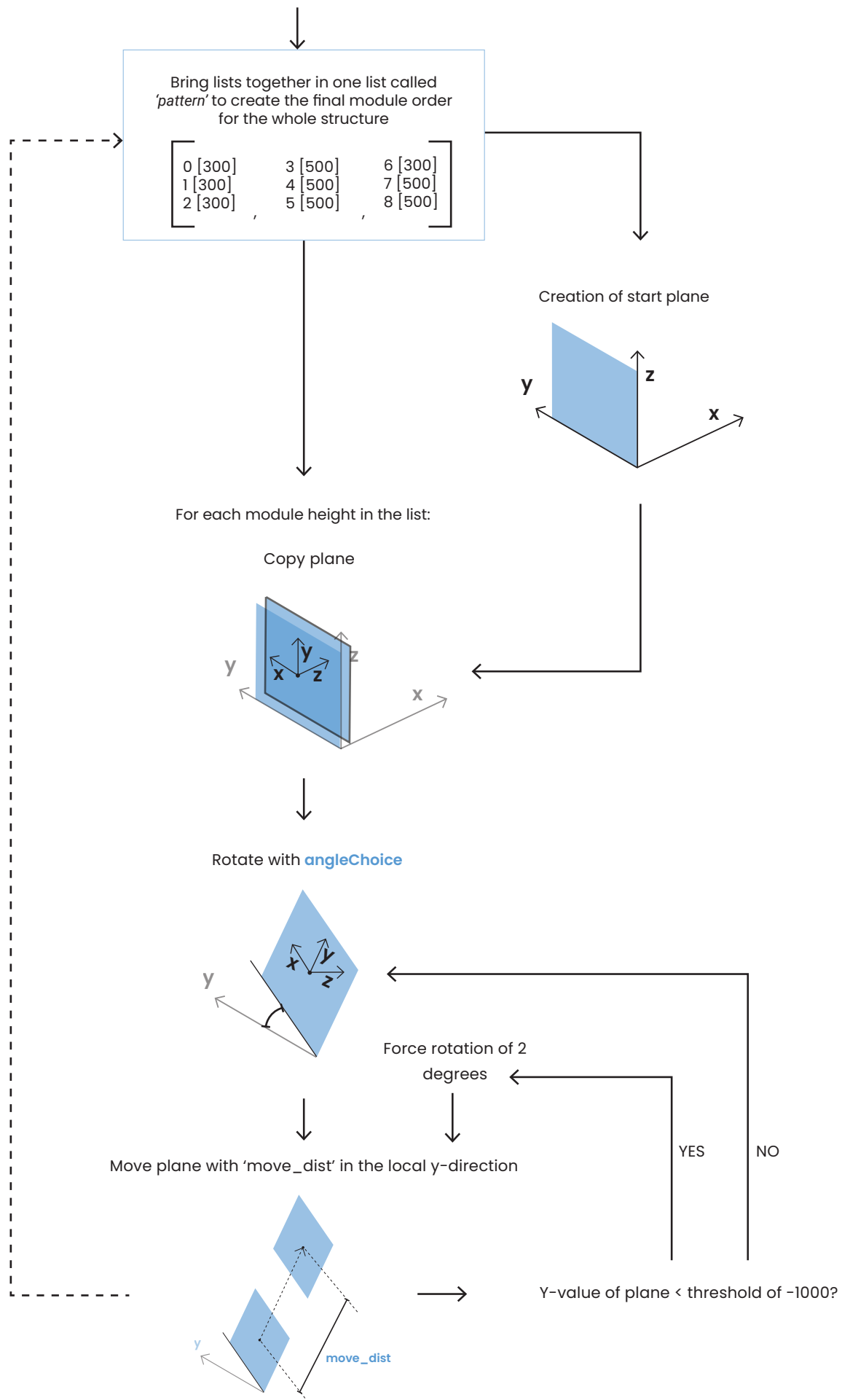
For each module in the list, a reference plane is created onto which the module geometry will later be projected. The process begins by generating a start plane at the origin. This plane is then copied, rotated according to the specified AngleChoice, and moved along its local y-axis. From that point on, the process is repeated iteratively: each new plane is derived from the previous one. The distance between consecutive planes is determined by the module height and the required interlocking depth between modules.

An additional restriction in the algorithm ensures that if a plane is rotated and translated in the negative y-direction too many times in a row – causing the curve to fold outward or form excessively sharp bends that could negatively impact the structural behavior – this is corrected, as shown at the end of the workflow.

Input parameters from the Grasshopper script

Loop -->





Demonstration of algorithm performance

This section briefly demonstrates how the algorithm works.

As an example: if the number of modules is set to 9 and the number of clusters to 8, each cluster must contain at least one module. This is calculated as follows:

base = amount_of_modules // amount_of_clusters = 1

The remainder is calculated as:

rest = 9 % 8 = 1

This one extra module is assigned to the first cluster, resulting in the following distribution of modules per cluster:

[2, 1, 1, 1, 1, 1, 1, 1]

As explained, each cluster can be assigned a ClusterMode. Figure 130 shows how each cluster is assigned a ClusterMode of 0, resulting in module repetitions of only 300 mm in height (Fig. 131).

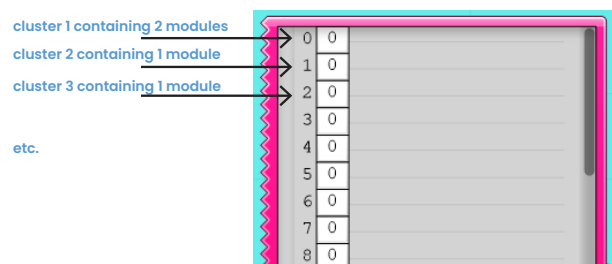


Figure 130: Each cluster is assigned a module height of 300 (own work, 2025)



Figure 131: Arch containing 9 modules of 300 in height (own work, 2025)

If the ClusterMode of Cluster 1 is changed from 0 to 1, the first two modules – belonging to that cluster – will switch from 300 mm to 500 mm in height (Fig. 132). As a result, the beginning of the arch will show a greater vertical offset. This illustrates how precisely the shape of the arch can be adjusted by modifying the number of modules per cluster.

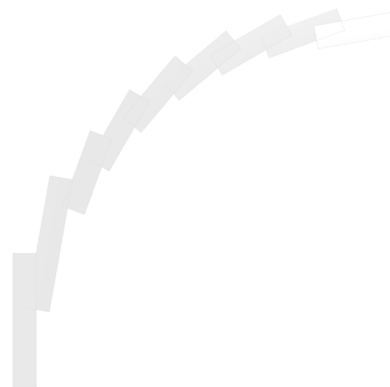
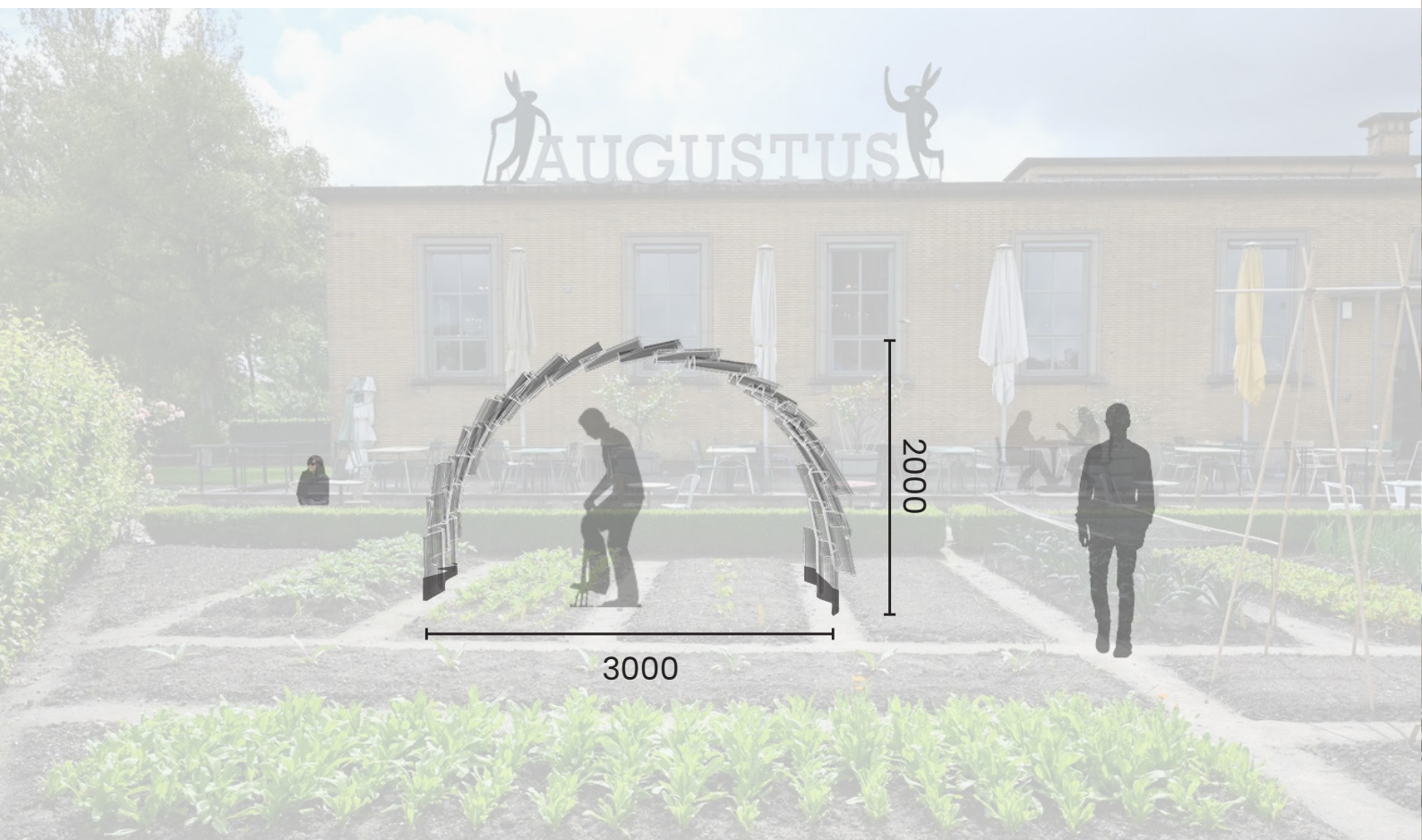


Figure 132: Greater vertical offset created by increasing the module height in Cluster 1 (own work, 2025)

The same principle applies to the interlocking angle, with the difference that it can be adjusted per module rather than per cluster.

7.1.3 Case studies

To demonstrate the system's adaptability, the structure is applied to different locations using alternative design options based on the two standardized modules. Only a selection of shapes is presented to give an overall impression. As additional output, the algorithm provides the required sequence of module heights and interlocking angles needed to construct the design.



Background image: by Van Wendel de Joode, R. (n.d.). Vegetable garden at Villa Augustus (Dordrecht)

Order of interlocking angles

0	300
1	500
2	300
3	300
4	300
5	500
6	500
7	300
8	500
9	500
10	500
11	500
12	500
13	500
14	500
15	500
16	300
17	300
18	500
19	500
20	300
21	300
22	300
23	500

Order of module heights

0	2
1	2
2	2
3	2
4	2
5	10
6	10
7	10
8	10
9	10
10	10
11	10
12	10
13	10
14	10
15	10
16	10
17	10
18	10
19	-2
20	-2
21	-2
22	-2
23	-2





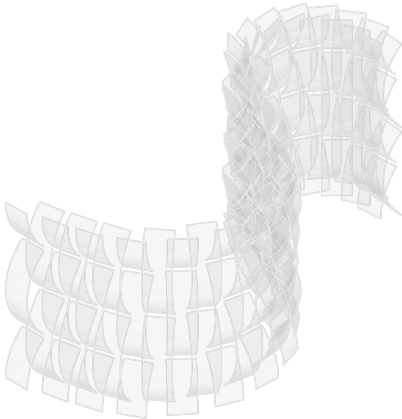
Background image: by De Meester, L. (2021). World Press Photo exhibition in the Koepelgevangen, Breda

Order of interlocking angles

0 10	21 -2
1 2	22 -2
2 2	23 -2
3 2	24 -2
4 2	25 -2
5 10	26 -10
6 10	27 -10
7 10	28 -10
8 10	29 -10
9 10	30 -10
10 10	31 -10
11 10	32 -10
12 10	33 -10
13 10	34 -10
14 10	35 -10
15 10	36 -10
16 10	37 -10
17 10	38 -10
18 10	39 -10
19 -2	40 -10
20 -2	41 -10

Order of module heights

0 300	21 300
1 300	22 300
2 300	23 300
3 300	24 300
4 300	25 300
5 300	26 300
6 300	27 300
7 300	28 300
8 300	29 300
9 300	30 300
10 300	31 300
11 300	32 300
12 300	33 300
13 300	34 300
14 300	35 300
15 300	36 300
16 300	37 300
17 300	38 300
18 300	39 300
19 300	40 300
20 300	41 300





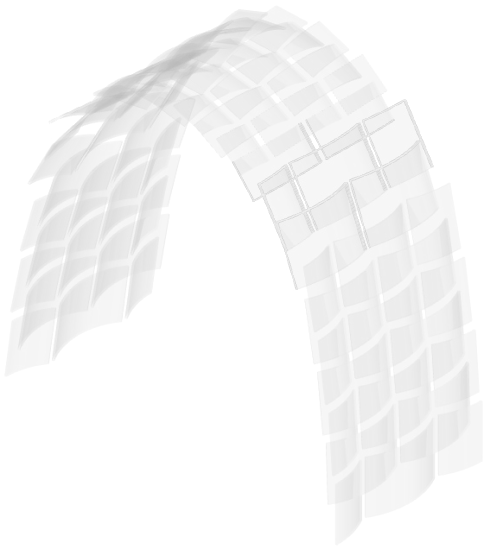
Background image: by Koolbergen, K. (2023). The Darwin Flower Garden

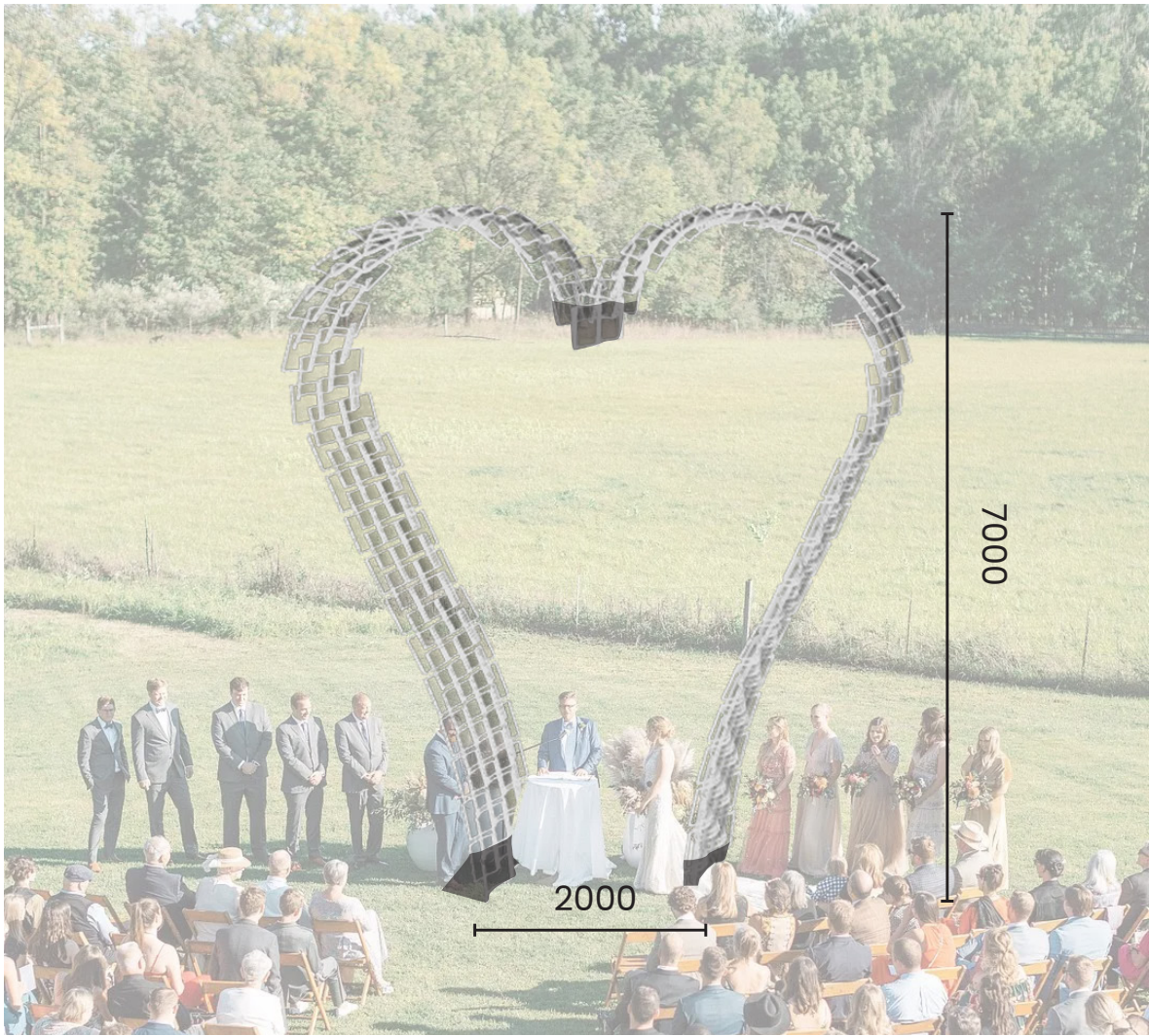
Order of interlocking angles

0	2
1	2
2	2
3	2
4	2
5	2
6	10
7	10
8	10
9	10
10	10
11	10
12	10
13	10
14	10
15	10
16	10
17	10
18	10
19	10
20	10
21	2
22	2
23	2
24	2
25	2
26	2

Order of module heights

0	500
1	500
2	500
3	500
4	500
5	500
6	500
7	500
8	500
9	300
10	300
11	300
12	300
13	300
14	300
15	300
16	300
17	300
18	500
19	500
20	500
21	500
22	500
23	500
24	500
25	500
26	500





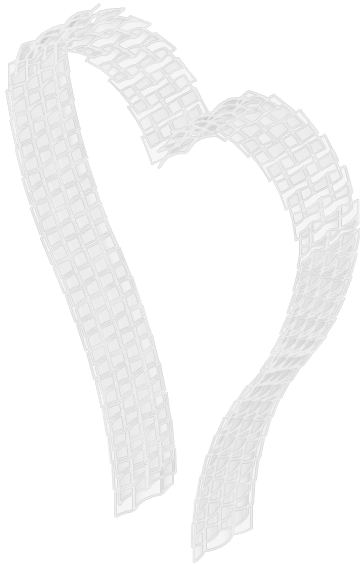
Background image: by Lobach, A. (n.d.)

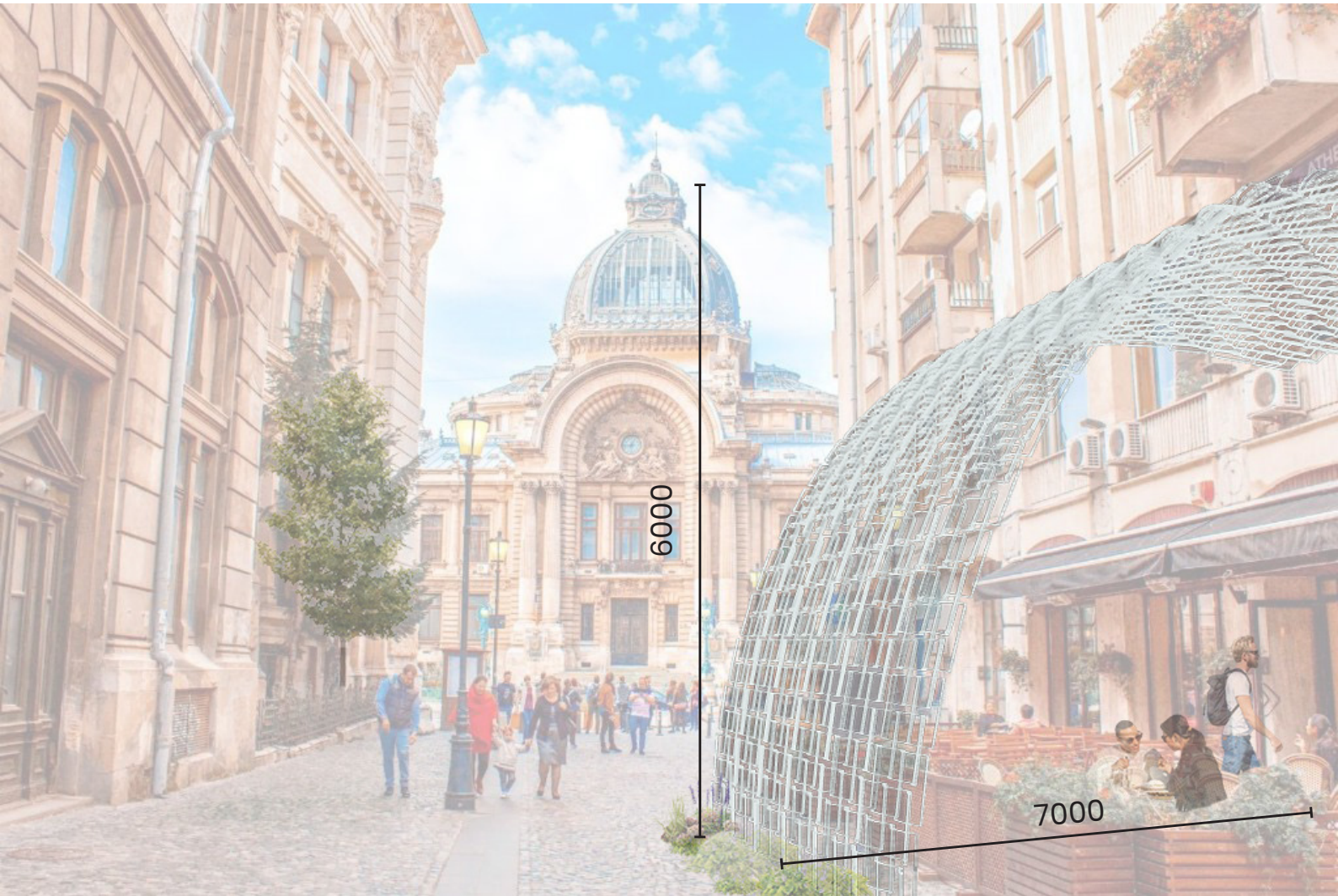
Order of interlocking angles

0 -2	28 2
1 -2	29 10
2 -2	30 10
3 -2	31 10
4 -2	32 10
5 -2	33 10
6 -2	34 10
7 -2	35 10
8 -2	36 10
9 -2	37 10
10 -2	38 10
11 -2	39 10
12 -2	40 10
13 -2	41 10
14 -2	42 10
15 -2	43 10
16 -2	44 10
17 2	45 10
18 2	
19 2	
20 2	
21 2	
22 2	
23 2	
24 2	
25 2	
26 2	
27 2	

Order of module heights

0 500	28 500
1 500	29 500
2 500	30 500
3 500	31 500
4 500	32 500
5 500	33 500
6 500	34 500
7 500	35 500
8 500	36 500
9 500	37 500
10 500	38 500
11 500	39 500
12 500	40 500
13 500	41 500
14 500	42 500
15 500	43 500
16 500	44 500
17 500	45 500
18 500	
19 500	
20 500	
21 500	
22 500	
23 500	
24 500	
25 500	
26 500	
27 500	





Background image: by Sibai, R. (2014). Bucharest, Romania

Order of interlocking angles

0 2
1 2
2 2
3 2
4 2
5 2
6 2
7 2
8 2
9 2
10 2
11 2
12 2
13 2
14 2
15 2
16 2
17 2
18 2
19 2
20 2
21 10
22 10
23 2
24 2
25 2

26 2
27 2
28 2
29 2
30 2
31 2
32 2
33 2
34 2
35 2
36 2
37 2
38 2
39 2
40 2
41 2
42 2

Order of module heights

0 500
1 500
2 500
3 500
4 500
5 500
6 500
7 500
8 500
9 500
10 500
11 500
12 500
13 500
14 500
15 300
16 300
17 300
18 300
19 300
20 300
21 300
22 300
23 300
24 300
25 300

26 300
27 300
28 300
29 500
30 500
31 500
32 500
33 500
34 500
35 500
36 500
37 500
38 500
39 500
40 500
41 500
42 500



7.1.4 Objective functions

The generative model enables the modular system to produce a wide variety of design solutions. As illustrated on the previous pages, the resulting arch shapes – and thus their spans – differ among these solutions.

However, the scope of this research extends beyond developing an adaptable system. Additional key objectives include weight reduction and manual assembly and disassembly simplicity without the need for complex instructions. By integrating these criteria into a multi-objective optimization, the range of design possibilities is refined to include solutions that are material-efficient and easier to build as well. Furthermore, a third and fourth design objective is introduced to select design solutions best aligned with the specific spatial requirements of a building location.

This chapter begins by outlining the four design objectives. It then describes the optimization process and discusses the resulting outcomes.

Objective 1: Minimize global structural displacement resulting from self-weight (max_d)

Since the shape has a significant impact on structural performance – and consequently on the amount of material required – the first design objective focuses on minimizing material usage by stimulating compressional force transfer. More specifically, this is defined as minimizing the global structural displacement under self-weight, as the structure is primarily subjected to its own weight.

Set-up of the structural model in Karamba3D

1. Definition of the structural material

First, the material properties are defined (Fig. 133), using the values listed in Tables 3 and 4 of the Appendix. The specific weight is calculated as follows:

$$\begin{aligned}
 \gamma &= \rho \cdot g \\
 &= 2500 \frac{\text{kg}}{\text{m}^3} \times 9.81 \frac{\text{m}}{\text{s}^2} \\
 &= 24525 \frac{\text{N}}{\text{m}^3} \\
 &= 24.525 \frac{\text{kN}}{\text{m}^3}
 \end{aligned}$$

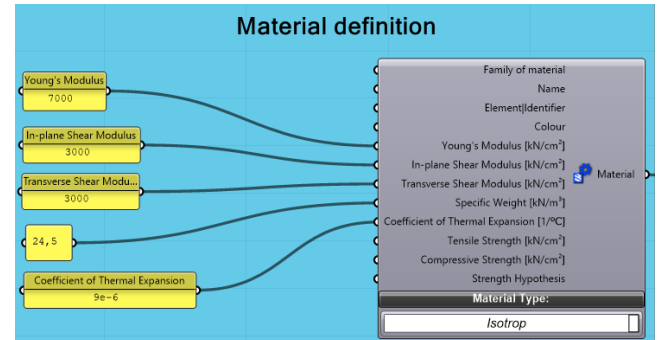


Figure 133: Material properties in Karamba3D (own work, 2025)

2. Definition of the the slots as joints

First, the start and end points of the slots were selected (Fig. 134).



Figure 134: Selection of start and end points of the slots (own work, 2025)

The start and end points are connected to form a line that represents the slot, which is subsequently converted into a linear element using Karamba. As these connections function more like hinges than rigid joints, they are modeled as rotational joints with one degree of freedom in the span direction of the structure, allowing for rotation around the x-axis. (Fig. 135).

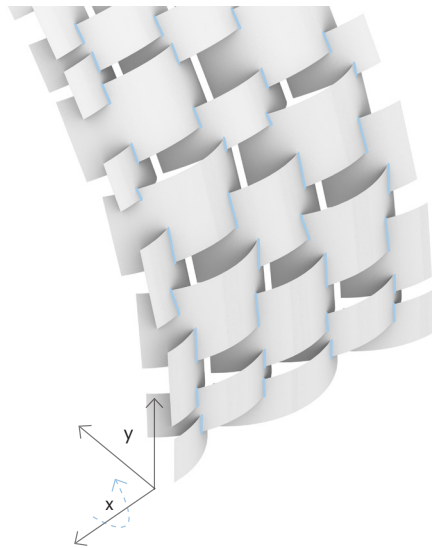


Figure 135: Slots defined as hinges, rotating around the x-axis (own work, 2025)

3. Definition of the supports

The fixed supports are defined at points located on the edges of the first and last rows of modules, representing linear supports (Fig. 136).

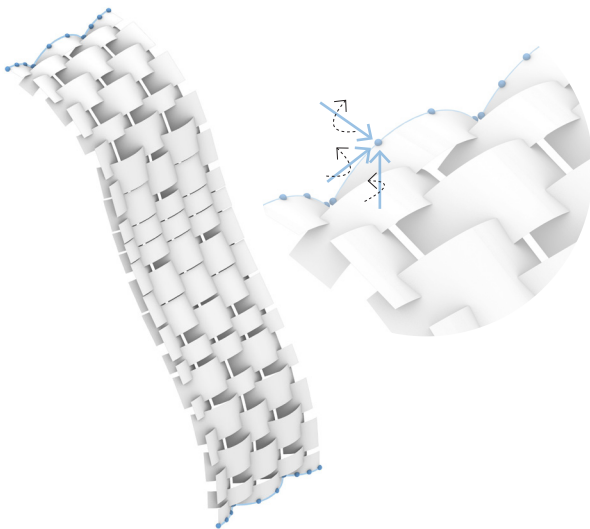


Figure 136: Fixed supports at the start and end module rows (own work, 2025)

4. Mesh creation

In Karamba, each surface element is converted into a mesh, which is then adapted to incorporate the vertices corresponding to both the supports and the slots (Fig. 137).

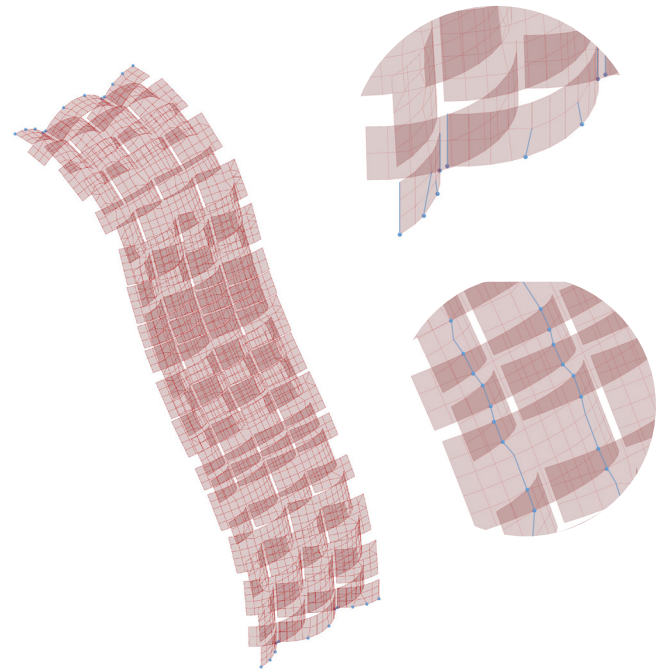


Figure 137: Generated mesh of the surfaces, including support and slot vertices (own work, 2025)

5. Application of loads

Since the objective is to optimize deflection under the primary load, a gravity load (Fig. 138) has been applied to the model. The resulting deflections are therefore based on this load case.

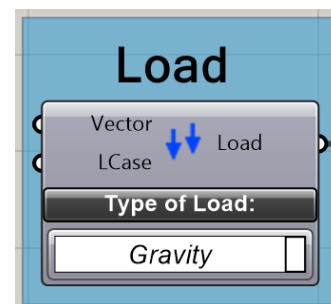


Figure 138: Self-weight load case in Grasshopper (own work, 2025)

Results

With the structural model established, the maximum displacement could be calculated for different design variations. Two examples are shown below (Fig. 139) clearly demonstrating that displacement increases as the distance from the supports grows.

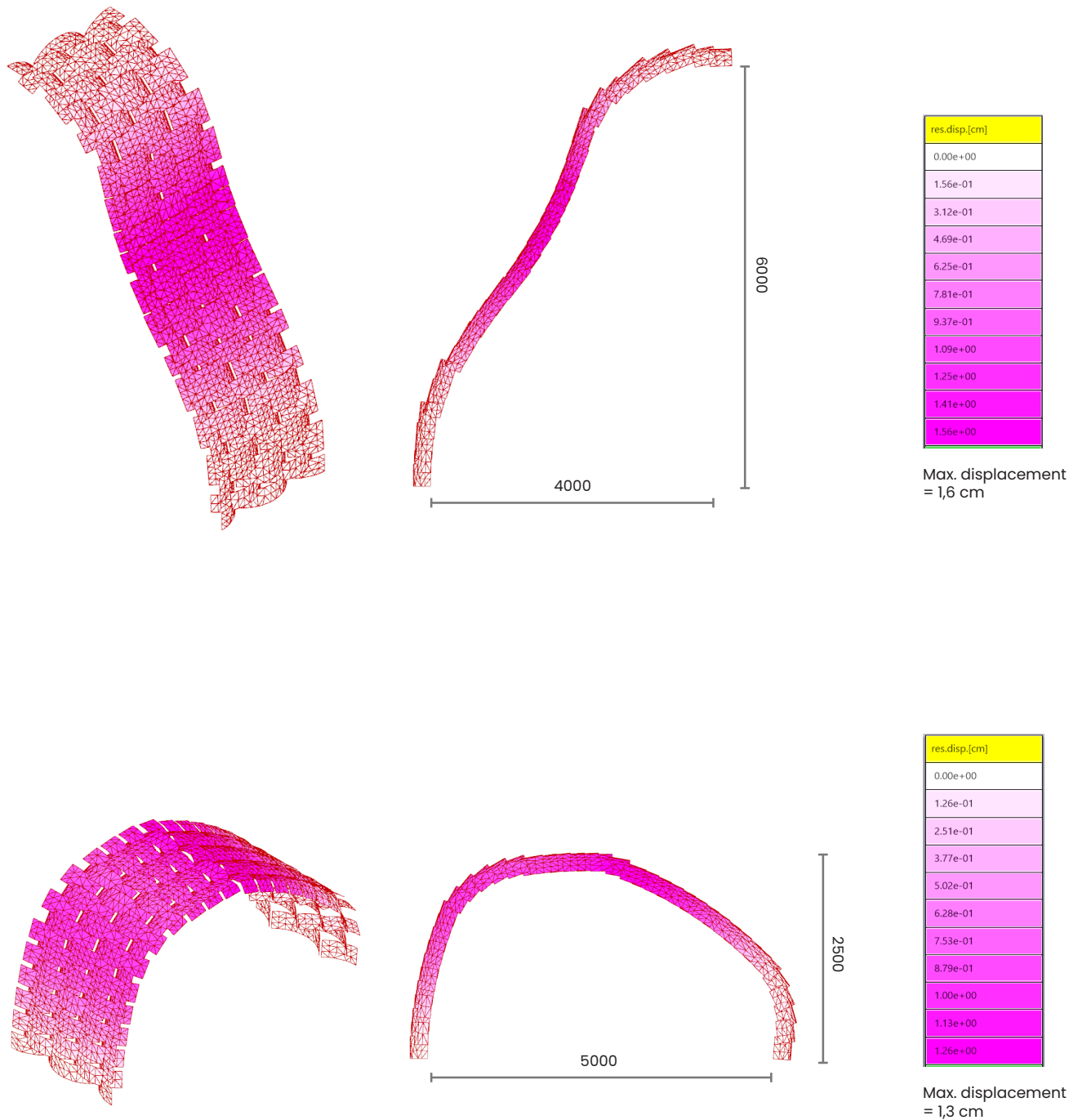


Figure 139: Displacement of two design options (own work, 2025)

Objective 2: Minimize alternation between module heights (amh)

The second objective function focuses on minimizing variation between module heights, which simplifies the construction process by reducing the complexity of assembly instructions.

For each design solution, the algorithm generates a list with module height sequences. To minimize height variation, the algorithm compares each module height in the list with the one that follows and calculates the difference. These differences are then summed to determine the total variation.

For example:

Pattern = [500, 300, 500, 300]

Differences = 200, 200, 200

Total difference = 600

Alternatively, if:

Pattern = [500, 500, 300, 300]

Differences = 0, 200, 0

Total difference = 200

The total difference reflects the degree of alternation between module heights. A lower total difference indicates fewer transitions between different heights. This value is used as an objective function to be minimized and is mathematically quantified as:

$$\text{Total difference} = \sum_{i=0}^{n-1} |h_i - h_{i+1}|$$

where:

- **i** is the index of the current module height in the list
- **n** is the total number of modules in the list
- **hi** is the height of the current module
- **hi+1** is the height of the next module in the sequence

Objective 3: Minimize deviation from desired span (span)

The metric associated with this objective aims to minimize the deviation from a user-defined span, ensuring that the final design solution closely aligns with the intended span requirement. The metric is defined using a square loss function (Wang et al., 2022):

$$\mathcal{L} = (S_{\text{actual}} - S_{\text{desired}})^2$$

where:

- **L** is the loss value, representing how far the actual span deviates from the desired span.
- **Sactual** is the actual span resulting from the algorithm (Fig. 140).
- **Sdesired** is the target span, entered with a number slider (Fig. 141).

First, the y-component of the end plane – onto which the last module is projected – is extracted (Fig. 140). Figure 141 shows how the rest of the loss function has been worked out in Grasshopper: The y-value is converted to metres for readability. The desired span is set via a number slider. The difference between the desired span and the actual span is then calculated. This value is squared to ensure a positive result and to assign greater penalty to larger deviations, guiding the optimization process toward more accurate solutions (Wang et al., 2022).

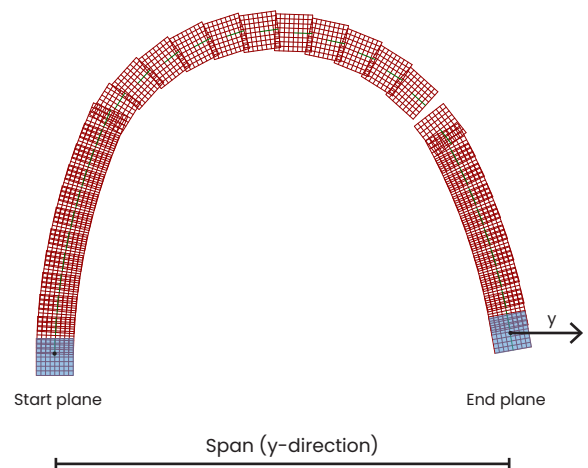


Figure 140: Extraction of the y-component from the end plane (own work, 2025)

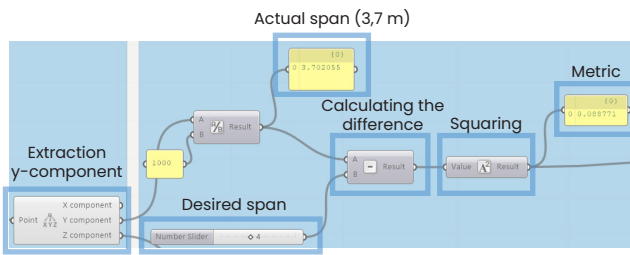


Figure 141: Implementation of the loss function used for objective 3 in Grasshopper (own work, 2025)

Objective 4: Deviation final module to ground level (h)

The metric associated with this objective indicates how close the final module is to ground level. The same square loss function is used to define this metric. In this case, the z-component is extracted from the end plane (Fig. 142).

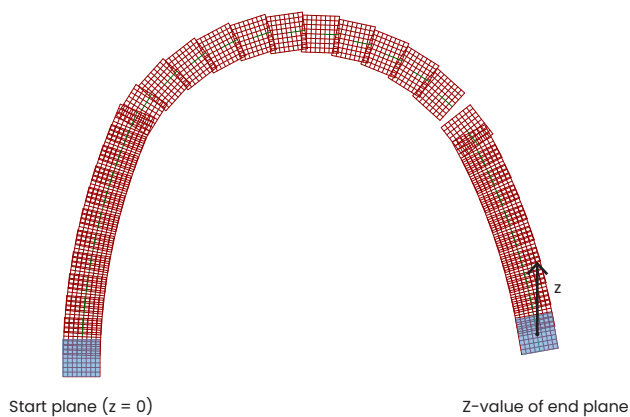


Figure 142: Extraction of the z-component from the end plane (own work, 2025)

The deviation from ground level is then calculated as the difference from $z = 0$. For example, when this difference is minimized, the algorithm tends to generate a regular arch shape, with both ends on the same level. Figure 143 shows how this is worked out in Grasshopper.

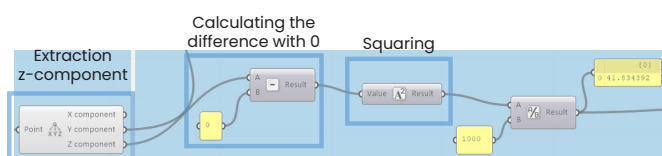


Figure 143: Implementation of the loss function used for objective 4 in Grasshopper (own work, 2025)(own

However, in practice, it is difficult to find design solutions of which the end modules perfectly end at $z = 0$. Therefore, if the algorithm is used in its current form, the system may require adaptable supports at the base to accommodate minor deviations from the ground.

Unlike the other objectives, this metric does not necessarily need to be minimized to achieve a desirable result. Instead, it allows users to explore a range of design solutions that share the same span but differ in shape and height. For example, if half an arch is preferred, the user can explore the objective space from the optimization to find such a shape, along with minimal variation in module height, and minimal deviation from the target span.

In summary, this objective adds design flexibility.

7.1.5 Multi-objective optimization

Operation of the algorithm

The optimization is performed using the Multi-Objective Optimization (MOO) engine Octopus, which employs an evolutionary algorithm inspired by biological evolution. This algorithm generates and evaluates a range of design variants, improving them iteratively by preserving the most successful solutions (Rohrmann, 2019).

In this process, the design parameters of the algorithm act as genes. New design variants – referred to as a new generation – are created through crossover of the most favorable solutions – based on the objective criteria – and through mutations (random modifications of the algorithm's variables) (Fig. 144). The set of solutions for each generation (the amount of offspring), can be controlled by adapting the population size in the algorithm.

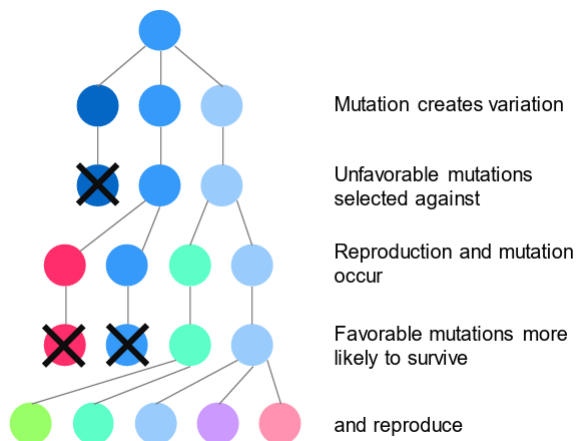


Figure 144: Explanation of the algorithm's functioning through analogy with natural selection (Rohrmann, 2019)

In multi-objective optimization, objectives often conflict, meaning that no single solution simultaneously satisfies all goals perfectly. Instead, a set of non-dominated solutions emerges - solutions that are not outperformed by any other when considering all objectives simultaneously. After each generation, a Pareto front is made, comprising solutions that are not dominated by others within that generation.

As the optimization progresses, the Pareto front typically stabilizes, indicating that further improvements across all objectives are no longer achievable. At this point, the user can select from the available non-dominated solutions, knowing that these represent the best possible trade-offs among competing objectives. When objectives are in conflict, the resulting Pareto front takes the form of a trade-off curve, representing the balance between competing performance criteria (Rohrmann & Vilgertshofer, 2019) (Fig. 145).

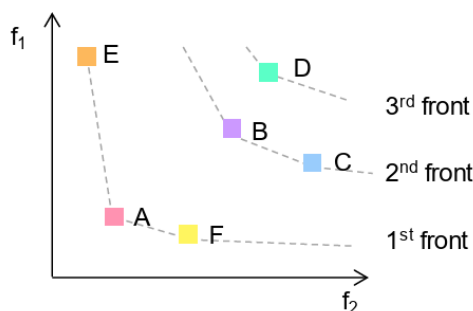


Figure 145: Pareto fronts over three generations showing trade-offs between objectives f1 and f2 (Rohrmann, 2019)

Implementation of the optimization

The integration of the MOO engine Octopus completes the development of the parametric tool. Figure 141 on the next page illustrates how the workflow is constructed, combining standard Grasshopper components with Python scripts. The full Python codes used in this workflow are provided in the Appendix.

The parameters from the generative algorithm are connected to the G (Genotype) input of the Octopus component, while the objective values are linked to the O (Objective) input (Fig. 146).

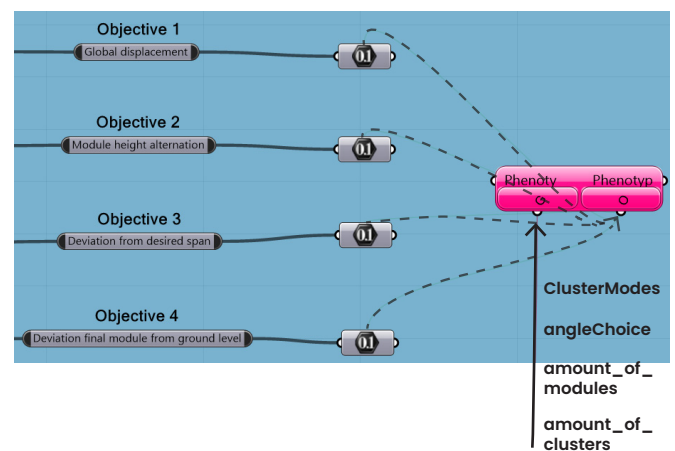


Figure 146: Connection of objectives and parameters to the Octopus optimizer component (own work, 2025)

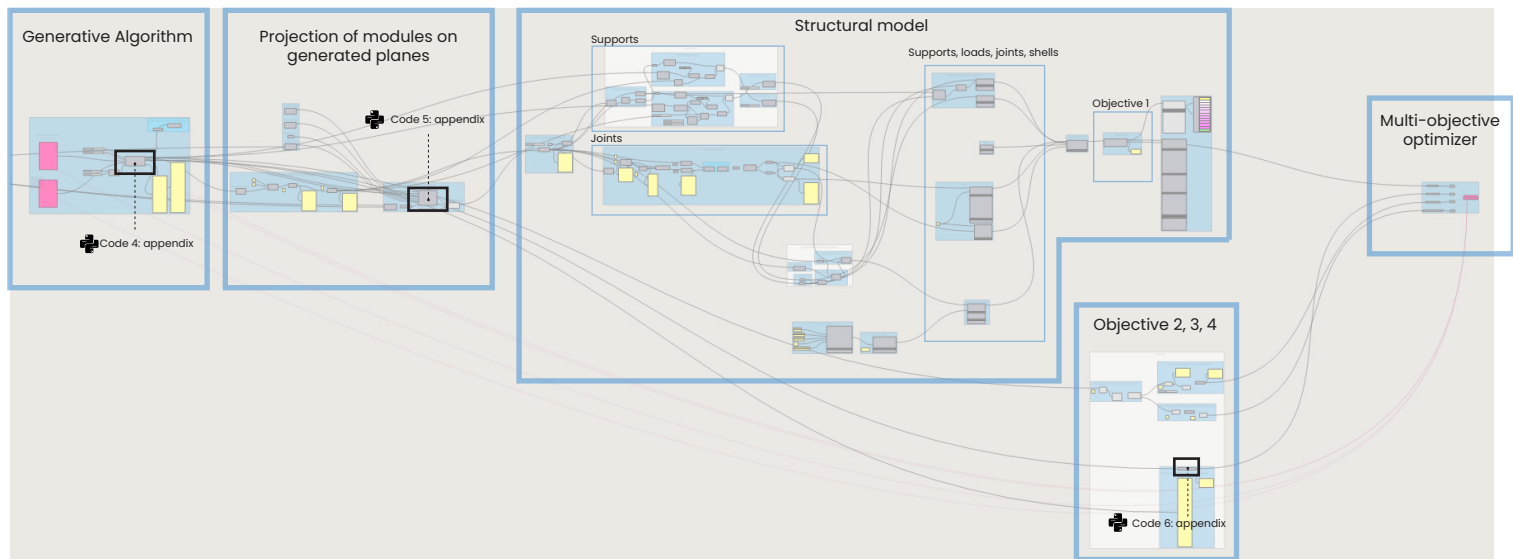


Figure 147: Overview of the parametric tool developed in Grasshopper, showing the full workflow from the generative algorithm to the structural model, objectives, and multi-objective optimizer (own work, 2025)

Optimization process and results

The optimization was carried out with a population size of 100. The optimization was stopped at 60 generations, as the design solutions showed no significant variation beyond this point. Figure 148 visualizes the relationship between the objectives in a three-dimensional plot, with each axis corresponding to one objective. Each cube represents a single design solution. The size of each cube reflects the value of the fourth objective: the deviation of the final module from ground level. Smaller cubes indicate a lower deviation from the ground. In this particular optimization, the desired span was set to 4 meters.

In the initial generations, random solutions are generated that cover a broad region of the objective space. As shown in Figure 149 (Generation 1), the design solutions are widely scattered, reflecting the algorithm's early-stage exploration. By generation 2 (Fig. 150), the population becomes denser and begins to form visible clusters.

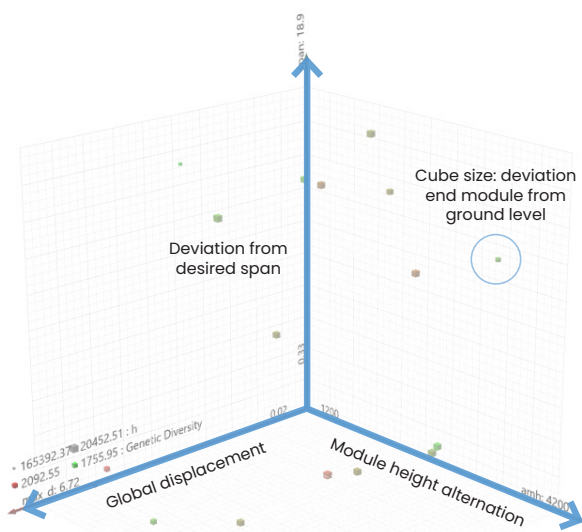


Figure 148: Objectives in a three-dimensional plot (own work, 2025)

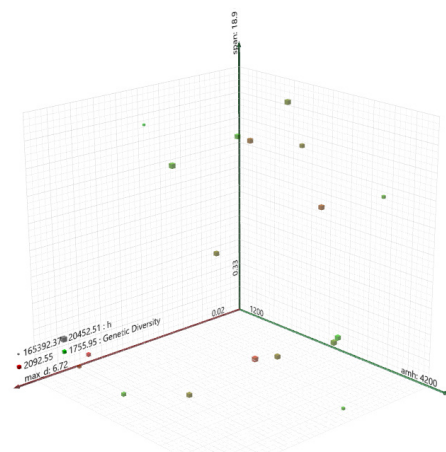


Figure 149: Objective space with design solutions in Generation 1 (own work, 2025)

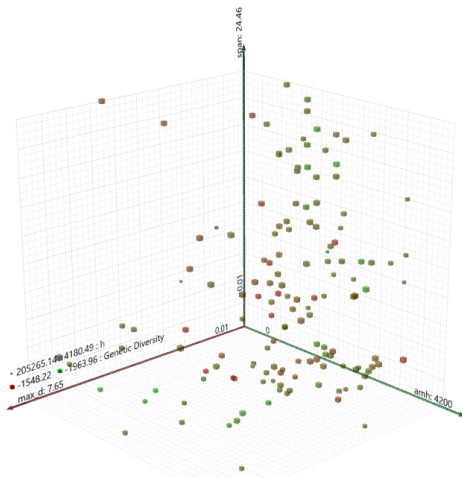


Figure 150: Objective space with design solutions in Generation 2 (own work, 2025)

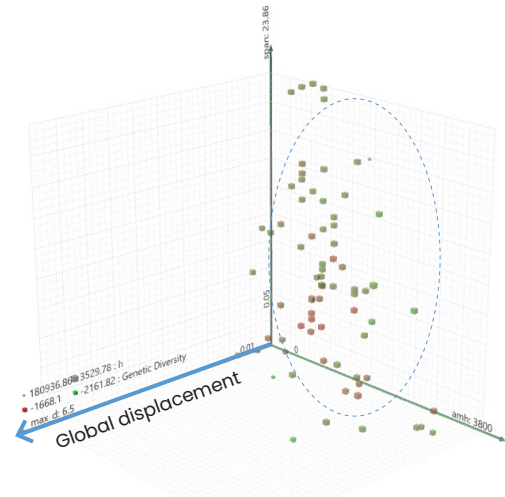


Figure 152: Design solutions in Generation 6, moving toward lower global displacement values relative to Generation 3 (own work, 2025)

Starting from generation 3, the design solutions begin to converge toward lower global displacement values. This trend is clearly visible in Figures 151, 152, and 153, where solutions move closer to zero along the displacement axis. Meanwhile, the distribution along the other two axes – module height alternation and deviation from the desired span – remains relatively wide. This may indicate that, in the early stages of the optimization, the algorithm prioritizes reducing displacement before refining trade-offs across the remaining objectives.

From Generation 7 (Fig. 153), an increased spread along the displacement axis is visible, with several outliers appearing further from zero. In Generation 8 (Fig. 154), this spread is reduced, and more solutions move again toward lower global displacement values. This fluctuation in the population may reflect the effect of crossover and mutation introducing new combinations into the solution set.

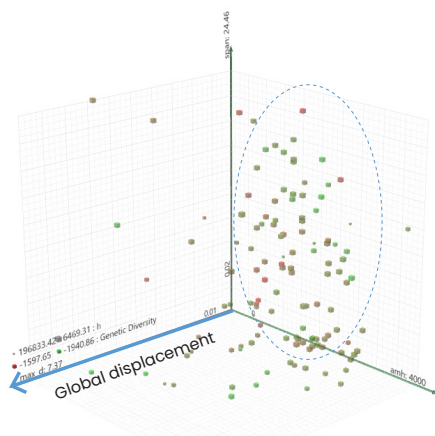


Figure 151: Design solutions in Generation 3, moving toward lower global displacement values (own work, 2025)

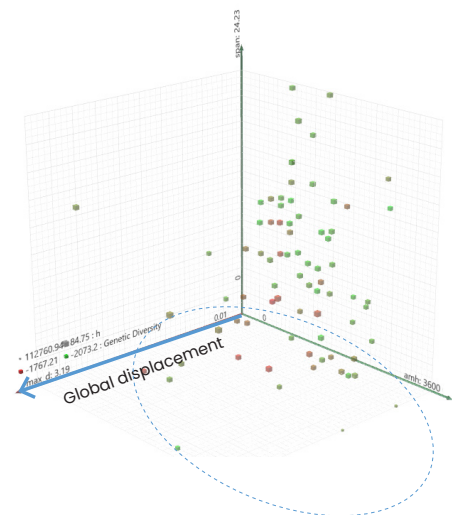


Figure 153: Design solutions in Generation 7, showing increased spread along the displacement axis (own work, 2025)

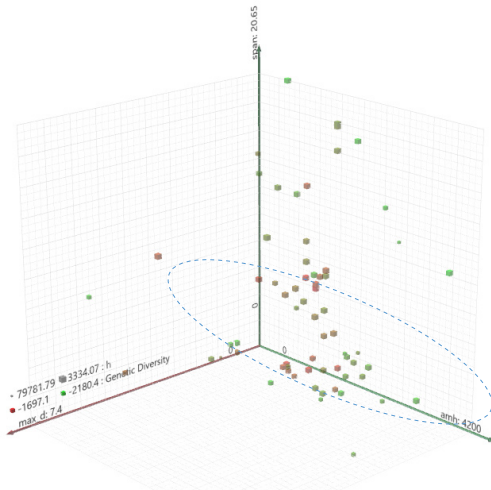


Figure 154: Design solutions in Generation 8, moving again toward lower global displacement values (own work, 2025)

From Generation 8 onward, the distribution of design solutions becomes increasingly concentrated near the origin, with more points moving toward lower values on all three objective axes (Fig. 155).

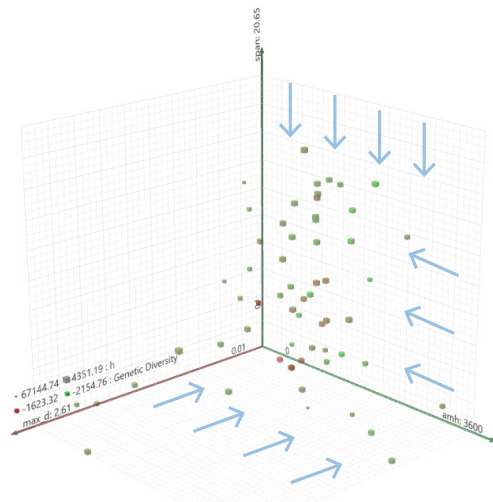


Figure 155: Design solutions showing movement toward lower values on all three objective axes. (own work, 2025)

Figures 156, 157, and 158 demonstrate that from around generation 48 onward, the solution space remains relatively stable. This indicates that the optimization has reached a state in which the best-performing solutions have been identified, and only minor refinements occur across generations.

The results show solutions with minimal deflection and minimal module height alternation, combined with a variety of span values. This final generation of solutions is referred to as the solution set (Rohrmann, 2019). From this set (Fig. 158), some design outcomes are discussed on the next page.

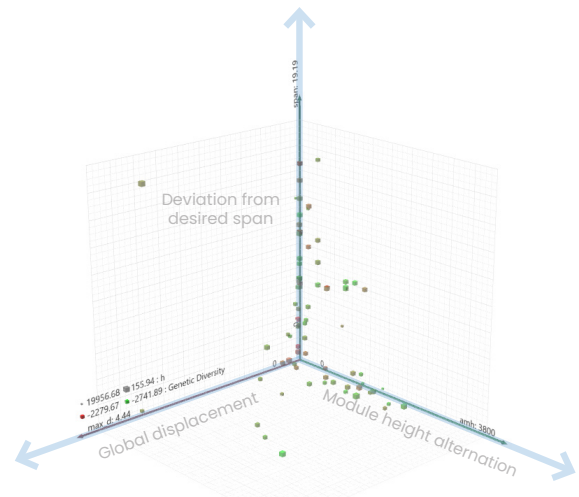


Figure 156: Solution space in Generation 48 (own work, 2025)

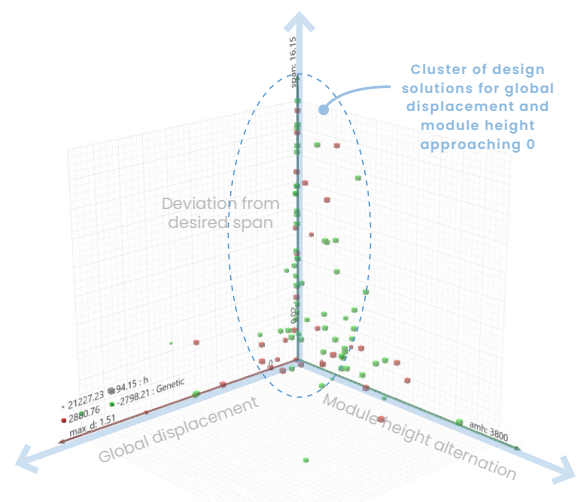


Figure 157: Solution space in Generation 54 (own work, 2025)

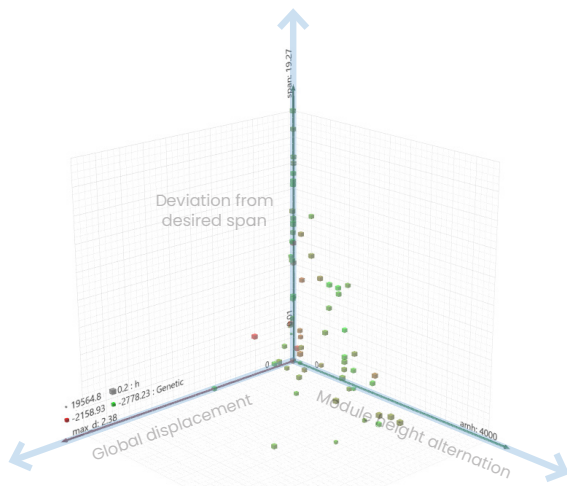


Figure 158: Solution space in Generation 60 (own work, 2025)

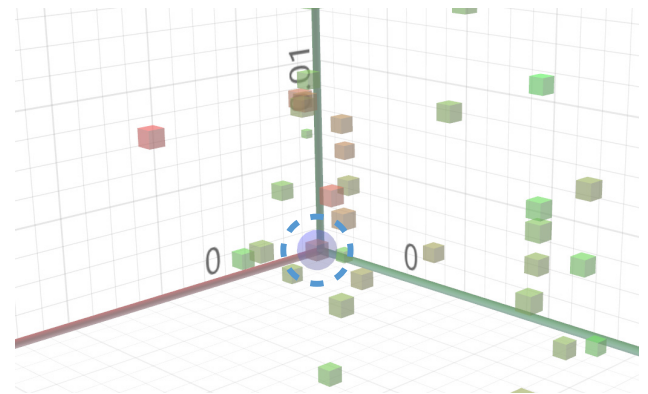


Figure 160: Design solution located near the origin, achieving optimal values for all three objective functions (own work, 2025)

Figure 159 highlights an optimal design solution, located near the origin of the three objective axes (see also Fig. 160). This solution achieves a minimal deviation from the target span of 4 metres, with a global displacement of only 0.76 cm (Fig. 161), and a module height alternation of 0 (Fig. 162), which corresponds to uniform modules of 0.5 metres in height. Additionally, the relatively large scale of the cube indicates a z-coordinate for the final module that is close to zero, stimulating a design solution that follows an arch-like shape.

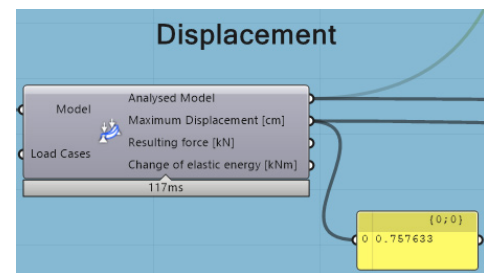


Figure 161: Maximum displacement value of the selected optimal design solution. (own work, 2025)

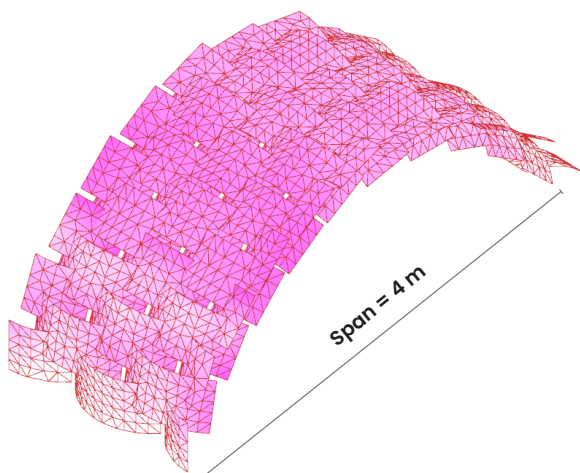


Figure 159: Visualization of an optimal design solution resulting from the multi-objective optimization, achieving a span of 4 metres (own work, 2025)

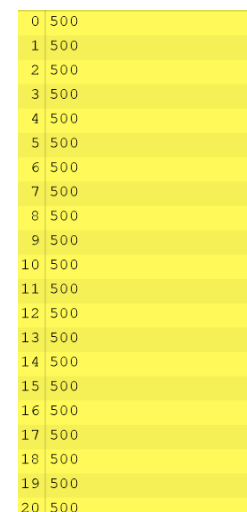


Figure 162: Uniform module height of 0,5 m, indicating no alternation in the optimal design solution (own work, 2025)

The full history of all elite design solutions from each generation can be visualized simultaneously (Fig. 163). This overview reveals that multiple solutions achieve equivalent performance in terms of deflection, module height alternation, and deviation from the desired span, yet differ in the position of the final module relative to ground level. Figure 164 shows two marked design solutions with equal performance but distinct structural shapes. The purple-highlighted solution was shown on the previous page, while the equally performing yellow-highlighted solution is presented in Figure 165. Although their performance is nearly identical, the solution shown in Figure 165 results in a noticeably different structural form.

This allows the designer to select not only based on span performance, but also on a structural configuration that best fits the context. For example, the set of solutions includes configurations suitable for both freestanding constructions (Fig. 166) and extensions. In the latter case, a half-arch form may be preferred due to the presence of an adjacent vertical element (Figure 167).

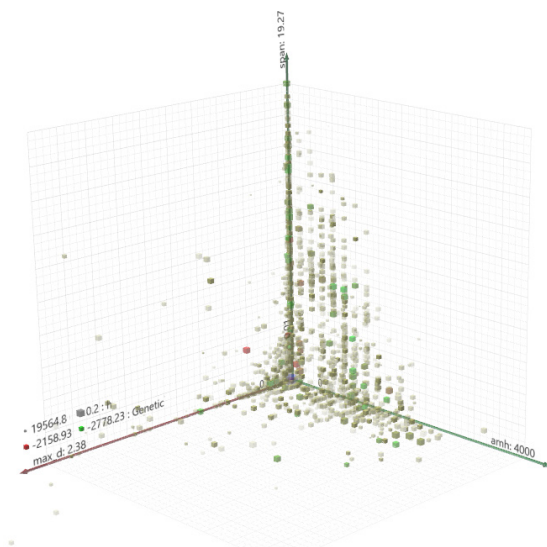


Figure 163: Full history of elite design solutions from each generation (own work, 2025)

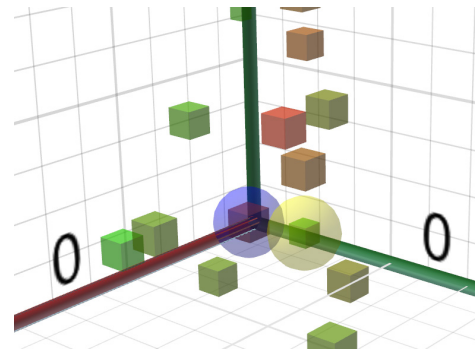


Figure 164: Two marked design solutions with identical performance but different structural shapes, based on variation in final module position (own work, 2025)

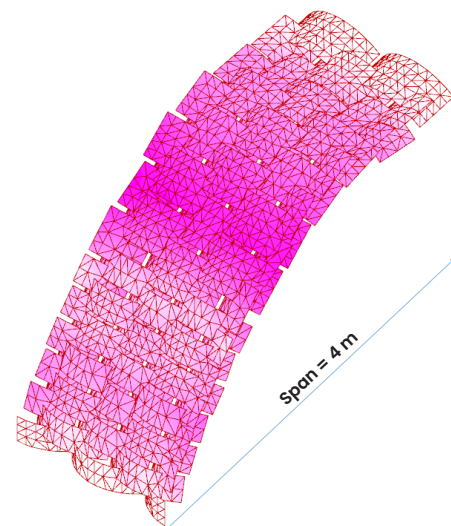


Figure 165: Yellow-marked solution with the same span, module height alternation, and deflection as the purple-marked design solution (own work, 2025)



Figure 166: Design solution of a free standing structure (own work, 2025)

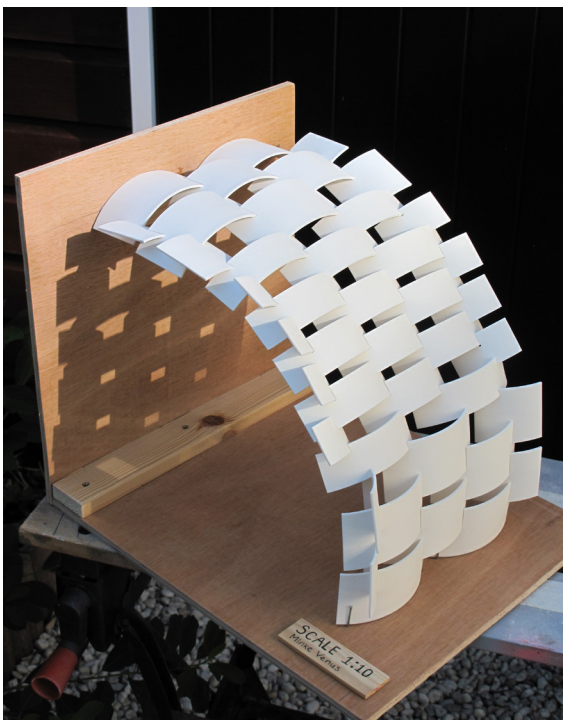


Figure 167: Half-arch configuration, suitable for locations with adjacent vertical elements (own work, 2025)

Conclusion

The results demonstrate that the objectives defined in this optimization are not inherently conflicting. It is possible to select design solutions that perform well across all objectives simultaneously. As a result, the distribution of solutions in the objective space does not form a typical Pareto trade-off curve, which is often seen when objectives are directly opposed.

Nevertheless, this does not diminish the value of the tool. On the contrary, it provides the designer with a range of equivalent solutions – given the objectives – that differ slightly. This flexibility allows for design choices based on contextual needs – such as extensions against vertical elements, irregular terrain conditions, or freestanding structures.

It became clear that the optimal design solutions, showing minimal deflection, are all single curves that transfer forces optimally in compression as expected. For the generation and practical application of free forms, the modules must be additionally tested on their bending resistance.

7.2 PART II: Preliminary Calculations and Stress Analysis

7.2.1 Structural behavior and preliminary hand calculations

Prior to the calculations, the structural behavior of the system is shortly outlined to provide clarity and context.

Each module carries, besides its own dead load, a possible additional snow load. These vertical loads are transferred downward through the contact points between modules – the small contact surfaces at the bottom of the slots (Fig. 168) – and ultimately to the supports of the arch.

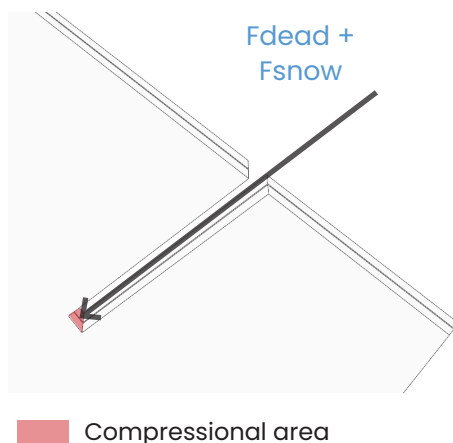


Figure 168: Contact surface between modules, where the compressive force is distributed (own work, 2025)

Modules positioned lower in the arch experience higher loads; the lower a module is positioned, the greater the cumulative load it must carry from modules above. Thus, the modules at the bottom support not only their own weight and snow load, but also the combined load from all modules positioned above. Consequently, reaction forces at the bottom row are greater than those in the upper rows (Fig. 169).

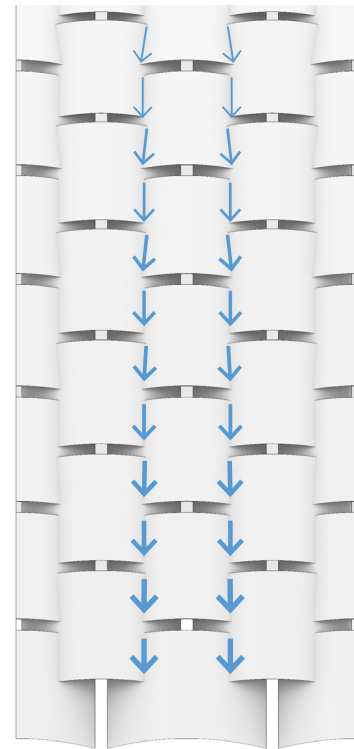


Figure 169: Load accumulation on lower modules (own work, 2025)

Vertical loads induce horizontal thrust forces at the base. These thrust forces must be counteracted by adequate supports. The presence of horizontal thrust is crucial, as it ensures that the modules primarily experience compression rather than bending.

Since compressive forces are concentrated on the relatively small contact surfaces at the bottom of the slots – where the applied load (action force F) is distributed – it is essential to verify whether these surfaces can withstand the resulting stress concentrations. These stress concentrations can be analysed in detail using Ansys. To do so, the expected design load F that acts in the slots of the bottom modules is first calculated manually.

To ensure compatibility with the physical testing setup, the module's length and height are selected to be manageable within a laboratory environment (Fig. 170 & 171).

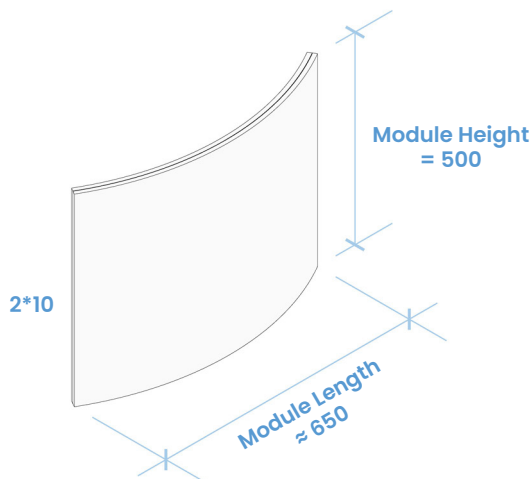


Figure 170: Module measurements for calculations
(own work, 2025)

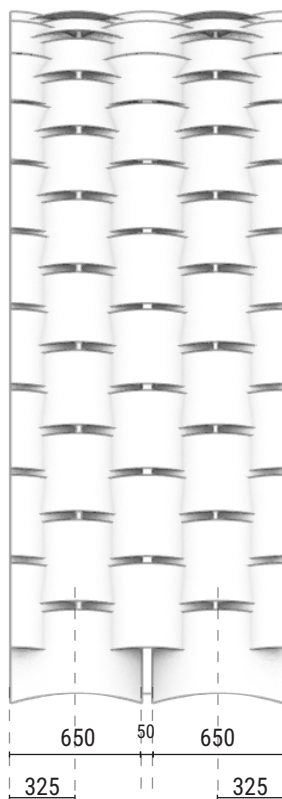


Figure 171: Module measurements for calculations
(own work, 2025)

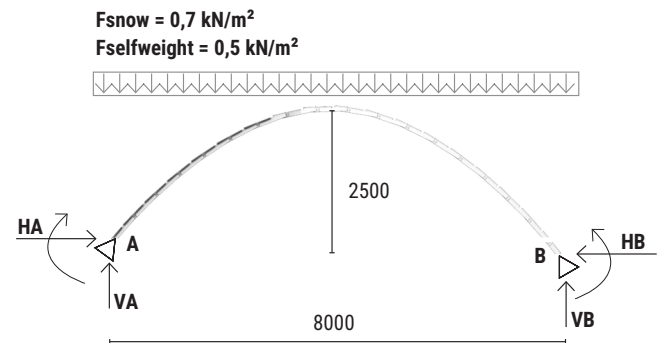
The calculation was carried out for a span of 8 meters – the maximum tested in this research – combined with a minimum rise of 2.5 meters. This minimum height was set to ensure enough freedom of movement under the curved structure. This rise results in a high span-to-height (L:h) ratio. Such a ratio typically produces a flatter arch profile, which deviates more from the ideal compressive thrust line and consequently introduces greater bending effects within the structure (Pournaghshband, 2016).

For the calculation of the self weight, a module thickness of 2x10 mm was assumed.

Calculation self weight

$$2500 \text{ kg/m}^3 * 10 = 25000 \text{ N/m}^3$$

$$= 25 \text{ kN/m}^3 * (2 * 0,01 \text{ m}) = 0,5 \text{ kN/m}^2$$



q-loads ULS

$$q_{\text{snow}} = 0,7 \text{ kN/m}^2 * \text{arch width} * \gamma_Q$$

$$= 0,7 \text{ kN/m}^2 * (2 * 0,65 \text{ m}) * 1,5$$

$$= 1,4 \text{ kN/m}$$

$$q_{\text{selfweight}} = 0,5 \text{ kN/m}^2 * \text{arch width} * \gamma_G$$

$$= 0,5 \text{ kN/m}^2 * (2 * 0,65 \text{ m}) * 1,35$$

$$= 0,9 \text{ kN/m}$$

$$q_{\text{total}} = 2,3 \text{ kN/m}$$

Ftotal

$$F_{\text{snow}} = q_{\text{snow}} * \text{span}$$

$$= 1,4 \text{ kN/m} * 8 \text{ m}$$

$$= 11,2 \text{ kN}$$

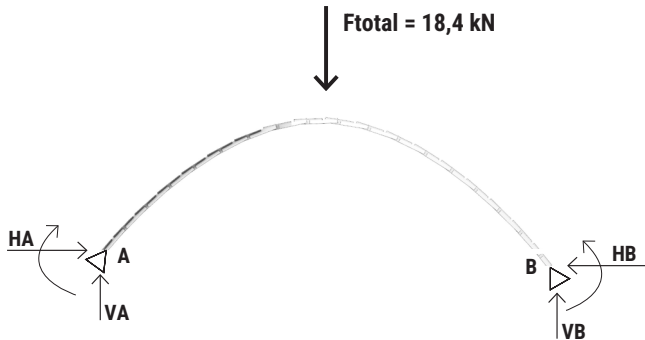
$$F_{\text{selfweight}} = q_{\text{selfweight}} * \text{span}$$

$$= 0,9 \text{ kN/m} * 8 \text{ m}$$

$$= 7,2 \text{ kN}$$

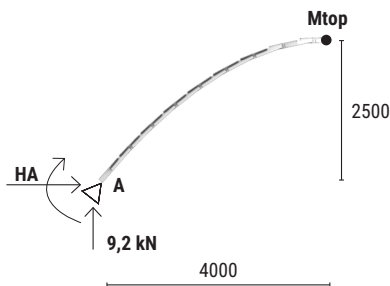
$$F_{\text{total}} = 18,4 \text{ kN}$$

According to the law of equilibrium of forces and moments, the sum of all horizontal and vertical forces acting on the structure must be zero for the structure to be stable (Feldmann et al., 2023).



Vertical reaction forces

$$VA = VB = F_{total} / 2 \\ = 9,2 \text{ kN}$$



Mtop

$$M_{top} = 1/8 * q_{total} * L^2 \\ = 1/8 * 2,3 \text{ kN/m} * 8^2 \\ = 18,4 \text{ kNm}$$

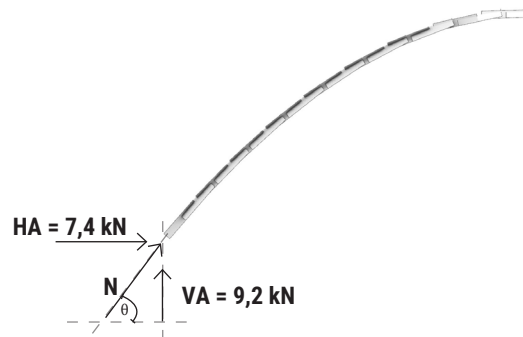
Horizontal reaction forces

$$MA = M_{top} \\ -2,5\text{m} * HA + 4\text{m} * 9,2 \text{ kN} = 18,4 \text{ kNm} \\ -2,5HA = -18,4 \\ HA = 7,4 \text{ kN}$$

Axial force in the arch

Because the system is designed to accommodate different spans - partly by using different interlocking angles - the initial angle of the first module can vary depending on the design. To evaluate a conservative / worst-case scenario for stress concentrations within the slot, a starting angle of 50° relative to the ground was used in the calculations, rather than assuming the first module is positioned vertically.

This smaller inclination angle results in a higher compressive force N along the module's axis, making it suitable for assessing the maximum expected stress in the slots.



$$N = HA * \cos(50^\circ) + VA * \sin(50^\circ) \\ = 7,4 * \cos(50^\circ) + 9,2 * \sin(50^\circ) \\ = 4,7 + 7,2 \\ = 11,9 \text{ kN}$$

Axial force per slot

To calculate the axial force for each slot, the axial force in the arch has to be divided by the amount of slots in each row:

$$12 \text{ kN} / 4 = 3,0 \text{ kN}$$

Glass thickness

$$q_{max} = F / A \text{ gives} \\ A = F / q_{max} \\ A = 3,0 * 10^3 \text{ N} / 60\text{MPa} \\ = 50 \text{ mm}^2$$

Since the length and width of the contact surface are equal, this area can be expressed as x times x , which must equal 50 mm^2 . Solving this results in a glass thickness of 5 mm per pane, giving a 2×5 mm laminated module.

7.2.2 Parameterization of the slot geometry

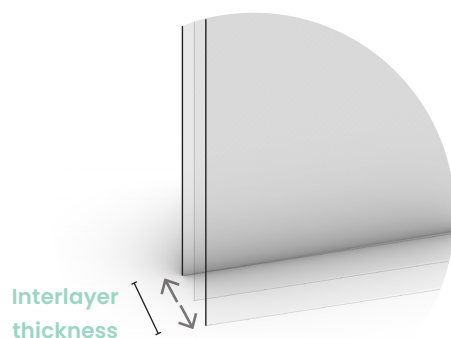
This section outlines, step by step, how the detailed geometry of a module has been parameterised to subsequently use as input for Ansys. Using this parametric setup, the glass thickness and slot corner radius could be quickly adjusted and reloaded in Ansys.



CREATION OF INTERLAYER

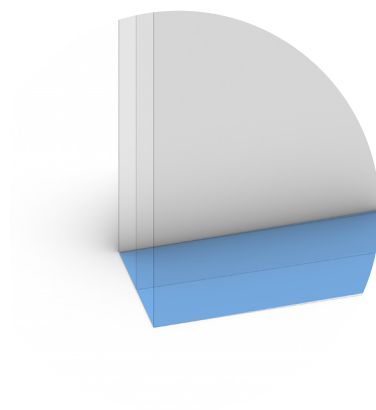
1

Offset of module surface



2

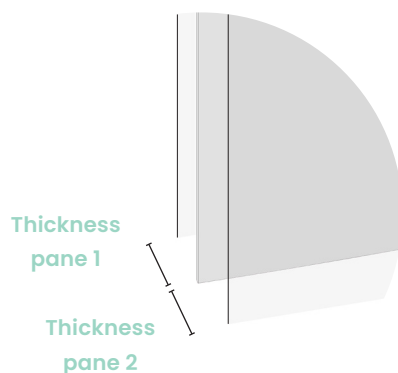
Creation of surface for extrusion



CREATION OF GLASS PANES

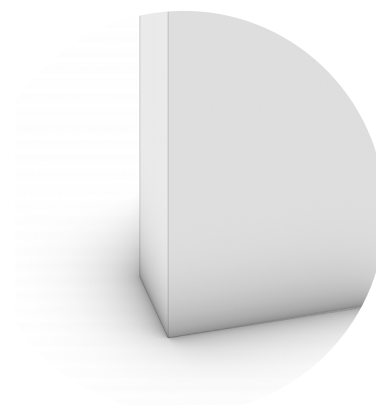
4

Creation of glass panes



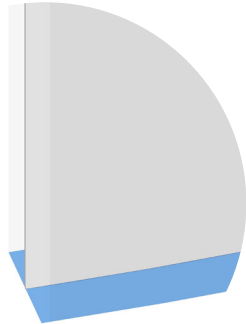
3

Creation of closed volume



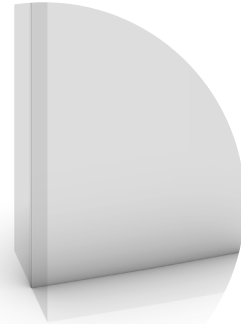
5

Creation of surfaces for
extrusion



6

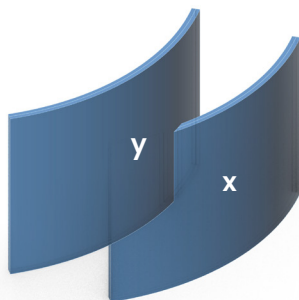
Creation of closed volumes



DEFINING FINAL GEOMETRY FOR THE GLASS

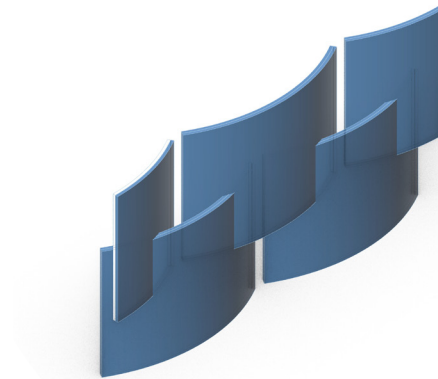
8

Cutting the slot in module x
with module y



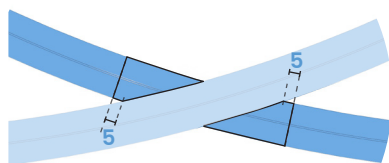
7

Module cluster with glass
panes and interlayer



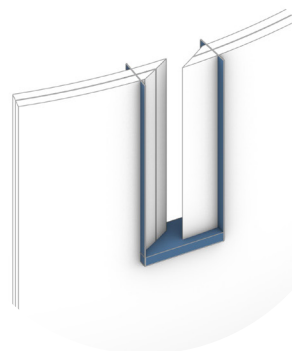
9

Creation slot infill-to-glass
distance



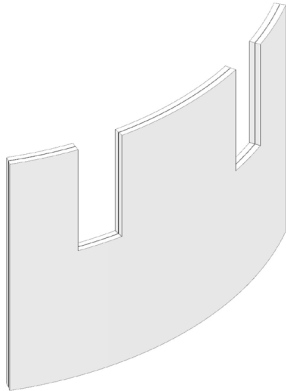
10

Creation of boundaries to cut
out the infill volume

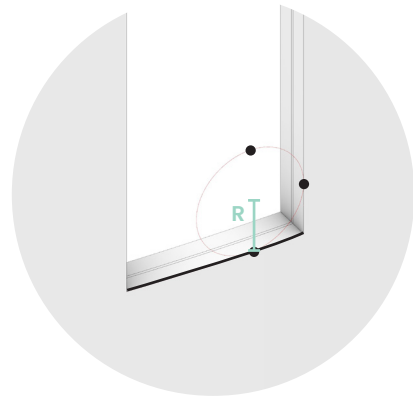


11

Final geometry for glass cut



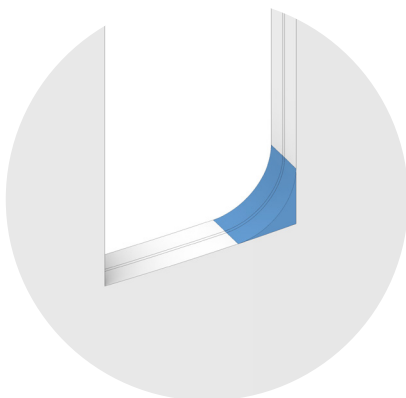
12

Creation of a circle with radius R 

CREATION OF SLOT CORNERS

14

Creation of closed breps



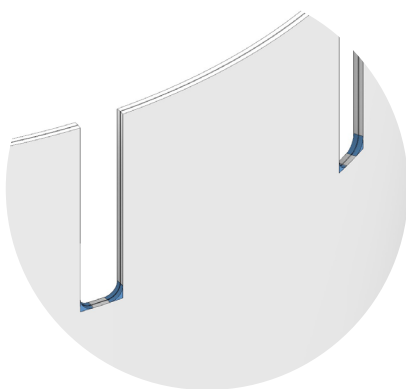
13

Creation of 'section lines' for each glass layer and interlayer



14

Integrating breps in all slot corners by mirroring



15

Joining each layer with corresponding corner volume



7.2.3 Ansys structural analysis

This section discusses the setup and results of the structural analysis.

Set-up of the model

The model is set up in a series of steps, as illustrated in Figure 172.

1. Selection of a Static Structural model

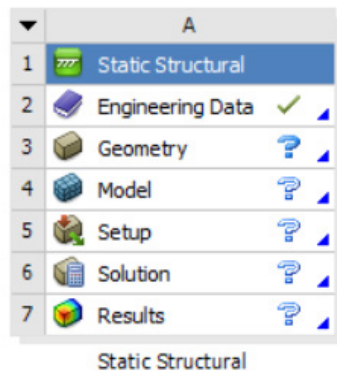


Figure 172: Standard steps in a Static Structural Analysis (own screenshot from Ansys, 2025)

2. Filling in the Engineering Data

The materials are manually filled in with the following mechanical characteristics:

Soda-lime Silica glass

- The material is selected as Isotropic Elastic
- Young's Modulus: 70e9 Pa (Table 3 - Appendix)
- Poisson's Ratio: 0,22 (average of Table 3 - Appendix)

PVB interlayer

PVB is selected for the simulation so that the results could be directly compared with the laboratory test in which the same interlayer is used.

- Young's Modulus: 2e6 Pa (Table 2 - Appendix)
- Poisson's Ratio: 0.45 (Table 1 - Appendix)

3. Loading in the Geometry

The analysis was carried out for the following module thicknesses: 2×5 mm, 2×6 mm, 2×8 mm, and 2×10 mm. These values were selected based on preliminary sizing, which indicated that a thickness with a starting value of 2×5 mm would be required. The analysed thicknesses represent common glass dimensions, as outlined in Chapter 5: Key Design Guidelines.

In addition, the influence of the slot corner radius on the stress concentration was analyzed. The additional geometry required for this analysis was created in Grasshopper. It turned out that this added geometry became a critical factor in the reliability of the simulation. When the new geometry was not properly joined to the existing glass layer geometry, Ansys interpreted it as a separate material body. As a result, the generated mesh was discontinuous (Figure 173), preventing a smooth flow of forces around the edges.

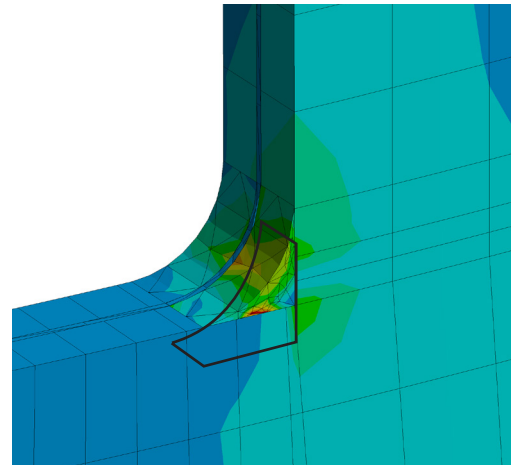


Figure 173: Corner geometry apart from the rest, causing unreliable results (own screenshot from Ansys, 2025)

To obtain reliable analysis results, the geometry had to be properly joined (Fig. 174).

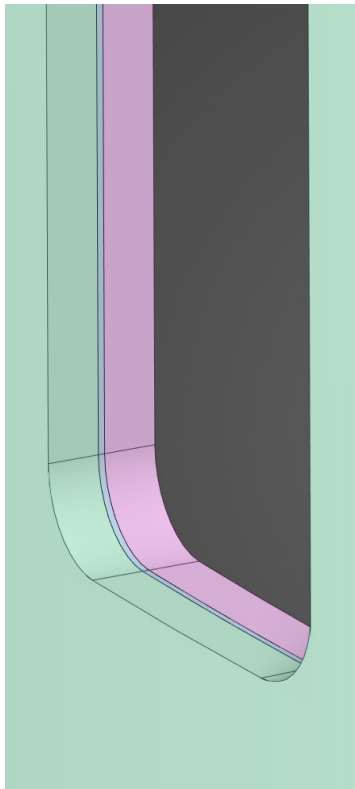


Figure 174: The corner geometry joined with the glass layer geometry (own screenshot from Ansys, 2025)

Calculation of the surface pressures:

for 2x5 mm:

$$\begin{aligned}\sigma &= F / A \\ &= 3000 \text{ N} / 490 \text{ mm}^2 \\ &= 6,12\text{e}6 \text{ Pa}\end{aligned}$$

for 2x6 mm:

$$\begin{aligned}\sigma &= F / A \\ &= 3000 \text{ N} / 672 \text{ mm}^2 \\ &= 4,46\text{e}6 \text{ Pa}\end{aligned}$$

for 2x8 mm:

$$\begin{aligned}\sigma &= F / A \\ &= 3000 \text{ N} / 1132 \text{ mm}^2 \\ &= 2,65\text{e}6 \text{ Pa}\end{aligned}$$

for 2x10 mm:

$$\begin{aligned}\sigma &= F / A \\ &= 3000 \text{ N} / 1710 \text{ mm}^2 \\ &= 1,75\text{e}6 \text{ Pa}\end{aligned}$$

Figure 175 illustrates the loads and supports that are applied in the simulation model.

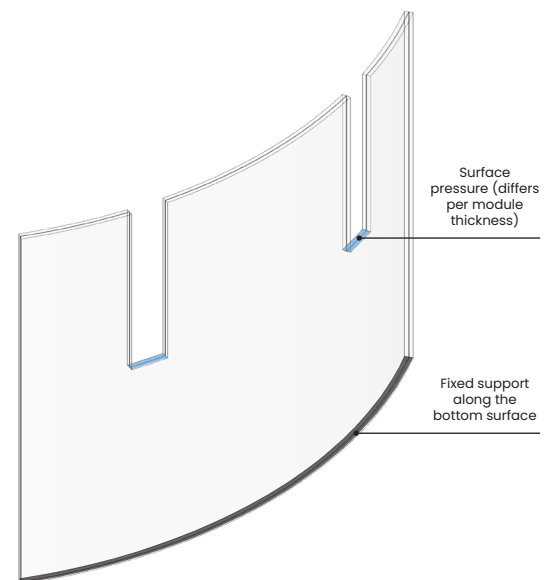


Figure 175: Applied forces and support in the model (own screenshot from Ansys, 2025)

4. Adding Applied loads and supports

A force of 3.0 kN is applied at the bottom of each slot and distributed over a small area. In Ansys, this is modeled as 'surface pressure.'

The compressional surface varies with each module thickness: it becomes longer and more rectangular to accommodate the interlocking of another module, and thicker due to the increased glass layer thickness. Accordingly, in the analysis of different module thicknesses, the following surface pressures are applied to the compressional area in the Ansys simulations:

6. Results

Result for 2x5 laminated glass and a sharp slot angle

It can be seen that the stress concentrates in the slot corners and along the edges of the module. However, the maximum principal stress measured in the corner of each slot is only 8,27 MPa (Fig. 176 - 179). This is well below the safe limit of 60 MPa.

To check whether these results are reliable, the subsequent glass thicknesses were analyzed, with the outcomes presented on the following pages.

A: Static Structural
Maximum Principal Stress
Type: Maximum Principal Stress
Unit: Pa
Time: 1 s
02/05/2025 10:21:51

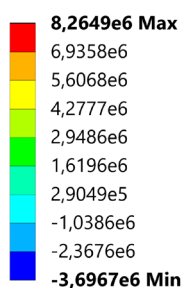


Figure 176: Maximum Principal Stress legend for a 2x5 module (own screenshot from Ansys, 2025)

Front view

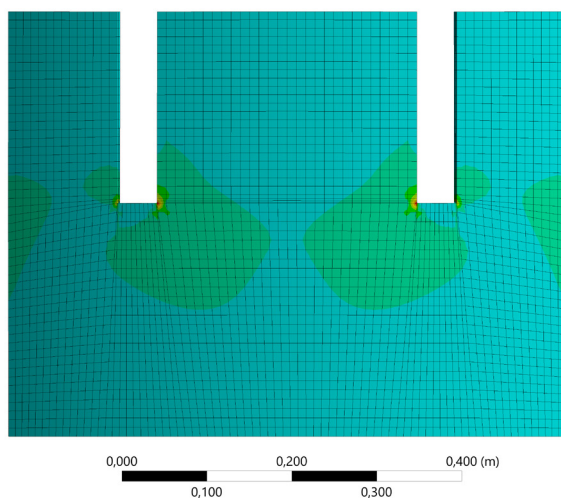


Figure 177: Front view of a 2x5 module (own screenshot from Ansys, 2025)

Back view

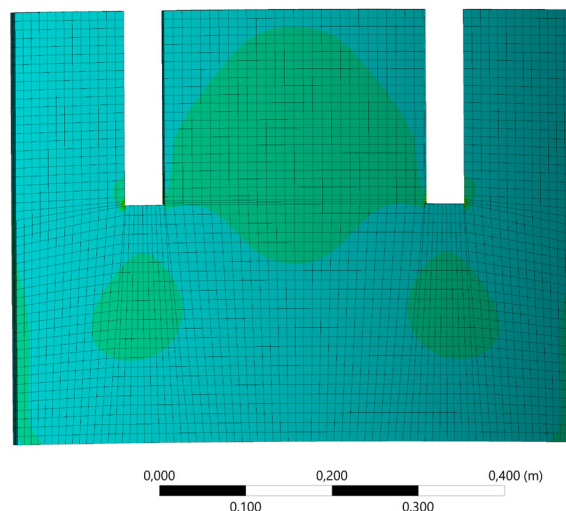


Figure 178: Back view of a 2x5 module (own screenshot from Ansys, 2025)

View of the slot

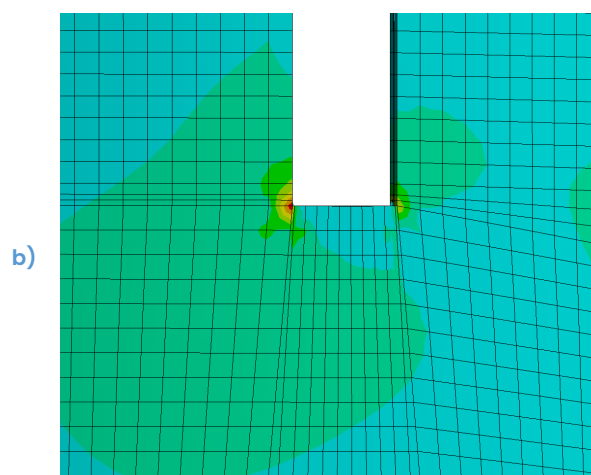
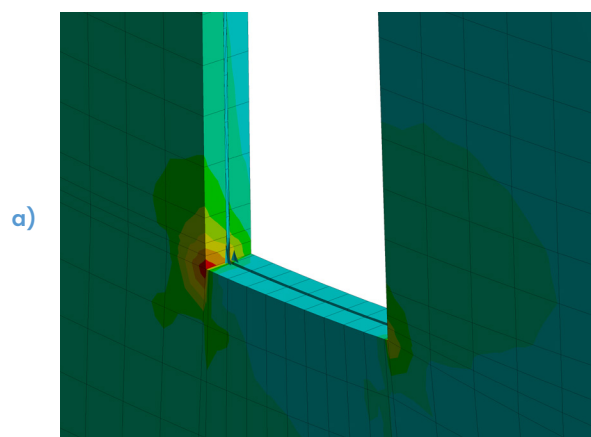


Figure 179: a) Perspective view and b) Front view of the slot (own work, 2025)

Result for 2x6 laminated fully toughened glass and a sharp slot angle

For the 2×6 mm laminate, the visual stress distribution remains largely the same, but the maximum principal stress decreases by an additional 1.7 MPa, reaching a value of 6.6 MPa (Fig. 180 – 183).

A: Static Structural

Maximum Principal Stress

Type: Maximum Principal Stress

Unit: Pa

Time: 1 s

02/05/2025 10:55:58

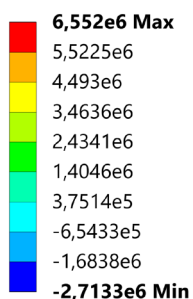


Figure 180: Maximum Principal Stress legend for a 2x6 module (own screenshot from Ansys, 2025)

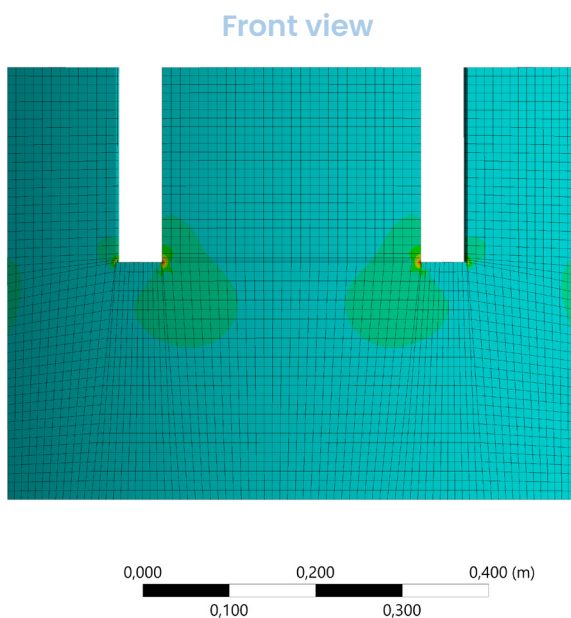


Figure 181: Front view of a 2x6 module (own screenshot from Ansys, 2025)

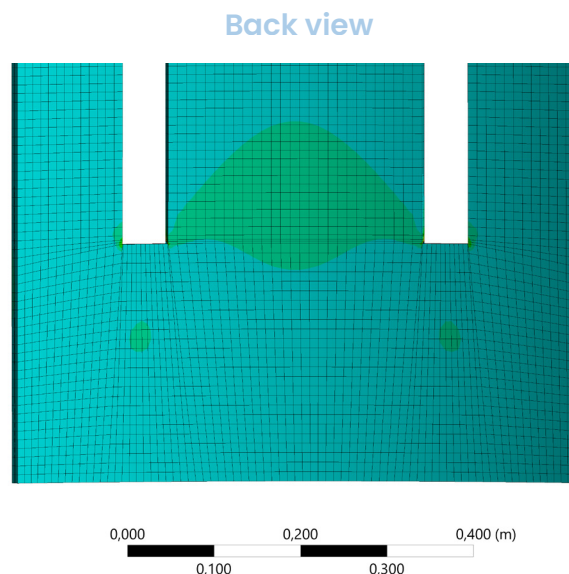


Figure 182: Back view of a 2x6 module (own screenshot from Ansys, 2025)

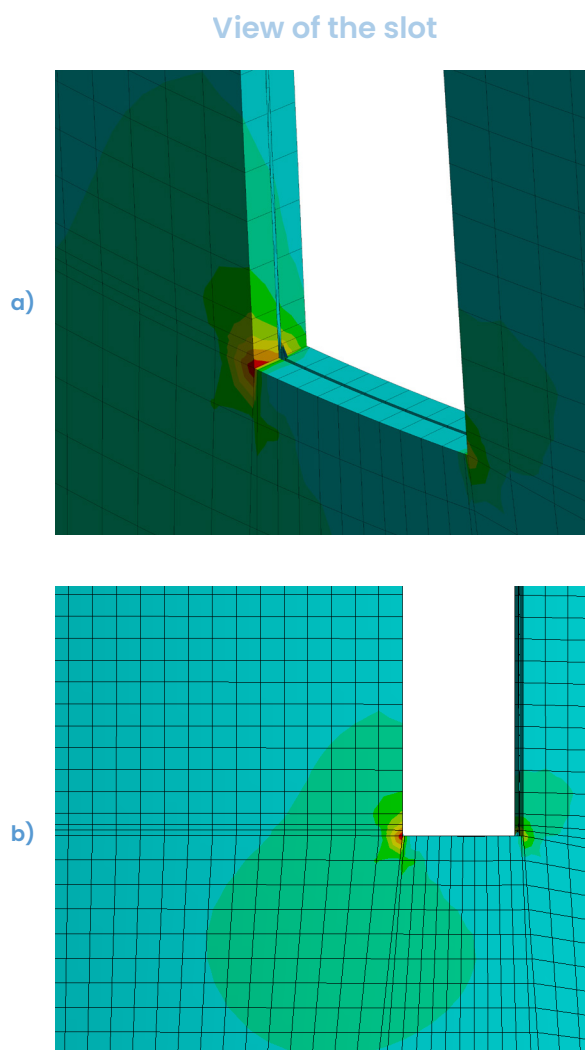


Figure 183: a) Perspective view and b) Front view of the slot (own work, 2025)

Result for 2x8 and 2x10 laminated fully toughened glass and a sharp slot angle

The results for the 2×8 mm laminated glass show a further decrease of 2.1 MPa, bringing the maximum principal stress down to 4.5 MPa. For the 2×10 mm module, the maximum principal stress is reduced even further to 3.2 MPa. These analyses are attached in the Appendix.

A line chart has been created to illustrate the consistent reduction in stress concentration with increasing glass thickness, reinforcing the reliability of the simulation outcomes (Fig. 184).

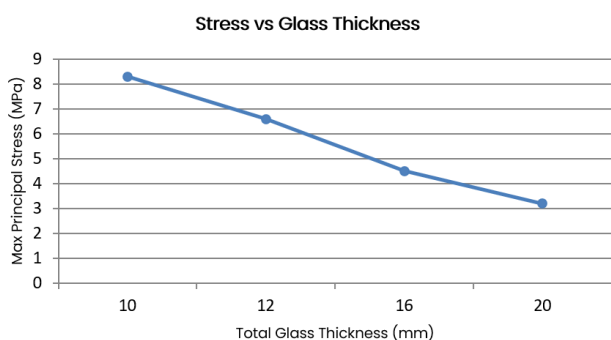
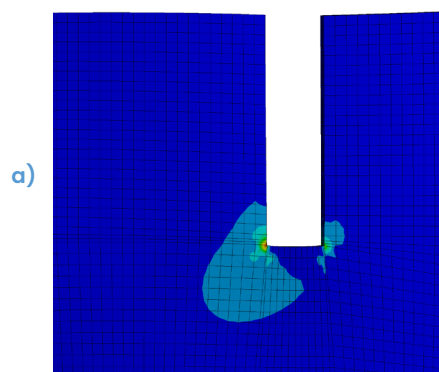


Figure 184: Line chart showing a consistent reduction in stress concentration for an increasing glass thickness (own work, 2025)

To assess the effect of increasing the slot corner radius on the peak stresses, an additional test was conducted using a 10 mm radius for the slot corner in a 2×6 mm glass module. The results clearly show that stress concentrations no longer accumulate at the sharp corner, but are instead more evenly distributed across the module (Fig. 185).

The peak stress decreased from 6.5 MPa to 4.7 MPa – a reduction of 1.8 MPa. This decrease is nearly as significant as the reduction achieved by increasing the thickness of the entire glass layer. Knowing that such a substantial stress reduction can be achieved by adding a small amount of material at the corners is valuable for designing a lightweight system.

Without slot corner radius



Slot corner radius of 10 mm

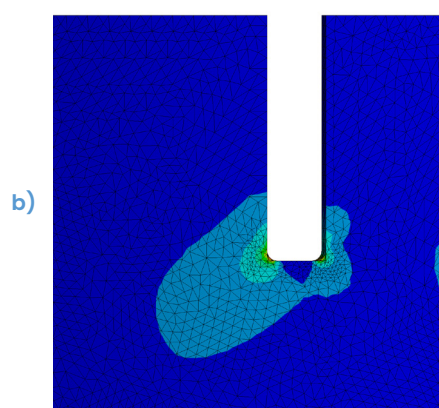


Figure 185: a) module without and b) with a slot corner radius of 10 mm, showing the effect on the stress distribution in the module (own screenshot from Ansys, 2025)

Conclusion

Based on the analysis, it can be concluded that the slot corners are the most critical and vulnerable areas within the system.

A module made of fully toughened laminated glass (2×5 mm) with a PVB interlayer and a sharp slot angle would already be sufficient to withstand an action force of 3.0 kN in each slot.

In that case, it may be preferable to use heat-strengthened glass instead of fully toughened glass. This has the advantage that, unlike laminated fully tempered glass, the modules retain some residual structural performance after breakage. As a result, the overall structure remains safe even if a module fails due to unforeseen loading.

7.3 PART III: Structural Verification through Laboratory Testing

In recent decades, an increasing number of guidelines and standards have been developed that have made structural design with glass safer and more accessible. An important milestone is prCEN/TS 19100, a draft European code available since early 2021. This technical specification provides a comprehensive set of guidelines, standards and requirements specific to the design of glass structures. However, as there is still no fully comprehensive code of practice, it remains necessary in many cases to carry out additional load tests to ensure the safety and performance (Feldmann et al., 2023).

7.3.1 Laboratory test setup

Figures 186 and 187 show the setup of the compression test, including the relevant measurements and materials. The test is conducted using three modules. A pressure head applies an increasing force $F = x \text{ kN}$, resulting in a reaction force of $1/2 F$ in each slot.

A steel U-profile is used at the bottom to support the cantilevering part of the structure that extends beyond the compression device. Additionally, the flanges serve to press the spruce timber – which encloses the modules – firmly against modules 2 and 3, ensuring that the glass is securely clamped in place (Fig. 187).

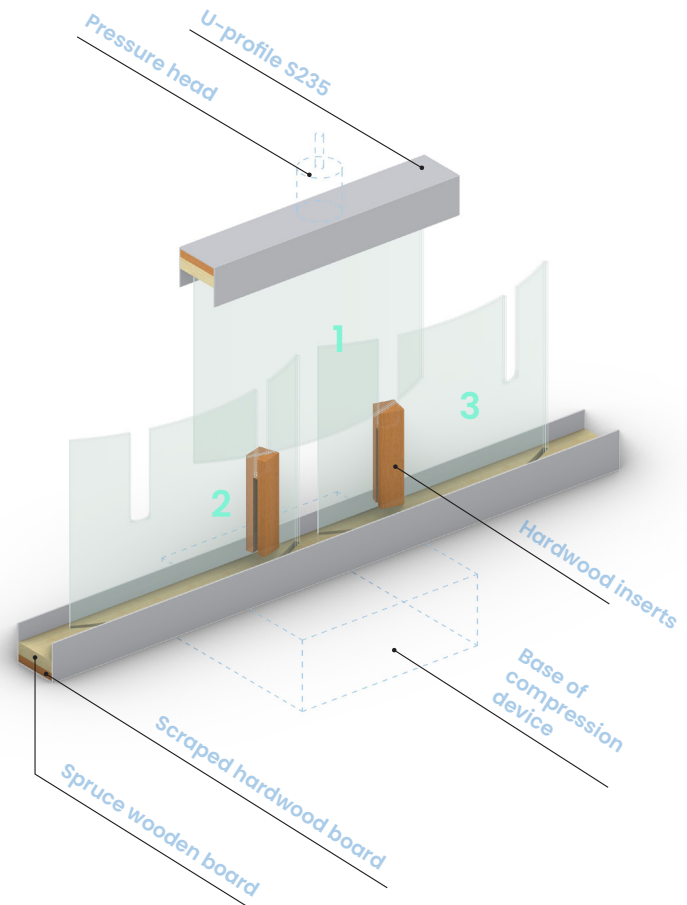


Figure 187: Axonometric view of the test setup with material indications (own work, 2025)

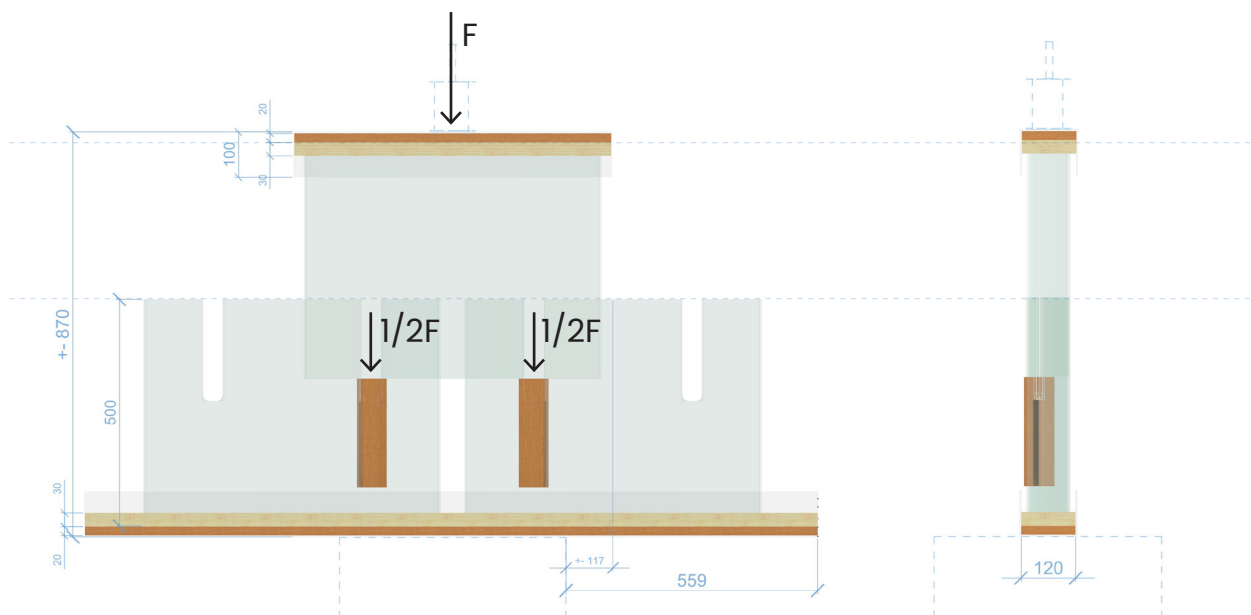


Figure 186: Front and side view with measurements of the laboratory test setup (own work, 2025)

This clamping mechanism is also applied at the top of the setup, where the steel profile wraps around module 1. Ensuring proper clamping at both the top and bottom is essential to prevent the modules from buckling when eccentricities are introduced. Such eccentricities are nearly unavoidable, as the pressure head is never perfectly aligned with the centerline of the structure. Besides, the center lines of the modules may not align precisely either (Fig. 188).

In addition, the steel profile at the top helps to evenly distribute the force from the pressure head across the entire upper edge of module 1. A layer of scraped hardwood board is used as a robust intermediate material between the glass and the steel profiles.

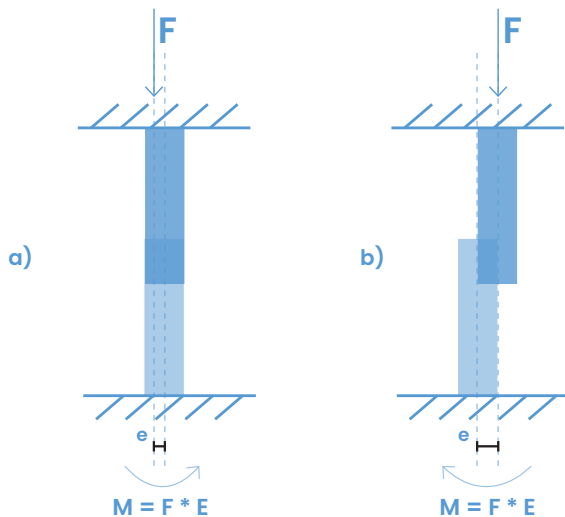


Figure 188: Side view showing bending moments resulting from eccentric loading due to: a) misalignment between applied load and the module centerline and b) a deviation in vertical alignment caused by a small offset between stacked modules (own work, 2025)

To further secure the glass and prevent the modules from making contact with the steel, rubbers are additionally applied (Fig. x).

The undersides of modules 2 and 3 are in direct contact with the scraped hardwood board (Fig. 189), which provides sufficient resistance to the compressive forces generated during the test and ensures an even supported surface.

Hardwood inserts are placed in the slots to prevent direct glass-to-glass contact, thereby avoiding peak stresses that could cause the modules to crack prematurely (Fig. 163).

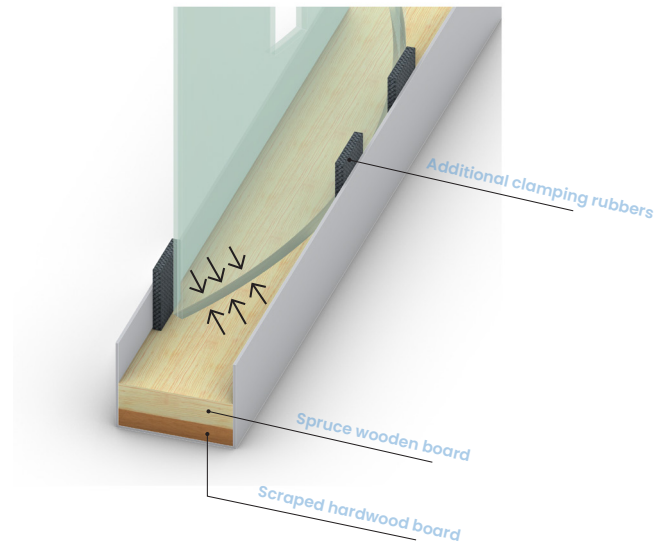


Figure 189: Modules supported by a scraped hardwood board and sandwiched between spruce and rubber to prevent buckling (own work, 2025)

7.3.2 Pre-test calculations for required materials

Some preliminary calculations were carried out to verify whether the selected materials can withstand the expected loads.

The Ansys analysis demonstrated that the peak stress concentration resulting from the applied compressive force remains well below the failure threshold of glass, which is 120 MPa (Table 5 Appendix). A theoretical compressive force of 3 kN applied within the slot yields a peak stress of only 6.6 MPa. This value is approximately 18 times lower than the material's failure limit ($120 / 6.6 \approx 18$). Given the linear elastic behavior of glass, it can be estimated that a compressive force up to 18 times greater could theoretically be applied before failure occurs. This corresponds to a maximum compressive force of approximately 54 kN per slot (18×3 kN).

Hardwood in the slots

Table 7 in the Appendix provides strength classes for hardwood perpendicular to the grain, ranging from D18 (4.8 MPa) to D80 (9.0 MPa). Since the specific type of hardwood used was not clearly identified as it was leftover wood, an average value of all classes was assumed: $f_{c,90,k,mean} \approx 5.5$ MPa (perpendicular to the grain) and $f_{c,0,k,mean} \approx 28.4$ MPa (parallel to the grain). If the glass were tested under the highest possible load (Fig. 190), the hardwood in the slot should be shaped so that it is loaded parallel to the grain. This orientation increases its compressive strength. As a result, the stress on the contact surface is calculated as follows:

$$\begin{aligned}\sigma &= \frac{F}{A} \\ &= \frac{54\,000 \text{ N}}{800 \text{ mm}^2} \\ &= 67,5 \text{ MPa} \longrightarrow 67,5 > 28,4 \text{ MPa} \quad \times\end{aligned}$$

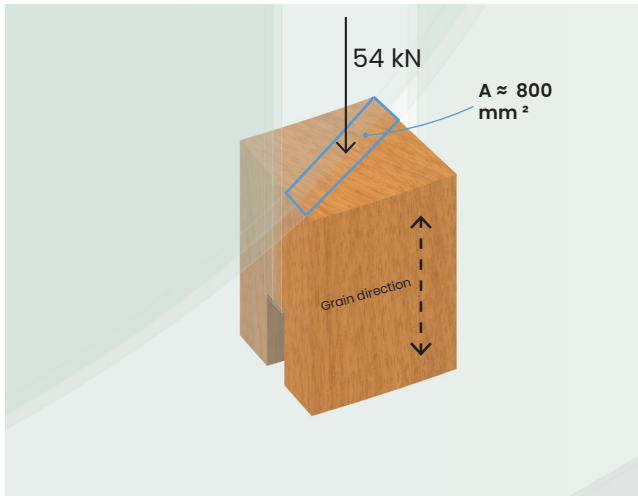


Figure 190: Slot with hardwood insert, loaded perpendicular to the grain direction with a maximum load of 54 kN (own work, 2025)

From this calculation can be concluded that the wood would fail before the glass does. However, the primary goal of the test is to determine whether the modules can withstand a load of at least 3 kN in each slot – corresponding to the self-weight and snow load acting on the most heavily loaded module. If this load is successfully resisted, additional force will be applied to evaluate whether the module can sustain a few extra kilonewtons beyond that threshold.

In that case, the system may be suitable for larger spans and/or unexpected higher loads, for example due to production tolerances.

To test the glass as close to its failure limit as possible – without the wood failing first and causing premature glass breakage – the stress at which the hardwood fails has been calculated:

$$\begin{aligned}F &= \sigma \times A \\ &= 28.4 \text{ MPa} \times 800 \text{ mm}^2 \\ &= 22\,720 \text{ N} \\ &= 22.7 \text{ kN}\end{aligned}$$

In addition to compression, the hardwood may also fail in shear. Based on the shear strength $f_{v,k}$ of the wood, the required height h (Figure 191) can be calculated. The mean shear strength value $f_{v,k,mean}$ was taken from Table x in the appendix and is approximately 4.35 MPa. Using the following formula, the minimum required height of the hardwood insert in the slot was determined:

$$\begin{aligned}T &= \frac{F}{bh} \longrightarrow h = \frac{F}{Tb} \\ h &= \frac{22\,000 \text{ N}}{4,35 \text{ MPa} \times 40 \text{ mm}} \\ &= \frac{22\,000}{174,0} \\ &= 126,44 \text{ mm}\end{aligned}$$

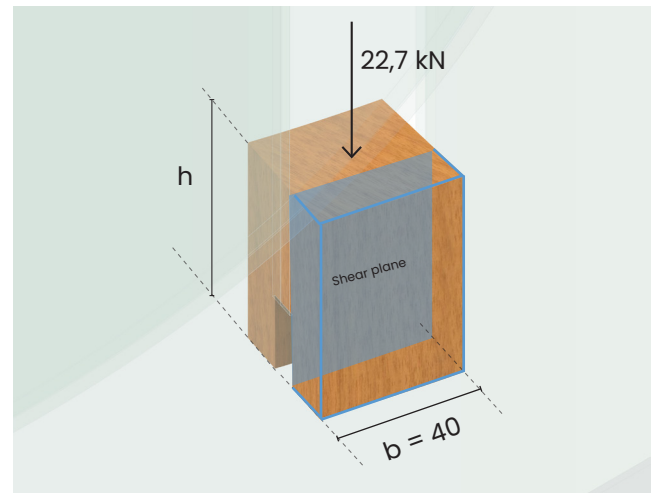


Figure 191: Determining the required height of the wooden insert based on the shear strength of the wood, the size of the shear plane, and the maximum expected load (own work, 2025)

Scraped hardwooden board - top

To verify whether the hardwood between the U-profiles and the glass can withstand the maximum compressive force applied to the structure, the following calculation is performed for the upper hardwood board (Fig. 192):

$$F_{\text{pressure_head}} = 2 \times 22\,700 \text{ N} \\ = 45\,400 \text{ N}$$

$$\sigma = \frac{F}{A} \\ = \frac{45\,400 \text{ N}}{8\,640 \text{ mm}^2} \\ = 5,26 \text{ MPa} \longrightarrow < 5,5 \text{ MPa} \quad \checkmark$$

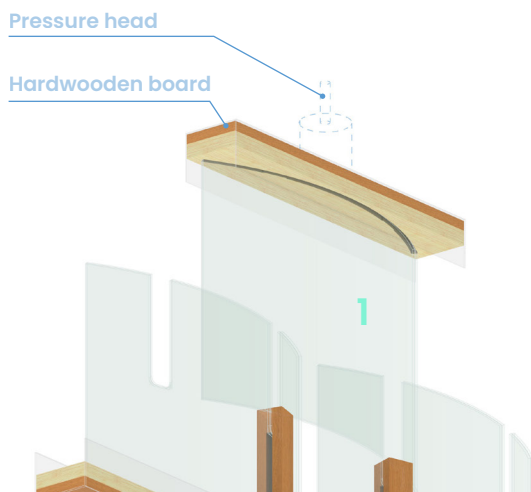


Figure 192: Upper edge of module 1 pressing against the upper scraped hardwooden board (own work, 2025)

$$\sigma = \frac{F}{A} \\ = \frac{22\,700 \text{ N}}{8\,640 \text{ mm}^2} \\ = 2,63 \text{ MPa} \longrightarrow < 5,5 \text{ MPa} \quad \checkmark$$

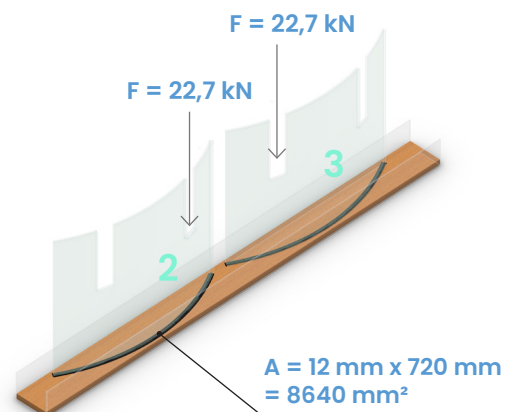


Figure 193: Bottom edges of module 2 and 3 pressing against the lower scraped hardwooden board (own work, 2025)

Scraped hardwooden board - bottom

The bottom edges of modules 2 and 3 each transfer a compressive force of 22.7 kN onto the lower hardwooden board, over a contact surface of 8640 mm² per module (Fig. 193). This results in a compressive surface stress calculated as:

Cantilevers

The lower steel profile cantilevers approximately half a meter on both sides (Fig. 194), carrying its own weight, a portion of the glass module, and the weight of the hardwood and spruce wooden board. A calculation of the maximum deflection has been carried out to ensure that the resulting deformation remains minimal, thereby guaranteeing even support for the glass modules throughout the test. Figure 195 shows the free body diagram of one cantilevered side with the applied loads used for the calculation.

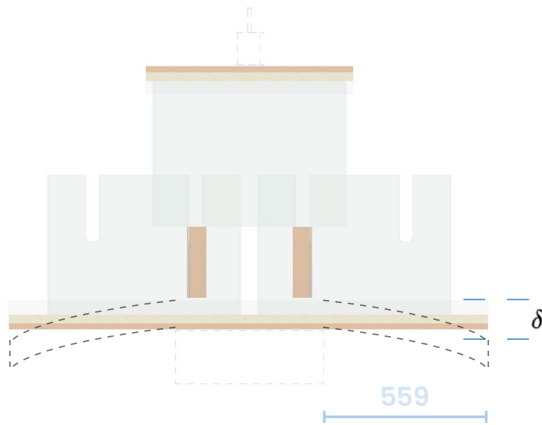


Figure 194: Front view of the test setup, illustrating how deflection may affect the cantilevered ends on both sides (own work, 2025).

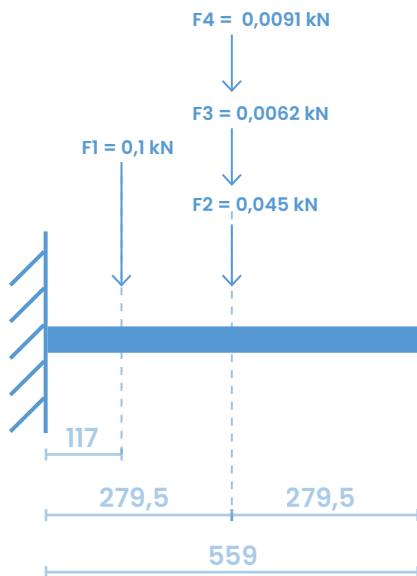


Figure 195: Free body diagram of one cantilevered side (own work, 2025).

These ULS loads were calculated as follows:

F_1 = self-weight of glass panel

$$\rho = 2500 \frac{\text{kg}}{\text{m}^3}$$

$$g = 10 \frac{\text{m}}{\text{s}^2} \Rightarrow \gamma = \rho \cdot g = 25000 \frac{\text{N}}{\text{m}^3}$$

$$V = 0.012 \text{ m} \times 0.5 \text{ m} \times 0.72 \text{ m} = 0.00432 \text{ m}^3$$

$$F_1 = \gamma \cdot V = 25000 \frac{\text{N}}{\text{m}^3} \times 0.00432 \text{ m}^3 = 108 \text{ N} = 0.1 \text{ kN}$$

F_2 = self-weight of steel profile

$$\rho = 7840 \frac{\text{kg}}{\text{m}^3}$$

$$g = 10 \frac{\text{m}}{\text{s}^2} \Rightarrow \gamma = \rho \cdot g = 78400 \frac{\text{N}}{\text{m}^3}$$

$$V = 9.6 \times 10^{-4} \text{ m}^2 \times 0.6 \text{ m} = 5.76 \times 10^{-4} \text{ m}^3$$

$$F_2 = \gamma \cdot V = 78400 \frac{\text{N}}{\text{m}^3} \times 5.76 \times 10^{-4} \text{ m}^3 = 45.18 \text{ N} \approx 45 \text{ N} = 0.045 \text{ kN}$$

F_3 = self-weight of hard wooden board

$$\rho = 430 \frac{\text{kg}}{\text{m}^3} \quad (\text{mean value from Table 7 in the appendix})$$

$$g = 10 \frac{\text{m}}{\text{s}^2} \Rightarrow \gamma = \rho \cdot g = 4300 \frac{\text{N}}{\text{m}^3}$$

$$V = 0.6 \text{ m} \times 0.12 \text{ m} \times 0.02 \text{ m} = 0.00144 \text{ m}^3$$

$$F_3 = \gamma \cdot V = 4300 \frac{\text{N}}{\text{m}^3} \times 0.00144 \text{ m}^3 = 6.192 \text{ N} \approx 0.0062 \text{ kN}$$

F_4 = self-weight of spruce wooden board

$$\rho = 420 \frac{\text{kg}}{\text{m}^3} \quad (\text{value from Table 8 in the appendix})$$

$$g = 10 \frac{\text{m}}{\text{s}^2} \Rightarrow \gamma = \rho \cdot g = 4200 \frac{\text{N}}{\text{m}^3}$$

$$V = 0.12 \text{ m} \times 0.6 \text{ m} \times 0.03 \text{ m} = 0.00216 \text{ m}^3$$

$$F_4 = \gamma \cdot V = 4200 \frac{\text{N}}{\text{m}^3} \times 0.00216 \text{ m}^3 = 9.072 \text{ N} \approx 0.0091 \text{ kN}$$

Next, the Moment of Inertia of the steel U-profile (Fig. 196) is calculated as:

$$\begin{aligned} I_y &= 2 \cdot \left(\frac{t_f \cdot h^3}{12} + A_f \cdot d^2 \right) + \frac{b \cdot t_b^3}{12} \\ &= 2 \cdot \left(\frac{3 \cdot 100^3}{12} + (3 \cdot 100) \cdot (58.5)^2 \right) + \frac{120 \cdot 3^3}{12} \\ &= 2 \, 553 \, 620 \text{ mm}^4 \end{aligned}$$

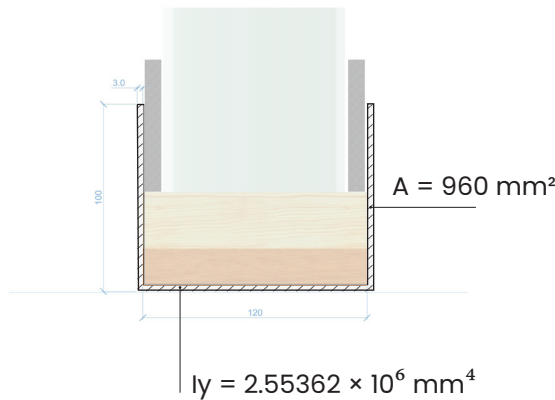


Figure 196: Side view of the steel U-profile, showing the dimensions, cross-sectional area (A), and moment of inertia (I_y) (own work, 2025).

The deflection caused by forces F_1 and $F_2 + F_3 + F_4$ was calculated separately and then summed to determine the total maximum deflection:

Deflection resulting from F_1 (self-weight glass panel)

$$\begin{aligned} \text{Deflection } (\delta) &= \frac{1}{3} \cdot \frac{F \cdot L^3}{E \cdot I} \\ \delta &= \frac{1}{3} \cdot \frac{100 \text{ N} \cdot (559 \text{ mm})^3}{210 \cdot 10^3 \text{ MPa} \cdot 2\,553\,620 \text{ mm}^4} \\ &= 0.0109 \text{ mm} \end{aligned}$$

Deflection resulting from self-weight of the steel, hard wood and spruce wood

$$\begin{aligned} F_{\text{total}} &= F_2 + F_3 + F_4 \\ &= 45 \text{ N} + 6.2 \text{ N} + 9.1 \text{ N} \\ &= 60.3 \text{ N} \\ \delta &= \frac{1}{3} \cdot \frac{60.3 \text{ N} \cdot (559 \text{ mm})^3}{210 \cdot 10^3 \text{ MPa} \cdot 2\,553\,620 \text{ mm}^4} \\ &= 0.00655 \text{ mm} \end{aligned}$$

Total deflection

$$\delta_{\text{total}} = 0.0109 \text{ mm} + 0.00655 \text{ mm} = 0.01745 \text{ mm}$$

The calculated total deflection of 0.01745 mm is so small that it will not influence the test results. This shows that the steel U-profile is stiff enough to provide proper support for the glass modules.

7.3.3. Test preparations

This section outlines the test preparations step by step:

1 Cutting the hardwood boards to size

The scraped hardwood boards were cut precisely to fit tightly between the steel U-profiles (Fig. 197). This was achieved by trimming the boards to match the exact height of the profile, after which they were gently hammered into place (Fig. 198). In particular, for the U-profile attached to the top module - module 1 - clamping the wood tightly was essential to prevent it from falling out.



Figure 197: Cutting the hardwood board to size (own work, 2025).



Figure 198: Hammering the hardwood board into the U-profile (own work, 2025).



Figure 199: Hardwood clamped into the upper and lower U-profiles (own work, 2025).

2 Cutting the spruce wood to size

Spruce wood was chosen to clamp the modules. Since its only function is to hold the modules in place, hardwood was not required. The pieces were not cut to fit exactly; instead, a small gap was intentionally left on one side to allow a wedge to be hammered in later, ensuring a tight final clamp (Fig. 200).



Figure 200: Spruce board cut to size, leaving space for a wedge (own work, 2025)

3 Marking out the modules on the spruce wood

Next, the module outlines are marked onto the spruce wood (Fig. 201), after which the wood is cut into two separate pieces (Fig. 202).



Figure 201: Marking the outlines of modules 1 and 2 on the lower spruce wooden board (own work, 2025)



Figure 202: Spruce board cut into two parts to enclose the modules (own work, 2025)

4 Creation of wooden inserts

Finally, some leftover hardwood was cut, milled (Fig. 203), and sanded (Fig. 204) to fit precisely around the slots. It is important that the pieces clamp tightly and that both wooden infills are of equal height, ensuring that module 1 stands evenly on top of modules 2 and 3. This promotes uniform force transfer across each slot. The alignment was verified using a spirit level. Figure 205 shows the final result of the wooden infills.



Figure 203: Milling the slots into the wooden insert (own work, 2025)

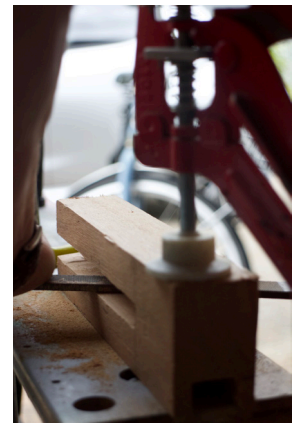


Figure 204: Sanding for a soft surface and tight fit with the glass (own work, 2025)

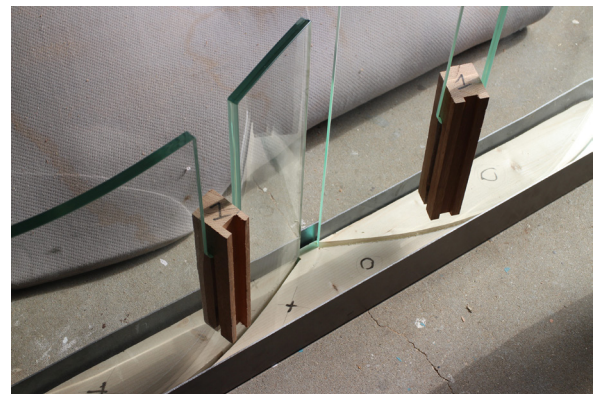


Figure 205: Final result of the hardwood infills (own work, 2025)

5 Inserting the wedge and clamping rubbers

Clamping rubbers were placed between the curvature of the glass and the steel U-profile (Fig. 206). Next, a wedge made from MDF was hammered in between the steel profile and the spruce wood (Fig. 207). This ensures that the wood clamps tightly around the module, slightly compressing the clamping rubbers. As a result, additional clamping force is created and there is no risk of the glass touching the steel during the test.



Figure 206: Clamping rubbers positioned between the glass and the steel U-profile (own work, 2025)

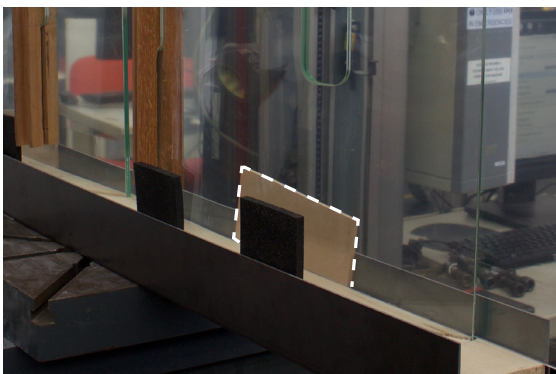


Figure 207: Wedge inserted between the spruce wood and the steel profile (own work, 2025)

The same procedure was followed to clamp module 1 into the shorter steel profile.

6 Clamping module 1 into the slots of module 2 and 3

Next, module 1 was inserted into the slots of modules 2 and 3. To ensure stability during testing and to avoid direct glass-to-glass contact, any remaining space in the slots needed to be filled. This was done by first applying a thick layer of silicone tape along the slot edge (Fig. 208), then carefully sliding the glass module into place, and finally securing it with a rubber insert (Fig. 209).



Figure 208: Application of clear silicone tape along the slot edge to prevent glass-to-glass contact (own work, 2025)



Figure 209: Rubber insert placed in the slot for clamping (own work, 2025)

The images on the following page provide an overview of the final test setup in the laboratory environment. For additional safety, plastic panels were installed on both sides of the structure.

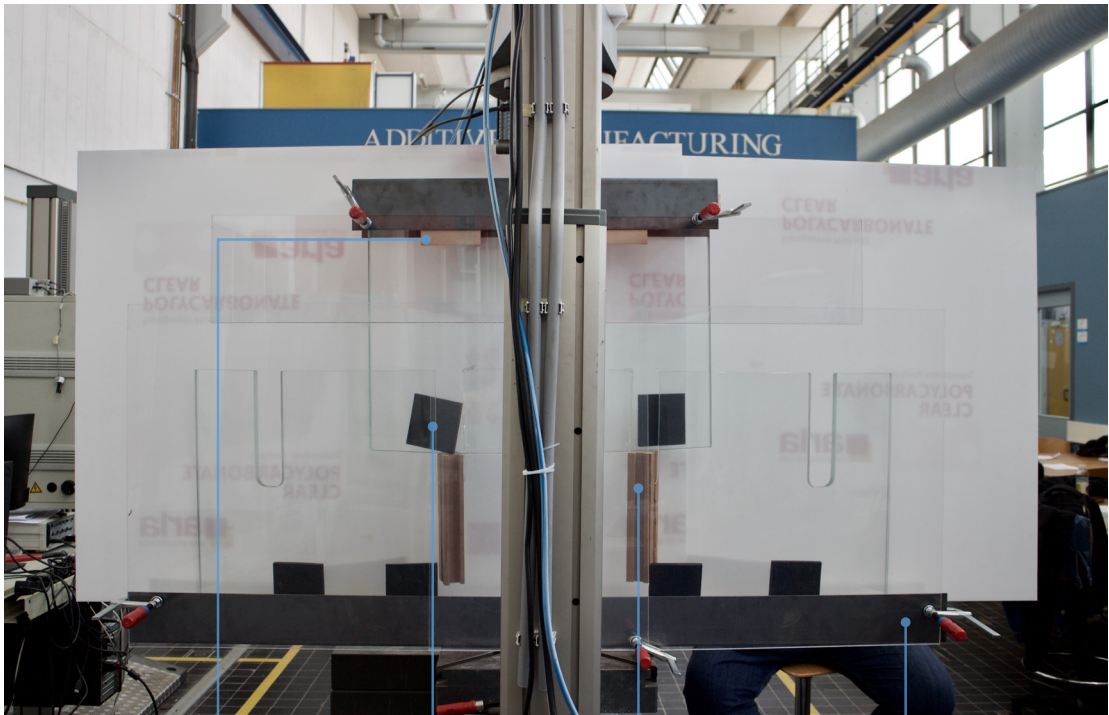
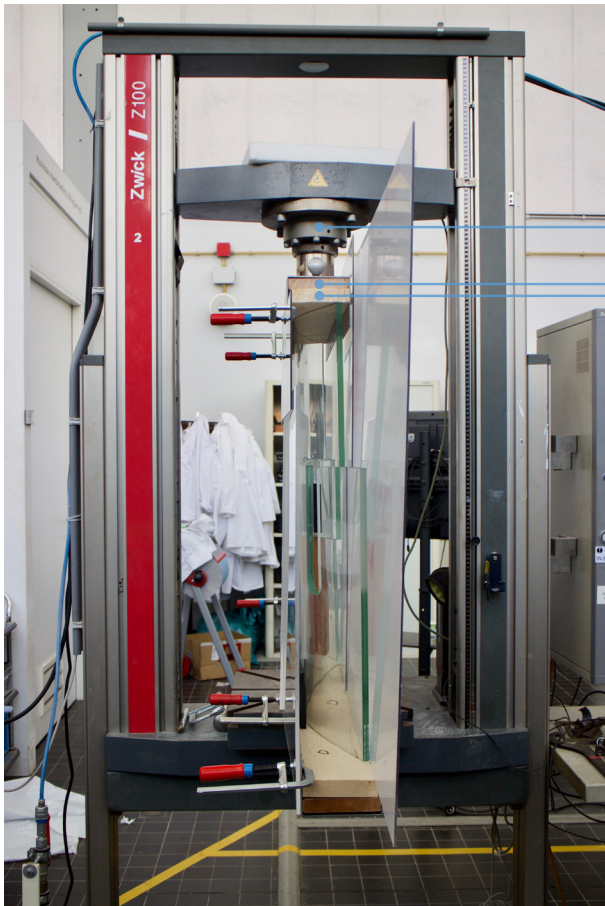


Figure 210: Front view of the laboratory test setup (own work, 2025)

MDF wedge Clamping rubber in the slot Hardwood infill Steel U-profile



Pressure head
Scraped hardwooden board Spruce wooden board

Figure 211: Side view of the laboratory test setup (own work, 2025)

7.3.4 Test execution and results

The test was carried out by applying loads incrementally, with a 5-minute pause between each step. This section outlines the load steps and their corresponding results.

The test began with a load below the design value of 3 kN per slot. The initial step involved applying 1 kN in each slot, totaling 2 kN via the pressure head (Fig. 212).

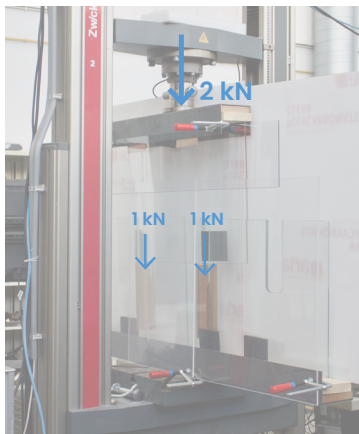


Figure 212: Application of the first load step – 1 kN per slot (own work, 2025)

Subsequently, the pressure applied by the pressure head was increased by 2 kN every five minutes until the design load of 3 kN per slot was reached (equivalent to a total applied force of 6 kN by the pressure head), see Figure 213.

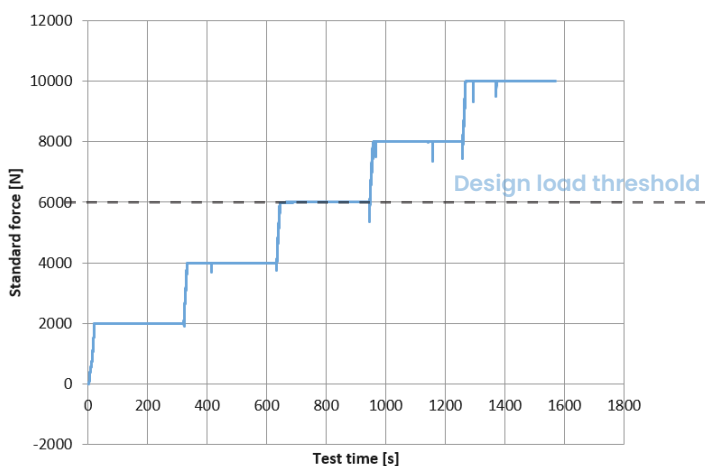


Figure 213: Graph showing the load increments of 2 kN applied every 5 minutes during the test (own work, 2025)

After the design load threshold was reached, the applied force from the pressure head was further increased in 2 kN increments every 5 minutes to explore the modules' capacity under higher loads.

Figure 214 shows the displacement plotted against time. With each increase in applied force, the displacement grows by approximately 2 mm, primarily due to the slight compression of the wood. During this phase, cracking sounds from the wood could also be heard.

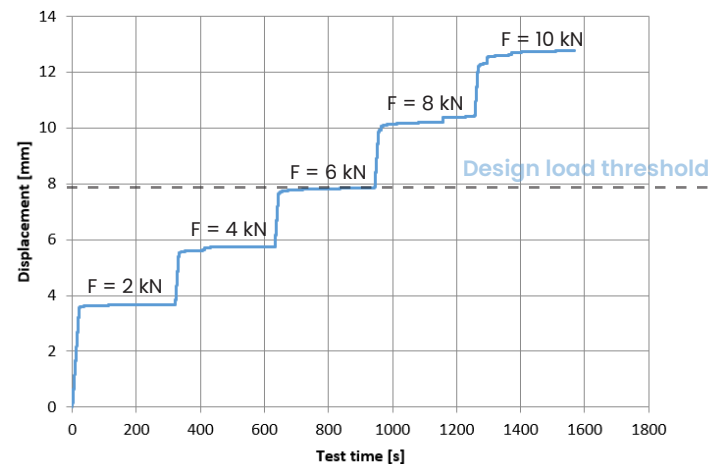


Figure 214: Graph showing the displacement measured over time during incremental loading steps (own work, 2025)

During the first three intervals, when the pressure head presses with 2 kN, 4 kN and 6 kN, the displacement is quite constant during the 5 minutes. From 8 kN, it was slightly visible that the spruce wooden board started to move a bit at the top (Fig. 215) and that the hardwood in the slots showed slight local failure (Fig. 216).



Figure 215: Spruce wood started moving around 8 kN (own work, 2025)



Figure 216: Small local failure in the hardwood slot around 8 kN (own work, 2025)

Figure 214 shows that during the 5-minute holds at 8 kN and 10 kN, deflection continued to increase rather than remaining steady. This reflects both slight movement of the spruce elements – causing minor buckling of the structure – and the onset of hardwood failure. The glass slots sustained the load up to 10 kN, at which point the test automatically stopped.

To see how much additional load the glass slots could handle, the test was resumed at 10 kN and increased in 2.5 kN increments (Figure 217). As Figure 218 illustrates, deflection grew almost linearly during each 5-minute hold.

The test was terminated at 1.5 tonnes, demonstrating that the modules tolerate more than twice the design strength – in fact, about 2.5 times the specified load.

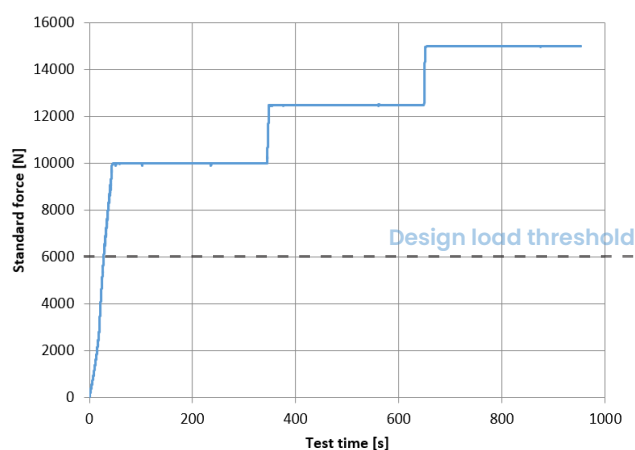


Figure 217: Graph showing load steps of 2.5 kN, each 5 minutes (own work, 2025)

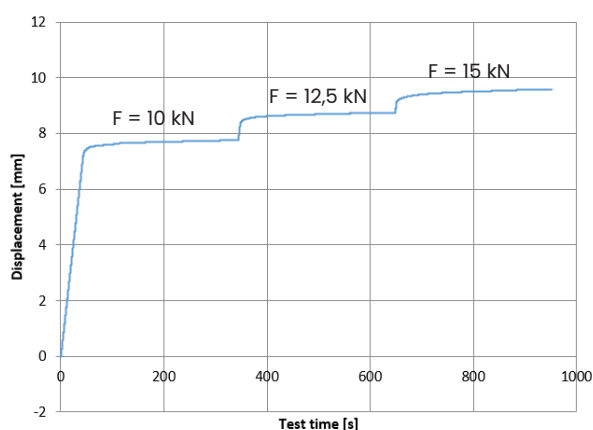


Figure 218: Graph showing displacement values during testing time from 10 to 15 kN (own work, 2025)

The test was carried out only once, as it was clear that the glass could withstand the applied loads while the wood began to fail first. A second test would very likely yield the same result.

The test confirmed that a design load of 3 kN per slot can be easily withstood, corresponding to the loading scenario of an arch with a maximum span of 8 meters and a minimum rise of 2.5 meters.

Since the tested modules were eventually 32 cm shorter than the needed length of 1 meter to integrate four slots for adaptability, the design strength will increase somewhat due to the increasing self-weight. Repeating the calculations from Chapter 7.2.1 results in a design load per slot of 4.4 kN. This shows that even somewhat longer modules of 1 meter should be able to withstand the reaction forces in the slots.

Conclusion

The results indicate that modules made from 2×6 mm fully toughened laminated glass have strong potential for use in compression-based structures with spans up to 8 meters, as the laboratory testing confirmed that a single slot could withstand at least 7.5 kN per slot, 2.5 times as much as the tested design load of 3 kN. It can be also concluded that longer modules of approximately 1 meter – proposed for increased adaptability (Chapter 7.1.2) – are structurally feasible.

It is expected that it is also structurally viable to use thinner modules of 2×5 mm; Ansys simulations showed that reducing the glass thickness from 2×6 mm to 2×5 mm increases the stress concentration from 6.6 MPa to 8.3 MPa – a modest increase of ≈ 2 MPa. Since the lab test showed that for the design load, the glass remained far from failure, it is likely that the actual stress at that load was still well below the safe threshold of 60 MPa, indicating that the test shows similarities with the Ansys results. When made from fully toughened glass, 2×5 mm laminated modules therefore appear to remain within acceptable safety margins.

To improve post-breakage performance and overall safety, the use of heat-strengthened glass may be preferable. Assuming a tensile strength of 40 MPa (Fig. 67 from Chapter 5 – Design Guidelines) and a safety threshold of 20 MPa, a design load of maximum 4,4 kN per slot would result in an estimated stress concentration of 12 MPa based on the Ansys analysis. This still remains below the safety threshold.

However, due to potential deviations between simulations and real-world behavior, only the use of 2×6 mm fully toughened laminated modules can be conclusively verified based on this research. Additional testing is recommended to confirm the performance of heat-strengthened glass modules. If further reduction in structural weight is desired by switching to 2×5 mm laminated modules, additional testing is also required to confirm that a thinner module, especially in heat-strengthened form, can reliably handle the design loads. When fully toughened glass is used, it is also necessary to verify that additional loads, when loads are redistributed in case of failure of a module, can be withstood.

8. Conclusion

Answers to the research questions

1. What types of adaptable structural systems exist?

This research question led to the conclusion that both modular and transformable structures offer the potential for expansion along the x and y axes while maintaining an open floor plan, but they achieve this in different ways. The modular approach was selected due to its greater potential for a simplified design comprising standardized components, resulting in simplified production and assembly, and the preservation of visual transparency by avoiding the complex connection mechanisms often required in transformable structures.

2. Which external and internal geometries are suited for glass as a structural material with the aim of minimizing structural mass?

This research question concluded that, to design a lightweight structural glass system, the overall geometry should primarily transfer loads through compression, such as in an arch form. This is due to glass's relatively low characteristic tensile strength, making it more efficient under compressive forces. This information was used to create the generative algorithm that primarily generates curved design options

To support the transfer of external forces in compression, the internal geometry should avoid moment-resisting connections. For example, using pinned joints helps minimize bending moments and ensures that forces are transferred more effectively through axial compression. Additionally, it is important to design connections where a softer material is in direct contact with the glass. This prevents local damage and accommodates stress concentrations caused by production or assembly tolerances.

3. What key design guidelines should be considered when working with structural glass?

It became clear that designing with structural float glass involves several safety considerations, such as glass lamination and thermal tempering. Laminated float glass is typically available in standard thicknesses. It also became evident that float glass can be bent, which opens up opportunities to increase structural stiffness or explore more complex design geometries.

In addition, Near-Infrared (NIR) shielding can be applied to protect the structure from solar heat gain, which adds a layer of functional performance to the glass elements. This standard knowledge was applied during the concept development and technical elaboration phases.

4. What potential design concepts can be developed for an adaptable float-glass structure?

Concept 5 was selected due to its combination of high adaptability enabled by multiple interlocking angles, its high transparency, simple and manual assembly and disassembly, structural stability provided by V-shaped modules, and minimal variation in building components.

Other concepts were less suitable because they appeared visually heavier, required more complex connections, or were less adaptable for modular expansion due to – for instance – the need for multiple unique components.

5. Which design parameters influence the adaptability of the system?

It became clear that the sequence of different module heights and the interlocking angles between modules have a significant influence on the overall geometry and the resulting span of the system. This knowledge was subsequently used to create a generative algorithm capable of adapting the sequence of module heights and the interlocking angles between modules, driven by relevant parameters, and subsequently generate multiple design solutions for a specific span requirement die optimaal presteren op constructief gewicht en assembly eenvoud.

It became clear that the sequence of different module heights and the interlocking angles between modules have a significant influence on the overall geometry and the resulting span of the system. This knowledge was subsequently used to create a generative algorithm capable of adapting the sequence of module heights and the interlocking angles between modules, driven by relevant parameters. In this way, the algorithm can generate multiple design solutions with minimal structural weight and optimal assembly simplicity, for a specific span requirement.

6. Can the critical location in the structure withstand the expected primary load, as verified by numerical simulation and experimental testing?

Numerical simulations identify the inner corners of the slots as the most critical locations in the structure. However, stress concentrations under compressive loading remain well below the allowable stress limit, indicating that each slot can safely carry a design load of approximately 3 kN.

This was confirmed through physical testing, assuming a tested net module length of 684 mm. It was verified that the design load per slot increases to approximately 4.4 kN when the module length reaches 1 meter – still well below the maximum tested reaction force of 7.5 kN per slot. It can therefore be concluded that a 1-meter-long module with a height of 0.5 meters, made from 2×6 mm fully toughened glass, is structurally feasible when used in a compression-driven global form.

Final conclusion

This research set out to develop a reusable float glass system that is spatially **adaptable in both the x and y-direction while maintaining an open floor plan**, and can be **manually assembled and disassembled by a small team** – promoting reusability. It offers an initial, potentially applicable design solution that helps extend the functional lifespan of structural glass, contributing to the reduction of waste, conservation of resources, and avoidance of unnecessary energy use in the building industry.

This ambition led to the central research question:

“Which structural elements and connections enable the design of a structurally feasible and spatially adaptable float glass system that can be manually assembled and disassembled by a small team for reconfiguration at different locations, ensuring its reusability?”

To further elaborate on manual assembly and disassembly, the components were required to be **lightweight** and **easy to assemble and disassemble without the need for complex instructions**. Further design requirements included:

- Maintaining the visual transparency typical for all-glass structures
- Minimizing the number of different components to simplify manufacturing and construction, and to optimize the reuse potential of the structural components.
- Providing basic resistance to rain and overheating.

The final design is a structurally feasible modular float glass system, proven to span up to 8 meters in a compression-oriented global shape. The system consists of only two standardized components with integrated connections. This simplified design facilitates ease of production and assembly, and enables optimal reuse of structural components at new sites

Since the modules are made of curved glass and have integrated slots at the top, they can interlock without the need for additional connectors. The integration of the connection into the module itself, combined with the position of the slots – which keeps the module edges clear – enhances the visual transparency and lightness of the structure. In addition, the interlocking mechanism enables straightforward assembly and disassembly, as the modules only need to be slid together or apart.

In the final design, four slots are integrated into a single module with a net length of approximately one meter and a bending radius of 650 mm. This curvature maximizes the range of possible interlocking angles while keeping the module length minimal for ease of manual handling. Each module includes two positive and two negative interlocking angles. Two standardized heights have been chosen to allow adaptability in the y-direction, while adaptability in the x-direction can be achieved by duplicating larger modular units.

The combination of two negative angles (-2° and -10°) and two positive angles (2° and 10°) enables the formation of both convex and concave shapes, allowing precise control over the global geometry and, consequently, the span. The integration of these angles, in turn, supports the generation of curved external geometries that primarily transfer forces through compression, promoting lightweight construction.

The modules vary in height. One has a maximum height of 500 mm, allowing for easy manual handling in combination with a length of one meter, while a height of 300 mm creates a clear contrast with the 500 mm module, stimulating variation in span outcomes.

Clear acrylic inserts are placed within the slots to slightly clamp the inserted module and prevent glass-to-glass contact. The material also helps to avoid stress concentrations caused by production or assembly tolerances. It is proposed to keep these inserts transparent in order to maintain the overall transparency of the system. Due to the slight clamping, the joints behave more like pinned connections than rigid ones, promoting force transfer through compression and allowing the modules to remain relatively thin.

To promote lightweight construction, ease of assembly, and spatial fit to a specific location, a parametric tool with a multi-objective optimizer enables the generation of arch-shaped design solutions that deviate minimally from the desired target span. Various arch shapes can be selected, ranging in how much they deviate from a full arch. Despite these variations, the design solutions are optimized for minimal deflection – and therefore indirectly for structural weight – as well as for ease of assembly.

This allows for selecting a design variant suited to either an even or uneven ground surface. In cases where the structure needs to connect to a vertical element, a half arch can be a design solution. In addition, design solutions that are less optimal in terms of deflection can also be selected, often resulting in freer, more expressive forms. This serves as an open exploration of the system's potential and acts as a visual trigger to engage a broader audience in discussions about the future of the built environment.

Numerical simulations showed that stress concentrations at the slots remained low and were not a limiting factor for structural strength. A full-scale lab test confirmed that a module could withstand at least 7.5 kN per slot – 2.5 times the design load of 3 kN. This test has demonstrated that the outcomes generated by the multi-objective optimizer are also structurally feasible. These outcomes show near-zero deflection and rely primarily on load transfer through compression.

Comparing the test results with the Ansys analysis results, 2×5 mm laminated modules appear to remain within acceptable safety margins, as well as changing the glass type to heat-strengthened. However, additional testing is required to verify this.

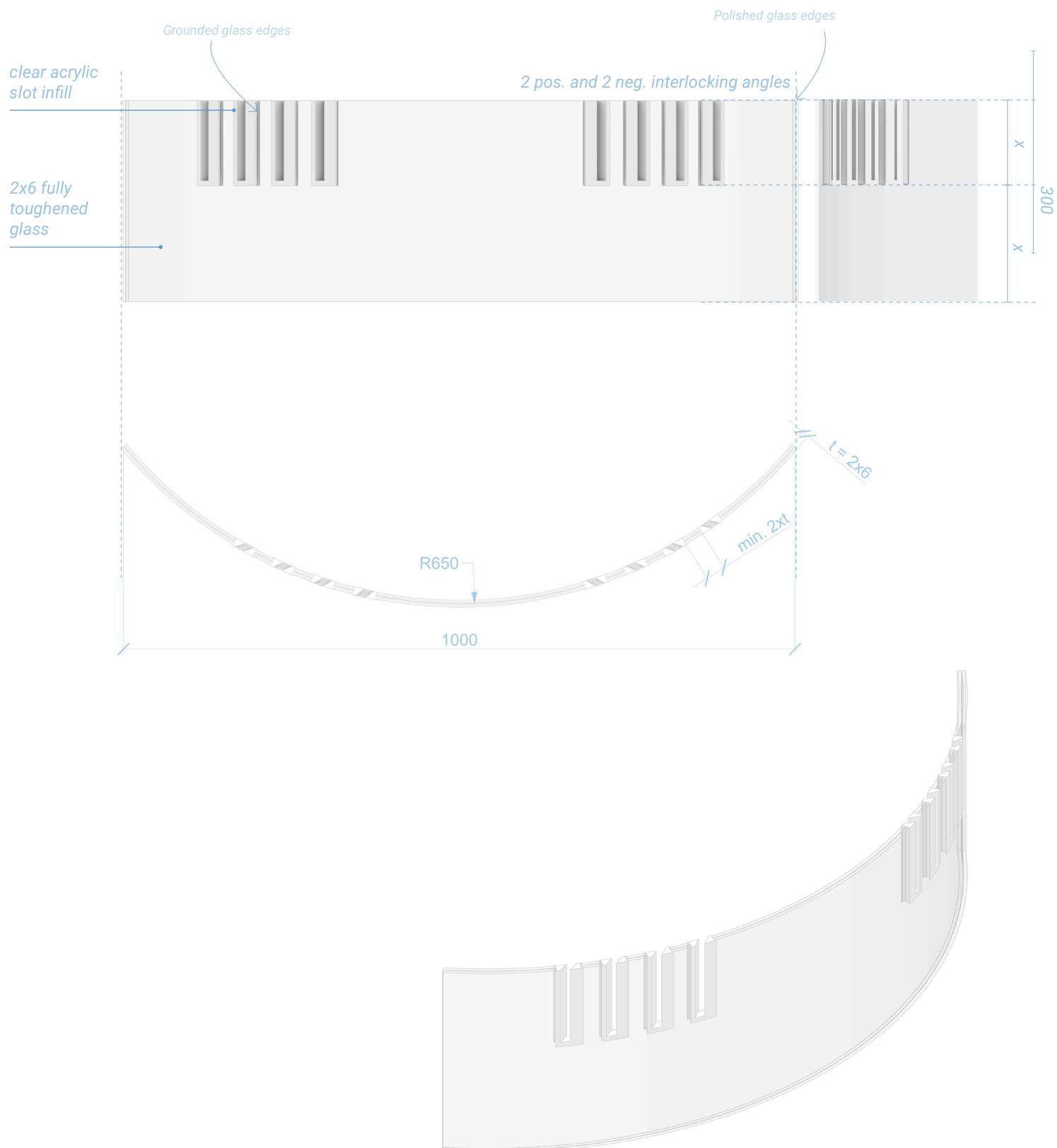
On top of that, if the practical application of the free forms generated by the algorithm is desired, additional testing on bending resistance and analysis of potential arising stress concentrations on the side surfaces of the module slots is necessary.

A challenge that emerged was achieving consistent rain protection. Certain height sequences can create gaps in the structure due to the shorter module's limited interlocking depth. Therefore, watertightness varies by configuration.

As for solar protection, detailed implementation was not developed further. It was assumed, based on theory, that NIR-blocking elements can be integrated either in the lamination layer or as a surface coating.

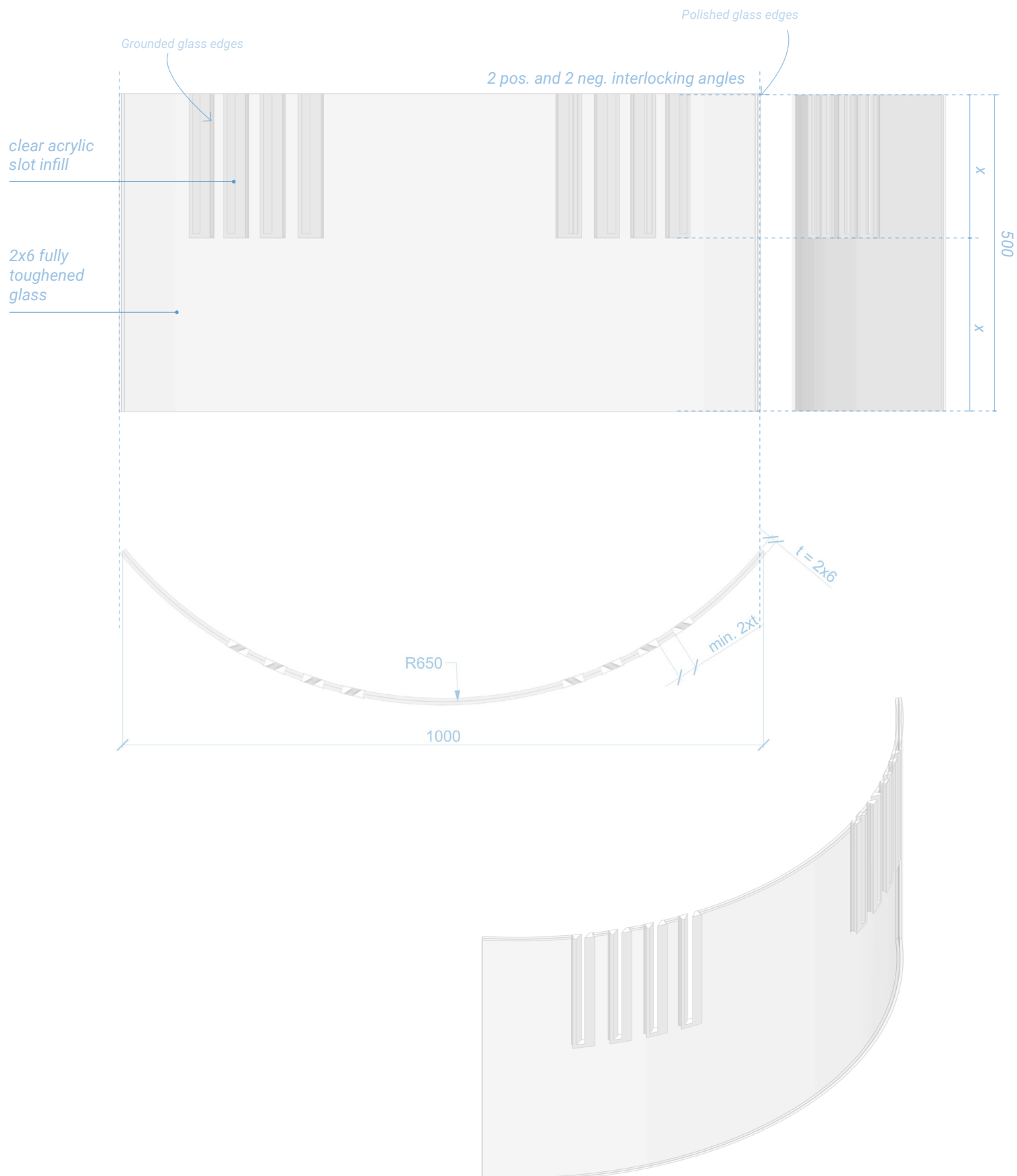
Final drawings of the modules and connections

Module 1 - height = 300



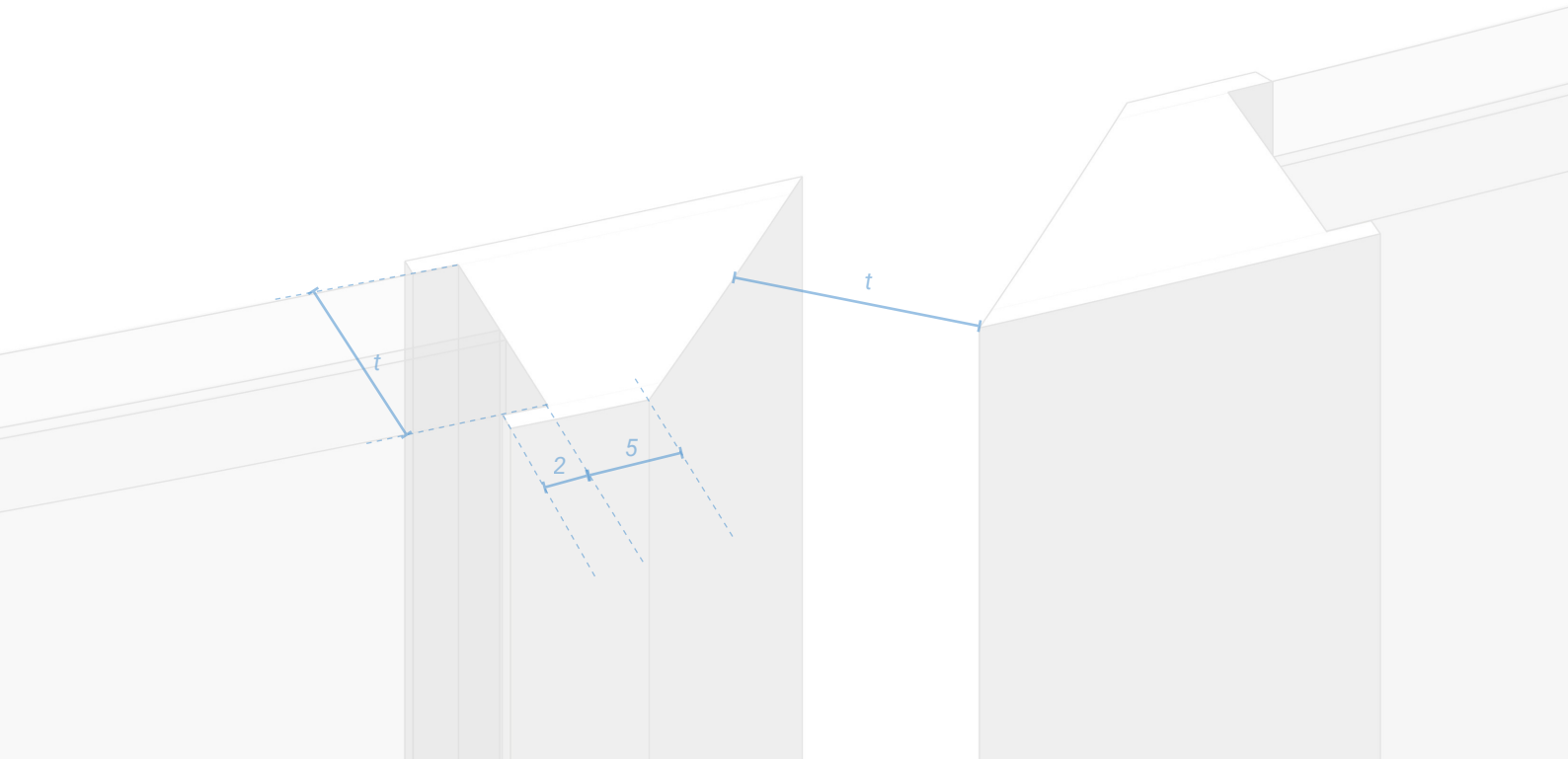
Final drawings of the modules and connections

Module 1 - height = 500



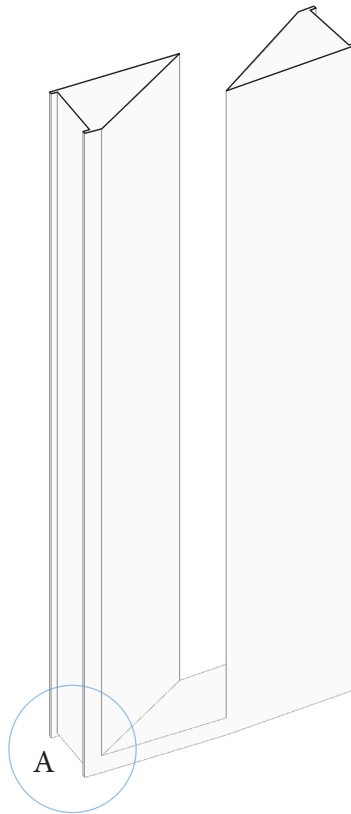
Final drawings of the modules and connections

Slot infill from clear acrylic

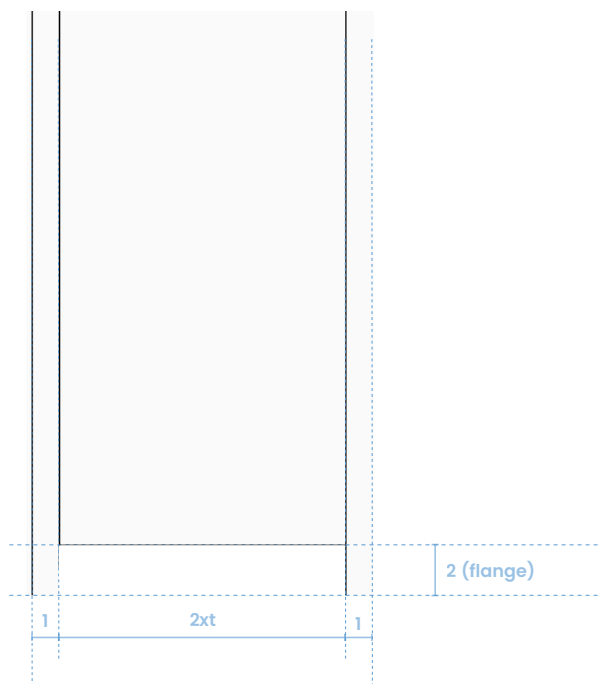


Final drawings of the modules and connections

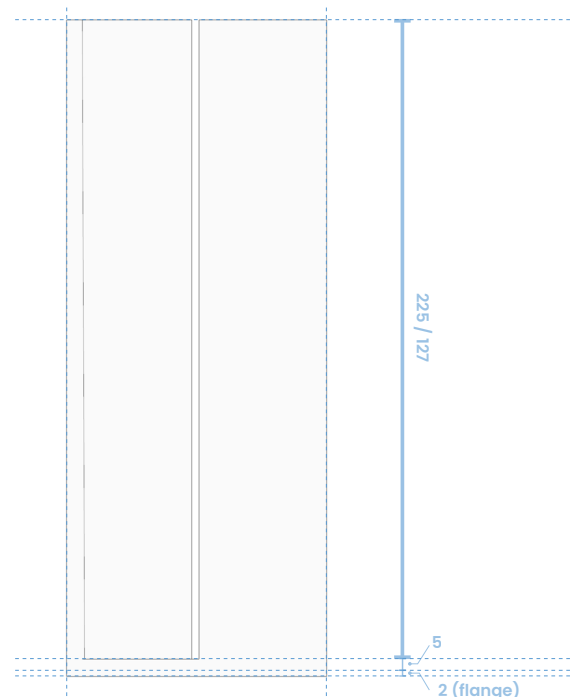
Slot infill from clear acrylic



A SIDE VIEW, BOTTOM



FRONT VIEW



9. Discussion and further research

Although the main objectives of the study were achieved, there are areas that could serve for further research.

A next step is to further refine the slot geometry within the modules. Depending on the selected interlocking angle, each slot is inclined at a corresponding angle. It should be investigated how these various slot angles can be best distributed along the module's length, what the minimum spacing between them should be, and how the presence of multiple slots affects the structural performance of the glass. Besides, the introduction of multiple slots may increase the risk of glass failure.

In addition, the position of a slot along the length of the module has a direct impact on the resulting span. For instance, slots placed closer to the edge of the module cause interlocking to occur further inward, as illustrated in Figure 127 of the report. In this study, a simplified approach was taken, assuming that each interlocking angle occurs at the same position on the module. However, further development of the design should consider that the resulting spans are influenced not only by the interlocking angles themselves, but also by the specific placement of the slots along the module length.

There are several focus areas related to structural performance that can be explored in future research:

- The influence of excessive differences in interlocking angles between adjacent modules deserves attention, especially if more freeform shapes – beyond those generated by the optimizer – are to be constructed. Such variations may introduce kinks in the structure, potentially reducing overall structural performance.
- A risk analysis should be carried out to identify potential hazards and determine appropriate measures.
- Assessing overall structural stability and the effects of asymmetric loading conditions.

- It is essential to test whether the acrylic infill is strong enough to withstand the design load, while also allowing for slight deformation under load to mitigate excessive internal stresses caused by manufacturing or installation tolerances. Additionally, the infill needs to be further refined in detail to accurately accommodate the desired interlocking angles.

- Testing the structural performance of the modules in freeform configurations, where force transfer through compression is not optimal. This requires evaluating the bending resistance of the modules.

- Development of supports for the first and last rows of modules. Adjustable supports may be required, as the algorithm can generate design solutions that slightly deviate from the predefined spatial constraints.

- Since the maximum spans achievable by the structure are relatively limited, future research could focus on exploring larger spans.

- Another interesting direction for further research is the structural validation of freeform applications. For example, it would be valuable to investigate whether the system can also be used by rotating a generated arch onto its side, allowing it to function as a transparent partition wall (see page 85). Additionally, combining multiple curves to create new structural or spatial configurations presents further potential for architectural expression and functional diversity (see page 87).

Concluding, as already mentioned, resistance to rain is a concern. If a lower module has to interlock into a higher module, the slot of the larger module should not be too deep. However, a reasonable depth is desirable to avoid large openings in the structure.

References

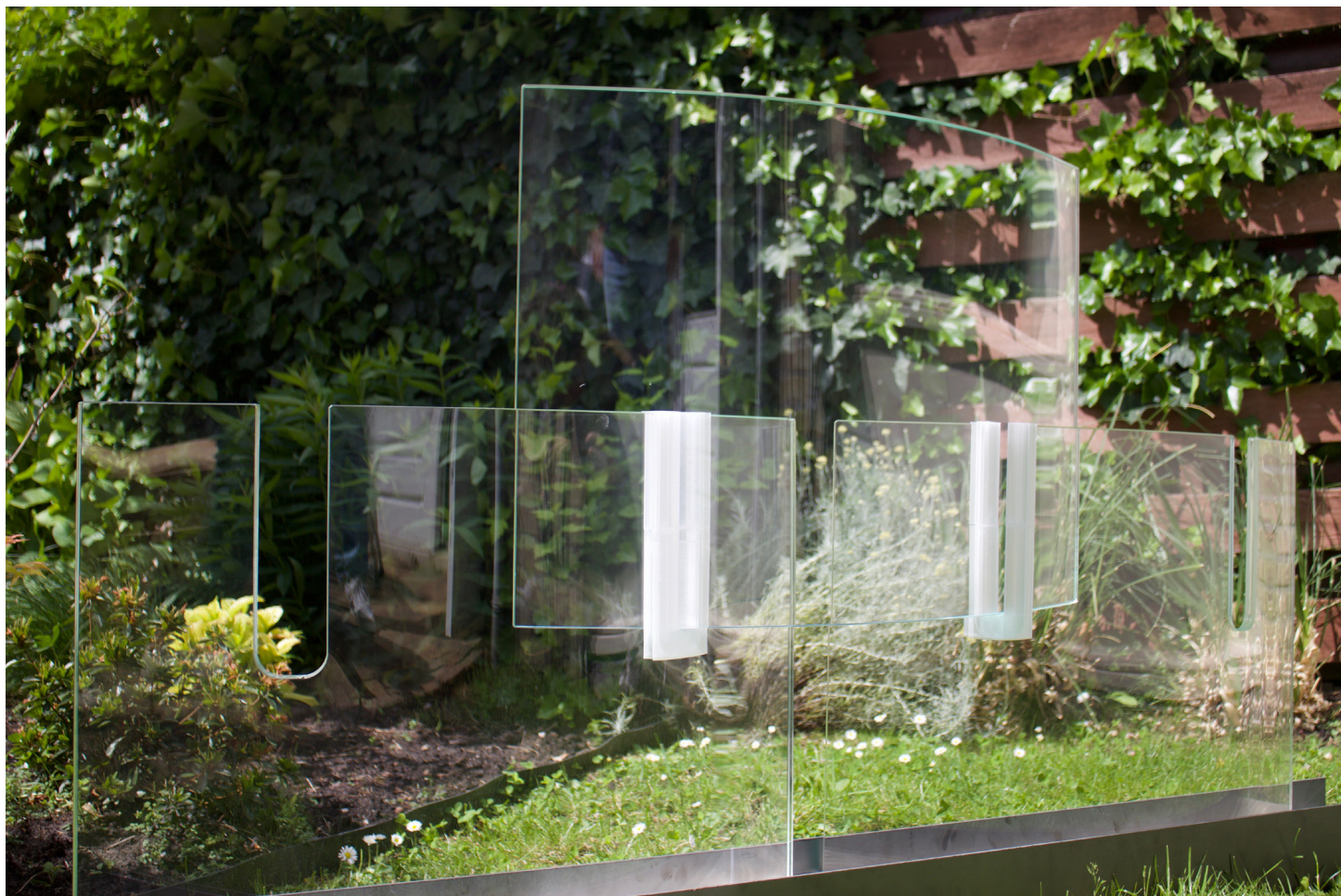
- Barou, L., Oikonomopoulou, F., Bristogianni, T., Veer, F., & Nijse, R. (2018). Structural glass: A new remedial tool for the consolidation of historic structures. *Heron*, 63(1–2), 159–197.
- Berardi, U., & Khaled, K. (2024). Architectural glass solar and thermal control coating technologies. *Encyclopedia of Sustainable Technologies*, 2nd ed.; Abraham, MA, Ed, 361–386.
- Brancart, S., Paduart, A., Vergauwen, A., Vandervaeren, C., De Laet, L., & De Temmerman, N. (2017). Transformable structures: Materialising design for change. *International Journal of Design & Nature and Ecodynamics*, 12(3), 357–366.
- Bühlmeier, T., & Hilcken, J. (2023). Structural glass assembly with a novel mortise and tenon joint.
- Dalalbashi, A., Pinto, J., Reis, C., Pimenta, F., Ferreira, N. O., & Pereira, N. B. (2024). A proposal for an alternative structural modular solution. *Journal of Building Engineering*, 85, 108709.
- Datsiou, K. (2017). *Design and Performance of Cold Bent Glass*. (PhD). University of Cambridge, Cambridge.
- Elstner, M., Contino, A., & Zaccaria, M. (2024, June). Recycle Glass: A Contribution to the Circularity of Flat Glass. In *Challenging Glass Conference Proceedings* (Vol. 9).
- European Committee for Standardization. (2016). EN 338:2016 – Structural timber – Strength classes. Brussels: CEN.
- Feldmann, M., Laurs, M., Belis, J., Buljan, N., Criaud, A., Dupont, E., ... & Sikynova, A. (2023). The new CEN/TS 19100: Design of glass structures. *Glass Structures & Engineering*, 8(3), 317–337.
- Ganapathi, H., & Phukan, M. (2020). Environmental hazards of limestone mining and adaptive practices for environment management plan. *Environmental Processes and Management: Tools and Practices*, 121–134.
- Giese, F., Wolf, S., Hindelang, L., & Krauter, A. (2024). *Glass in Architecture from the Pre-to the Post-industrial Era: Production, Use and Conservation* (p. 335). De Gruyter.
- Haldimann, M., Luible, A., & Overend, M. (2008). *Structural Use of Glass*. Zurich, Switzerland: IABSE-AIPC-IVBH.
- Yuan, F., & Huang, L. (2014). Brittle to Ductile Transition in Densified Silica Glass. *Scientific Reports*, 4(1), 1–8. <https://doi.org/10.1038/srep05035>
- Hussein, H. E., Agkathidis, A., & Kronenburg, R. (2021). Towards a Free-form Transformable Structure-A critical review for the attempts of developing reconfigurable structures that can deliver variable free-form geometries. *eCAADe proceedings*, 2, 381–390.
- Isaksson, T., Thelandersson, S., Crocetti, R., Johansson, M., Kliger, R., Lidelöw, H., Mårtensson, A., Norlin, B., & Pousette, A. (2022). *Design of timber structures. Volume 2: Rules and formulas according to Eurocode 5* (3rd ed.). Swedish Wood.
- Jóźwik, A. (2022). Application of Glass Structures in Architectural Shaping of All-Glass Pavilions, Extensions, and Links. *Buildings*, 12(8), 1254. <https://doi.org/10.3390/buildings12081254>.
- Krousti, A., Snijder, A., & Turrin, M. (2018). Kinematics of folded glass plate structures: Study of a deployable roof system. In *Challenging Glass 6: International Conference on the Architectural and Structural Application of Glass* (pp. 53–70). Delft University of Technology.

- Laccone, F. (2019). Reinforced and post-tensioned structural glass shells: Concept, morphogenesis and analysis.
- Louter, C. (2011). *Fragile yet Ductile*. (PhD). TU Delft, Delft.
- Lu, Y., Seyedahmadian, A., Chhaddeh, P. A., Cregan, M., Bolhassani, M., Schneider, J., ... & Akbarzadeh, M. (2022). Funicular glass bridge prototype: design optimization, fabrication, and assembly challenges. *Glass Structures & Engineering*, 7(2), 319–330.
- Matheou, M., Phocas, M. C., Christoforou, E. G., & Müller, A. (2023). New perspectives in architecture through transformable structures: A simulation study. *Frontiers in Built Environment*, 9, 1051337. <https://doi.org/10.3389/fbuil.2023.1051337>.
- Mesa, J., Maury, H., Arrieta, R., Bula, A., & Riba, C. (2015). Characterization of modular architecture principles towards reconfiguration: a first approach in its selection process. *The International Journal of Advanced Manufacturing Technology*, 80, 221–232.
- Mesnil, R., Baverel, O., Douthe, C., Caron, J. F., & Léger, B. (2017). Structural morphology and performance of plated structures with planar quadrilateral facets. *Journal of the International Association for Shell and Spatial Structures*, 58(1), 7–22.
- Mitsimponas, D., & Symeonidou, I. (2024). Identifying Trends and Typologies of Modular Constructions in Architecture. *Nexus Network Journal*, 26(1), 49–69.
- Naboni, R., & Marino, S. D. (2021). Wedged kerfing. Design and fabrication experiments in programmed wood bending. *Proceedings of the SIGraDi*.
- Platform CB'23 – Framework Circulair Bouwen: Raamwerk voor eenduidig taalgebruik en heldere kaders (version 1.0, juli 2019), p. 35.
- Phocas, M. C., & Matheou, M. (2021). Revisiting transformable structures in architecture. In *Proceedings of the 2nd International Conference on Architecture, Technology and Innovation* (pp. 24–09).
- Pour-Moghaddam, N. (2020). Glass Properties and Refinement Processes. On the Fracture Behaviour and the Fracture Pattern Morphology of Tempered Soda-Lime Glass, 7–15.
- Pournaghshband, A. (2016). *Form-finding of arch structures* (Doctoral dissertation, University of Warwick).
- Qdel. (n.d.). Saflex® Solar PVB interlayer. Qdel Laminating Supplies.
- Rammig, L. M. (2022). *Advancing Transparency: Connecting glass with heat – An experimental approach to the implementation of heat bonding into glass connection design for structural applications*. [Dissertation (TU Delft), Delft University of Technology].
- Rammig, L. (2022). The pursuit of transparency. In *Rethinking Building Skins* (pp. 89–115). Woodhead Publishing.
- Reshamvala, M., Rauh, K., Kießlich, P., Ayvaz, I., Länge, J., Elstner, M., ... & Schuster, M. (2024, June). Case Study on the Re-use Potential of Insulated Glass Units. In *Challenging Glass Conference Proceedings* (Vol. 9).
- Robeller, C., & Weinand, Y. (2015). Interlocking folded plate–integral mechanical attachment for structural wood panels. *International Journal of Space Structures*, 30(2), 111–122.
- Rohrmann, J. (2019). Design optimization in early project stages.

- Rota, A., Zaccaria, M., & Fiorito, F. (2023). Towards a quality protocol for enabling the reuse of post-consumer flat glass. *Glass Structures & Engineering*, 8(2), 235–254.
- Sandaker, B. N. (2007). *On Span and Space: exploring structures in architecture*. Routledge.
- Sedak GmbH & Co. KG. (n.d.). Production capabilities. Retrieved March 22, 2025, from <https://www.sedak.com/en/company/production-capabilities/>
- Trometer, S., & Krupna, M. (2006). Development and design of glass folded plate structures. *Journal of the international association for shell and spatial structures*, 47(3), 253–260.
- Van Dooren, T. T., & Ponk, I. A. A. (2014). *Transparent structural glass-glass connection: for the development of free-form frameless glass structures* [Master Thesis, Technical University of Eindhoven].
- Wang, Q., Ma, Y., Zhao, K., & Tian, Y. (2022). A comprehensive survey of loss functions in machine learning. *Annals of Data Science*, 9, 187–212. <https://doi.org/10.1007/s40745-020-00253-5>
- Wurm, J. (2007). *Glass structures: design and construction of self-supporting skins*. De Gruyter.
- Yost, J. R., Bolhassani, M., Chhadeh, P. A., Ryan, L., Schneider, J., & Akbarzadeh, M. (2022). Mechanical performance of polyhedral hollow glass units under compression. *Engineering Structures*, 254, 113730.
- Zhu, Y., & Filipov, E. T. (2024). Large-scale modular and uniformly thick origami-inspired adaptable and load-carrying structures. *Nature Communications*, 15(1), 2353.

APPENDIX

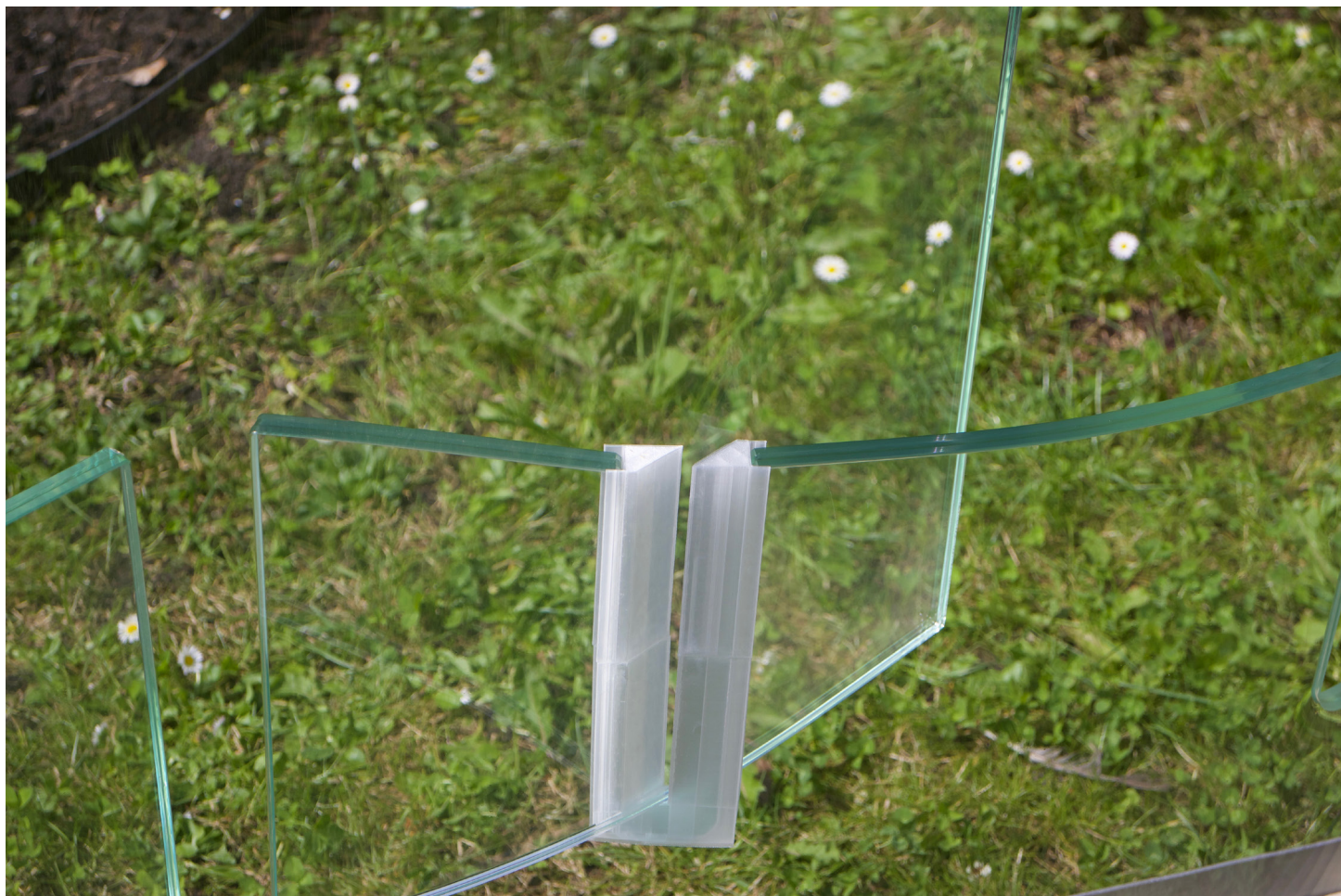
Physical model
1:1



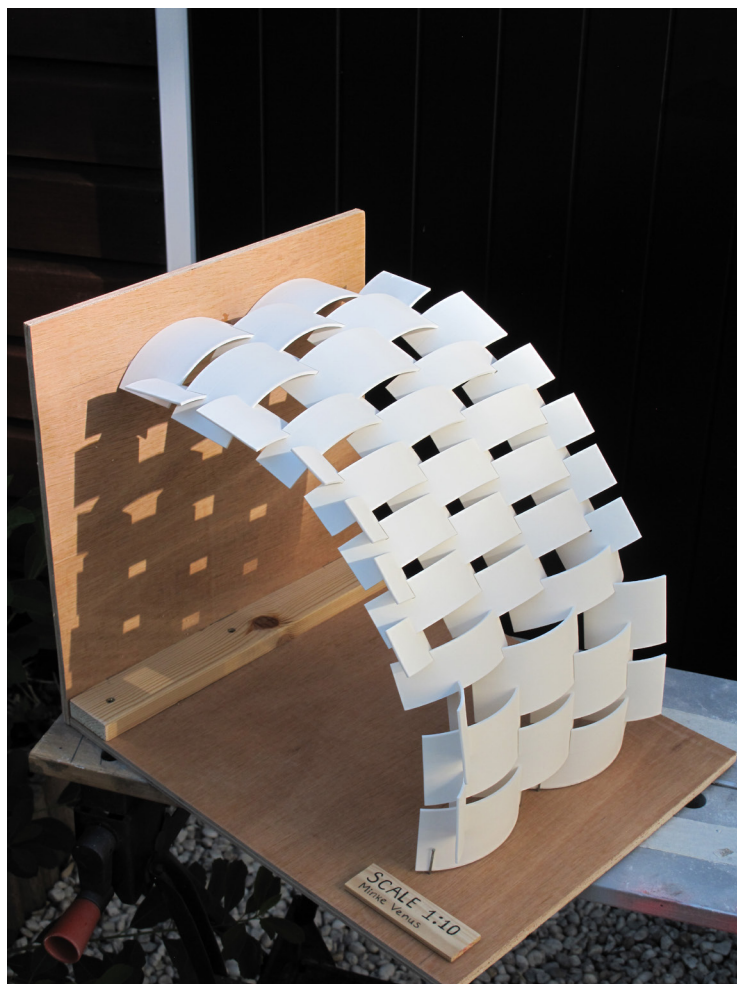
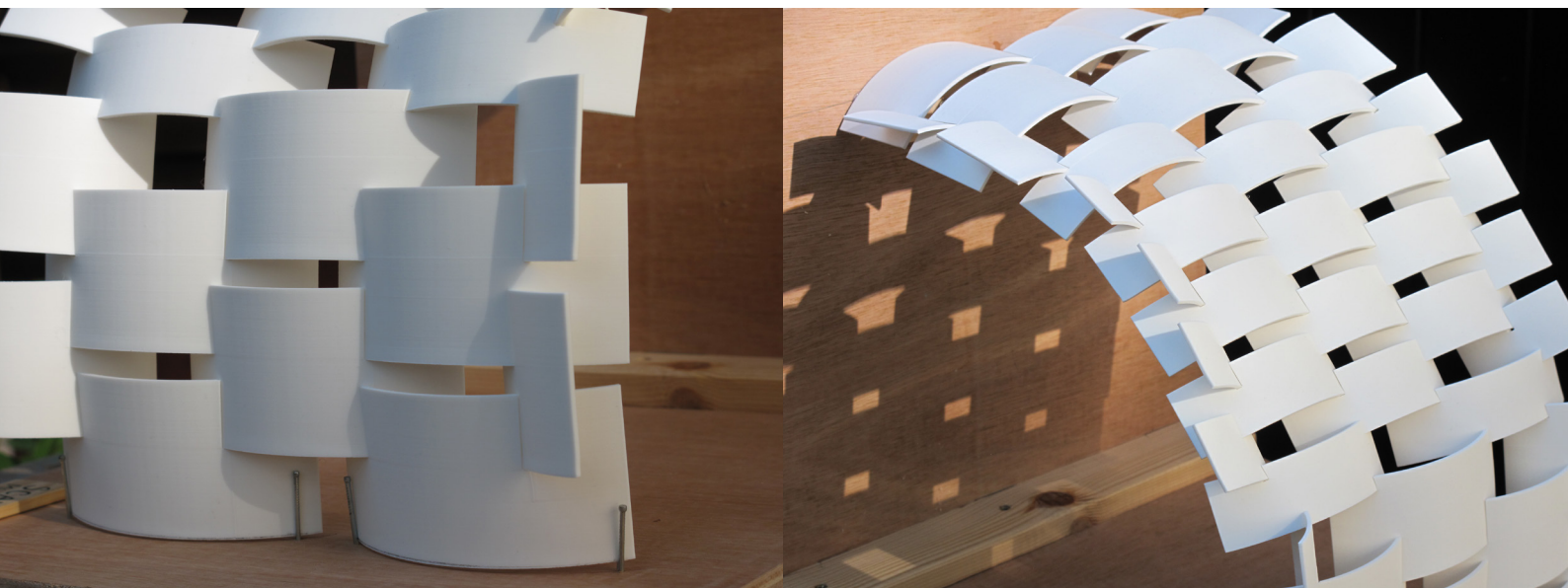
Physical model
1:1



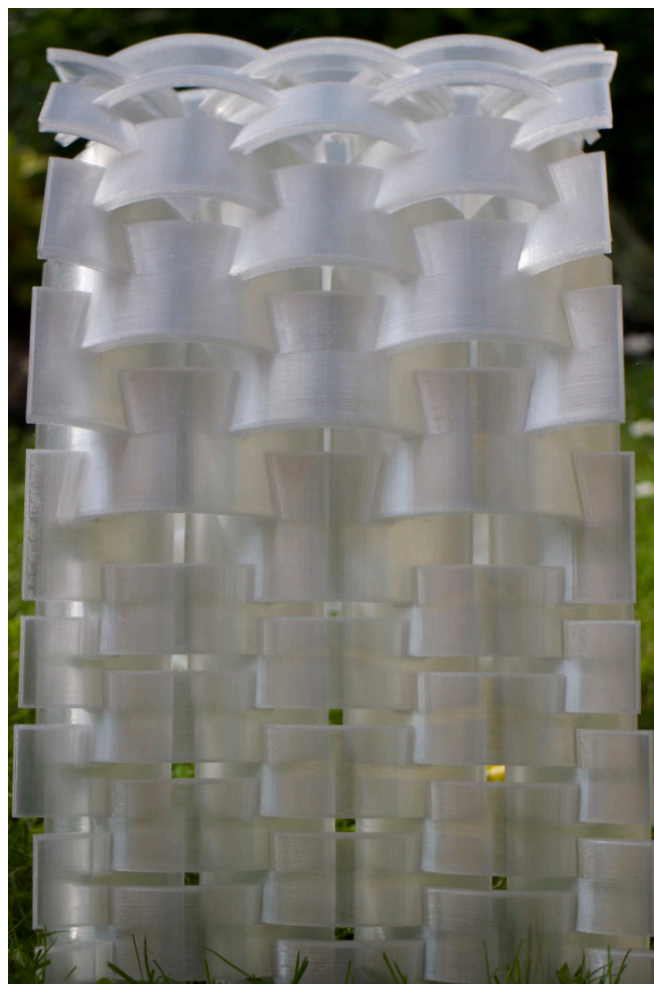
Physical model
1:1



Impression of the global structure
Scale model 1:10



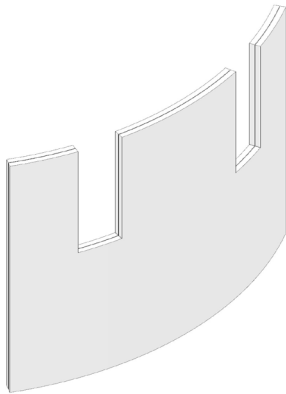
Impression of the global structure
Scale model 1:10



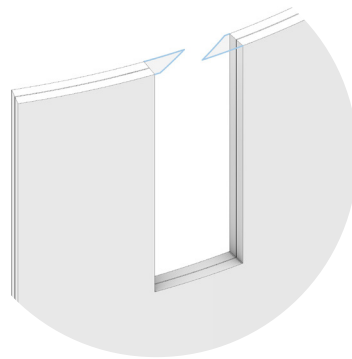
Parametric design workflow for slot infill creation

CREATION OF SLOT INFILL

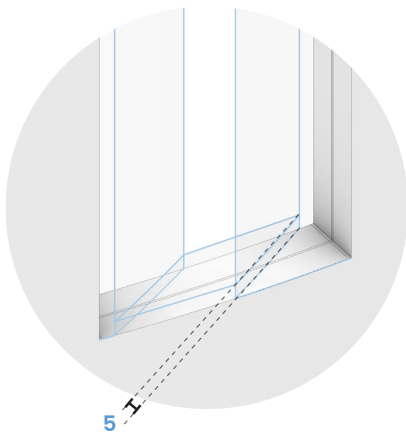
11 Final geometry for glass cut



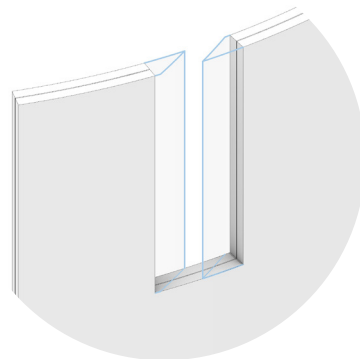
12 Creation surfaces for slot infill



14 Creation bottom volume

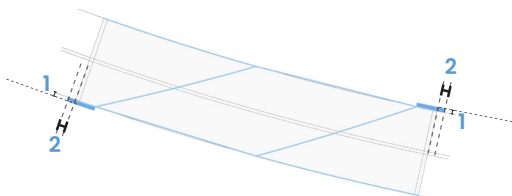


13 Creation infill volume

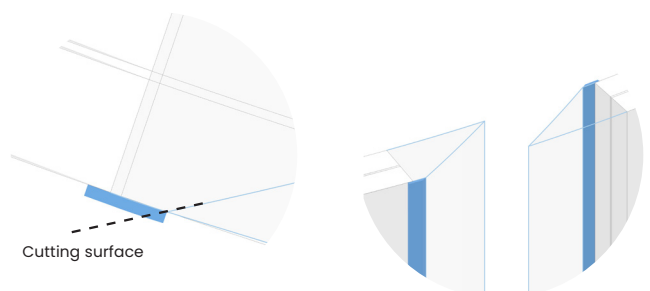


CREATION OF RECESSES

15 Creation of surfaces of first two recesses



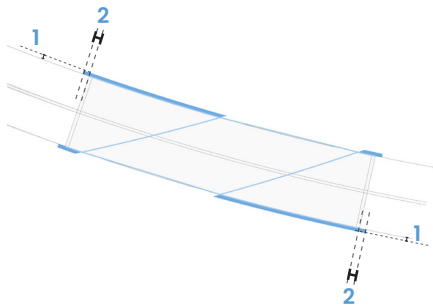
16 Creating the volumes by extruding the surfaces and cutting away the corners



Parametric design workflow for slot infill creation

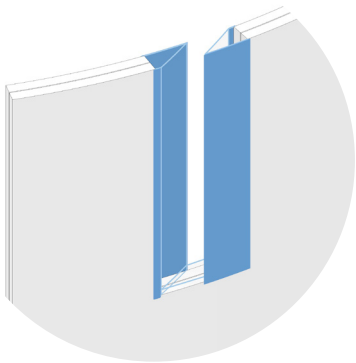
17

Creation surfaces of recess 2 and 3



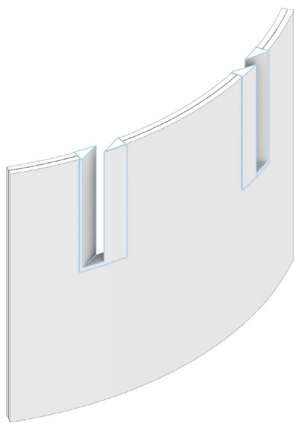
18

Creation of volumes by extruding the surfaces



20

Final geometry slot infill

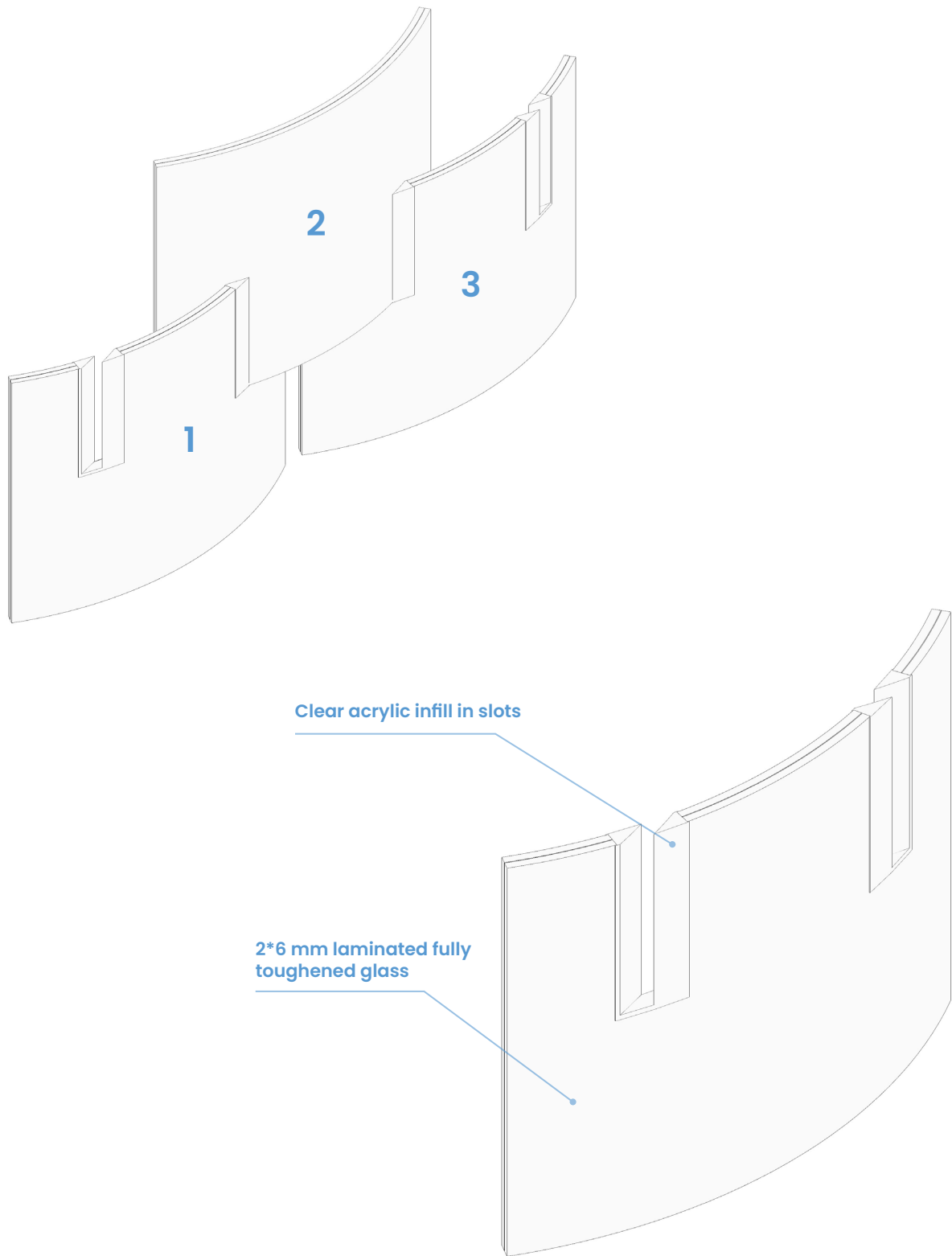


19

Creation of recess 4 and 5 at the bottom

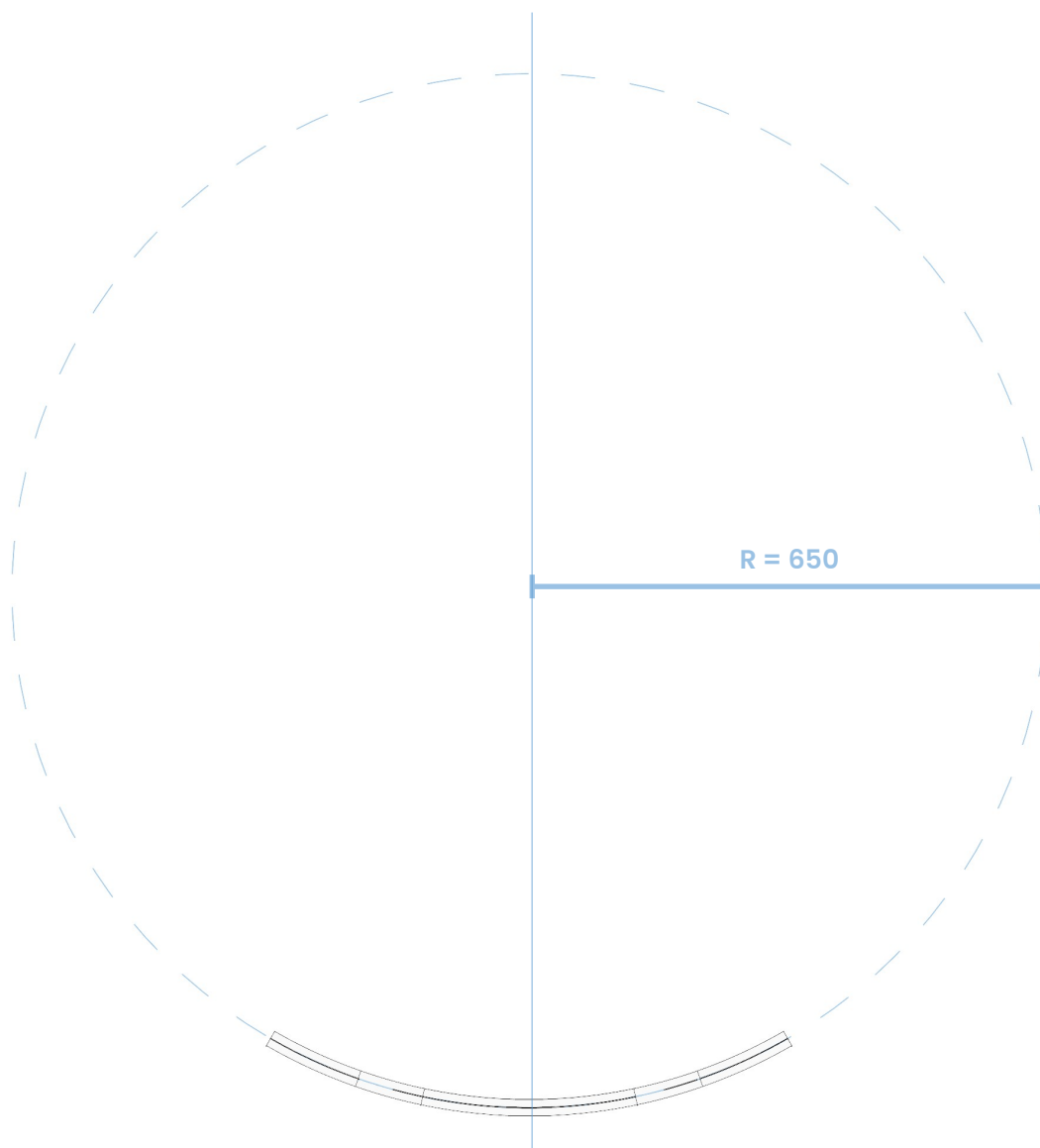


Technical drawings for fabrication of test setup



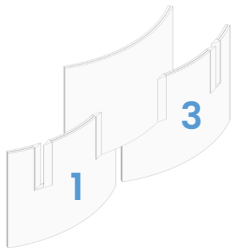
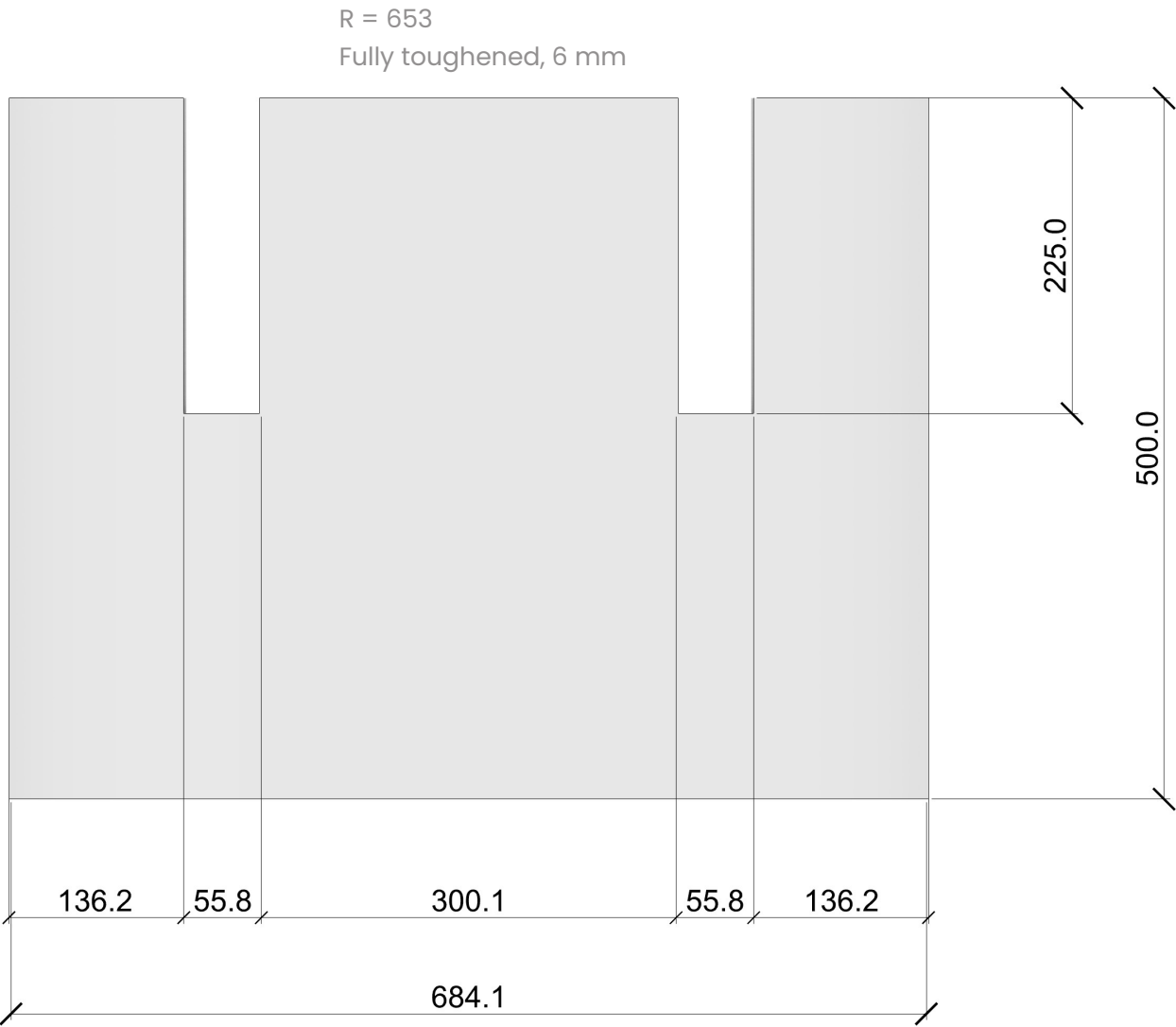
Technical drawings for fabrication of test setup

Bending radius - measured from the center line of the laminated panes



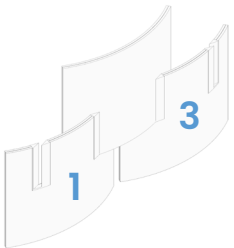
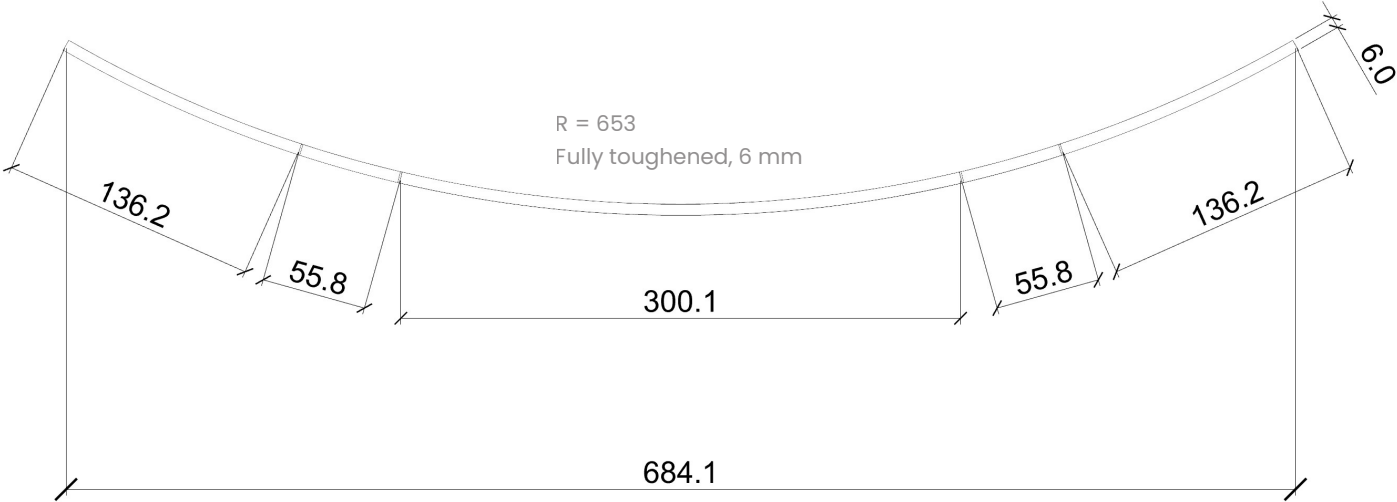
Technical drawings for fabrication of test setup

Front view - outer glass pane
Module 1 & 3



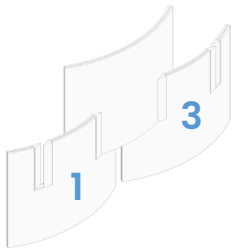
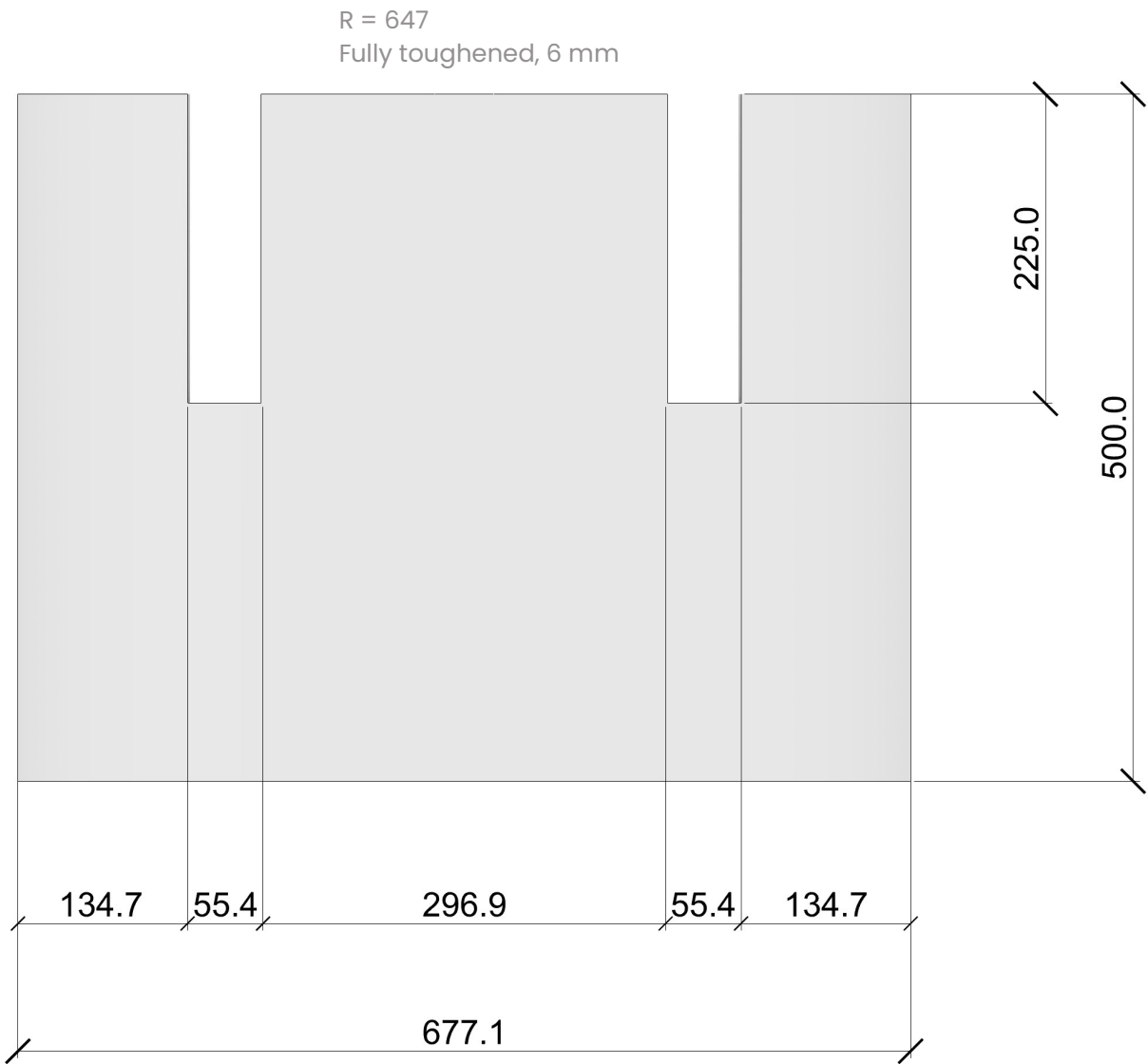
Technical drawings for fabrication of test setup

Top view - outer glass pane
Module 1 & 3



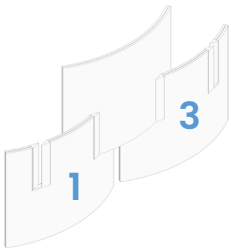
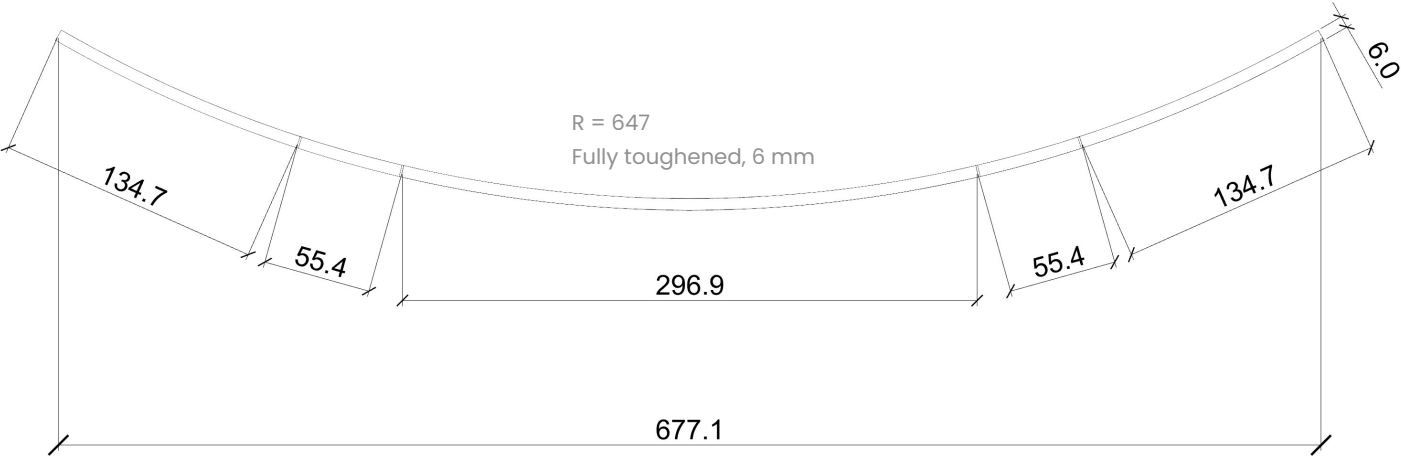
Technical drawings for fabrication of test setup

Front view - outer glass pane
Module 1 & 3



Technical drawings for fabrication of test setup

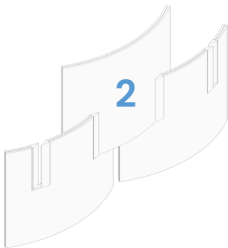
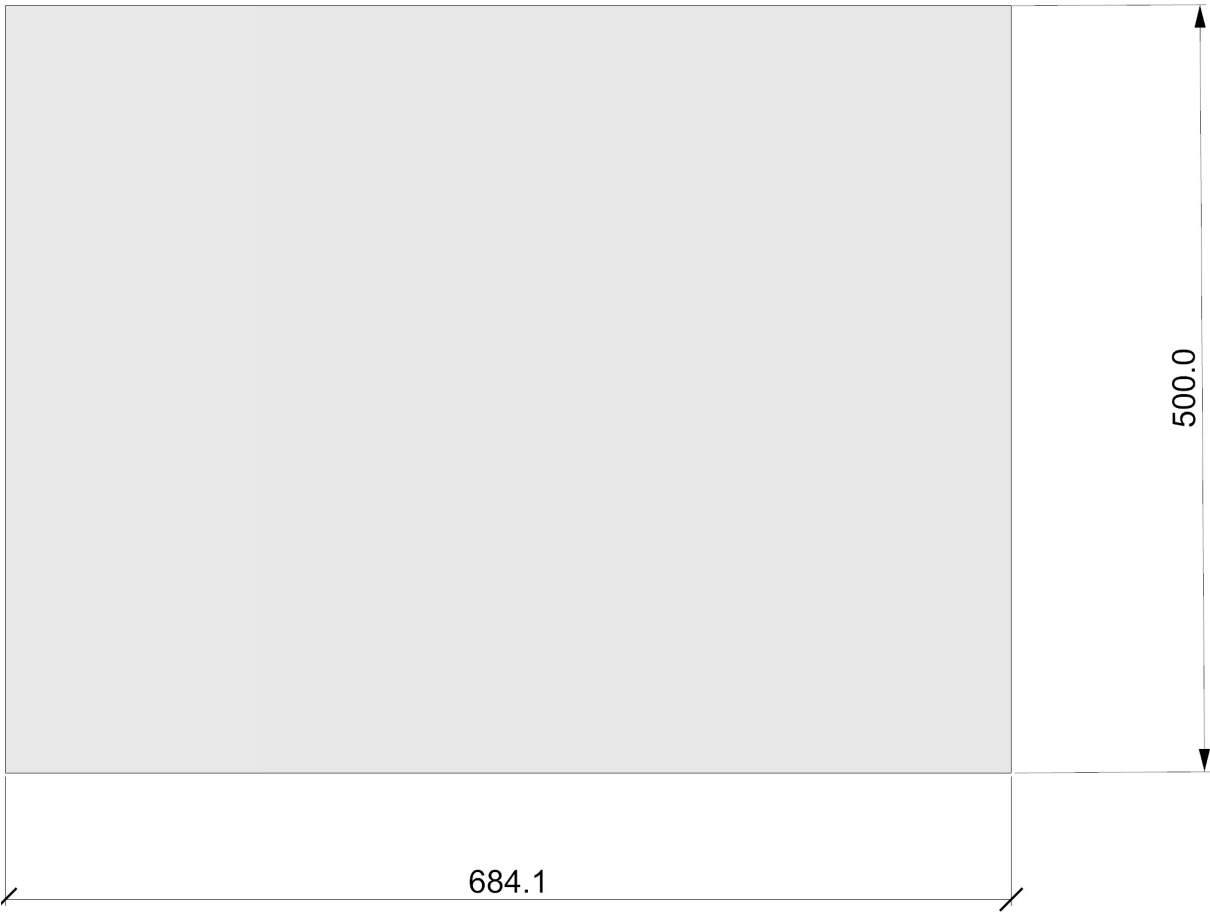
Top view - inner glass pane
Module 1 & 3



Technical drawings for fabrication of test setup

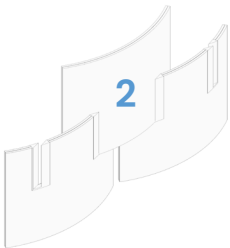
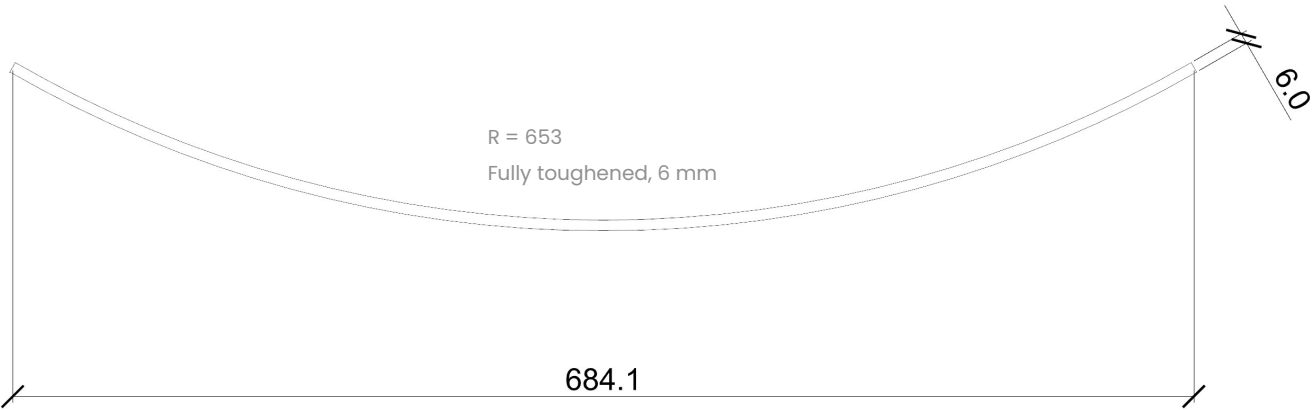
Front view - outer glass pane
Module 2

R = 653
Fully toughened, 6 mm



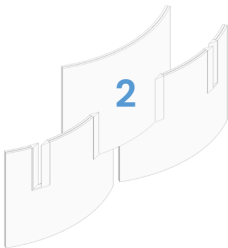
Technical drawings for fabrication of test setup

Top view – outer glass pane
Module 2



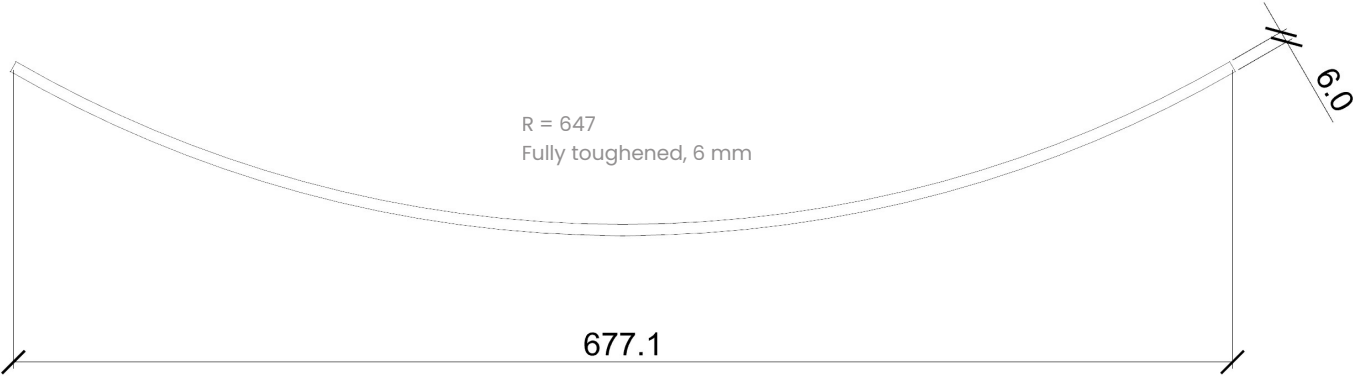
Technical drawings for fabrication of test setup

Front view – inner glass pane
Module 2



Technical drawings for fabrication of test setup

Top view – inner glass pane
Module 2



Tables

Parameter	Notation (unit)	Value
Density	$\rho(kg/m^3)$	1070
Shear modulus	$E(N/mm^2)$	0 - 4000
Poisson coefficient	$\nu(-)$	$\simeq 0.5$
Coefficient of thermal expansion	$\alpha_t(10^{-6} K^{-1})$	80
Tensile strength	$f_{t,PVB}(N/mm^2)$	≥ 20
Elongation at failure	$\epsilon_t(\%)$	≥ 300

Table 1: Poisson’s Ratio of PVB (Mesnil, 2019)

Property	symbol	unit	value
Density	ρ	kg/m ³	2500
Hardness (Knoop)	$HK_{0,1/20}$	GPa	6
Young’s modulus	E	GPa	70
Poisson’s ratio	ν	-	0.2 ^(a)
Tensile bending strength	f_t	MPa	45 ^(b)
Specific thermal capacity	c_p	J·kg ⁻¹ ·K ⁻¹	720
Thermal expansion coefficient (between 20 and 300°C)	α	K ⁻¹	$9 \cdot 10^{-6}$
Thermal conductivity	λ	W·m ⁻¹ ·K ⁻¹	1
Mean refractive index to visible radiation (380 to 780 nm)	N	-	1.5

Table 4: Properties of Soda-Lime Silica Glass (Louter, 2011)

Load Duration	Young’s relaxation modulus E(t) (MPa)											
	Temperature (°C)											
	10	15	20	25	30	35	40	45	50	55	60	
3 sec	1727	1585	1005	489	138	25	5.5	2.2	1.4	1.19	1.18	
10 sec	1723	1419	828	317	72	12	3.2	1.6	1.2	1.18	1.14	
30 sec	1713	1272	649	208	33	6	2.0	1.3	1.2	1.16	1.05	
1 min	1698	1168	556	139	19	4	1.7	1.2	1.2	1.13	0.95	
5 min	1600	924	324	57	7.1	2.0	1.25	1.2	1.1	0.93	0.71	
10 min	1514	816	254	34	4.5	1.7	1.20	1.17	1.07	0.81		
30 min	1356	639	143	15	2.9	1.4	1.19	1.13	0.91			
1 hour	1265	546	94	10	2.2	1.2	1.18	1.08	0.79			
6 hours	988	296	30	3.5	1.40	1.19	1.11	0.80				
12 hours	891	229	18	2.7	1.25	1.18	1.03	0.71				
1 day	776	158	12	2.0	1.20	1.16	0.92					
5 days	539	65	4.2	1.4	1.18	1.04						
1 week	489	52	3.7	1.3	1.18	0.99						
3 weeks	330	21	2.4	1.2	1.14	0.79						
1 month	292	17	2.1	1.2	1.12	0.74						
1 year*	81	3.8	1.2	1.1								
10 years*	16	1.7	1.2	0.9								
15 years*	13	1.6	1.2	0.8								
50 years*	5.9	1.2	1.1									

Table 2: Young’s Modulus of PVB (Mesnil, 2019)

Property	Abbr.	Soda lime silica glass
Transition temperature	T_g	550-600°C
Annealing temperature	T_a	520-600°C
Melting temperature	T_m	1500°C
Young’s modulus	E	70 GPa
Poisson’s ratio	ν	0.2-0.25
Density	ρ	2500 kg/m ³
Fracture toughness	K_{Ic}	0.72-0.82 MPa·m ^{1/2}

Table 3: Properties of Soda Lime Silica Glass (Datsiou, 2017)

Characteristic tensile bending strength	
Annealed	45 MPa
Heat-strengthened	70 MPa
Fully tempered	120 MPa

Table 5: Characteristic tensile bending strength values for differeng glass types (Louter, 2011)

	Soda lime Glass
Density [kg/m ³]	2490
Scratch hardness on the Mohs hardness scale	6-7
Coefficient of mean linear expansion $\alpha 10^{-6}$ [K ⁻¹] (20-300 °C)	8.4
Thermal conductivity [W/mK]	1.06
Softening point [°C]	720
Processing temperature [°C]	1040
Modulus of elasticity E [N/mm ²]	70000
Poisson Ratio μ	0.2
Bending Strength [N/mm ²]	30
Compressive Strength [N/mm ²]	700-900
Tensile strength [N/mm ²]	30-80
(at constant load)	7

Table 6: Properties of Soda Lime Glass (Rammig, 2022)

Tables

	Class	D18	D24	D27	D30	D35	D40	D45	D50	D55	D60	D65	D70	D75	D80
Strength properties in N/mm²															
Bending	$f_{m,0,k}$	18	24	27	30	35	40	45	50	55	60	65	70	75	80
Tension parallel	$f_{t,0,k}$	11	14	16	18	21	24	27	30	33	36	39	42	45	48
Tension perpendicular	$f_{t,90,k}$	0,6	0,6	0,6	0,6	0,6	0,6	0,6	0,6	0,6	0,6	0,6	0,6	0,6	0,6
Compression parallel	$f_{c,0,k}$	18	21	22	23	25	27	28	30	31	33	34	35	36	38
Compression perpendicular	$f_{c,90,k}$	4,8	4,9	5,1	5,3	5,4	5,5	5,8	6,2	6,6	7,0	8,0	9,0	9,0	9,0
Shear	$f_{v,k}$	3,5	3,7	3,8	3,9	4,1	4,2	4,4	4,5	4,7	4,8	5,0	5,0	5,0	5,0
Stiffness properties in kN/mm²															
Mean modulus of elasticity parallel bending	$E_{m,0,mean}$	9,5	10,0	10,5	11,0	12,0	13,0	13,5	14,0	15,5	17,0	18,5	20,0	22,0	24,0
Characteristic modulus of elasticity parallel bending	$E_{m,0,k}$	8,0	8,4	8,8	9,2	10,1	10,9	11,3	11,8	13,0	14,3	15,5	16,8	18,5	20,2
Mean modulus of elasticity perpendicular	$E_{m,90,mean}$	0,64	0,67	0,70	0,74	0,80	0,87	0,90	0,94	1,04	1,14	1,24	1,34	1,47	1,61
Mean shear modulus	G_{mean}	0,59	0,63	0,66	0,69	0,75	0,81	0,84	0,88	0,97	1,06	1,16	1,25	1,38	1,50
Density in kg/m³															
Characteristic density	ρ_k	475	485	510	530	540	550	580	620	660	700	800	900	900	900
Mean density	ρ_{mean}	570	580	610	640	650	660	700	740	790	840	960	1080	1080	1080
<p>NOTE 1 Values given above for tension strength, compression strength, shear strength, char. modulus of elasticity in bending, mean modulus of elasticity perpendicular to grain and mean shear modulus, have been calculated using the equations given in EN 384.</p> <p>NOTE 2 The tabulated properties are compatible with timber at a moisture content consistent with a temperature of 20 °C and a relative humidity of 65 %, which corresponds to a moisture content of 12% for most species.</p> <p>NOTE 3 Characteristic values for shear strength are given for timber without fissures, according to EN 408.</p>															

Table 7: Strength properties of hardwoods
(European Committee for Standardization, 2016)

Property	C24	C27	C30	C35	C40
Strength values					
Bending parallel to grain $f_{m,k}$	24	27	30	35	40
Tension parallel to grain $f_{t,0,k}$	14,5	16,5	19	22,5	26
Tension perpendicular to grain $f_{t,90,k}$	0,4	0,4	0,4	0,4	0,4
Compression parallel to grain $f_{c,0,k}$	21	22	24	25	27
Compression perpendicular to grain $f_{c,90,k}$	2,5	2,5	2,7	2,7	2,8
Shear $f_{v,k}$	4,0	4,0	4,0	4,0	4,0
Stiffness value for capacity analysis					
Elastic modulus $E_{0,05}$	7 400	7 700	8 000	8 700	9 400
Stiffness values for deformation calculations, mean values					
Elastic modulus parallel to grain $E_{0,mean}$	11 000	11 500	12 000	13 000	14 000
Elastic modulus perpendicular to grain $E_{90,mean}$	370	380	400	430	470
Shear modulus G_{mean}	690	720	750	810	880
Density					
Density $\rho_k^{1)}$	350	360	380	390	400
Density $\rho_{mean}^{1)}$	420	430	460	470	480

Table 8: Properties of structural timber
(Isaksson et al., 2022)

Grasshopper Python code 1

Experimenting with a consistent interlocking angle

Chapter 7.1.1

```

1  #Import libraries
2  import Rhino.Geometry as rg
3  import math
4
5  #Define base plane as world YZ plane
6  base_plane = rg.Plane.WorldYZ
7
8  current_plane = base_plane
9  planes = []
10
11 #Read angle (in degrees) from the parameter angle_step
12 a = angle_step
13
14 for i in range(n):
15     #Add current_plane to the list
16     planes.append(current_plane)
17
18     #Copy current_plane for rotation
19     rotated_plane = current_plane.Clone()
20
21     #Rotate copied plane around its local Z-axis
22     rg.Plane.Rotate(rotated_plane, math.radians(-a), rotated_plane.ZAxis)
23
24     #Clone rotated plane to apply the displacement to it
25     moved_plane = rotated_plane.Clone()
26
27     #Create vector on local y-axis with size 'h'
28     move_vector = rotated_plane.YAxis * h
29
30     #Move cloned plane along the Y axis with distance h
31     moved_plane.Origin += move_vector
32
33     #Use this relocated plane as the basis for the next step
34     current_plane = moved_plane

```

```

1  #Separate even and odd planes
2  even_planes = []
3  odd_planes = []
4
5  for i, pl in enumerate(planes):
6      if i % 2 == 0:
7          even_planes.append(pl)
8      else:
9          odd_planes.append(pl)

```

Grasshopper Python code 2

Experimenting with different interlocking angles

Chapter 7.1.1

```

1  #Import libraries
2  import Rhino.Geometry as rg
3  import math
4
5  #Create XY world base plane
6  base_plane = rg.Plane.WorldYZ
7
8  current_plane = base_plane
9  planes = []
10
11 #Define arch midpoint
12 mid = n // 2
13
14 for i in range(n):
15     #Copy base plane
16     planes.append(current_plane)
17
18     #Make sure angle accumulates and mirrors
19     if i <= mid:
20         a = angle_step * i
21     else:
22         a = angle_step * (n - 1 - i)
23
24     #Copy base plane for rotation
25     rotated_plane = current_plane.Clone()
26
27     #Rotate the cloned plane by -a degrees around its local Z-axis
28     rg.Plane.Rotate(rotated_plane, math.radians(-a), rotated_plane.ZAxis)
29
30     #Clone rotated plane for translation
31     moved_plane = rotated_plane.Clone()
32
33     #Create a vector along the local Y-axis scaled by h
34     move_vector = rotated_plane.YAxis * h
35
36     #Move cloned plane along the vector
37     moved_plane.Origin += move_vector
38
39     #Set translated plane as the current plane for next iteration
40     current_plane = moved_plane

```

Grasshopper Python code 3

Experimenting with alternating module heights

Chapter 7.1.1

1/2

```
1  #Import libraries
2  import Rhino.Geometry as rg
3  import math
4  import Grasshopper
5
6  #Ensure there are at least 2 planes
7  if n < 2:
8      n = 2
9
10 #Ensure the number of clusters is at least 1
11 if num_clusters < 1:
12     num_clusters = 1
13
14 #Calculate the maximum number of planes per cluster
15 cluster_size = int(math.ceil(n / float(num_clusters)))
16
17 #Set the starting plane to the world YZ plane
18 base_plane = rg.Plane.WorldYZ
19 current_plane = base_plane
20
21 #List to store all clusters (each cluster is a list of planes)
22 all_planes = []
23
24 for cluster_index in range(num_clusters):
25     #Create a new list for this cluster's planes
26     current_cluster = []
27
28     for i in range(cluster_size):
29         #Compute the "absolute" index across all clusters
30         global_index = cluster_index * cluster_size + i
31         #Stop if we've already assigned all n planes
32         if global_index >= n:
33             break
```

Grasshopper Python code 3

Experimenting with alternating modul heights

Chapter 7.1.1

2/2

```

38     #Clone and rotate the current plane
39     rotated_plane = current_plane.Clone()
40     rg.Plane.Rotate(rotated_plane, math.radians(-angle_step), rotated_plane.ZAxis)
41
42     #Define the move distance and compute the move vector along the local Y axis
43     move_dist = 300
44     move_vector = rotated_plane.YAxis * move_dist
45
46     #Clone rotated plane for translation
47     moved_plane = rotated_plane.Clone()
48
49     #Move cloned plane along the Y axis with move_dist
50     #move_dist = manual adaptable given the different module heights
51     moved_plane.Origin += move_vector
52
53     #Update current_plane for the next iteration
54     current_plane = moved_plane
55
56     #Add this cluster's list of planes to all_planes
57     all_planes.append(current_cluster)
58
59
60     #Convert the list of clusters into a Grasshopper DataTree (one branch per cluster)
61     tree = Grasshopper.DataTree[object]()
62     for i, cluster in enumerate(all_planes):
63         for p1 in cluster:
64             path = Grasshopper.Kernel.Data.GH_Path(i)
65             tree.Add(p1, path)
66
67     #Output
68     planes = tree

```

```

1     #Separate even and odd planes
2     even_planes = []
3     odd_planes = []
4
5     for i, p1 in enumerate(planes):
6         if i % 2 == 0:
7             even_planes.append(p1)
8         else:
9             odd_planes.append(p1)

```

Grasshopper Python code 4

Generative algorithm

Chapter 7.1.2

1/4

```

1  #Import libraries
2  import Rhino.Geometry as rg
3  import math
4  import random
5  from Grasshopper import DataTree
6  from Grasshopper.Kernel.Data import GH_Path
7  from System import Int32
8
9  #Amount of patterns you want to calculate
10 n_samples = 1
11
12 #Inputs
13 amount_of_modules = int(amount_of_modules)
14 amount_of_clusters = int(amount_of_clusters)
15 module_heights = [int(h) for h in module_heights]
16 clusterModes = list(clusterModes)
17 angleChoice_start = list(angleChoice)
18
19 #Calculate amount of modules in a cluster (cluster_sizes)
20 if amount_of_clusters == 1:
21     cluster_sizes = [amount_of_modules]
22 else:
23     base = amount_of_modules // amount_of_clusters
24     rem = amount_of_modules % amount_of_clusters
25     cluster_sizes = [
26         base + 1 if i < rem else base
27         for i in range(amount_of_clusters)
28     ]
29
30 #Define start index numbers for different clusters and add to the list
31 starts = []
32 cum = 0
33 for sz in cluster_sizes:
34     starts.append(cum)
35     cum += sz
36
37 #Define index numbers before a next cluster starts
38 prev_starts = []
39 for s in starts:
40     if s > 0:
41         prev_starts.append(s - 1)

```


Grasshopper Python code 4

Generative algorithm

Chapter 7.1.2

2/4

```

42
43 #Add clusters to the list if a cluster has at least 1 module
44 valid_clusters = []
45 for i, module_amount in enumerate(cluster_sizes):
46     if module_amount > 0:
47         valid_clusters.append((i, module_amount))
48
49 #Setup of data structures and lookup tables
50 planes_tree = DataTree[rg.Plane]()
51 patterns_tree = DataTree[Int32]()
52 angle_map = [10, -10, 2, -2]
53 rad_map = [math.radians(a) for a in angle_map]
54
55 #Create list to store angles used for output
56 angles_used = []
57
58
59 #Set max. Y-value to prevent negative, unrealistic curves
60 threshold = -1000
61
62
63 for i in range(n_samples):
64     path = GH_Path(i)
65     current = rg.Plane.WorldYZ
66     #create list pattern to store all clusters
67     pattern = []
68     #add all angle choices in the list angles
69     angles = angleChoice_start[:]
70
71     #Create list of module heights for each cluster
72     for ci, module_count in valid_clusters:
73         mode = clusterModes[ci]
74         if mode == 0:
75             block = [module_heights[0]] * module_count
76         elif mode == 1:
77             block = [module_heights[1]] * module_count
78         elif mode == 2:
79             block = [random.choice(module_heights) for _ in range(module_count)]
80         else:
81             block = [module_heights[0]] * module_count
82         pattern.extend(block)

```

Grasshopper Python code 4

Generative algorithm

Chapter 7.1.2

3/4

```

83
84     #Add angles with angle choice 0 if amount of planes < amount of angles input
85     L = len(pattern)
86     if len(angles) < L:
87         angles += [0] * (L - len(angles))
88     else:
89         angles = angles[:L]
90
91     #Loop through each plane in the structure
92     for idx, H in enumerate(pattern):
93         #add world YZ plane to the data tree
94         planes_tree.Add(current, path)
95
96         #Retrieve angle index
97         angle_idx = angles[idx]
98         #Link angle map value to correct angle index
99         angle_deg = angle_map[angle_idx]
100        rad        = rad_map[angle_idx]
101
102        #Determine shift on Y axis depending on module height
103        H_prev = pattern[idx-1] if idx > 0 else None
104        H_next = pattern[idx+1] if idx < len(pattern)-1 else None
105
106        if idx in prev_starts:
107            # eerst checken of H_next geen None is
108            if H_next is not None and H_next <= H:
109                move_dist = H - (0.5 * H_next) + 25
110            else:
111                move_dist = H - (0.5 * H) + 25
112
113        elif H_next is None:
114            move_dist = (0.5 * H) + 25
115
116        elif H_next < H:
117            move_dist = H - (0.5 * H_next) + 25
118
119        elif H_next > H:
120            move_dist = H - (0.5 * H) + 25
121
122        elif H_prev is not None and H_prev <= H:
123            move_dist = H - (0.5 * H) + 25

```

Grasshopper Python code 4

Generative algorithm

Chapter 7.1.2

4/4

```

123         move_dist = H - (0.5 * H) + 25
124
125     else:
126         move_dist = H - (0.5 * H_next) + 25
127
128     #Create plane
129     temp_plane = rg.Plane(current)
130     #Rotate plane
131     temp_plane.Rotate(rad, temp_plane.ZAxis, temp_plane.Origin)
132     #Move along Yaxis with move_dist
133     temp_plane.Origin += temp_plane.YAxis * move_dist
134
135     #Check if temporary plane doesn't move beyond the boundary distance
136     if temp_plane.Origin.Y < threshold:
137         #If it does, force plane to rotate in other direction
138         override_deg = -2
139         override_rad = math.radians(override_deg)
140         new_plane = rg.Plane(current)
141         new_plane.Rotate(override_rad, new_plane.ZAxis, new_plane.Origin)
142         new_plane.Origin += new_plane.YAxis * move_dist
143         angles_used.append(override_deg)
144     else:
145         #Just use the temp_plane
146         new_plane = temp_plane
147         angles_used.append(angle_deg)
148
149     #Save pattern to branch
150     patterns_tree.Add(Int32(H), path)
151
152     #Update current plane for next iteration
153     current = new_plane
154
155 #Outputs
156 planes = planes_tree
157 modulePattern = patterns_tree
158 spanY_list = [
159     abs(branch[branch.Count - 1].Origin.Y - rg.Plane.WorldYZ.Origin.Y)
160     for branch in planes_tree.Branches
161 ]
162 angles_list = angles_used

```

Grasshopper Python code 5

Projection of module geometry on generated planes

Chapter 7.1.2

```
1  import Rhino.Geometry as rg
2
3  output_geometries = []
4
5  for i in range(len(planes)):
6      plane = planes[i]
7      height = heights[i]
8      current_amount = amounts[i]
9
10     if height == 300 and current_amount == 2:
11         geom = geom_300_2
12     elif height == 300 and current_amount == 3:
13         geom = geom_300_3
14     elif height == 500 and current_amount == 2:
15         geom = geom_500_2
16     elif height == 500 and current_amount == 3:
17         geom = geom_500_3
18     else:
19         continue
20
21     #Create a list of geometries
22     if not isinstance(geom, list):
23         geom = [geom]
24
25     xform = rg.Transform.PlaneToPlane(base_plane, plane)
26
27     for srf in geom:
28         g = srf.Duplicate()
29         g.Transform(xform)
30         output_geometries.append(g)
```

Grasshopper Python code 6
Objective 2: module height alternation
Chapter 7.1.4

```
1  #Create list to store differences between subsequent module heights
2  Differences = []
3
4  for i in range (len(modulePattern)-1):
5      current_height = modulePattern[i]
6      next_height = modulePattern [i+1]
7
8      differences = abs(current_height - next_height)
9
10     Differences.append(differences)
11
12 #Metric
13 Total_difference = sum(Differences)
```

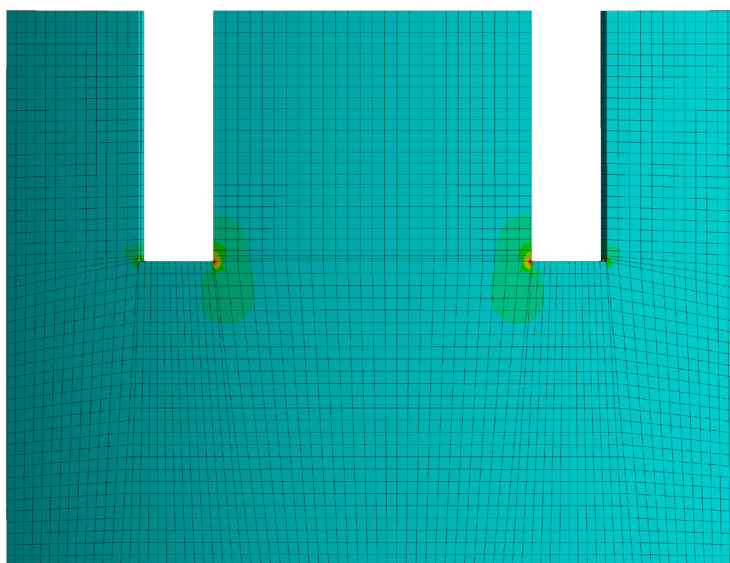
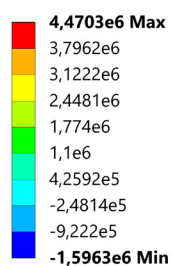

Other Ansys analysis results

Results for 2x8 mm laminated glass – front and back view

Chapter 7.2.3

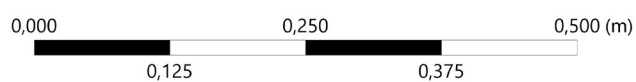
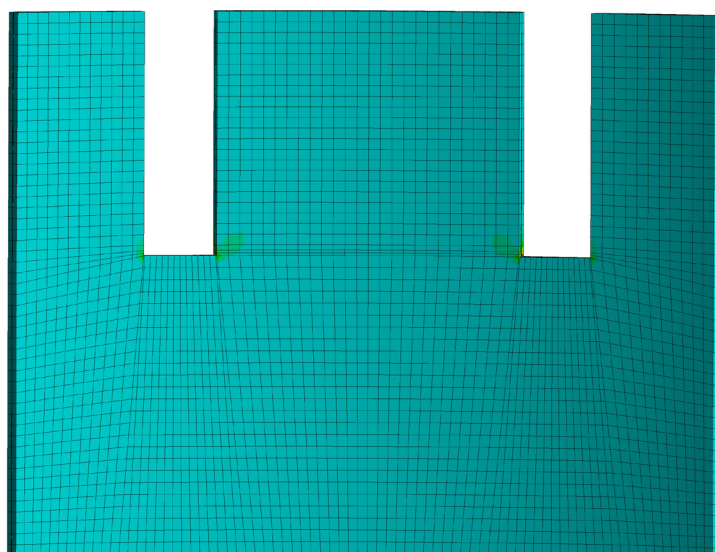
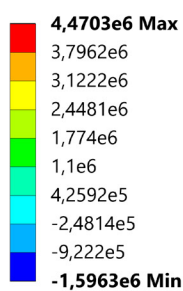
A: Static Structural

Maximum Principal Stress
Type: Maximum Principal Stress
Unit: Pa
Time: 1 s
02/05/2025 12:29:54

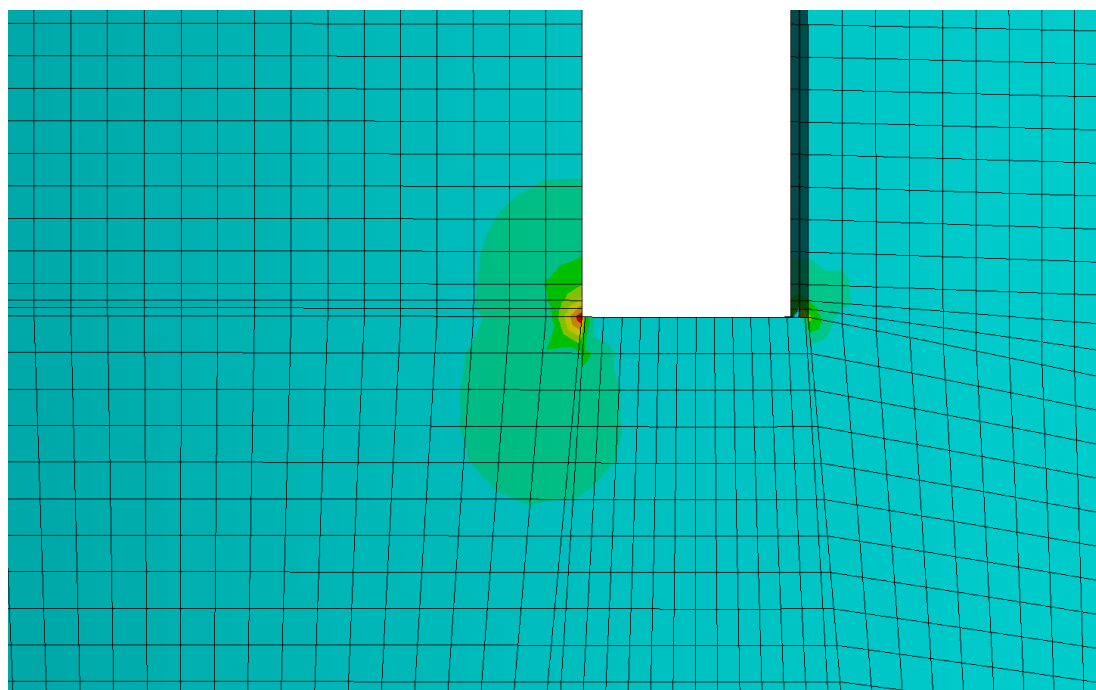
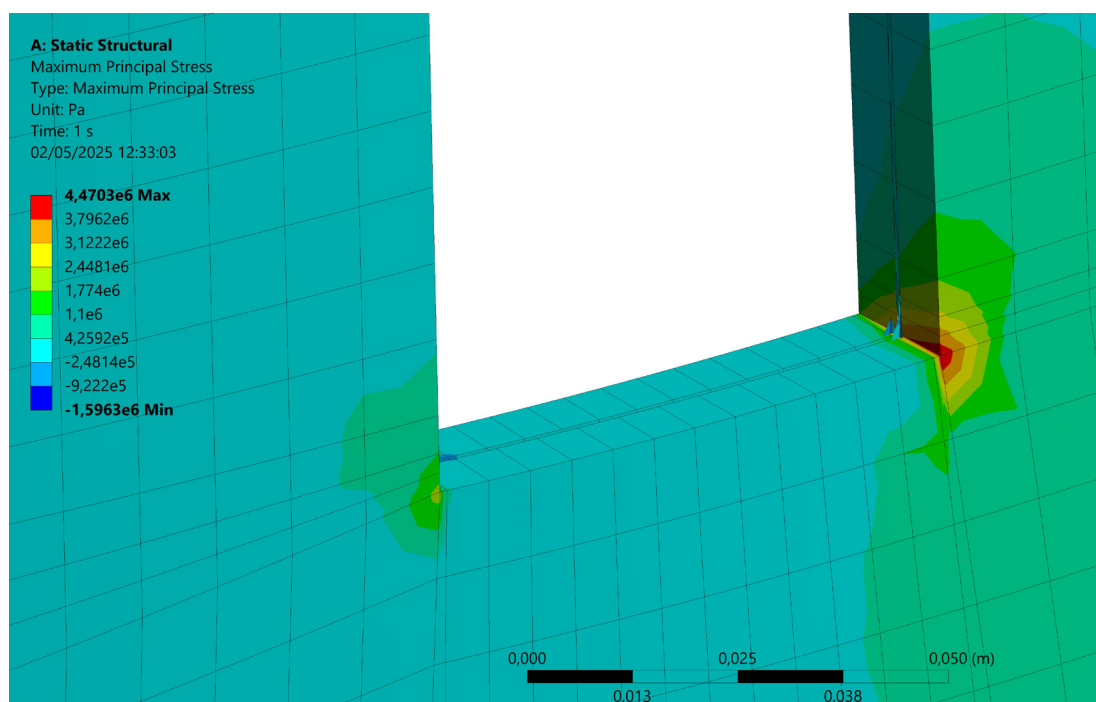


A: Static Structural

Maximum Principal Stress
Type: Maximum Principal Stress
Unit: Pa
Time: 1 s
02/05/2025 12:31:25



Other Ansys analysis results
Results for 2x8 mm laminated glass – perspective and front slot view
Chapter 7.2.3



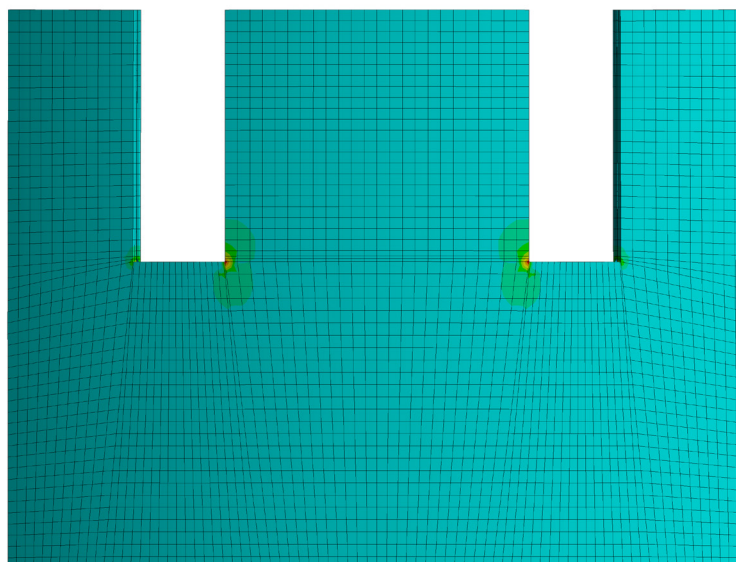
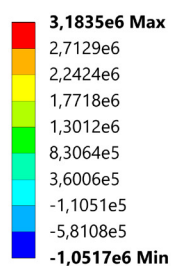
Other Ansys analysis results

Results for 2x10 mm laminated glass – front and back view

Chapter 7.2.3

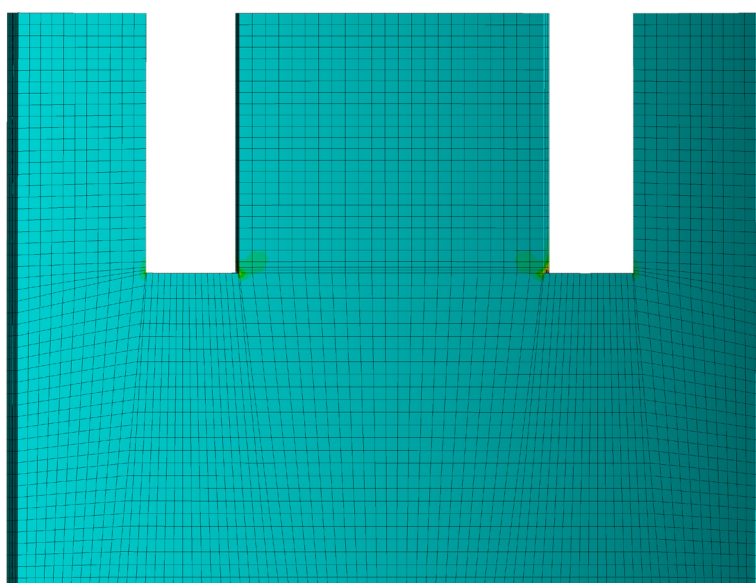
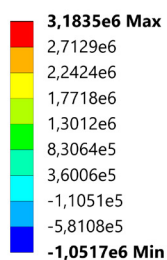
A: Static Structural

Maximum Principal Stress
Type: Maximum Principal Stress
Unit: Pa
Time: 1 s
02/05/2025 12:48:29



A: Static Structural

Maximum Principal Stress
Type: Maximum Principal Stress
Unit: Pa
Time: 1 s
02/05/2025 12:49:18



Other Ansys analysis results
Results for 2x10 mm laminated glass – perspective and front slot view
Chapter 7.2.3

